Implantable Antennas for Biomedical Applications

THÈSE N^O 5110 (2011)

PRÉSENTÉE LE 2 SEPTEMBRE 2011
À LA FACULTÉ SCIENCES ET TECHNIQUES DE L'INGÉNIEUR
LABORATOIRE D'ÉLECTROMAGNÉTISME ET ACOUSTIQUE
PROGRAMME DOCTORAL EN GÉNIE ÉLECTRIQUE

ÉCOLE POLYTECHNIQUE FÉDÉRALE DE LAUSANNE

POUR L'OBTENTION DU GRADE DE DOCTEUR ÈS SCIENCES

PAR

Francesco MERLI

acceptée sur proposition du jury:

Prof. J.-Ph. Thiran, président du jury
Prof. A. Skrivervik Favre, directrice de thèse
Prof. A. Freni, rapporteur
Prof. K. Ito, rapporteur
Prof. F. Rachidi-Haeri, rapporteur

EPFL

ÉCOLE POLYTECHNIQUE
FÉDÉRALE DE LAUSANNE

Suisse
2011

Alla mia famiglia,
dal Nonno a Giorgio

Abstract

Since the introduction of implantable pacemakers in the early 1960s, implantable medical devices have become more and more interesting for healthcare services. Nowadays, the devices designed to monitor physiological data from inside the human body have great promises to provide major contributions to disease prevention, diagnosis and therapy. Furthermore, minimally invasive devices allow reducing hospitalization terms, thus improving the patients' quality of life.

Planning how transmitting information from inside the body to the external world requires a multidisciplinary approach. Such a challenging task combines concepts, models and applied solutions drawing from several fields, including electromagnetism, electronics, biology, and package engineering. More specifically, this work focuses on antennas to be integrated in implantable devices with far field data telemetry capabilities. Thus, in collaboration with the Laboratory of Microengineering for Manufacturing 2 and the Laboratory of Stem Cell Dynamics at the École Polytechnique Fédérale de Lausanne, we have designed, assembled and successfully tested in vivo a Body Sensor Node for telemedicine use. Among its components, the antenna plays a key role. The presence of the human body, which is "hostile" to radio frequency propagation, the need of miniaturization and the necessity of biocompatibility participate all in determining the final characteristics of implantable antennas. Taking into account a wide range of technical and medical concerns, this thesis addresses the analysis, design, realization, in vitro characterization and in vivo testing of such radiators.

The analysis is built upon the fundamental theory of antennas in lossy matter, the features of electrically small radiators and the modeling of the human body. This approach allows a clear identification of the main challenges related to implantable antennas, thus setting a solid base for the work presented further on. For instance, biocompatible insulation was found of paramount importance. Accordingly, we have elaborated and implemented physical and mathematical models showing that the proper choice of insulating layers substantially improves the radiation efficiency. The design of implantable antennas takes into account theoretical inputs, packaging considerations and technological constraints. Thus, we propose an effective design strategy that combines these three aspects, and that has been applied to design the Multilayered Spiral Antenna. This radiator integrates with the necessary electronics, power supply and bio-sensor so as to form a Body Sensor Node. In vitro characterization is discussed and carried out for the implantable antenna itself, as well as for the entire implantable device. More specifically, the former characterization is detailed so as to give the possibility of prototyping antennas at the component level. Finally, in vivo testing of the proposed Body Sensor Node was performed in a porcine animal. We believe that our results pave the way for future research oriented to the making of complete telemedicine systems.

Keywords: antennas in lossy matter, biocompatible insulation, body centric wireless communications, Body Sensor Node (BSN), electrically small antennas, implantable antennas, Medical Device Radiocommunications Service (MedRadio), Medical Implanted Communication System (MICS), Multilayered Spiral Antenna (MSA), Spherical Wave Expansion (SWE).

Sintesi

I dispositivi elettronici impiantabili, dall'introduzione dei pacemaker nei primi anni '60, sono diventati sempre più interessanti per le applicazioni mediche. Attualmente i sistemi per monitorare i valori fisiologici dall'interno del corpo umano mostrano un grande potenziale per la prevenzione, la diagnosi e la terapia. Da sottolineare inoltre che i dispositivi di ultima generazione, sempre meno invasivi, consentono di ridurre i periodi di ospedalizzazione e di migliorare la qualità della vita dei pazienti. La trasmissione di informazioni dall'interno del corpo umano verso il mondo esterno richiede un intervento multidisciplinare. Solo l'utilizzo di strumenti messi a punto in ambiti di ambiti scientifici diversi, quali l'elettromagnetismo, la biologia e l'ingegneria, permette di raggiungere risultati significativi. La ricerca in oggetto, infatti si è svolta in collaborazione con il *Laboratory of Microengineering for Manufacturing 2* e il *Laboratory of Stem Cell Dynamics* del Politecnico Federale di Losanna. Questa tesi si concentra sulle antenne per dispositivi impiantabili con capacità di telemetria a grande distanza. Nel determinare le caratteristiche delle antenne impiantabili sono stati presi in considerazione i seguenti elementi: la natura del corpo umano, "ostile" alla propagazione delle onde elettromagnetiche, la necessità di miniaturizzazione e le esigenze di biocompatibilità. Il lavoro si è articolato nell'analisi, la progettazione, la realizzazione, la caratterizzazione in vitro e la sperimentazione in vivo di antenne impiantabili con particolare attenzione agli aspetti tecnici e medici. L'analisi si è basata sulla teoria delle antenne in ambienti con perdite e ha esaminato le caratteristiche di quelle elettricamente piccole in presenza del corpo umano. Questo studio ha permesso una chiara identificazione delle principali sfide legate alle antenne impiantabili e ha offerto una solida base per gli sviluppi successivi del lavoro. Per esempio è stato rilevato che l'isolamento biocompatibile è un componente di primaria importanza. Un modello fisico e uno matematico, appositamente elaborati, hanno dimostrato la migliore efficienza di radiazione ottenibile con la corretta scelta di isolanti. La progettazione ha preso in considerazione gli input teorici e i vincoli tecnologici per giungere alla proposta di una efficace strategia per il disegno di antenne impiantabili. Tale strategia è stata applicata alla realizzazione di un'antenna spirale su multistrato. Questa antenna si integra con la necessaria circuiteria, l'alimentazione e i sensori fino a costituire un dispositivo impiantabile completo. La caratterizzazione in vitro è stata discussa e applicata sia per le singole antenne impiantabili, così come per l'intero dispositivo. In particolare è stato indicato come ottenere la corretta verifica delle caratteristiche di tali antenne senza richiedere la progettazione di specifici alimentatori. La sperimentazione in vivo è stata effettuata su un suino fino a realizzare un sistema di telemedicina. I risultati ottenuti costituiscono un passo in avanti nella la ricerca di tecniche mediche ed informatiche per la cura di un paziente a distanza.

Parole chiave: antenna spirale su multistrato (MSA), antenne elettricamente piccole, antenne impiantabili, antenne in ambienti con perdite, comunicazioni senza fili intorno al corpo umano, espansione in onde sferiche (SWE), isolanti biocompatibili, sensore per il corpo umano (BSN), servizio di radio-comunicazioni per i dispositivi a scopo medico (MedRadio), sistema di comunicazioni per dispositivi impiantati a scopo medico (MICS).

Résumé

Depuis l'apparition de pacemakers au début des années 60, les systèmes médicaux implantables se sont développés pour les services de soin de santé. Les systèmes actuellement conçus pour surveiller les données physiologiques à l'intérieur du corps humain montrent un grand potentiel pour l'aide à la prévention de maladies, leur diagnostique et leur thérapie. Ainsi, les systèmes de dernière génération, qui sont moins invasifs, permettent de réduire les durées d'hospitalisation ce qui améliore la qualité de vie du patient. Pour réaliser de tels systèmes, il est nécessaire de comprendre comment transmettre au mieux les informations de l'intérieur du corps vers le monde extérieur. Cela exige une approche multidisciplinaire où des concepts provenant à la fois de l'électromagnétisme, de l'électronique et de la biologie. Ce travail se concentre sur les antennes intégrées dans des systèmes implantables dédiés à la transmission de données sans fil. En collaboration avec le Laboratoire de Production Microtechnique 2 and le Laboratoire de Dynamique des Cellules Souches de l'École Polytechnique Fédérale de Lausanne, nous avons conçu, assemblé et testé in vivo avec succès une unité de contrôle pour capteurs corporels ("Body Sensor Node", BSN en abrégé) pour la télémédecine. Parmi les différents composants, l'antenne joue un rôle majeur. La présence du corps humain, qui est "hostile" à la propagation radiofréquence, le besoin de miniaturisation et la nécessité de biocompatibilité sont des facteurs qui contribuent à déterminer les caractéristiques finales des antennes implantées. Cette thèse traite de l'analyse, de la conception, de la réalisation et de la caractérisation in vitro et in vivo de ces antennes. L'analyse est basée sur la théorie fondamentale des antennes en milieu à pertes, les caractéristiques des antennes électriquement petites et la modélisation du corps humain. Cette approche permet d'identifier clairement les principaux défis liés aux antennes implantées. Par exemple, le choix de la couche biocompatible entourant l'antenne est primordial. Un modèle physique et mathématique, spécialement développé, a montré que le bon choix de cette couche améliore de manière non négligeable l'efficacité en rayonnement de l'antenne. La conception d'antennes implantables tient compte à la fois des contributions théoriques, de l'encapsulation et des contraintes technologiques. En combinant ces trois aspects, une stratégie de conception d'antennes implantées est proposée puis appliquée à la conception d'une antenne spirale multicouche. Cette antenne est intégrée avec l'électronique, la batterie et le bio-capteur afin de former le BSN. La caractérisation in vitro est discutée et réalisée d'abord pour l'antenne implantable seule, puis pour le système implantable complet. La caractérisation de telles antennes est détaillée de manière à envisager le prototypage des antennes au niveau des composants. Enfin, les tests in vivo du BSN ont été réalisés en implantant le système dans un cochon. Les résultats obtenus constituent un pas en avant vers de futures recherches sur la réalisation de systèmes de télémédecine complet.

Mots clefs: antennes électriquement petites, antennes en milieu à pertes, antennes implantées, antenne spirale multicouche (MSA), communications sans fils sur le corps, couche biocompatible, décomposition en ondes sphériques, Medical Device Radiocommunications Service (MedRadio), Medical Implanted Communication System (MICS), unité de contrôle pour capteurs corporels (BSN).

Acknowledgements

This thesis is the result of many, as colleagues, but also the extra laboratory friends, undoubtedly contributed to my PhD research. It has been a privilege for me to collaborate, discuss and share some parts of this *route* with such great people, both from the human and the professional points of view.

First and foremost, I would like to deeply thank my thesis advisor, Prof. Anja K. Skrivervik, for supporting this research, for giving me liberty in both my choices and my way of working and for her trust and support all along this thesis.

I would also like to acknowledge the members of my thesis jury, Prof. Angelo Freni from University of Florence, Prof. Koichi Ito from Chiba University and Prof. Farhad Rachidi from EPFL, for having accepted to examine this work and for their valuable comments and insights. My particular gratitude goes to Prof. Freni, not just for participating in my committee, but for initiating me to Electromagnetism and for his constant guidance and advice. Thanks also to Prof. Jean-Philippe Thiran for chairing this jury.

My most sincere appreciation is addressed to Prof. Juan R. Mosig for his invaluable scientific help, extraordinary human qualities and for making me feel at LEMA like at my second home throughout our collaborations, meetings and event organizations.

Special thanks (and a big hug) to "my" post-docs for all the great time we spent together in and out the lab: first Iviça and Pedro, without you my PhD experience would have not even started, and then Thanos and Benji for sharing your competence and friendship with me. You all have been extraordinary examples and sources of motivation for me. High honors to Michael, *der Zauberlehrling*, for your unfailing capability to help me in any lab matter.

Thank you, Mrs. Eulalia Durussel, for assisting and helping me in these four years. Coming to your office has always been the best way to address and solve any practical issue.

I would like to deeply acknowledge the contribution of Mr. Jean-François Zürcher for having taught me many "secrets" about antenna design and measurements. Together with Mr. Philippe Vosseler and Mr. Manuel Leitos, thank you very much for always providing me with the best solutions to overcome any technological problem while prototyping.

This thesis is based on the collaboration with the best team of the *Laboratoire de Production Microtechnique*: Dr. Léandre Bolomey, Mr. Eric Meurville and Mr. Giancarlo Corradini. I have a great debt with you, Léandre, as you complemented my expertise, taught me a couple of millions of things and for the time we shared together discussing, designing and testing. I'm thankful to Eric and Giancarlo for their positive spirit, genuine incitement and constant help. I would also like to express my gratitude to Prof. Yann Barrandon and his PhD student François Gorostidi for their kindness and for giving us the possibility to perform in vivo tests.

Thank you, to all former and current LEMA members, with a special mention to Greg, Eden, Ioannis and my two charming office mates, Ruzica and Maddalena: because of you working has always been a pleasure even throughout the most stressing time. Likewise, my students Javier, Karim and Camillo who have given me opportunities to learn more than what I was trying to teach them.

Out with the work setting, I would like to offer my fondest regards to my closest "Swiss"

Table of Contents

1. Introduction

Since the first X-ray medical experiments at the end of the 19th century, electromagnetism has been continuously increasing its presence in medicine. Nowadays radio frequency/microwaves applications provide major contributions to disease prevention, diagnosis and therapy [1, 2]. A nonexhaustive list would include imaging, septic wound, cancer treatment by hyperthermia, and enhancement of drug absorption to mention but a few. In particular, wireless capabilities are extremely useful in modern medicine in order to improve the patient's comfort and care, for instance by reducing the invasiveness of electromagnetic (EM) medical instruments.

The introduction of pacemakers in the early 1960s and the first swallowable pills with sensing capabilities showed the great importance of implantable devices enabling the monitoring and the treatment within the human body. Such devices called for the use of wireless communication in order to control the functioning of the system and report the patient's status. Today, glucose monitoring, insulin pumps, deep brain stimulation and endoscopy are a few examples of the medical applications that could take advantage of remote monitoring and control of an implantable unit [3, 4].

In addition to the clear benefits to the healthcare system provided by wireless implantable devices, economical aspects are also relevant. Remote monitoring systems facilitate the prevention of diseases and favour the *hospital at home** . Both aspects decrease healthcare costs (for instance of nearly one-third by reducing the hospitalization period keeping the patient at home). An example of a home healthcare monitoring system is illustrated in Fig. 1.1.
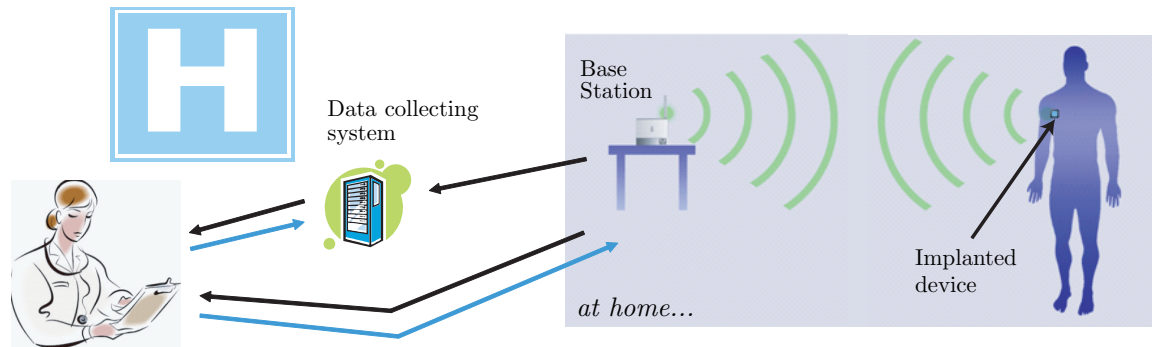
Figure 1.1.: Sketch of a generic home healthcare system with a wireless implantable device working in a Wireless Body Area Network (WBAN).

The challenging request of wireless performances for implantable devices reflects on the difficulties of the design of implantable antennas. In fact, despite the fact that the use of antennas inside a living body goes back as far as five decades [5, 6], the topic is still open and has a great research interest given the new applications. When targeting implantable devices for communication in a Wireless Body Area Network (WBAN) of a few meters range, the design of specific antennas is required. In fact, among all the components

---

*Hospital at home: Johns Hopkins School of Medicine, http://www.hospitalathome.org/dgm/

necessary for implanted telemetry applications, the antenna plays a key role to obtain robust communication links and the miniaturization of the whole device.

This thesis deals with the analysis, design, realization and characterization of implantable antennas for data telemetry. It is a multidisciplinary topic that combines several EM aspects -such as antenna design and theory, field propagation in lossy matter and interactions with biological tissues, etc.- with telecommunication and package engineering [7, 8], material and biological science [9], and security and privacy matters [10].

1.1. Salient Aspects of a Wireless Implantable System for Data Telemetry

The main goal of a healthcare monitoring system with a wireless implantable device is to provide reliable information from inside of the human body to an external Base Station (BS). A wireless implantable system for data telemetry comprises several salient aspects. Such aspects, identified from the antenna engineer point of view, are illustrated in Fig. 1.2.
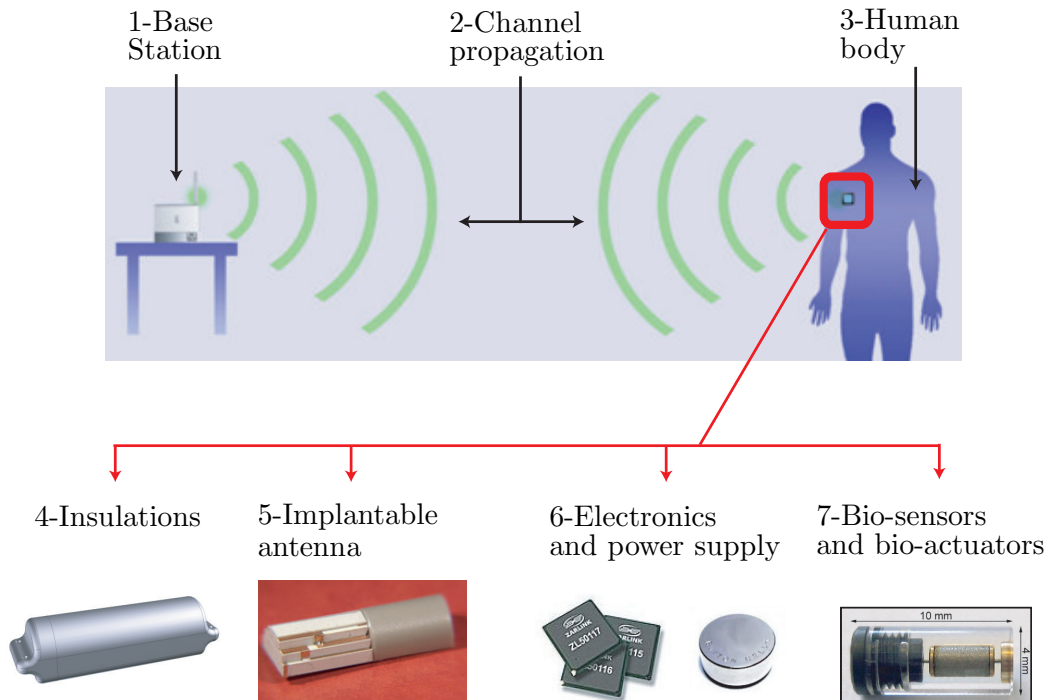
Figure 1.2.: Salient aspects in a wireless implantable system for data telemetry from the implantable antenna engineer point of view.

Besides the seven aspects illustrated in Fig. 1.2, it is necessary to add an 8th point "Characterization and Experiments" which is required to validate the correct functioning of the entire system.

1-Base Station

A general Base Station comprises several sub-systems, for instance:

- a control module to drive the entire system and to store the measurements.

- a receiver module including antennas;

- an internet modem (or any other device to connect to the data collecting system);

- ...

The sensitivity of the receiver, the performance of its antennas (in terms of directivity, efficiency, polarization) and its portability are of fundamental importance for the realization of a system that targets real life applications.

2-Channel Propagation

The analysis of the EM propagation from the implant to the Base Station is another important aspect. As implantable devices mainly target indoor application - *"No antenna for a MedRadio transmitter shall be configured for permanent outdoor use"* [11, Section 9.1211]- the study of the multi-path propagation of the radiated EM waves and the scattering because of the nearby objects is necessary. This analysis, together with the design of antennas for the Base Station, can noticeably improve the performances of the entire system.

3-Human Body

The human body is of primary relevance for an implantable device. Its complex, dispersive and highly lossy characteristics unavoidably affect the analysis, design, realization and characterization of implantable antennas, thus the wireless performances of the entire system.

4-Insulations

The presence of a biocompatible insulation is mandatory for any implantable device so as to avoid any adverse reaction of the living tissues. Such an insulation is of paramount interest from the antenna point of view, as the human body is an "hostile" environment for the Radio Frequency (RF) radiation. In fact, insulating layers, either placed around the antenna or on the surface of the human skin, enhance the EM transmission from an implantable radiator to the Base Station.

5-Implantable Antennas

The design of a specific radiator is the key aspect of an implantable device working in a WBAN of a few meters range. Characteristics such as radiation efficiency, bandwidth, the coupling with the lossy biological tissues and the use of the available volume are essential for the data communication. In a few words, an implantable antenna aims at minimizing the volume occupation, at facilitating the integration with all the components constituting the device, and at obtaining the required EM performances.

6-Electronics and Power supply

The electronic components of an implantable device allow the functioning of the system, provide data communication and signal processing capabilities and delineate the working power requirements. It thus defines the overall capabilities of the device itself. The power supply, often having the largest volume occupation, sets the life time of the apparatus. Several solutions such as energy harvesting, internal power supplies, or wireless power transfer are possible.

7-Bio-sensors and Bio-actuators

The bio-sensors and/or bio-actuators determine the application of an implantable device and its placement in the human body. Monitoring devices (for instance measuring temperature, pH, glucose, etc.) or active system (drug delivery apparatus) are nowadays being investigated for implantable applications.

8-Characterization and Experiments

Each component constituting the healthcare monitoring system must be characterized to validate its proper functioning, and the conformity with safety and regulatory requirements. Fur these purposes, In vitro and in vivo (in animal) experiments are necessary steps before the application in humans.

1.2. Frequency Bands, Power Limits and Link Budgets

Wireless implantable devices operate in several frequency bands depending on the data rate, working range, power transfer capability, and the different standards of different countries. This thesis focuses on the EM radiation occurring in the Medical Device Radiocommunications Service (MedRadio) [11] and in the 2.45 GHz Industrial, Scientific and Medical (ISM) band. Equivalent Isotropic Radiated Power (EIRP) limitations and frequency spectrum allocations are reported in Table 1.1 based on the information available from [11–13]. As different regulatory requirements may apply from a country to another, the reader is invited to refer to the national licensing authority.

Table 1.1.: Frequency Bands Main Characteristics.

Band	Frequency	Maximum EIRP
MedRadio	401-406 MHz	-16 dBm
ISM	2.4-2.5 GHz	20 dBm

Power limitations are also set to prevent hazardous heating of the biological tissue. The maximum power for the transmission from any implantable device must comply with the peak spatial-average Specific Absorption Rate (SAR) limitations (1.6 W/kg per 1-g averaging [14] and 2 W/kg per 10-g averaging [15].

Examples of a link budget can be found in [13] and [16] in the MedRadio and ISM band, respectively. To make the reader familiar with the power levels in implantable applications,

and to set a common reference for the evaluation of the antennas and system presented in this thesis, values extrapolated from the aforementioned references are reported in Table 1.2.

Table 1.2.: Examples of Power Link Budgets from Implant to Base Station.

Parameter	MedRadio [13]	ISM [16]
Frequency	401 MHz	2.45 GHz
Bandwidth	200 KHz	200 KHz
Tx power	-2.0 dBm	-36.0 dBm
Implant antenna gain	-31.5 dBi	-26.5 dBi
EIRP	-33.5 dBm	-62.5 dBm
Free space path loss (2 m)	30.5 dB	46.2 dB
Excess Loss & Fade Margin	25.0 dB	2.0 dB
Base Station antenna gain	2.0 dBi	2.1 dBi
Rx power	-87.0 dBm	-108.6 dBm
Receiver noise	-101.0 dBm	-120.0 dBm

1.3. Thesis Outlook

While a complete healthcare monitoring system has been always kept in mind, the main focuses of this thesis are on the following salient aspects of a wireless implantable system for data telemetry:

- 3-Human Body;

- 4-Insulations;

- 5-Implantable Antennas;

- 8-Characterization and Experiments.

The context of the work and the outline of this thesis are presented here below.

1.3.1. Context of the Work: Research Projects and Objectives

The main research activities carried out in this thesis have been accomplished in the framework of two projects, namely:

- EPFL School of Engineering (STI): "Implantable antennas for biomedical applications", 2007-2009;

- NANO-TERA Swiss federal program funding for engineering complex systems for health, security and the environment: "BioAnt (Bio Implantable Antennas)", 2010-present.

The STI project has been done in close collaboration with the *Laboratory of Microengineering for Manufacturing 2* (LPM) at EPFL. The project aimed at investigating implantable antennas for far field off-body communication. The analysis, design, realization and characterization of implantable radiators, aside from their academic interest, targeted the realization of a Body Sensor Node for real life applications [17]. In the context of this project, the collaboration with the *Laboratoire de Dynamique des Cellules Souches* (LDCS) at EPFL-UNIL-CHUV¶ allowed us to carry on in vivo experiments. The continuous monitoring of the subcutaneous local temperature of a porcine animal was performed to investigate the effects of temperature on the skin stem cells behavior, as they might find application in the healing of burned skin of humans.

Despite the fact that this project was founded only for two years, active collaboration with E. Meurville and Dr. Bolomey from LPM has been carried on till the end of this thesis.

The NANO-TERA "BioAnt" aims first at investigating the effect of a complex environment on the antenna characteristics (radiation efficiency, bandwidth, etc.) and then at elaborating theoretical limits for the radiators performances when inserted into biological tissues. A third objective of this project is to consider the adequacy of standard antenna measurement procedure for the in vitro testing of implantable antennas. In the framework of this project, we investigated also the further miniaturization of implantable antennas, the presence of a real body models and the wireless power transfer capability.

Practical realizations are foreseen in collaboration with the *Integrated Systems Laboratory* (LSI) at EPFL in the framework of the NANO-TERA "i-IronIC: Implantable/Wearable System for on-line Monitoring of Human Metabolic Conditions" project. This collaboration aims at studying an innovative, multi-metabolites, highly integrated, fully implantable, and real-time monitoring system for human metabolism.

1.3.2. Outline and Original Contributions

This section summarizes the contents and the original contributions of the chapters of this thesis. While each chapter contains a selective literature review, the two main parts of the state of the art given in this thesis focus on the human body models and the implantable antennas. These reviews are presented in Chapter 2 and Chapter 4, respectively.

Chapter 2: Antennas in Lossy Matter and Human Body Models

Description: the comprehensive knowledge required for the design of antennas surrounded by lossy biological tissues is presented. Theoretical aspects related to the presence of lossy matter and their consequences on the characteristics of antennas are discussed. As the description of the antenna performance (radiation efficiency, bandwidth, etc.) is highly dependent on the selected body model, we present and discuss the available possibilities to mimic the human body in terms of numerical analysis and physical realizations.

Original contribution: the concepts and results discussed in this chapter are not new. However, the effects of the presence of lossy biological tissues and their modeling are originally reviewed from the point of view of antenna engineers.

¶Université de Lausanne (UNIL) and Centre Hospitalier Universitaire Vaudois (CHUV).

Chapter 3: The Effect of Insulating Layers on the Performance of Implanted Antennas

Description: the positive effects of insulating layers on the radiated power of implanted sources are investigated. Three simplified models of the human tissues consisting in concentric spherical geometries and excited by ideal sources (electric dipole, magnetic dipole and Huygens sources) are analyzed. Analytical and numerical implementations of a code are described to obtain information about the effect of the presence of both the internal insulation -surrounding the implanted radiator- and the external insulation, that is placed upon the human skin layer.

Original contribution: this chapter presents an extensive analysis of both internal and external insulations for implanted antennas in the MedRadio band. Our results show that a proper choice of the insulating layers improves the radiation efficiency of implanted antennas. This work gives insights on the power radiation of implanted sources. Therefore, it provides valuable information for the design of implanted antennas.

Chapter 4: Guidelines for the Design of Implantable Antennas

Description: the requirements for implantable antennas are presented along with the existing designs. This knowledge allows some preliminary investigations from both the design conception and the technological realization point of view. This research work leads to the formulation of a strategy for the design of implantable antennas.

Original contribution: the state of the art of implanted antennas is presented in a way to clearly identify the challenges of the design of such radiators. Based on the understanding of the implantable antennas characteristics, we present three new radiators. Based on the acquired knowledge, an original strategy for the design of implantable antennas is proposed.

Chapter 5: Design, Realization and In Vitro Characterization of an Implantable Antenna

Description: an implantable antenna is designed according to the strategy formulated in the previous chapter. The resulting radiator has dual band capability and allows for the placement of all the necessary components for the sensor control, data processing, communication and power supply of a an implantable sensor. The realization and in vitro characterization are described and discussed. We also present some advanced numerical analysis including the modeling of a real human body, and the versatility of the proposed design.

Original contribution: the presented antenna answers to miniature size requirements, tight packaging constraints and EM dual band demands. The new design optimally integrates with all the components of an implantable device for data telemetry. Five body phantoms (including a realistic human model) are considered providing extensive information on the radiating performances of the implanted antenna. The analysis comprises technological realization aspects, in vitro characterization, and further evolutions towards future implantable devices.

Chapter 6: Packaging, Realization, In Vitro Characterization and In Vivo Experiment of a Body Sensor Node

Description: we present a complete Body Sensor Node (BSN) including the antenna presented in the previous chapter, and comprising all the components for control, data processing, communication and power supply. All the elements constituting the device, and its in vitro characterization are described. In vitro experiments are reported showing the application of this BSN.

Original contribution: the proposed BSN is conceived and realized from the data transmission point of view. This results in a versatile device that finds its use in several different applications. The in vitro characterization and the in vivo experiment are discussed identifying the challenges of an implantable real life application, thus providing valuable information to the antenna engineers.

Chapter 7: Antenna Measurements for In Vitro Characterization

Description: this chapter deals with the measurement of implantable antennas at the component level. Undesired effects related to the presence of a feeding cable, when characterizing the matching properties of radiators inserted into a body phantom, are discussed. Three different setups are presented to clearly identify and possibly mitigate such effects. The usefulness of these three setups is validated by numerical and experimental analysis.

Original contribution: we address the challenges of the in vitro characterization of implantable antennas when fed by a coaxial cable. The investigations and solutions presented in this chapter focus on presenting and providing solutions for the correct in vitro characterization of implantable antennas.

Chapter 8: Conclusions and Future Work

Summary and general assessment of the work achieved in this thesis are presented while also discussing possible future research directions.

Appendix

Two appendices are provided, treating some aspects of the mathematical model used in Chapter 3 and reporting the precise description of the implantable antennas presented in Chapter 4.

2. Antennas in Lossy Matter and Human Body Models

2.1. Introduction

One of the main aspects of implanted antennas is the presence of the human body. The lossy tissues surrounding the radiator modify significantly the antenna performance, and interact with the electromagnetic wave. This part of the thesis aims at providing a review of the knowledge required for the design of antennas surrounded by lossy biological tissues. In particular, the two main goals of this chapter are:

1. to discuss the modification of antenna properties when radiators are inserted into lossy matter;

2. to describe the available human body models in terms of numerical analysis and physical realization.

In order to reach these goals, this chapter is organized as follows: we first recall in Section 2.2 the relevant important aspects and theoretical results for antennas in lossy matter. Problems and consequences are therein discussed to better appreciate the difficulties and the limitations characterizing such radiators. Particular attention is also paid to the small electrical size of implantable antennas; comments on the fundamental limitations of implantable antennas in analogy with submarine applications are given.

As the antenna performance parameters (radiation efficiency, bandwidth, SAR, etc.), are highly dependent on the selected body model, Section 2.3 deals with the available possibilities to mimic the human body. The human body is a very complicated environment (lossy, dispersive, inhomogeneous, etc.), thus several solutions have been presented in the literature. Such solutions are commonly known as "body phantoms" or simply "phantoms". Both the numerical and practical points of view are taken into consideration.

The analysis presented in this chapter serves as a common base for all the investigations and results presented later on. The theoretical aspects presented in Section 2.2 find their applications in the design of implantable radiators in Chapters 4 and 5, while different human body models based on this analysis are used in all the rest of this thesis.

2.2. Antennas in Lossy Matter

The dielectric properties of surrounding lossy tissues strongly affect a radiator. They modify the electrical size of an antenna. Thus, given fixed dimensions, a lower resonant frequency is obtained if compared to the free space case. This is illustrated by the case of an implantable spiral antenna, based on the design presented in [18], which is simulated in free space and in a lossless phantom. A sketch of the antenna proposed in [18] is illustrated in Fig. 2.1-(a).

This radiator was here modified removing the superstrate and including the presence of a 1 mm thick plastic insulation that required minor changes of the spiral design. The antenna is implanted in a human body model made of a homogeneous rectangular cuboid (surrounded by air) having dimensions equal to 72 x 80 x 50 [mm]‡ as illustrated in Fig. 2.1-(b).
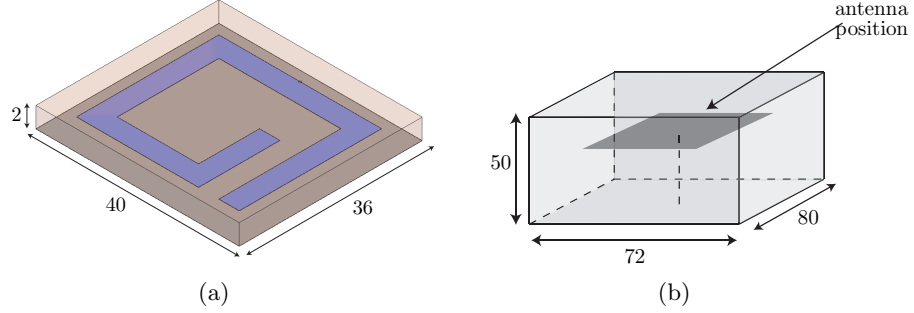
Figure 2.1.: Sketch of the implantable spiral antenna based on [18]: (a) model and (b) body phantom. Dimensions are in [mm]. Considering the presence of a the biocompatible insulation dimensions equal to 38.0 x 42.0 x 4.0 [mm]. The radiator is placed at a depth of 5 mm from the external free space.

Simulated reflection coefficients when the antenna is surrounded by its body phantom and by free space are reported in Fig. 2.2. A 12% downward frequency shift occurs when the dielectric constant of the surrounding medium changes from 1 to 49.6, with respect to the free space case. The selected dielectric value is used in [18] to mimic the skin tissue in the MedRadio frequency range.
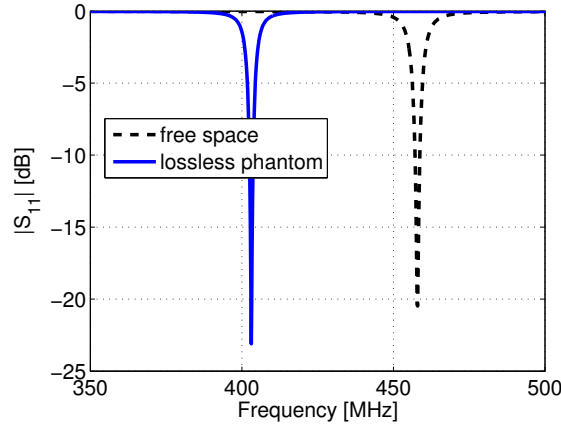
Figure 2.2.: Simulated reflection coefficients of an implanted radiator based on [18] surrounded by free space and a lossless skin equivalent body model (phantom) with $\varepsilon'_e = 49.6$.

When losses are taken into account, more than a simple dielectric loading effect occurs. In fact, the presence of the losses can modify the current distribution of the antenna, thus its radiation behavior. King [19, ch. 1, sec. 1.4] presents different current distributions for an insulated monopole depending on the surrounding lossy media, the dimension of the

---

‡Dimensions are indicated by "[mm]" meaning that all the given values are in mm. The same notation is used also for cylinders (diameter x height [mm]) and spheres (diameter [mm]) otherwise stated.

antenna, and the properties of the insulation. The variation of current distribution is one of the reasons why the presence of an insulator layer becomes mandatory for implanted antennas for telemetry applications [19, p. 171]. Indeed, a bare antenna turns out to have excellent capabilities for sensing applications only. On the contrary, when the main purpose is to radiate power out of a complex lossy media, the insulator presence provides a more stable current distribution, i.e., working behavior, [19, p. 6]. This means that the antenna becomes less sensitive to its exact placement in the body. Considering all the possible locations for different implantable applications and the diversities from patient to patient, such a robustness is of great interest.

In order to appreciate how much the radiation characteristics of an antenna inserted into lossy media differ from its free space counterpart case, we first recall the constitutive parameters of a medium to set a common notation valid throughout this thesis. Subsequently, we discuss the parameters used to characterize such antennas (radiated power and efficiency, radiation pattern, bandwidth, SAR and fundamental limits of electrically small antennas) focusing on the issues related to the presence of a surrounding lossy medium.

2.2.1. Medium Constitutive Parameters

The permittivity ε, permeability μ and conductivity σ of a linear, homogeneous and isotropic medium are in general complex quantities

$$\varepsilon = \varepsilon_0(\varepsilon_r' - j\varepsilon_r'') \tag{2.1}$$

$$\mu = \mu_0(\mu_r' - j\mu_r'') \tag{2.2}$$

$$\sigma = \sigma' - j\sigma'' \tag{2.3}$$

where ε_0 and μ_0 are the permittivity and permeability of vacuum, respectively. The imaginary terms ε_r'' and μ_r'' account for the losses due to the damping of the vibrating dipole moments (electric and magnetic) and to the time lag responses of the medium [19, section 5.18]. The frequency dependency ($\omega = 2\pi f$) is omitted in the notation for clarity reason, i.e., $\varepsilon = \varepsilon(\omega)$, $\mu = \mu(\omega)$, $\sigma = \sigma(\omega)$.

The human body does not have any particular magnetic properties ($\mu_r' = 1$, $\mu_r'' = 0$), thus, focusing on (2.1) and (2.3), we can define the real relative effective permittivity ε_e' and conductivity σ_e' as

$$\varepsilon_e' = \varepsilon_r' - \frac{\sigma''}{\omega\varepsilon_0} \tag{2.4}$$

$$\sigma_e' = \sigma' + \omega\varepsilon_0\varepsilon_r'' \tag{2.5}$$

Substituting the previous expressions into Maxwell's equations one can define the complex effective permittivity ε_e

$$\varepsilon_e = \varepsilon_0(\varepsilon_e' - j\varepsilon_e'') = \varepsilon_0\left(\varepsilon_e' - j\frac{\sigma_e'}{\omega\varepsilon_0}\right) \tag{2.6}$$

The EM power dissipation in a medium is often indicated by the loss tangent $\tan\delta$ and by the

skin depth δ (for $\sigma'_e \gg \omega\varepsilon_0\varepsilon'_e$) reported here below:

$$\tan\delta = -\frac{\text{Re}\{\varepsilon_e\}}{\text{Im}\{\varepsilon_e\}} = \frac{\sigma'_e}{\omega\varepsilon_0\varepsilon'_e} \qquad \delta = \sqrt{\frac{2}{\mu\omega\sigma'_e}} \qquad (2.7)$$

Finally, given (2.6), the wave number k_e and the wavelength λ_e in the medium are:

$$k_e = \omega\sqrt{\mu_0\varepsilon_0}\,\sqrt{\varepsilon'_e - \text{j}\frac{\sigma'_e}{\omega\varepsilon_0}} \qquad \lambda_e = \frac{2\pi}{\omega\sqrt{\varepsilon_0\mu_0}}\,\text{Re}\left\{\sqrt{\frac{\omega\varepsilon_0}{\omega\varepsilon_0\varepsilon'_e - \text{j}\sigma'_e}}\right\} \qquad (2.8)$$

at the angular frequency ω.

It is worth reminding that "*...it is impossible to distinguish between σ' and $\omega\varepsilon_0\varepsilon''_r$ or $\varepsilon_0\varepsilon'_r$ and $\sigma''/\omega\varepsilon_0$ without a molecular or atomic interpretation*" [19, section 6.1]. Therefore, in the following sections of this thesis we consider simpler relations ($\varepsilon''_r = 0$, $\sigma'' = 0$) and the use of the common engineering formulation (2.6) with $\sigma'_e = \sigma'$.

Dielectric properties of the biological tissues are taken from the pioneering work of Gabriel [20].

2.2.2. Radiated Power and Radiation Efficiency

In order to understand the main characteristics of antennas surrounded by lossy media, let us consider the following power expression: the available source power P_{source} is

$$P_{\text{source}} = P_{\text{rad}} + P_{\text{abs}} \qquad (2.9)$$
$$= \oint_{S_r} \text{Re}\{\mathbf{S}\cdot\hat{r}\}dS + \tfrac{\omega}{2}\int_V \varepsilon_0\varepsilon''_e|\mathbf{E}|^2 dV,$$

where P_{rad} is the average power flow through a spherical surface S_r of a volume V in which the power absorption, P_{abs}, occurs, and $\mathbf{S}$ is the Pointing vector ($\tfrac{1}{2}\mathbf{E}\times\overline{\mathbf{H}}$).

Let us further manipulate the previous expression so as to formulate P_{source} as a sum of different terms, more precisely:

$$
\begin{aligned}
P_{\text{source}} &= \oint_{S_r} \text{Re}\{\mathbf{S}(1/r^2) + \mathbf{S}(1/r^n)\}\cdot\hat{r}dS + \tfrac{\omega}{2}\int_V \varepsilon_0\varepsilon''_e[|\mathbf{E}|^2(1/r^2) + |\mathbf{E}|^2(1/r^n)]dV \\
&= P_{\text{rad}-\text{FF}} + P_{\text{rad}-\text{NF}} + P_{\text{abs}-\text{FF}} + P_{\text{abs}-\text{NF}} \qquad (2.10)
\end{aligned}
$$

where the radial dependency is explicitly indicated. In fact, the $1/r^2$ dependency identifies exclusively the Far Field (FF) component, while $1/r^n$, with $n > 2$, refers to the Near Field (NF) components of the electromagnetic radiation. The power terms $P_{\text{rad}-\text{FF}}$, $P_{\text{rad}-\text{NF}}$, $P_{\text{abs}-\text{FF}}$ and $P_{\text{abs}-\text{NF}}$ can be defined to separate the radiated and absorbed power with respect of the nature ($1/r^n$ dependency) of the EM field. Obviously, $P_{\text{rad}-\text{NF}}$ is only appreciable within a small distance from the source.

Such a classification is very useful to understand the physical phenomena happening for antennas in lossy matters. In a free space environment, the near field is mainly reactive, thus neither affecting the radiated nor the absorbed power. In our case, on the contrary, the NF strongly couples with the closest surrounding material, thus increasing the lost power [21, ch.

24] [19, 22]. Indeed, the high near field coupling with lossy tissues is the main cause of the extremely low radiation efficiencies for any implanted antennas. That is the reason why the insulation plays an important role in the electromagnetic radiation from an implanted source by reducing this coupling in the nearest-by environment of the antenna.

The fact that near field terms do contribute to both losses and radiation implies that the computation of P_rad in (2.9) depends on the radial distance r, as different average power flows through S_r of different radii. Such a dependency is clearly seen considering the simplified expressions (neglecting the displacement currents) given in [21, p. 449] for the radiated powers in close proximity of a short electric dipole (P_TE) and a small loop (P_TM):

$$P_\mathrm{TE} = \frac{1}{6\pi\mu\omega}\left(\frac{Idl}{\sigma'_e}\right)^2\frac{1}{r^3\delta^2} \qquad P_\mathrm{TM} = \frac{\sigma'_e\mu^2\omega^2}{12\pi r}(IdA)^2 \qquad (2.11)$$

Comparing the TE and TM expressions, one immediately notices the specific $1/r^3$ dependency of the electric case. Such a dependency, characteristic to the electric near field terms of the electric source, makes the short dipole less efficient than a small loop[‡].

The previous considerations led to the definition of several figures of merit to evaluate the radiation efficiency of an antenna surrounded by lossy media (infinite or half-space). Fenwick [23] defined the relative communication efficiency that takes into account the position, orientation and polarization of the source, and the prescribed observation point in comparison with a perfect quarter wave monopole. Hansen [24] proposed the relative gain that is the "*vertically polarized electric field strength squared in air (produced by the antenna in lossy half space) divided by the field strength squared produced with the same power radiated isotropically in free space*". A modification of the gain is also proposed by Moore [25], defining "*the ratio of the radiation intensity in a particular direction to the radiation intensity of a hypothetical isotropic antenna at the same location and delivering the same power*" in the purpose of avoiding the radial dependence r of the radiation intensity. All these definitions pointed out the necessity of defining the position of the source relatively to the lossy medium-air interface. More recently, Karlsson [26] and Johansson [27] presented another radiation efficiency definition which is also used in [28] discussing the effective area concept for radiators in a lossy medium. Quite surprisingly, they presented a radiation efficiency formula whose evaluation gives values larger than one.

This thesis focuses on implantable antennas for far field telemetry. This means that the external receiver is placed off-the-body within a WBAN with a few meters range. The finiteness of the human body geometry and the radiation towards an external receiver at far-field distance, considerably simplify the theoretical issues discussed in the previous references about the radiation efficiency. Thus, we use the classical definition:

$$e_\mathrm{rad} = \frac{P_\mathrm{rad}}{P_\mathrm{source}} \qquad (2.12)$$

where P_rad is evaluated in free space at far field distance with mismatch losses not taken into account[*].

[‡]The radiated power of a magnetic source presents the same $1/r^3$ dependency only if magnetic losses ($\mu''_r \neq 0$) are taken into account.

[*]Given the importance of the radiation efficiency, values with three decimal digits are reported in this thesis while gain and directivity are always rounded to one decimal in [dB]. That is the reason why different

When considering receivers placed in close proximity of the body such as wearable devices or when investigating communication among implants, other considerations apply [29]; surface waves can be excited and they may result to be the best way to transmit information as shown in [24, Fig. 3]. In these cases, the different radiation efficiency definitions, based on [23–25], might be of a better use to properly evaluate the radiator capability.

Given (2.12), a preliminary result showing the importance of the insulation presence is illustrated in Fig. 2.3. The implantable antenna depicted in Fig. 2.1-(a) was simulated varying the thickness of the insulation when introduced in the same human lossy body model as illustrated in Fig. 2.1-(b). The biocompatible material reduces the coupling between the near field and the lossy tissue. In fact, e_{rad} values show that increasing the insulation dimension from 0.25 to 5 mm leads to a ten times more efficient power transfer from the radiator to an external receiver.
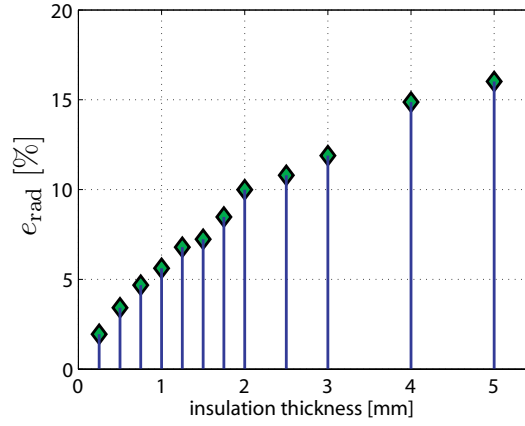
Figure 2.3.: Normalized e_{rad} while increasing the biocompatible insulation for the spiral antenna based on [18]. Values are normalized to the max radiation obtained when the radiator is inserted into a lossless body model with 1 mm thick insulation (corresponding to the blue solid line in Fig. 2.2).

2.2.3. Radiation Pattern

Moore [25] pointed out the "failure" of the standard definition of far field antenna pattern when considering antennas in lossy matter. In fact, the radiation from different parts of the antenna are not attenuated in the same way. This may result in evaluations leading to erroneous conclusions, depending on the relative position between the antenna and the origin of the coordinate system. For an easier understanding, Fig. 2.4 reports the results presented by Moore in [25]. A one full wave long wire antenna is investigated inserted into air and into a conducting medium. Two different origins for the coordinate system are indicated in Fig. 2.4-(a). Radiation patterns are computed when the radiator is in free space and in a conducting medium when the coordinate system is set at the center of the antenna in Fig. 2.4-(b), and at one of its extremes in Fig. 2.4-(c). As expected, the former case shows that the presence of a lossy or lossless medium has no effect on the radiation pattern. On the contrary, the latter

---

values than what reported can be obtained making the ratio between the gain and the directivity could be evaluated.

case presents different radiation patterns which are not representative of the real radiation of the investigated antenna.

(a)   (b)   (c)
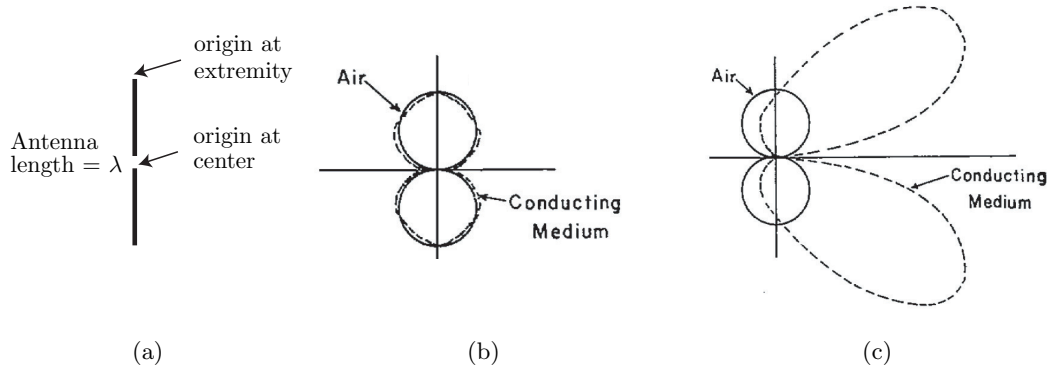
Figure 2.4.: Results taken from [25] to show the effect of the position of the coordinate origin on polar diagrams of a hypothetical linear antenna carrying a uniform current: (a) model with the two coordinate system origins, (b) patterns in air and in a conducting medium with the origin at the center, and (c) patterns in air and in a conducting medium with the origin at the top extreme of the radiator.

When focusing on implantable antennas, the problem becomes even more complicated as the human body is a complex finite environment. In this case, not only the close lossy surrounding of the antenna, but also the entire human geometry affects the far field pattern. Furthermore, the human body is a physical dynamic, and uncontrolled structure. A simple proof of what stated can be found considering again the implantable antenna depicted in Fig. 2.1. This time the radiator was inserted into two phantoms which differ only in their lateral extensions. For the problem under investigation (typology, electrical size, insulation, depth), Fig. 2.5 shows the radiation patterns that are obtained when modifying the phantom.   Indeed, different
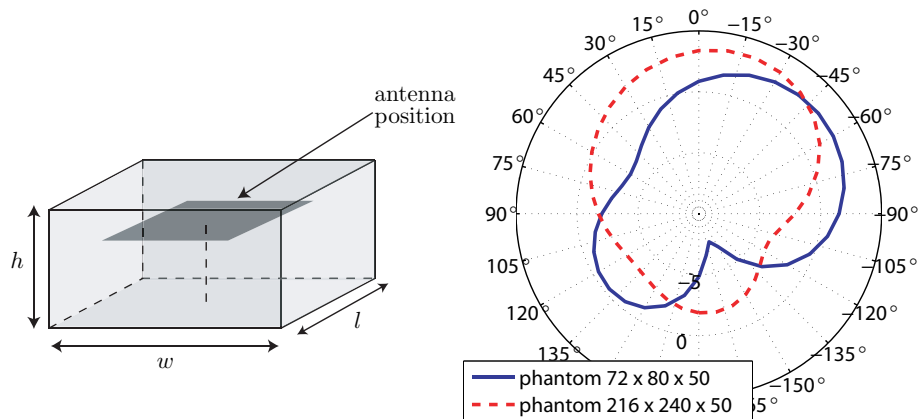
Figure 2.5.: Simulated radiation patterns in [dBi] for the spiral antenna depicted in Fig. 2.1 when modifying the lateral extensions of the phantom. On the left, the rectangular cuboid human model is depicted; the dimensions indicated in the legend correspond to l x w x h, respectively, in [mm].

direction of maximum radiation (up to 45°) and back scattering (more than 5 dB variation in amplitude) are appreciable.

2.2.4. Bandwidth

The bandwidth identifies the frequency spectrum where the antenna is matched and the provided power is radiated (minus the losses due to the radiator itself). When considering sources in lossy media, the near field terms of the electromagnetic field strongly dissipate in the surrounding environment. Therefore, P_{abs} (2.9) can be much higher than P_{rad}, and can be almost equal to P_{source}. In fact, most of the provided power is absorbed by the body and, no matter of how efficient the radiator is, a small percentage of P_{source} is actually reflected back to the generator. This may result in unusual wide band behaviors.

The phenomenon is clearly identified by the reflection coefficients, $|S_{11}(f)|$, depicted in Fig. 2.6. The implanted antenna depicted in Fig. 2.1 was simulated when introduced in its body phantom with and without losses. For this investigated problem (typology, electrical size, insulation), it can be appreciated that the bandwidth at -10 dB increases more than ten times when considering the losses (from 0.3% in a homogeneous lossless body to 4% with $\varepsilon_e'' = 22.9$). Obviously, the near field coupling with the lossy tissue has not the same "beneficial" effect on the radiation performances, as the presence of the lossy human model reduces the radiated power.
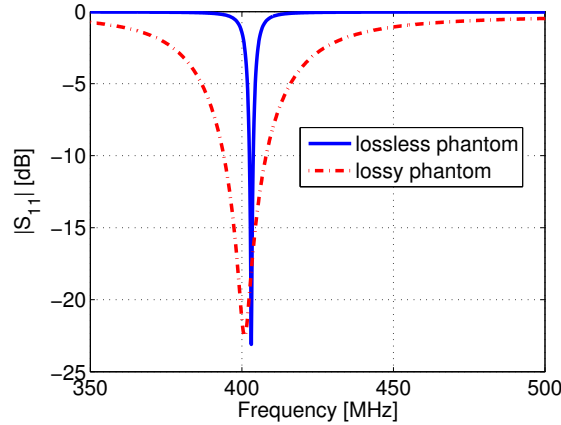
Figure 2.6.: Simulated reflection coefficients of the implanted radiator based on [18] surrounded by a lossy and lossless skin equivalent body model ($\varepsilon_e' = 49.6$, $\varepsilon_e'' = 22.9$).

2.2.5. Specific Absorption Rate

In the presence of biological tissues, the main drawback of the power dissipation in the lossy surrounding media is the generated heat which may be hazardous.

The Specific Absorption Rate (SAR) has therefore been introduced for the analysis of EM waves in biological tissues. The evaluation of SAR is a way to compute the dissipation of EM power per unit mass (with different averaging techniques or peak values), in order to estimate the heating of the tissues that may have harmful effects. Indeed, the maximum input power for the transmission from any implantable device must comply with the SAR limitations (1.6 W/kg per 1-g averaging [14] and 2 W/kg for 10-g averaging [15].

Peak SAR is defined as [30]:

$$\text{SAR}(r_0) = \frac{1}{2} \frac{\sigma_e'(r_0)|E(r_0)|^2}{\rho(r_0)} \tag{2.13}$$

where σ_e' and ρ are the conductivity and the mass density of the medium, respectively, while $\frac{1}{2}\sigma_e'|E|^2$ is the average power density absorbed at the point of observation r_0.

The spatial-average SAR is computed at every point of the tissue by averaging the values enclosed in a region R with a mass M in a finite volume V . More specifically, the spatial-average SAR is computed as [30]

$$
\begin{aligned}
\text{SAR}(V) &= \frac{1}{\text{mass}(V)} \int_V \text{SAR}(r)\,dm \\
&= \frac{1}{\text{mass}(V)} \int_V \frac{\sigma_e'(r)|E(r)|^2}{2}\,dv
\end{aligned}
\tag{2.14}
$$

Its maximum value, over different volumes is denominated peak spatial-average SAR. The definition of the volume is critical and it is not unique; different solutions are indeed implemented in commercial software. Without entering the discussion about the previous definition (see [31, 32]), a detailed human body model must be considered to obtain accurate SAR values. In fact, only a precise description of the geometry and the compositions of the human body leads to accurate computation of the electric field distribution, and thus, of SAR [33]. Indeed, SAR values highly depend on:

- the SAR computation techniques (averaging);

- the specific body model;

- the fluid dynamics and thermoregulatory biological responses;

- the implant location;

as discussed in [32]. That is the reason why SAR is not always evaluated for the radiators immersed in simplified human models in Chapter 4. Accurate and meaningful results are computed with a realistic body model in Chapter 5.

2.2.6. Electrically Small Antennas and Fundamental Limits

The previous considerations apply to any antenna surrounded by a lossy medium as no stringent electrical size requirements were taken into account. However, implanted radiators do require extreme miniaturization so as to facilitate the implantation procedure and the comfort of the patient. This aspect increases the challenges of the design including the problematic related to Electrically Small Antennas (ESAs) [34].

Abundant works have been published about the limitations in terms of bandwidth, quality factor, and gain of ESAs [35–39] (and references therein). These studies are not directly applicable here, as they were all derived considering the EM radiation in a lossless environment. The situation is more complex when analyzing implantable antennas. The near

field coupling with the lossy tissues and the propagation of the radiated EM wave are deeply affected by the specific human body model (geometry, compositions, implant placement, etc.). Thus, it is hard to define what the antenna is, and thus identify the minimum sphere enclosing the radiator which is a key point to evaluate the limits as for the free space analysis [35–39]. For instance, body parts such as arms and shoulders are found to affect the radiation performances for implants in the chest or the head [18, 40]. This means that also these human body parts should be included in the volume of the antenna. Such assumptions would lead to unrealistic limits following the expression given in [35–39].

Motivated by geophysical and submarine applications, extensive results and investigations are found in the literature about antennas surrounded by infinite or half space lossy media. Among others, four excellent sources are called to the attention of the reader. In a chronological order, they are: the "Special Issue on Electromagnetic Waves in the Earth" [41], the work by Wait [21, ch. 24] and the books by Baños [42] and King [19]. These early works usually neglect the displacement currents against the conduction ones [21, ch. 24]. Despite this approximation, that no longer holds given the dielectric properties of the body and frequency bands of interest in this thesis, very useful discussions are still found in the aforementioned references. Indeed, they provide a helpful physical insight about the radiation of antennas surrounded by lossy media, thus for implanted radiators also.

Submarine and Underground Applications

Clear investigations on the radiation performance in the presence of a lossy surrounding are given by Wheeler [43, 44] (and recalled in [24, 25] by Moore and Hansen, respectively) for Very Low Frequency (VLF) submarine applications[§].

Analyzing the propagation of a EM signal from submerged antennas to the air above, the most efficient orientation of the source is immediately identified. In fact, horizontal, i.e., parallel to the sea surface, dipoles must be considered [43]. This is also true for implanted radiators for far field telemetry considering orientations parallel to the skin.

Wheeler introduced also the radiation power factor p and the interception area A_m to determine the capability of an antenna to radiate and to receive EM power, respectively. These parameters depend on the radius of the source, its radome and the skin depth of the sea water [43]. As for free space limits [35–39], such factors are proportional to the volume of the radiator, and they decrease when reducing the electrical size. For a spherical coil at great distance from the surface, depicted in Fig. 2.7, these parameters are

$$p = \frac{a^3}{a'\delta^2} \frac{1}{1/k + 1/2} \tag{2.15}$$

$$A_m = \frac{3\pi^2 a' \delta^2}{2\lambda} \exp\left(-\frac{2d}{\delta}\right) \tag{2.16}$$

[§]As previously mentioned, the work by Karlsson [26] used particular definitions, thus it is not discussed here.

$$
\text{where} \begin{cases}
a = \text{radius of the spherical coil} \\
a' = \text{radius of the spherical radome} \\
k = \text{magnetic ratio of core in coil} \\
\delta = \text{skin depth} \\
d = \text{depth of dipole from surface} \\
\lambda = \text{free space wavelength}
\end{cases}
$$
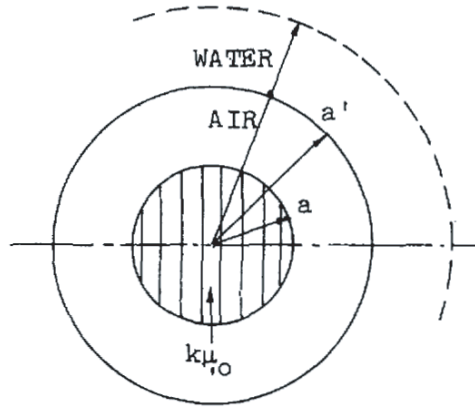
Figure 2.7.: Coil in a submerged radome from [43].

It is worth noticing that considering $a = a'$, these expressions are independent of the coil and radome geometrical characteristics and (2.15) gives the maximum p.

Comparing the expression (2.16) with its electrical counter part (as in [43]), it is shown that the magnetic source is a more efficient solution in agrement with the conclusion drawn from (2.11). As matter of fact, Wheeler proposed a simple formula for the radiation efficiency of this source when immersed in a half space lossy medium [44]. Under the assumptions that the radiator itself is lossless and the lossy medium behaves as a good conductor ($\sigma_e' \gg \omega \varepsilon_0 \varepsilon_e'$), Wheeler defined

$$
e_{\text{rad}} = \left(\frac{2\pi\delta}{\lambda} \right)^3 \left(\frac{a}{\delta} \right) \; \exp\left(-\frac{2d}{\delta} \right) \tag{2.17}
$$

where all the parameters are the same as for (2.15)-(2.16). The portion of the power available above the lossy surface is dependent on the different properties of the two media, the antenna size and its depth.

Implanted Antennas in Analogy with Submarine Radiators

Assuming biological lossy tissues as good conductors and infinite half space media, are hypothesis that are not true for implantable antennas. Indeed, they provide worse condition for

the power transfer than when considering a finite human model. Nevertheless, the discussion and results presented by Wheeler are very useful. In fact, using the dielectric properties of the muscle or skin, explicitly given in the following section, we can evaluate e_{rad} expressed by (2.17). Fig. 2.8 reports values in both the MedRadio range and at 2.45 GHz for two implantation depths. The radius of the sphere enclosing the radiator, a, varies from 1 to 20 mm; these are dimensions that cover the majority of real implantable radiators.
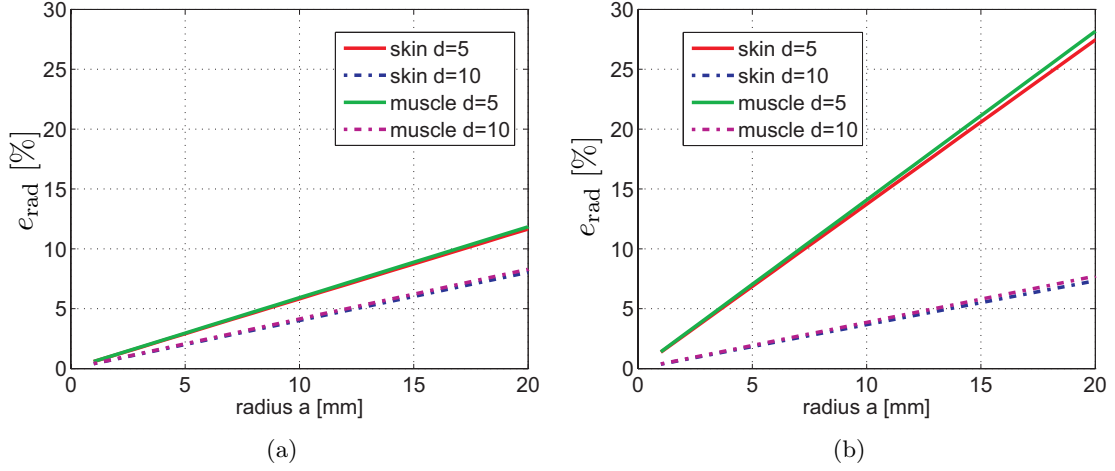
Figure 2.8.: Radiation efficiencies [%] computed via (2.17) for different tissues and immersion depths d (in [mm]) at (a) 403.5 MHz and (b) 2.45 GHz.

Despite the approximate validity of the assumptions and the worse conditions previously discussed, Wheeler's formula gives values that can be used to obtain preliminary ideas of the radiation of implantable antennas. Indeed, to the best knowledge of the author, all the performances of proposed antennas do not overcame the values reported in Fig. 2.8.

In conclusion ESA's limits are not in general available for radiators surrounded by lossy media, and are not identified in the implanted antenna case. Nevertheless, submarine and geophysical early analysis provide valuable information (source selection, radiation efficiency definitions and limitations), that are useful for the design of subcutaneous devices with telemetry capabilities.

2.3. Human Body Models

A large number of models to predict the effects of the human body on the characteristics of implanted antennas are available in the literature.

Since the early works focused on the interaction between the electromagnetic radiation and the biological tissues [45–47], an extremely broad selection of body phantoms has been proposed and investigated. Extensive work for both the numerical analysis and the physical realizations has been performed by Ito [48]. Body phantoms describe the human body with different accuracies in terms of geometry, number of tissues, voxel precision, etc. Particular attention is paid to the fact that the human body is constituted by highly lossy materials for

the case of RF propagation.

The dielectric properties of the human tissues are nowadays available over a broad frequency spectrum (10 Hz-100 GHz). The values obtained from the pioneering work of Gabriel [20] are, at least in the microwave range, world wide established and commonly used in both academic and industrial worlds[‡].

The choice of a body phantom affects both the design and performances of implanted antennas, as it is almost impossible to separate the performance of a implanted radiator from the investigated body phantom. Indeed, the radiated field out of the body is strongly related to the model, as clearly pointed out even via the wearable applications investigations [51, 52]. Therefore, it is important to discuss the available models. The review presented here is by no means exhaustive as, depending on the targeted applications (dosimetry, hyperthermia, telemetry, propagation, etc.) and working frequencies, a countless number of different phantoms have been proposed. Only the main solutions are here recalled and discussed from the viewpoint of both the numerical analysis and the antenna testing. This will be helpful to better understand the performed choices in the following chapters of this thesis.

2.3.1. Body Phantoms for Numerical Analysis

In order to better appreciate the large differences among available human body models for numerical analysis, it is useful to classify them according to their:

- Geometry (Shape);

- Composition (Constituting Materials);

- Dimension (and implant placement).

Each of these three classes comprehends several variations. As a result, it is quite difficult (sometimes even meaningless) to compare the EM performances of implanted radiators when such different surrounding environments are taken into account.

Geometry (Shape)

Canonical geometries are often used when designing implanted radiators. For instance, rectangular cuboid (box) phantoms are considered in [16], while the cylindrical geometry, modeled in [53, 54], is recommended as a standard by the European Telecommunications Standards Institute (ETSI) [55, Annex A 1.1.3]. Quite interestingly, a lossy cylinder was also used in the first experimental validations of theoretical studies on the EM wave propagation through a lossy medium (sea water) in [56]. Spherical geometries were also used to model the whole body [47], but found their main application in equivalent head phantoms [18, 57, 58].

The use of such simplified geometries is very common as they do allow to reduce the simulation time, and to use analytical formulae. Furthermore, they provide standard and easy to realize conditions for the radiator measurements. Three examples, one for each canonical

---

[‡]There is only little disagreement concerning the fat properties: Gabriel data indicates $\varepsilon'_e = 5.58$, $\sigma'_e = 0.042$ and $\tan \delta = 0.328$ while, for instance, $\varepsilon'_e = 11.62$, $\sigma'_e = 0.081$ and $\tan \delta = 0.310$ are used in the Virtual Family models [49, 50] in the MedRadio band.

geometry, are reported in Fig. 2.9.

(a)   (b)   (c)
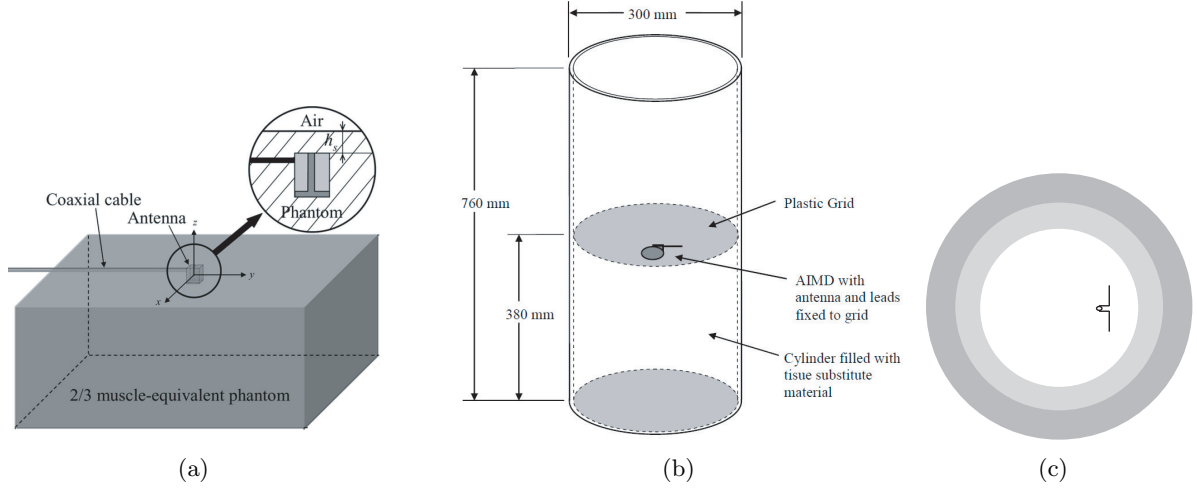
Figure 2.9.: Examples of canonical geometries used to mimic the human body: (a) rectangular cuboid (box) [16], (b) cylindrical [55] and (c) spherical [18].

Canonical geometries can be combined for a better representation of the human body. Human body models made of boxes or cylinders are modeled in the MedRadio band for implants in [59, 60] and at 2.4 GHz for on-body applications in [61], respectively. These two models are depicted in Fig. 2.10. Another example is given in [62], where a cylinder is used to mimic the human torso and it is integrated with realistic lungs.

(a)   (b)
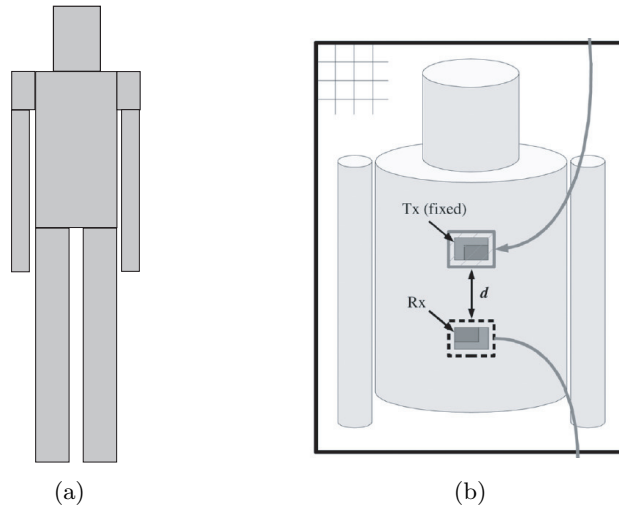
Figure 2.10.: Approximations of a complete human model combining canonical geometries: (a) box and (b) cylindrical. Images taken from [59] and [61], respectively.

More accurate models of the human shape, focusing on body worn applications, are proposed in [63], where the dynamic movement of two avatars (*James* = male and *Jessica* = female) is

considered.

The most detailed human body geometries are obtained when extracting information from medical imaging data, for instance from the Visible Human Project [64]†. In this case, a complete human male model, named *Hugo*, is built out of images of an adult male whose body was sliced after execution. This body phantom is used in [65–68] with ideal sources, and in [69] with a helical antenna, to evaluate the EM propagation within the body.

Other complete male models are shown in [70], [71] and [72]. In particular, the latter two are considered to compare the performances of implanted antennas in [18] and [73, 74]. Also based on medical data, complete Japanese male and female models are developed in [75], including the possibility of modifying their postures [76]. These phantoms are considered, among other works, in [77] for on-body applications, and compared with the *Hugo* model in [78] with ideal implanted sources.

Finally, the Virtual Family and Virtual Classroom [49, 50] consist of high-resolution models of a complete family and of four kids based on magnetic resonance images. These phantoms describe accurately the human body geometry but also allow for the investigations of different body constitutions (according to age and gender). The characteristics of these models are reported in Table 2.1, while possible postures are illustrated in Fig. 2.11.

Table 2.1.: Virtual Family and Virtual Classroom Models.

Virtual Family	Virtual Classroom
Ella: a 26-year-old female adult	*Louis*: a 14-year-old male child
Duke: a 34-year-old male adult	*Eartha*: an 8-year-old female child
Billie: an 11-year-old female child	*Dizzie*: an 8-year-old male child
Thelonius: a 6-year-old male child	*Roberta*: a 5-year-old female child
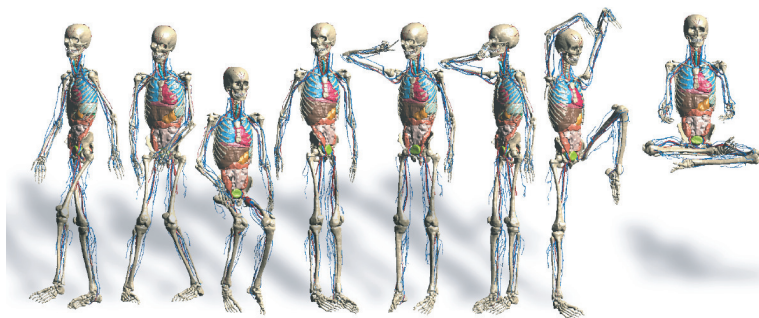
Figure 2.11.: Examples of different body postures for the Virtual Family models. Image from [79, Reference guide ch. 19].

---

†Data from the Visible Human project are also available at http://visiblehuman.epfl.ch/index.php.

Composition (Constituting Materials)

The presented geometries are considered either homogeneous or constituted of several biological tissues. For instance, homogeneous and multilayered box phantoms are investigated and compared in [18, 80]. While the homogeneous models are mainly composed of muscle, 2/3 muscle[§] or equivalent head properties, multilayered phantoms are usually made of three materials, i.e., muscle-fat-skin as in [81]. The dielectric properties of the latter tissues are reported in Table 2.2 for the two working frequencies of interest in this thesis. Obviously other

Table 2.2.: Dielectric Properties of Different Body Tissues.

Phantom	403.5 MHz				2.45 GHz			
	ε'_e	σ	$\tan\delta$	ε''_e	ε'_e	σ'_e	$\tan\delta$	ε''_e
2/3 muscle [16, 82]	38.10	0.530	0.620	23.61	35.15	1.16	0.242	8.51
muscle [20]	57.10	0.797	0.622	35.51	52.73	1.73	0.242	12.70
fat [20]	5.58	0.042	0.328	1.83	5.28	0.105	0.145	0.77
skin [20]	43.50	0.87	0.799	34.75	39.20	1.80	0.336	13.20
eq. head [p. 36][83]	43.50	0.87	0.799	34.75	39.20	1.80	0.336	13.20

tissue are also considered; for instance, a wide example of different homogenous compositions is reported in [54].

An interesting analysis investigating the effect of different fat layer thicknesses is presented in [27]. For a better comprehension, examples are reported in Fig. 2.12.
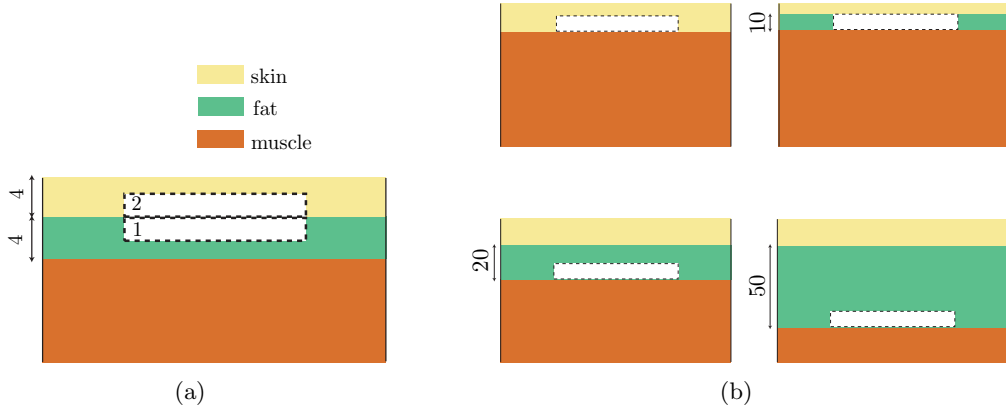
Figure 2.12.: Cross-view of multilayered box phantoms: (a) three layered models with antenna placements (dashed box) 1 and 2 as in [18] and [80], respectively; (b) different fat layer thicknesses from [27]. Dimensions are in [mm].

A different multilayered model is proposed in [84, 85]. In this case, in order to model a human arm, the very same three layers are simulated as coaxial boxes, which means that the muscle tissue is surrounded, along its length, by the fat and skin materials.

[§]2/3 muscle means that the properties of muscle are scaled by a factor of 0.66.

As previously mentioned, the spherical geometry is largely used for equivalent head model whose properties are reported in Table 2.2. With this shape, homogeneous compositions are still found useful for SAR evaluation in [86, Section 5.1.3], while multilayered spherical shells are used in [18, 27, 57, 58, 87–90]. The spherical geometry represents indeed a good average of more complex models, therefore provides exploitable insights. For instance, radiation efficiencies with SAR considerations and power profiles are presented in [18, 58, 89] and [57, 90], respectively.

The accurate geometrical models of the human body consider also a high number of tissues. While the avatars from [63] are homogeneous phantoms, the torso simulator presented in [18] uses 30 different materials. Thirty-four media are available in [72], while the Japanese models [75] are made of 51 tissues. The *Hugo* model [64] needs the definition of the dielectric properties of the desired organs, thus different number of materials can be implemented. For instance, 9 tissues are used in [65].

Highest inhomogeneity is provided by the Virtual Family and Virtual Classroom [49, 50], where up to 84 tissues are taken into account. Indeed, these models allow the simulation of a scenario close to the reality. For an appreciation of the provided accuracy, the model of *Billie* is illustrated in Fig. 2.13.

(a)   (b)

Figure 2.13.: The human body model of *Billie* -11 years old- for the Virtual Family: (a) front and (b) side views. Colors are used to indicate different organs and tissues.

Dimension (and Implant Placement)

In addition to the geometry and composition of phantoms, the dimension of the selected body model is a very important variable. For instance, the most detailed models (*Hugo*, Japanese male and female, Virtual Family) differ in heights, physical constitution and mass, as discussed in [78]. Furthermore, methods to develop patient-dependent phantoms are recently becoming available [91]. Of course, this vast choice gives us the possibility to consider

the phantom closest to the targeted case but, as a drawback, it makes harder the comparison among different radiators.

When focusing on canonical geometries, the differences in size are even more striking. For an easier comparison, Table 2.3 reports the dimensions of the most relevant solutions. The list is not exhaustive, but it does show the large variation of the investigated dimensions ranging from a minimum of 8.5 to a maximum of 1000 mm.

Table 2.3.: Examples of Different Dimensions of Phantoms composed of Canonical Geometries and Implant Depths.

References	Frequency Range	Phantom Dimensions* [mm]	Implant Depth [mm]
[92]		50 x 40 x 20	7
[93]		60 x 50 x 20	7
[82]		100 x 100 x 50	4
[80]		103 x 103 x 8.5	3
[94]	MedRadio	50 x 100 x 100	1.3-3.8
[95]		1000 x 1000 x 50	5
[55]		300 x 760	150 (minus ant. size)
[96]		150 x 75	71
[97]		250 x 250	not specified
[18]		180	90
[98]	865-956 MHz	50 x 100 x 100	5
[98]		63 x 63 x 63	9
[99]	1.4 GHz	350 x 350 x 200	not specified
[74]	1.575 GHz	180 x 60 x 60	3
[16]		180 x 60 x 60	4
[100]		152 x 152 x 20	8
[80]	2.40-2.45 GHz	103 x 103 x 8.5	3
[84]		70 x 70 x 300	4
[101]		50 x 50 x 50	25
[54]	3.5-4.5 GHz	30 x 40	10

*[mm]. Three values are for box geometries, two for cylinders (diameter x height),

and one for spheres (diameter).

Besides the different dimensions, the placement of an implantable antennas in a body phantom deeply affects the EM performances; Table 2.3 reports the implant depth for each listed body model. Obviously, locations (such as head, shoulder, abdomen, etc.) and depths are

chosen depending on the targeted applications. Although values ranging from 3 to 10 mm are usually used for subcutaneous applications, the distance of the radiator from the external "surface", i.e., implant depth, is not in general established. For instance, values from 1.3 up to 150 mm are reported in [94] and [55], respectively.

Reported Effects and Comments on the Body Phantom Choice

The performances of implanted antennas do not depend only on the phantom and the radiator placement; the specific design of the antenna, its electrical size, the presence and choice of biocompatible insulation, the working frequency are aspects that all play an important role in the overall EM performances, thus commenting the body phantom choices reported in open literature is not an easy task. Nevertheless, some useful information is extractable from previous works.

Homogeneous and three layered models are compared in [102] for several ISM bands. Considering bare straight dipoles, it is shown that the homogeneous model tends to overestimate the losses compared to the multilayered phantom (muscle-fat-skin). Such an overestimation makes the homogeneous model a preferable choice for safety requirements. Three layered phantoms are also discussed in [84] with the radiator still in direct contact with the human tissues. As for the previous work, placing the antenna in different tissues (muscle or fat) may result in large variation compared to the homogeneous case. However, different performances are obtainable with different antennas. For instance, the comparisons between three layers and homogenous phantoms in [18, 80, 103] show little variation of the reflection coefficients, while changes within 4% (at 1.575 GHz) and up to 10% (in the MedRadio band) are reported in [74] and [92], respectively.

The performances of implantable radiators, inserted into simplified or realistic phantoms, are compared in [18, 74, 92]. Almost negligible matching effects are reported in [18] at 400 MHz, but results vary within 4% in [74] at 1.575 GHz and up to 10% in [92] back in the MedRadio band. Consequently, the knowledge of a tuning technique is of great interest, as presented in [99] which focuses on the design of an ingestible antenna working at 1.4 GHz. In the attempt of reducing the differences between the matching performances of antennas implanted in simple and realistic models, particular solutions were presented in [101] and [40]. A careful selection the dimension of a homogeneous box phantom with muscle-like properties is presented in [101], while new dielectric properties are proposed in [40].

The importance of a precise model of the human body when computing radiation patterns is discussed in [18, 74]: important shadowing, due to the phantom size and shape, is appreciable considering the realistic models instead of the homogeneous one. Furthermore, effects of human posture on the radiation are also emphasized in [27, 40]; indeed, the movement of the arms deeply affects the radiation patterns of an implantable radiator in the human chest.

Different realistic models (*Hugo* and both the Japanese male and female models) are compared in [78] evaluating the radiation patterns and efficiencies of ideal sources. This study demonstrates that the radiation performances depend on the body mass index of the subject showing the importance of customized phantoms [91].

Effect of different depths of the radiator is discussed in [74, 104]. On the one hand, undesired thermal profiles are obtained modifying the insertion of a helical antenna for hyperthermia applications at 915 MHz. On the other hand, different box dimensions are

discussed in [74] showing minimal matching variation for a GPS application.

In addition to the EM performances, computational power requirements must be also considered. Despite the availability of extremely detailed models, important simplifications are mandatory when designing implanted antennas. In fact, the computational costs and simulation times often prevent use of realistic phantoms for the design and optimization of radiators. For instance, the numerical analysis of Virtual Family is worthless without the use of graphic card acceleration, and simulations take more than a day using the model given in [72], as reported in [74]. On the contrary, simplified geometries and compositions provide fast results, which is extremely useful when designing and optimizing and/or tuning the investigated antenna.

In conclusion, when focusing on the matching performances of subcutaneous implantable antennas, both the homogeneous and three layers models are satisfactory representations. The presence of different tissues is instead of crucial importance when investigating deep implanted devices, and a precise assessment of the radiation performances of antenna under test requires the simulation of a realistic model (or at least of a portion of it).

2.3.2. Physical Realizations for In Vitro Characterization

While the numerical analysis is extremely rich of body phantoms, more limitations appear when realizing a human body model to test the desired implantable radiator. Several solid phantoms do exist, an example is illustrated in Fig. 2.14-(a). More interesting to the current work are liquid and gel alternatives. Other advantage of these models is the possibility to closely represent the external human shape considering anthropomorphic casings. For a better comprehension, an anthropomorphic housing is shown in Fig. 2.14-(b). Unfortunately, a

<center>(a)   (b)</center>
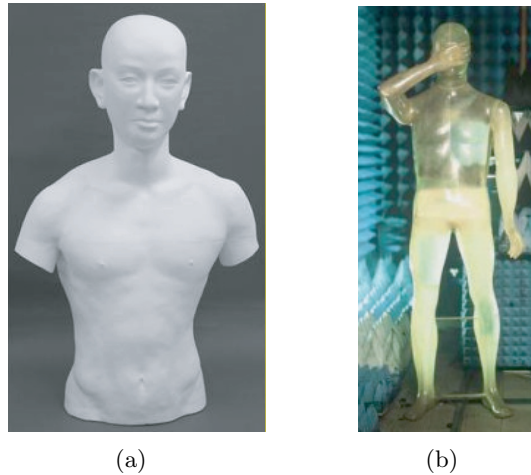
Figure 2.14.: Examples of anthropomorphic phantoms: (a) semi-hard model from [48] and human shaped plastic shell for liquid realization available at the Body-Centric Wireless Sensor Lab of Queen Mary University of London, UK.

detailed description of the inhomogeneity of the human body is currently impossible to achieve with liquids, and very hard with gels. A box three layered structure (muscle-fat-skin) is presented in [98] exclusively for applications at 868 MHz.

The dielectric properties of human tissues have a large dynamic (dispersion) in the microwave frequency range. Indeed, building a phantom whose dielectric properties are similar to the human tissues in a wide frequency band is a challenging task. Ultra-WideBand (UWB) phantoms are currently available (to the best knowledge of the author) in the 2-10 GHz [105], while a broad frequency range (200-2000 MHz) is realized only with skull equivalent properties in [106]. Homogenous liquid phantoms were used in this work. In agreement with the recommendation of [55], we decided to use models with muscle-like dielectric properties for each frequency band. The realization of these phantoms is detailed in the following section.

Liquid Body Phantoms: Realization and Characterization

Several recipes are available for the liquids mimicking the human tissues. Examples are discussed in [86, Annex C] for different targeted materials. Recent solutions are mainly based on [107–110], while classical examples can be found in [111, 112], and specific attention to equivalent skin tissue is paid in [113, 114].

The realization of these chemical components requires a well controlled ambient temperature. According to [111], solutions at $22°$ C are equivalent to real muscle tissue at $37°$ C. Recently, recipes with more robust temperature resilience were presented in [115]. Life time of liquid solutions may vary. However, with a safe and a proper storing, and avoiding bacterial contamination, liquid phantoms last up to 80 days [115].

The recipes of liquid phantoms used in this thesis, and the obtained muscle-like dielectric properties tissue, are reported in Table 2.4 where:

- relative value, "%", refers to the weight;

- water is actually distilled water. The use of deionized water was not found to perceptibly modify the results although not recommend in the MedRadio range [116];

- salt is pure NaCl[‡];

- DGBE stands for *Diethylene Glycol monoButyl Ether*. This is a toxic product that must be handled with care;

- temperature is set to $22°$ C.

Table 2.4.: Recipes and Dielectric Properties of the Equivalent Muscle Body Phantoms.

	Frequency	Recipe	Target values [20]	Measured values
1	MedRadio, 403.5 MHz inspired by [22, Sec. 9.2.3]	water 51.30 % sugar 47.30 % salt 1.40 %	$\varepsilon'_e = 57.10$ $\tan\delta = 0.622$	$\varepsilon'_e = 57.36$ $\tan\delta = 0.580$
2	ISM, 2.45 GHz [117, pp. 36]	water 73.20 % salt 0.04 % DGBE 26.76 %	$\varepsilon'_e = 52.73$ $\tan\delta = 0.242$	$\varepsilon'_e = 53.76$ $\tan\delta = 0.241$

[‡]It is commonly available as dishwasher salt.

These results are also depicted graphically in Figs. 2.15 and 2.16, where the dispersive characteristics of both muscle and the solutions can be observed. A larger disagreement between the targeted and measured relative permittivity (ε'_e) can be noted at 2.45 GHz. Nonetheless, the relative error is within 2%, which makes this solution still useful to test implantable antennas. It is worth reminding that the accuracy of the HP dielectric probe kit 85070E [118] used during the measurements is 5% according to [118].
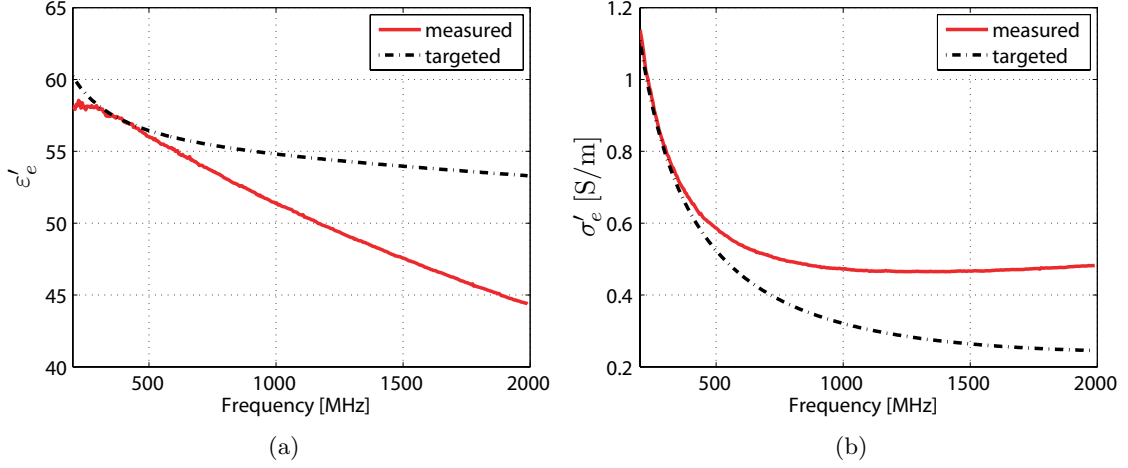
Figure 2.15.: Comparison between the dielectric properties of the targeted muscle tissue [20] and the realized liquid phantom (recipe 1) from 200 to 2000 MHz: (a) relative permittivity and (b) conductivity.
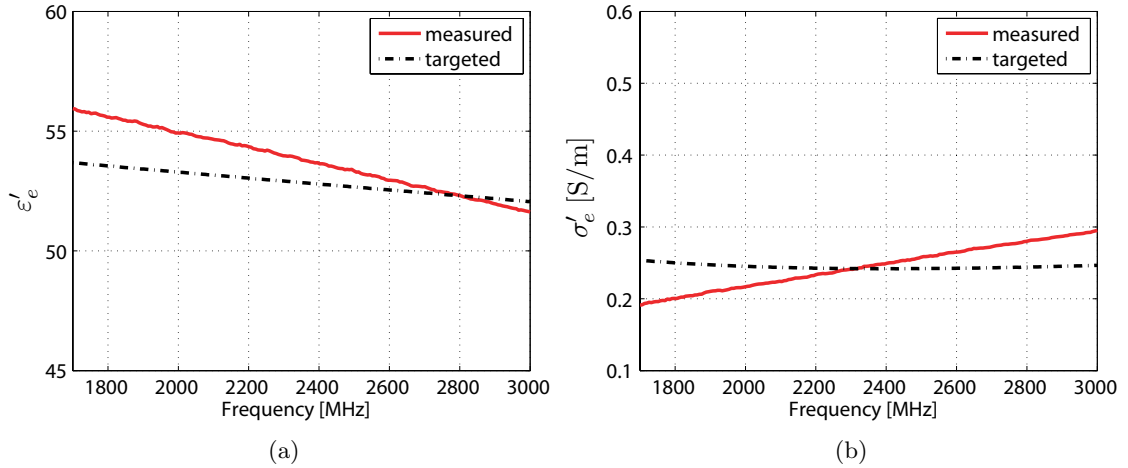
Figure 2.16.: Comparison between the dielectric properties of the targeted muscle tissue [20] and the realized liquid phantom (recipe 2) from 1700 to 3000 MHz: (a) relative permittivity and (b) conductivity.

Basically, distilled water is a dielectric with a high dielectric permittivity ($\varepsilon'_e \simeq 80$). Precise quantity of sugar and salt is added to reduce its ε'_e and increment the conductivity, respectively. An example of the weighting process of the materials used is illustrated in Fig. 2.17.

The recipe for the MedRadio band may be modified with the addition of 1% of the toxic *HydroxylEthylCelulose* (HEC) (accordingly reducing the concentration of sugar) [22, Sec. 9.2.3]. This addition requires a longer preparation, mixing details in [112], providing a more dense solution (gel) that could be useful in some applications. Other solutions involve the use of *polyethylene glycol mono phenyl*(Triton-X 100) [110], *agar* [82] or the addition of a bactericide to extend the life time of the liquid solutions [110].

Figure 2.17.: Weighting process and materials used (from left to right: salt, sugar and distilled water).

The dielectric properties of the liquid solutions were measured with the HP dielectric probe kit 85070E. As illustrated in Fig. 2.18, an open-ended coaxial cable was inserted into the liquid; the probe is connected to a network analyzer and the reflection coefficient values are processed to evaluate the dielectric properties[§]. The calibration using short-open-water, at 22° C, was found to be well suited for the liquid measurements. Using water as reference material increases the accuracy of the measurements as its properties are close to the ones of the liquid under test. The evaluation of the dielectric characteristics is based on the knowledge of both amplitude and phase of the reflection coefficient. Besides the recommendations given in [116] and [118], it is also very useful to:

- consider an oblique position for the open-ended coaxial probe to reduce the presence of undesired bubbles at the probe surface (Fig. 2.18-(b));

- avoid any movement of the cable connecting the probe to the network analyzer. Moving the liquid under test is much more easier and provides less variation;

- reduce the network analyzer Intermediate Filter (IF) bandwidth (down to 30 Hz) for both calibration and measurements. This will increase the sweep time but it is mandatory to try to increase the nominal accuracy.

2.4. Conclusion

In this chapter, we recalled some fundamental theoretical aspects related to antennas in lossy matter, and we discussed several phantoms to model the human body. This analysis serves as common base for all the investigations and results presented later on in this thesis.

[§]Average values of several measurements are presented in Table 2.4 and Figs. 2.15 and 2.16.

       (a)   (b)

Figure 2.18.: HP Dielectric Probe Kit to measure the dielectric properties of the realized phantoms: (a) probe and (b) complete measurement system.

The coupling between the near field terms and the surrounding lossy medium is the most important phenomenon for implantable antennas. Thus, radiated power, common antenna parameters (radiation efficiency, pattern, bandwidth) should be carefully evaluated for a radiator immersed in a lossy medium. Since the biocompatible insulation interacts with the near field dissipation, the next chapter extensively focuses on this aspect providing numerical analysis, results and physical understandings that are very useful for the design of implantable antennas.

Given the selected MedRadio frequency band, implanted antennas result in electrically small radiators. This increases the difficulty of the design. Although classic ESA's limits are not applicable anymore, early discussions for submarine and geophysical applications are still of interest for the case of implantable antennas. For instance, the source choice and its orientation are immediately identified via these early analysis.

The definition of the Specific Absorption Rate has also been recalled, and discussion about its evaluation is given. This parameter is dependent on the selected body phantom. Therefore, a list of available human body models has been discussed and revisited in the point of view of antenna engineers. Phantoms such as the Virtual Family closely represent the reality. However, the computation burden may prevent their use for the design of implantable antennas. The numerical effort is even more cumbersome taking into account the specific aspects of implanted antennas (such as three dimensional miniaturized design) as described in Chapter 4. Furthermore, despite the large choice available during the design process, a few possibilities are actually practicable for the assessment of the realized prototypes.

The realization of homogeneous liquid phantoms has been presented, and we discussed their chemical recipes and measurements. These phantoms have always been used in the following of the work of this thesis. Their approximation is rather rough, but it does allow to reduce the simulation time, and it gives standard and easy to realize conditions for the measurements of the radiator.

3. The Effect of Insulating Layers on the Performance of Implanted Antennas[†]

3.1. Introduction

Insulating layers deeply interact with the radiation and the EM field propagation of sources within the human body. Two layers are investigated in this work: the internal insulation - surrounding the implanted radiator- and the external insulation that is placed upon the human skin tissue.

The internal insulation is of crucial importance from the biological and mechanical points of view; the biocompatible material is necessary to avoid any adverse tissue reaction [119] and to isolate the device from the humid and corrosive human environment [120], preventing metallic oxidation. Additionally, it precludes any short-circuiting effects due to the high conductivity of some human body tissues.

Less stringent chemical and mechanical constraints apply to the external insulation, although biocompatibility and flexibility are still mandatory requirements.

The work performed in this part of the thesis aims at evaluating the power transmission enhancements that can be obtained with an internal and external insulations from an implanted source. In particular, the three main goals of this chapter are:

1. to present a generic physical model that allows the assessment of EM phenomena related to the presence of the biocompatible insulations;

2. to describe the electromagnetic model developed to analyze the physical one;

3. to evaluate of the power transmission enhancement because of insulations. This analysis leads to the formulation of some design considerations that will be applied in the next chapters.

In order to reach these goals, this chapter is organized as follows: Section 3.2 describes the EM phenomena under investigation and the used physical model, while the mathematical model is presented in Section 3.3. General formulation, selected excitations, and numerical techniques and their implementation are here discussed. Particular care has been paid to the selection of truncation criterion of the used Spherical Wave Expansion (SWE).

The mathematical model is applied to the physical model so as to investigate the power transmission enhancement due to the presence of internal and external insulations in Section 3.4. Numerical results together with the characteristics of the selected insulators are reported here. Finally, conclusions are drawn in Section 3.5.

[†] -F. Merli, B. Fuchs, and A.K. Skrivervik, "Influence of insulation for implanted antennas," in *Proc. 3*[rd] *European Conference on Antennas and Propagation (EuCAP 2009)*, Berlin, Germany, Mar. 23–27, 2009.
- F. Merli, B. Fuchs, J.R. Mosig and A.K. Skrivervik, "The effect of insulating layers on the performance of implanted antennas," *IEEE Trans. Antennas Propag.*, Vol. 59 (1) : 21-31, 2011.

3.2. EM Phenomena and Physical Model

Focusing on the EM radiation of implanted sources, this section presents the EM phenomena and the physical model that are considered in this work to analyze the effect of insulating layers on the power transmission from implanted antennas to external receiver.

3.2.1. EM Phenomena

Let us refer to the sketch illustrated in Fig. 3.1. A source (yellow arrow) is at the center of several layers including an internal insulation (green), lossy matter (blue) and an external insulation (violet). The far and near field terms of the EM radiation of the source are identified by black and red arrows, respectively. Asterisks (*) show the discontinuities encountered by the EM wave. A discontinuity results in a reflection and thus in higher dissipation of energy.
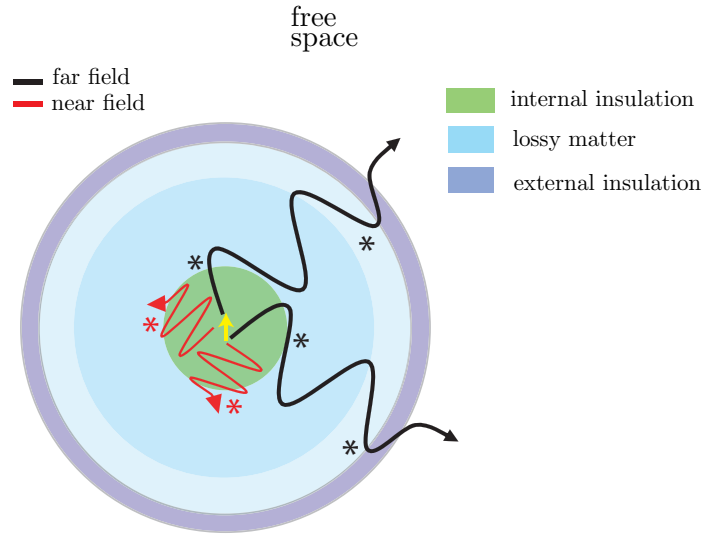
Figure 3.1.: Sketch of an implanted antenna in lossy matter with internal and external insulation.

The considered EM phenomena related to the internal biocompatible insulation are:

- matching the transition of the propagating radiating wave between the source and the body model;

- reducing the coupling, thus the dissipation, of the high near field terms of the electromagnetic radiation in the close living tissue;

Clearly the first phenomenon relates to the far field term of the radiated field that could be obtained with a one dimensional (1D) multilayered model with a plane wave excitation. On the contrary the second phenomenon cannot be handled by a 1D plane wave analysis. This model would not take into account the dissipation of power due to the coupling of the near field which is very relevant analyzing the interaction of EM field with biological tissues [46, 121] and of uppermost importance for implanted antennas.

To underline the importance of such phenomena on implantable antennas, it is worth to point the reader's attention to the investigations presented in [19, 22, 92, 100]. Prominent work has been performed by King [19, Ch. 1, 8 and 10] analyzing theoretically and numerically the effect of insulation on the current distributions of antennas in lossy matter. Radiation

efficiencies and/or matching levels versus insulation properties are compared in [22, 92], while [100] emphasizes the impact of coating thickness over time. Furthermore, theoretical results on the broad band matching properties achievable by insulating implanted antennas are presented in [54].

The considered EM phenomenon related to the external biocompatible layer is:

- matching the transition of the EM wave between the biological tissue and the free space;

This phenomenon may affect both the near field and far field components of the radiated field depending on the source position. Only in the case of an electrically large distance between the source and the external layer, thus considering exclusively far field term, the one dimensional transmission line model with a plane wave excitation provides correct results [122].

The presence of an external layer has already been investigated for many applications. Among them, let us mention: SAR distribution and the microwave power coupling in hyperthermia [123–129], the electromagnetic absorption due to the presence of clothing (for instance [130, 131]), the microwave coupling in medical imaging system [122] and SAR reduction from an undesired external source [132]. According to the application, the external insulator is called clothing, bolus, matching layer, shield, etc.

To the author's knowledge, the effect of the external insulating layer has not been investigated for implanted antennas for telemetry purposes in the MedRadio band. Performing a 1D analysis, the amplitude of the reflection coefficient of a plane wave going through the skin-air interface at 403.5 MHz is equal to 0.77 considering a normal incidence. This high reflection coefficient (due to the large dielectric properties difference) shows how it is mandatory to mitigate (or avoid, if possible) the reflection of the transmitted wave.

3.2.2. Physical Model

In order to take into account the aforementioned phenomena, the physical model consists in multilayered spherical shells in the presence of infinitesimal (electric, magnetic, Huygens) sources. Spherical multilayered models have been considered for various biomedical applications. As discussed in the previous chapter, it turns out that, although being a rough approximation of the human body, such multishell models provide meaningful insights [18, 27, 57, 58, 87–90].

In this analysis, the spherical model is composed of several concentric spherical shells whose dielectric properties are similar to those of real human tissues [20]. Three compositions, two homogeneous (with properties as the equivalent head and muscle tissues) and one multilayered (muscle, fat and skin) are investigated. These body phantoms are representative of the overall performed investigations. The spherical model is enriched with the presence of a lossless air shell embedding the source, and internal and external insulations. Illustrations are given in Fig. 3.2.

The selected excitations allow for the analysis of the interaction of the near field terms of the EM radiation with the insulations and biological tissues. Ideal excitations are considered in order to fix the current distribution of the source otherwise affected by the insulation properties [19]. Details about their characteristics and the mathematical explanation of the presence of the air shell [133] is given in Section 3.3.2 while presenting the mathematical model.
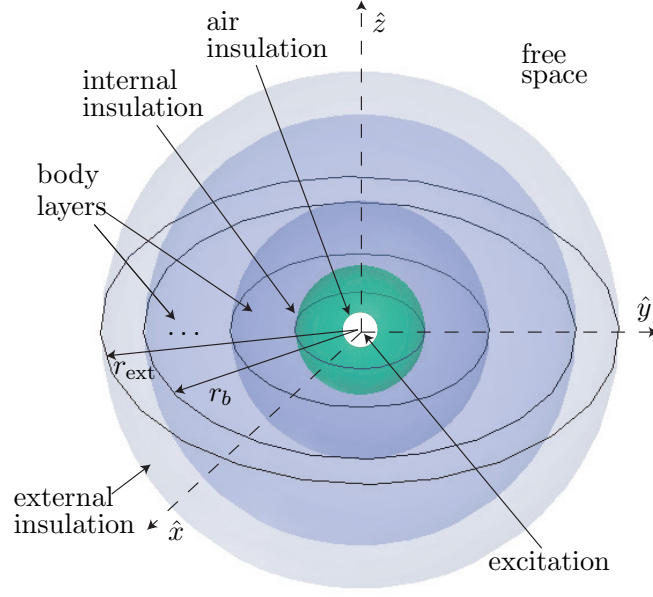
Figure 3.2.: Three-dimensional view of the analyzed structure . The excitation is placed at the center of several concentric spherical dielectric shells. The spherical shells enable one to model the air (immediately surrounding the source), the internal insulation, the body layers and the external insulation.

3.3. Mathematical Model

This section presents the mathematical model and its numerical implementation in Matlab that have been used to solve the physical model previously described.

3.3.1. Spherical Wave Expansion

The mathematical notations and the way how to compute the electromagnetic field are described here. The following standard Spherical Wave Expansion (SWE) development, although well known from classical works [134, ch. 7] and more recent publications [135–137] is summarized here for the sake of completeness and for a better understanding of the next Sections.

The electromagnetic field, considering a linear, homogeneous and isotropic medium, in the absence of any source verifies the wave equation:

$$\Delta \left\{ \begin{array}{c} \mathbf{E} \\ \mathbf{H} \end{array} \right\} + k^2 \left\{ \begin{array}{c} \mathbf{E} \\ \mathbf{H} \end{array} \right\} = \mathbf{0}, \tag{3.1}$$

where k is the wave number, Δ is the laplacian operator and time harmonic dependence is set to e^{jwt}. Due to the dispersive and lossy characteristics of the human body the wave number is a complex variable

$$k = \omega \sqrt{\mu(\omega)\varepsilon_c(\omega)} \tag{3.2}$$

where ε_c is the complex effective frequency dependent permittivity as detailed in Section 2.2.1

$$\varepsilon_e = \varepsilon_0(\varepsilon_e' - j\varepsilon_e'') = \varepsilon_0 \left(\varepsilon_e' - j\frac{\sigma_e'}{\omega\varepsilon_0} \right) \tag{3.3}$$

The solution of the wave equation (3.1) is obtained solving first the scalar Helmholtz equation

$$\Delta\Psi + k^2\Psi = 0 \tag{3.4}$$

where Ψ is scalar function.

Given the spherical geometry under investigation depicted in Fig. 3.2, the Helmholtz equation is expressed in the spherical coordinate system illustrated in Fig. 3.3 and solved using the separation of variables method:

$$\Psi(r,\theta,\varphi) = R(r)\Theta(\theta)\Phi(\varphi), \; r \geq 0, \theta \in [0,\pi], \varphi \in [0,2\pi[, \tag{3.5}$$

obtaining

$$\Psi(r,\theta,\varphi) = \sum_{n,m,v,s} \alpha_{mn}^{vs}\Psi_{mn}^{vs}(r,\theta,\varphi), \text{ where } \sum_{n,m,v,s} = \sum_{n=1}^{+\infty}\sum_{m=0}^{n}\sum_{v=e,o}\sum_{s=1,4}, \tag{3.6}$$

with $\Psi_{mn}^{vs}(r,\theta,\varphi) = Z_n^s(kr) \; P_n^m(\cos(\theta)) \; f_m^v(\varphi)$,

$$f_m^v(\varphi) = \begin{cases} \sin(m\varphi) \text{ if } v = o \\ \cos(m\varphi) \text{ if } v = e \end{cases},$$

$Z_n^1 = $ spherical Bessel function of the first kind and of order n,
$Z_n^4 = $ spherical Hankel function of the second kind and of order n,
$P_n^m = $ associated Legendre polynomial of degree n and order m.

The extension of the scalar solution (3.6) is done through the use of the spherical wave vectors for the solution of the wave equation (3.1). This basis is constituted by the spherical wave vectors for $n = 1, 2, \ldots + \infty$, $m = 0, 1, \ldots n$, $v \in \{e, o\}$ et $s \in \{1, 4\}$:

$$\mathbf{M}_{mn}^{vs} = \nabla \times (\Psi_{mn}^{vs}\mathbf{r}) \tag{3.7}$$

$$\mathbf{N}_{mn}^{vs} = \frac{1}{k}\nabla \times \nabla \times (\Psi_{mn}^{vs}\mathbf{r})$$

$$\mathbf{L}_{mn}^{vs} = \frac{1}{k}\nabla\Psi_{mn}^{vs}$$

Several properties of the vector basis function can be found in [135, 136, 138]. For the purpose of this work, it is worth reminding that $\mathbf{L}_{mn}^{vs}$ characterizes the sources ($\nabla \cdot \mathbf{L}_{mn}^{vs} \neq 0$), therefore is not present in the expression of the EM field in a region free of excitations.
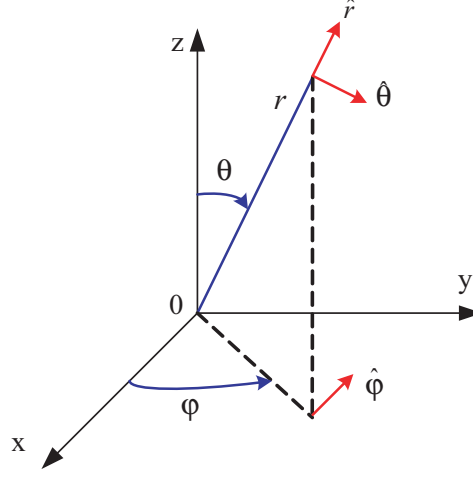
Figure 3.3.: Spherical coordinate system.

The sum in (3.6) generally considers both $s \in \{1, 4\}$ cases, thus it is worth discussing some physical explanations about the proper choice of the s value. This choice depends on the relative position of the observer to the source. Let us consider the problem presented in Fig. 3.4 where a given source distribution is included in a spherical shell limited by r_{int} and r_{ext}.
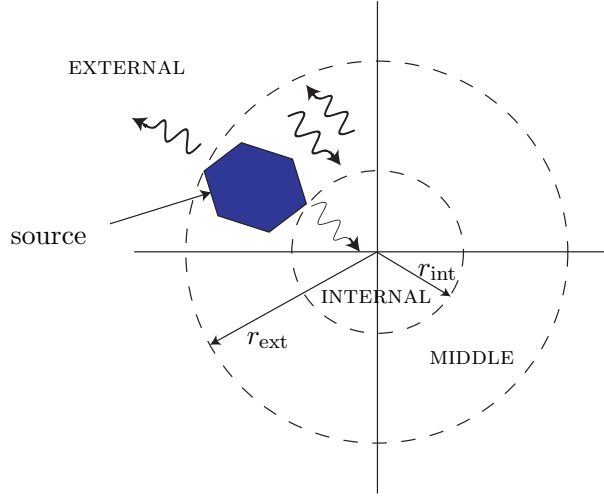
Figure 3.4.: Different regions for the selection of the spherical functions $s \in \{1, 4\}$.

Following Wilcox [139] we can define three spheres:

- External shell for all the radii $r > r_{\text{ext}}$. For all the observation points in this region only the spherical Hankel function of the second kind ($s = 4$), representing an outward traveling wave, is necessary as it verifies the finiteness of the EM field at infinity.

- Middle shell for all the radii $r_{\text{int}} < r < r_{\text{ext}}$. For all the observation points (different from the source) in this region both inward and outward waves are necessary ($s \in \{1, 4\}$).

- Internal shell for all the radii $r < r_{\text{int}}$. For all the observation points in this region only the spherical Bessel function of the first kind ($s = 1$), representing an inward traveling wave, is necessary as it verifies the finiteness of the EM field at the origin.

Electromagnetic Field Expression

Following the previous development, the EM field verifying (3.1) in a region without any excitations is expressed as:

$$\left\{ \begin{array}{c} \mathbf{E} \\ -j\zeta\mathbf{H} \end{array} \right\} = \sum_{n,m,v,s} a_{mn}^{vs} \left\{ \begin{array}{c} \mathbf{M}_{mn}^{vs} \\ \mathbf{N}_{mn}^{vs} \end{array} \right\} + b_{mn}^{vs} \left\{ \begin{array}{c} \mathbf{N}_{mn}^{\bar{v}s} \\ \mathbf{M}_{mn}^{\bar{v}s} \end{array} \right\} \qquad (3.8)$$

where a_{mn}^{vs} and b_{mn}^{vs} are the spherical modal coefficients, m and n are the mode indexes and ζ is the intrinsic medium impedance. $\mathbf{M}_{mn}^{vs}$ and $\mathbf{N}_{mn}^{vs}$ at observation point (r, θ, φ) are:

$$\mathbf{M}_{mn}^{vs} = -t_{mn}^{v1}(\theta) \, Z_n^s(z) \, f_m^v(\varphi) \, \hat{\theta} + t_{mn}^{v2}(\theta) \, Z_n^s(z) \, f_m^{\bar{v}}(\varphi) \, \hat{\varphi} \qquad (3.9)$$

$$\mathbf{N}_{mn}^{vs} = t_{mn}^{v3}(\theta) \, Z_n^s(z)/z \, f_m^{\bar{v}}(\varphi) \, \hat{r} - t_{mn}^{v2}(\theta) \, K_n^s(z) \, f_m^{\bar{v}}(\varphi) \, \hat{\theta} - t_{mn}^{v1}(\theta) \, K_n^s(z) \, f_m^v(\varphi) \, \hat{\varphi}$$

$$\text{where} \begin{cases} z = kr, \ k \text{ is the wave number (3.2)} \\[2mm] t_{mn}^{v1}(\theta) = \bar{v}(-1)m\dfrac{P_n^m(\cos\theta)}{\sin\theta} \\[3mm] t_{mn}^{v2}(\theta) = -\dfrac{\partial}{\partial\theta} P_n^m(\cos\theta) \\[3mm] t_{mn}^{v3}(\theta) = n(n+1)P_n^m(\cos\theta) \\[3mm] K_n^s(z) = \dfrac{1}{z}\dfrac{d}{dz}\left(zZ_n^s(z)\right) = Z_{n-1}^s(z) - \dfrac{n}{z} \, Z_n^s(z) \\[3mm] v(-1) = \begin{cases} +1 \ \text{ if } \ v = e \\ -1 \ \text{ if } \ v = o \end{cases} \\[3mm] \bar{v} \text{ is its complement in the set } \{e, o\} \end{cases}$$

It is worth calling the attention of the reader to the fact that the expression (3.8) is valid at any observation point $r \in \{0, +\infty\}$, $\theta \in [0, \pi]$, $\varphi \in [0, 2\pi[$, while, the spherical modal coefficients a_{mn}^{vs} and b_{mn}^{vs} can be interpreted as transverse-electric and magnetic modes, respectively.

Radiated Power: by substituting (3.8) and (3.7) into (2.9) and using the orthogonality properties of spherical modal vectors, presented in [135, 136, 138, 140] and given in Appendix A.1, one gets, after some manipulations, the analytical expression of the radiated

power through a spherical surface at any distance r:

$$P_{\text{rad}}(r) = \oint_{S_r} \tfrac{1}{2}\text{Re}\{\mathbf{E} \times \overline{\mathbf{H}}\} \cdot \hat{r}dS = \frac{r^2}{2}\text{Re}\left\{\frac{\text{j}}{\overline{\zeta}} \sum_{n,m,v,s} \cdots \right.\tag{3.10}$$

$$\left.\left(Z_n^s(z)\lambda_{mn}^v\left(|a_{mn}^{vs}|^2\overline{K_n^s(z)} + a_{mn}^{vs}\,\overline{a_{mn}^{v\bar{s}}}\,\overline{K_n^{\bar{s}}(z)}\right) + \overline{Z_n^s(z)}\lambda_{mn}^{\bar{v}}\left(|b_{mn}^{vs}|^2 K_n^s(z) + b_{mn}^{vs}\,\overline{b_{mn}^{v\bar{s}}}\,K_n^{\bar{s}}(z)\right)\right)\right\}$$

$$\text{where}\quad \begin{cases} \lambda_{mn}^v = \pi\dfrac{e_m^{\bar{v}}}{c_{mn}} \\[2mm] \overset{o}{e_m^e} = 1 \pm \delta_m,\ \delta \text{ is the Krönecker symbol} \\[2mm] c_{mn} = \dfrac{2n+1}{2n(n+1)}\dfrac{(n-m)!}{(n+m)!} \end{cases}$$

Four main terms can be identified in (3.10), namely $|a_{mn}^{vs}|^2$, $|b_{mn}^{vs}|^2$, $a_{mn}^{vs}\overline{a_{mn}^{v\bar{s}}}$ and $b_{mn}^{vs}\overline{b_{mn}^{v\bar{s}}}$. The first two represent the power of the inward and out ward traveling waves (according to s). Obviously, the inward term is relevant only for the calculation of radiated power in proximity of the origin, while the outward wave is the only important term when focusing on the far field radiation.

The latter two consist in the cross product between the inward and outward waves (s and $\bar{s}$). These terms become very relevant to the computation of radiated power in the near proximity of the source surrounded by lossy media.

Specific Absorption Rate: knowing the electromagnetic field, excluded the source region, it is possible to evaluate the local Specific Absorption Rate defined as

$$SAR = \frac{1}{2}\frac{\sigma_e'|E|^2}{\rho}\tag{3.11}$$

where σ_e' is the conductivity (see Section 2.2.1) and ρ the mass density of the medium and $\sigma_e'|E|^2$ is the absorption energy at the point of observation. Explicit expression of local SAR following 3.8 results in a rather tedious formulation as no cross-product simplifications occur (in opposition to the radiated power case (3.10) when integrating over a spherical surface). Therefore, it is simpler to compute the following expression

$$SAR = \frac{1}{2}\frac{\sigma_e'(|E_r|^2 + |E_\theta|^2 + |E_\varphi|^2)}{\rho}\tag{3.12}$$

also from the implementation point of view once the electric field values are known.

Far Field Approximation

The expression of the electromagnetic field in the far field region can be further simplified. First of all, only a forward propagating wave ($s = 4$) is of interest. Second, substituting the asymptotic expression for large arguments (given in Appendix A.2.3) in (3.8), the EM field

equals to:

$$E_r = O\big(1/|kr|^2\big) \tag{3.13}$$

$$E_\theta = -\frac{e^{-jkr}}{kr} \sum_{n,m,v} \mathrm{j}^n\big[\mathrm{j}\, a_{mn}^{v4} t_{mn}^{v1}(\theta) + b_{mn}^{v4} t_{mn}^{\bar{v}2}(\theta)\big] f_m^v(\varphi) + O\big(1/|kr|^2\big)$$

$$E_\varphi = \frac{e^{-jkr}}{kr} \sum_{n,m,v} \mathrm{j}^n\big[\mathrm{j}\, a_{mn}^{v4} t_{mn}^{v2}(\theta) - b_{mn}^{v4} t_{mn}^{\bar{v}1}(\theta)\big] f_m^{\bar{v}}(\varphi) + O\big(1/|kr|^2\big)$$

$$H_r = O\big(1/|kr|^2\big) \tag{3.14}$$

$$H_\theta = -\frac{e^{-jkr}}{\zeta kr} \sum_{n,m,v} \mathrm{j}^{n+1}\big[a_{mn}^{v4} t_{mn}^{v2}(\theta) + \mathrm{j}\, b_{mn}^{v4} t_{mn}^{\bar{v}1}(\theta)\big] f_m^{\bar{v}}(\varphi) + O\big(1/|kr|^2\big)$$

$$H_\varphi = \frac{e^{-jkr}}{\zeta kr} \sum_{n,m,v} \mathrm{j}^{n+1}\big[-a_{mn}^{v4} t_{mn}^{v1}(\theta) + \mathrm{j}\, b_{mn}^{v4} t_{mn}^{\bar{v}2}(\theta)\big] f_m^v(\varphi) + O\big(1/|kr|^2\big)$$

Radiated Power: the expression of the radiated power through a spherical surface in a lossless medium (ζ is real) at large distance from the source is

$$P_{\mathrm{rad}}(r) = -\frac{r^2}{2\zeta}\mathrm{Re}\left\{\sum_{n,m,v}\left[|a_{mn}^{v4}|^2 \lambda_{mn}^v \,\mathrm{j}\, Z_n^4(kr)\overline{K_n^4(kr)} + |b_{mn}^{v4}|^2 \lambda_{mn}^{\bar{v}} \,\overline{\mathrm{j}\, Z_n^4(kr)\overline{K_n^4(kr)}}\right]\right\} \tag{3.15}$$

where only the "powers" of the outward waves are considered ($|a_{mn}^{v4}|^2$, $|b_{mn}^{v4}|^2$). Taking advantage of asymptotic expressions of the spherical Hankel functions for large arguments (A-9) one obtains a more compact version:

$$P_{\mathrm{rad}} = \frac{1}{2\zeta k^2} \sum_{n,m,v} \lambda_{mn}^v \big[|a_{mn}^{v4}|^2 + |b_{mn}^{\bar{v}4}|^2\big] \tag{3.16}$$

3.3.2. Excitations

This work aims at providing some insights on the insulation layer influence. Ideal excitations are considered. This choice fixes the current distribution of the source otherwise affected by the insulation properties [19]. It is possible to model more realistic sources, but, this leads to a significant increase of computational burden and it would produce results that are dependent on the selected radiating structure.

The ideal source is surrounded by an insulation layer. Infinitesimal electric (Hertzian) and magnetic dipoles are used. A Huygens source is also modeled. It consists of crossed electric and magnetic dipoles and it has the properties of focusing the radiated field in a desired half space [141] (if both dipoles have the same amplitude). It can therefore be considered as representative of some relatively directive antennas, with a preferred off-body direction of radiation.

As pointed out by Tai in [133], an ideal dipole radiating in an unbounded lossy medium must be supplied with infinite power to maintain a finite field at distance. Clearly, this is not physically meaningful. To overcome this problem, Tai suggested to insulate the dipole with a lossless sphere. This problem remains if the dipole is placed at the center of a bounded lossy layer (in this case spherical), as shown in Appendix A.3. Thus, the excitation is first insulated by an air shell, in turn surrounded by a biocompatible material, as shown in Fig. 3.2. It can be said that our acting source is a mathematical dipole source, surrounded and insulated by an air shell.

3.3.3. Mode Matching Technique for Concentric Spheres

A Mode Matching Technique (MMT) based on spherical wave functions is used to compute the interaction between concentric spherical homogeneous layers and the selected source. This method is well suited to analyze our problem since, a priori, there are no limitations regarding the dimensions and electromagnetic properties (permittivity, permeability and losses) of the layers. The MMT gives direct access to the field everywhere in a source free region, with controlled accuracy as further discussed in Section 3.3.4.

In order to solve the EM problem described in Section 3.2 and express the field as in (3.8), it is necessary to know the spherical modal coefficients (a, b).

Due to the linearity of the problem of interest and to the selected excitations (Section 3.3.2), it is possible to separate the contribution of the source alone from the one due to the diffraction of the spherical shells as in [136, 137]*. It is then straightforward to add the two contributions. That means that in each investigated shell (3.8) is actually rewritten as

$$\text{source shell:} \quad \left\{ \begin{array}{c} \mathbf{E} \\ -j\zeta\mathbf{H} \end{array} \right\} = \sum_{n,m,v,s} (a^{i\,vs}_{mn} + a^{d\,vs}_{mn}) \left\{ \begin{array}{c} \mathbf{M}^{vs}_{mn} \\ \mathbf{N}^{vs}_{mn} \end{array} \right\} + (b^{i\,vs}_{mn} + b^{d\,vs}_{mn}) \left\{ \begin{array}{c} \mathbf{N}^{\bar{v}s}_{mn} \\ \mathbf{M}^{\bar{v}s}_{mn} \end{array} \right\} \tag{3.17}$$

$$\text{othwerwise:} \quad \left\{ \begin{array}{c} \mathbf{E} \\ -j\zeta\mathbf{H} \end{array} \right\} = \sum_{n,m,v,s} a^{d\,vs}_{mn} \left\{ \begin{array}{c} \mathbf{M}^{vs}_{mn} \\ \mathbf{N}^{vs}_{mn} \end{array} \right\} + b^{d\,vs}_{mn} \left\{ \begin{array}{c} \mathbf{N}^{\bar{v}s}_{mn} \\ \mathbf{M}^{\bar{v}s}_{mn} \end{array} \right\} \tag{3.18}$$

where $(a^{i\,vs}_{mn}, b^{i\,vs}_{mn})$ and $(a^{d\,vs}_{mn}, b^{d\,vs}_{mn})$ are the incident and diffracted coefficients, respectively, whose evaluation is detailed in the following paragraphs. Obviously, the choice between inward and outward waves $(s \in \{1, 4\})$ follows the considerations given by Wilcox [139] previously reported.

It is important to underline that an elegant evaluation of the diffracted coefficients is achievable in all regions of interests applying the MMT given the knowledge of the incident coefficients.

---

*If the source characteristics are modified by the spheres presence (for instance for implanted real source or radiators in close proximity of the shells), more sophisticated techniques such as the Method of Auxiliary Sources (MAS) [58] or the Method of Moments (MoM) with dedicated Green's functions [88, 138] must be used.

Incident Coefficients

Among several ways to compute the incident coefficients [136], we considered the one based on the knowledge of the current constituting the source. The method is detailed in [135, pp. 73-76] where it is shown that

$$
\left\{ \begin{array}{c} a^{ivs}_{mn} \\ b^{i\overline{v}s}_{mn} \end{array} \right\} = -\frac{k^2\zeta}{\pi e_m}\, c_{mn} \int_{V_0} \left[\mathbf{J^e_v}(\mathbf{r}) \cdot \left\{ \begin{array}{c} \mathbf{M}^{v\bar{s}}_{mn}(\mathbf{r}) \\ \mathbf{N}^{v\bar{s}}_{mn}(\mathbf{r}) \end{array} \right\} - \frac{\mathrm{j}}{\zeta}\,\mathbf{J^m_v}(\mathbf{r}) \cdot \left\{ \begin{array}{c} \mathbf{N}^{v\bar{s}}_{mn}(\mathbf{r}) \\ \mathbf{M}^{v\bar{s}}_{mn}(\mathbf{r}) \end{array} \right\} \right] dv(\mathbf{r}) \quad (3.19)
$$

$$
\text{with } e_m = \left\{ \begin{array}{l} 2 \text{ if } m = 0 \\[2mm] 1 \text{ if } m \neq 0 \end{array} \right.
$$

where J^e_v and J^m_v are the electric and magnetic volumetric currents of the sources while k and ζ corresponds to medium where the excitations are placed in. One can easily recognize that $\mathbf{M}$, $\mathbf{N}$ in (3.19) can be interpreted as the Green's functions of the investigated problem.

The ideal excitations, positioned at $(r_0, \theta_0, \varphi_0)$, are characterized by the electric and magnetic dipole moments $(\mathbf{p}^e, \mathbf{p}^m)$. These are linked to the infinitesimal current distribution as

$$
\mathbf{J}^e(\mathbf{r}) = \mathbf{p}^e\, \delta(\mathbf{r} - \mathbf{r}_0) \tag{3.20}
$$

$$
\mathbf{J}^m(\mathbf{r}) = \mathbf{p}^m\, \delta(\mathbf{r} - \mathbf{r}_0) \tag{3.21}
$$

$$
\text{with } \delta(\mathbf{r} - \mathbf{r}_0) = \frac{1}{r^2 \sin\theta}\, \delta(r - r_0)\delta(\theta - \theta_0)\delta(\varphi - \varphi_0)
$$

Substituting (3.20) and (3.21) in (3.19) one obtains

$$
\left\{ \begin{array}{c} a^{ivs}_{mn} \\ b^{i\overline{v}s}_{mn} \end{array} \right\} = -\frac{k^2\zeta}{\pi e_m}\, c_{mn} \left[\mathbf{p}^e \cdot \left\{ \begin{array}{c} \mathbf{M}^{v\bar{s}}_{mn}(\mathbf{r}_0) \\ \mathbf{N}^{v\bar{s}}_{mn}(\mathbf{r}_0) \end{array} \right\} - \frac{\mathrm{j}}{\zeta}\mathbf{p}^m \cdot \left\{ \begin{array}{c} \mathbf{N}^{v\bar{s}}_{mn}(\mathbf{r}_0) \\ \mathbf{M}^{v\bar{s}}_{mn}(\mathbf{r}_0) \end{array} \right\} \right] \tag{3.22}
$$

The dipole moment $\mathbf{p}^e_m$ is a vector whose components $(p_\mathbf{r}, p_\theta, p_\varphi)$ describe the source orientation with respect to the origin of spherical coordinate system. In this work the origin coincides with the center of the concentric spherical shells as illustrated in Fig. 3.2.

Diffracted Coefficients

Once the incident (i.e., source) coefficients are known in the source shell, the use of the MMT allows the analytical evaluation of the diffracted ones in all regions of interests due to the properties of the vector basis [135].

Let us consider the geometry described in Fig. 3.5 depicting a multilayered spherical structure with q shells and concentric to the origin of the coordinate system. Applying the continuity of the tangential components of the electromagnetic field at each spherical boundary, i.e,

$$
\hat{r} \times \left\{ \begin{array}{c} \mathbf{E}(r^-_p) \\ \mathbf{H}(r^-_p) \end{array} \right\} = \hat{r} \times \left\{ \begin{array}{c} \mathbf{E}(r^+_p) \\ \mathbf{H}(r^+_p) \end{array} \right\} \text{ with } r^{\pm}_p = r_p \pm 0. \tag{3.23}
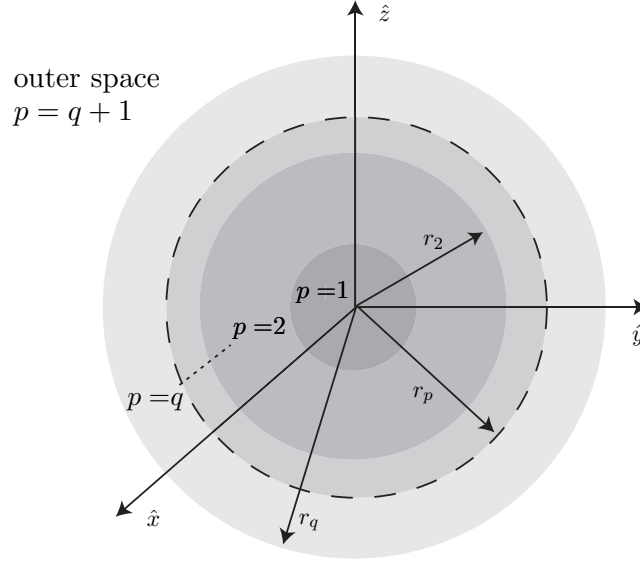$$

Figure 3.5.: Multilayered Spherical structures and notations used for the expression of the diffracted coefficients; q dielectric shells are considered and the $q + 1$ sphere corresponds to the infinite homogenous external medium. Dashed line indicates the r_p $(1 \leq p \leq q)$ shell.

it is possible, thanks to spherical wave vectors properties [135, 136], to relate the coefficients in the $p + 1$ shell with the ones in the previous layer p

$$
\begin{bmatrix} a^{p+1v,1}_{mn} \\ a^{p+1v,4}_{mn} \end{bmatrix} = \begin{bmatrix} M_n^{a,p} \cdot a^{pv,1}_{mn} \\ M_n^{a,p} \cdot a^{pv,4}_{mn} \end{bmatrix} \tag{3.24}
$$

$$
\begin{bmatrix} b^{p+1v,1}_{mn} \\ b^{p+1v,4}_{mn} \end{bmatrix} = \begin{bmatrix} M_n^{b,p} \cdot b^{pv,1}_{mn} \\ M_n^{b,p} \cdot b^{pv,4}_{mn} \end{bmatrix} \tag{3.25}
$$

where $M_n^{a,p} = [Z_n^{a,p+1}]^{-1} \cdot Z_n^{a,p}$ and $M_n^{b,p} = [Z_n^{b,p+1}]^{-1} \cdot Z_n^{b,p}$

$$
Z_n^{a,p+1} = \begin{bmatrix} Z_n^1(z_p^+) & Z_n^4(z_p^+) \\ K_n^1(z_p^+) & K_n^4(z_p^+) \end{bmatrix}
\qquad
Z_n^{b,p+1} = \begin{bmatrix} K_n^1(z_p^+) & K_n^4(z_p^+) \\ Z_n^1(z_p^+) & Z_n^4(z_p^+) \end{bmatrix}
$$

$$
Z_n^{a,p} = \begin{bmatrix} Z_n^1(z_p^-) & Z_n^4(z_p^-) \\ \tau_p K_n^1(z_p^-) & \tau_p K_n^4(z_p^-) \end{bmatrix}
\qquad
Z_n^{b,p} = \begin{bmatrix} K_n^1(z_p^-) & K_n^4(z_p^-) \\ \tau_p Z_n^1(z_p^-) & \tau_p Z_n^4(z_p^-) \end{bmatrix}
$$

with $\tau_p = \dfrac{\zeta_{p+1}}{\zeta_p}$, $z_p^+ = k_{p+1} r_p$ and $z_p^- = k_p r_p$.

It is then straight forward to extend previous expressions cascading the effect of all the spherical shells. Hence, the coefficients in layer $p + 1$ can be expressed in terms of the ones of the

innermost shell $(p = 1)$ as[†]

$$\begin{bmatrix} a^{p+1}{}^{v,1}_{mn} \\ a^{p+1}{}^{v,4}_{mn} \end{bmatrix} = T^a_{p,n} \cdot \begin{bmatrix} a^{1}{}^{v,1}_{mn} \\ a^{1}{}^{v,4}_{mn} \end{bmatrix} \quad \text{where } T^a_{p,n} = \prod_{i=p}^{1} M^{a,i}_n \tag{3.26}$$

$$\begin{bmatrix} b^{p+1}{}^{v,1}_{mn} \\ b^{p+1}{}^{v,4}_{mn} \end{bmatrix} = T^b_{p,n} \cdot \begin{bmatrix} b^{1}{}^{v,1}_{mn} \\ b^{1}{}^{v,4}_{mn} \end{bmatrix} \quad \text{where } T^b_{p,n} = \prod_{i=p}^{1} M^{b,i}_n \tag{3.27}$$

with $\prod_{i=p}^{1} M^{a,i}_n = M^{a,p}_n \cdot M^{a,p-1}_n \cdots M^{a,1}_n$. It can be appreciated that T matrixes are actually Transmission matrixes to model the cascading of non-uniform (ζ varies with the radius r) spherical wave guides. The determinants of the matrixes $T^a_{p,n}$ and $T^a_{p,n}$ are never zero which assure their inversion to solve for the coefficients [135].

In order to evaluate the diffracted coefficients $(a^{d}{}^{vs}_{mn}, b^{d}{}^{vs}_{mn})$, it is necessary to consider the incident coefficients $(a^{i}{}^{vs}_{mn}, b^{i}{}^{vs}_{mn})$, and to properly chose the presence of inward and/or outward waves [139]. The analysis of sources placed in the innermost, intermediate and external shell (outer space) lead to different analytical formulation. Each condition is detailed in Appendix A.4.

3.3.4. Numerical Implementation

Once all the terms of the SWE of the electromagnetic field are known, we can proceed with the numerical implementation. For this purpose, some numerical aspects must be considered. First of all, the necessity of truncating the number of spherical modes to N_t in (3.8). A new truncation criterion is presented based on the amount of radiated power including near field terms.

Second, numerical aspects such as the evaluation of the EM field in close proximity of the source or in all the points with the same radial distance (regardless of θ or φ) are discussed. Finally, the implemented MMT code is compared to a commercial software, FEKO [142], validating the results and appreciating the effect of the proposed truncation criterion.

Truncation Criterion

The series $\sum_n$ (3.6) requires a truncation order N_t when numerically implemented for the evaluation of the EM field (3.8) and the radiated power (3.10). Many studies have discussed the choice of N_t in relation to the antenna size and with the focus on the far field accuracy (for instance [141, 143–145], [146] and references therein). A convergence criterion, inspired by [146], is implemented here to evaluate the relative amount of the truncated power $\xi^{N_t}_{P_{\text{tr}}}(r)$, at a given distance r including the near field ranges:

$$\xi^{N_t}_{P_{\text{tr}}}(r) = \frac{P^{N_t+1}_{\text{rad}}(r) - P^{N_t}_{\text{rad}}(r)}{P^{N_t}_{\text{rad}}(r)} \tag{3.28}$$

[†]The knowledge of the coefficients in the innermost shell makes trivial the evaluation of $(a^{d}{}^{vs}_{mn}, b^{d}{}^{vs}_{mn})$. However, it is also possible to relate the diffracted coefficients the ones in any other shell with more algebraic manipulations.

In the above formula $P_{\mathrm{rad}}^{N_t}$ equals to P_{rad} in (3.10) replacing $\sum_n = \sum_{n=1}^{\infty}$ by $\sum_{n=1}^{N_t}$. The truncation order N_t is first set to be equal to $\lceil k_0 r_{\mathrm{ext}} \rceil$, where k_0 is the free space wave number and r_{ext} the radius of the biggest shell. N_t is then automatically increased until the neglected power, $\xi_{P_{\mathrm{tr}}}^{N_t}(r)$, is below α:

$$\max_{\mathrm{r} \in \mathrm{R_{uo}}} \left\{ \xi_{P_{\mathrm{tr}}}^{N_t}(r) \right\} \leq \alpha \tag{3.29}$$

where R_{uo} is the subset of the radial distances under observation.

EM Field with large number of modes

In order to evaluate the effect of the insulating layers, it is necessary to focus the analysis on the near field components of the EM field in the close proximity of the source (for instance distances $< \lambda/750$). In fact, the coupling between these components and the biological lossy tissues predominantly affects the performances of implanted radiators.

Depending on the source position and orientations, this analysis requires an increasing number of spherical modes as the observation point approaches the excitation. Therefore, asymptotic behaviors [147] as $N \to +\infty$ are reported in Appendix A.2.1. Nonetheless, depending on the point of observation z and the number for modes, the computation of all the terms in 3.8 may reach *overflow* condition (even if the overall field has still a finite value). Therefore, intermediate normalizations of $Z_n^s(z)$ and $K_n^s(z)$ were introduced when evaluating incident and diffracted coefficients, the EM field and P_{rad} to compensate the numerical issue.

EM Field close to the origin

The computation of (3.8) can be problematic in the close proximity of the origin. Asymptotic behaviors for the functions $Z_n^1(z)$ and $K_n^1(z)$, as $|k|r \to 0$ for $n = 1, 2, ...$ converges (see Appendix A.2.2), but one should also consider the diverging nature of $Z_n^4(z)$ and $K_n^4(z)$ to evaluate the field when the excitation is at the origin. In this case the asymptotic formulas reported in Appendix A.2.2 provide a more robust implementation.

EM Field at $r = r_0$ (but far from the source)

The MMT gives access to the field everywhere except the source region, which, for the ideal sources chosen in this work, corresponds only to an infinitesimal point. Therefore the EM field can be evaluated as close as desired to the source provided the proper evaluation of necessary number of spherical modes. However, for all the points with $r = r'$ (regardless of θ or φ) the SWE is slowly converging and the evaluation of the EM field requires a very large number of modes [148]. For an easier comprehension, let us refer to the simple case depicted in Fig. 3.6.
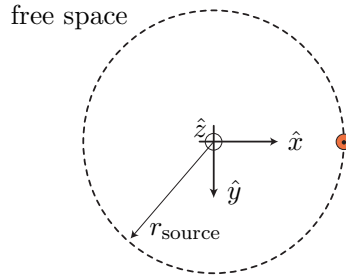

Figure 3.6.: Ideal electric dipole in free space. Dashed circle indicates only the points on the $\theta = \pi/2$ plane with $r = r_{\mathrm{source}}$.

An ideal electric dipole (red dot, oriented along the z axis) is placed at distance r_{source} at $(\theta = \pi/2, \varphi = 0)$ in a free space environment. The presence of an off-centered source gives rise to a discontinuity of the electric field not only at the source position but for all the points with the same radial distance, r_{source}, as illustrated in Fig. 3.7. This discontinuity, obviously, does not correspond to reality.
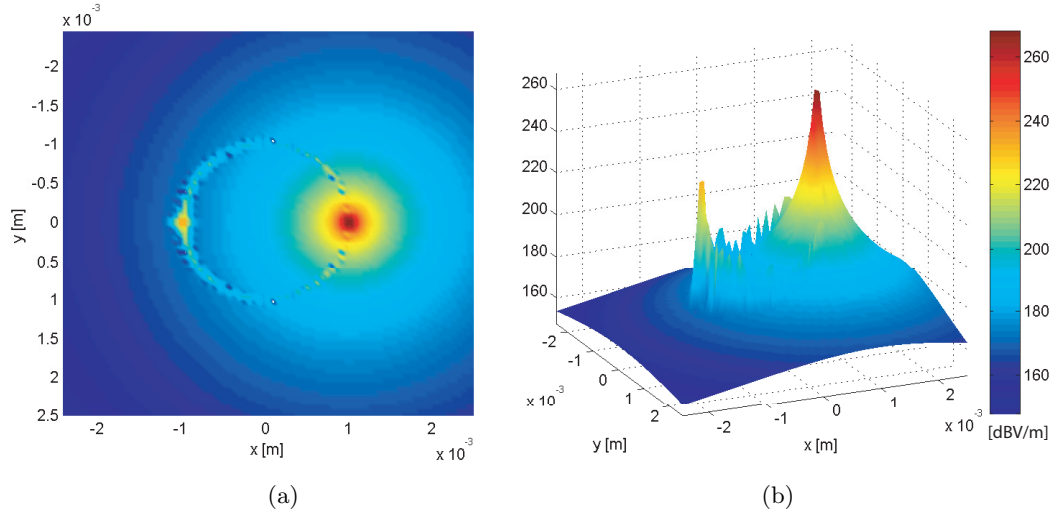

(a)   (b)

Figure 3.7.: $|\mathbf{E}_\theta|$ computed with the MMT code on the $\theta = \pi/2$ plane for the problem described in Fig. 3.6. A ring (radius $= r_{source}$) where the field is not continuous (not physically) is easily identified. Maximum value (dark red) occurs a the source position but it is possible to notice also a hot spot *symmetrical* to the source ($r = r_{source}$, $\theta = \pi/2$, $\varphi = $ -π).

The example illustrates also how the problem is intrinsic in the SWE formulation having no relation with the presence of any spherical shells (diffraction). Fig. 3.8 explicitly shows the slow convergent behavior of the SWE at $r = r_{source}$. The MMT evaluation of $|\mathbf{E}_\theta|$ is compared to FEKO [142] along the $-x$ axis ($\theta = \pi/2$, $\varphi = $ -π) where the excitation is not present. It can be appreciated that increasing the number of modes, it is possible to substantially reduce the area where the error occurs (although not reaching yet the correct result).

Solutions to the problem are presented in [87, 147–152] (and references therein). The use of asymptotic formulations in combination with the *addition-subtraction* method is presented in [148] when evaluating the potential in a spherical head model. Still focusing on biomedical applications, a method based on weighting the Legendre polynomial is investigated in [87], while an empirical based solution is presented in [149]. The *addition-subtraction* method is also used in [147, 151, 152], whilst [153] proposes a new formulation combining operations on scalar Green's function with a rotation of the coordinate system. An overview of possible numerical techniques is given in [150]. Following the ideas of these works, it is possible to considerably speed up the convergence of the SWE. This is useful for the analysis of eccentrically insulated radiators [19, ch. 1] or subcutaneous implants.
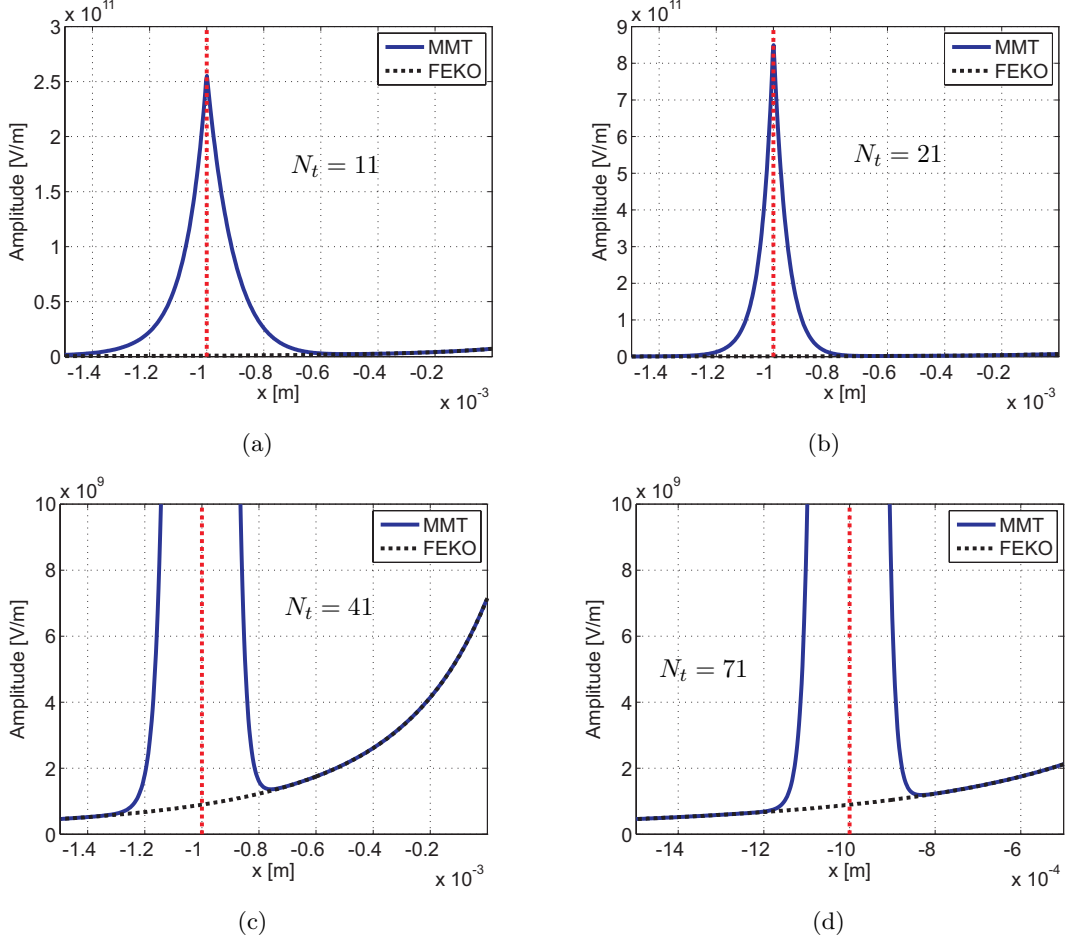
(a)   (b)

(c)   (d)

Figure 3.8.: $|\mathbf{E}_\theta|$ on the $\theta = \pi/2$, $\varphi = $ -π axis $(-x)$ for the problem described in Fig. 3.6. Vertical red dotted line indicates the radius corresponding to r_{source}. Higher accuracy is obtained increasing the number of modes: (a) $N_t = 11$, (b) $N_t = 21$, (c) $N_t = 41$, (d) $N_t = 71$.

MMT Validation

The presented MMT is validated against FEKO. A dual and a three spherical layered setups are considered with an electric source placed at the origin and off-centered, respectively. The latter case requires the computation of a higher number of spherical modes, thus allows us to appreciate the importance of the truncation procedure described in Section 3.3.4. For the sake of comparison, small spherical shells radii are used.

For the computation of near field results, the commercial software applies the Method of Moments (MoM) in combination with the Surface Equivalence Principle (SEP). This method calls for the meshing (with triangular basis function) of the surface of the spherical shells. The use of the numerical software FEKO has the only purpose to validate the presented numerical implementation. The MoM used by FEKO is a numerical method that requires a dense meshing to lead to accurate results for the targeted models. In this sense, the MMT is more efficient than FEKO and well suited to solve the investigated geometry. In fact, accurate numerical analysis using the MoM and SEP requires computational power which is beyond

the one available to the author (FEKO silver license[‡]).

Excitation at the origin: let us consider the electromagnetic problem described in Fig. 3.9-(a). A z-oriented electric dipole is placed at the center of three spherical shells whose properties are detailed in Fig. 3.9(b). The dielectric characteristics of the human tissues are extracted from [20]. The electric field along the x axis, R_{uo}, is computed at 403.5 MHz. The MMT code and FEKO results, shown in Fig. 3.10, are almost superimposed. The slight discrepancies, located at the dielectric interfaces, are due to FEKO's meshing.
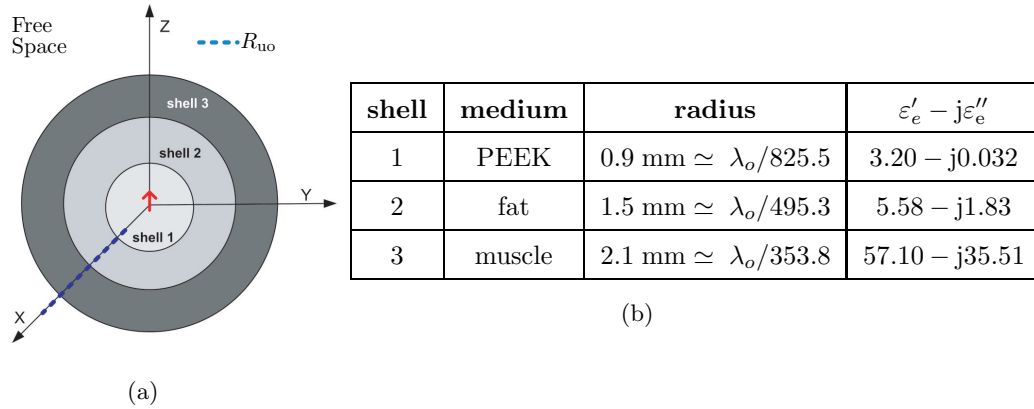

shell	medium	radius	$\varepsilon_e' - j\varepsilon_e''$
1	PEEK	0.9 mm $\simeq \lambda_o/825.5$	$3.20 - j0.032$
2	fat	1.5 mm $\simeq \lambda_o/495.3$	$5.58 - j1.83$
3	muscle	2.1 mm $\simeq \lambda_o/353.8$	$57.10 - j35.51$

(b)

(a)

Figure 3.9.: Description of the investigated electromagnetic problem: (a) geometry and (b) environment properties (λ_o is the free space wavelength at 403.5 MHz). The Hertzian dipole, $\hat{\theta} = 0$ and $\hat{\phi} = 0$ oriented, is placed at the origin.

(a)   (b)

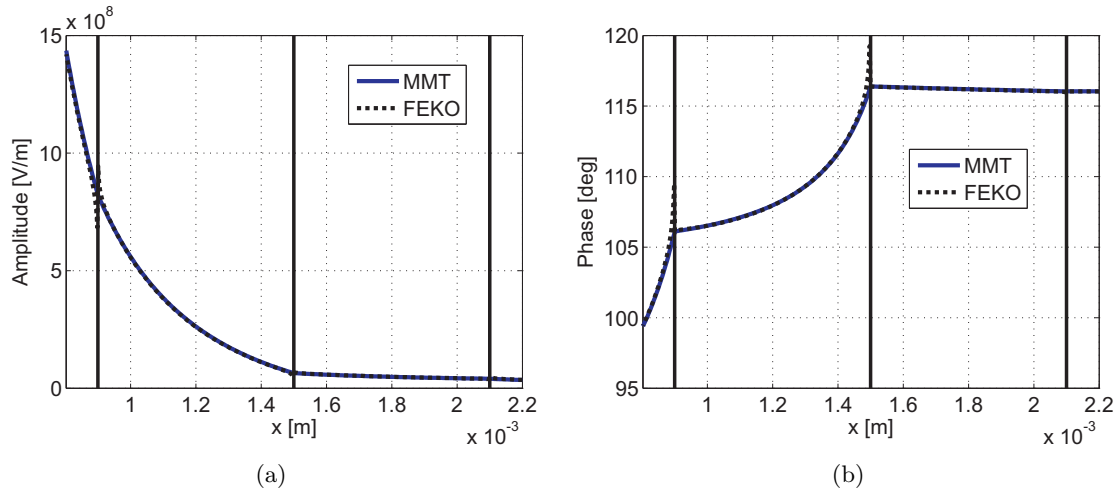**Figure 3.10.:** Comparison between the $E\hat{z}$, evaluated via the mode matching code and FEKO, as a function of the radial distance at 403.5 MHz for both (a) amplitude and (b) phase analyzing the problem described in Fig. 3.9(a).

[‡]Silver license (32-bit) can only address 2 GBytes of RAM per process. Further information may be found in http://www.feko.info/feko-product-info/platforms.

Off-centered tilted excitation: let us consider the electromagnetic problem described in Fig. 3.11-(a), where an off-centered tilted Hertzian electric dipole is surrounded by two spherical shells. As in the previous example, dielectric characteristics of the human tissues, reported in Fig. 3.11-(b), are extracted from [20].

The electric field is again computed at 403.5 MHz. The MMT code and FEKO results are very close, as shown in Fig. 3.12. Logically, the agreement is improved when $N_t = 21$ (Fig. 3.12(b)) than when $N_t = 11$ (Fig. 3.12(a)). Again slight discrepancies exist at the dielectric interfaces due to the FEKO's meshing of the spherical surfaces.
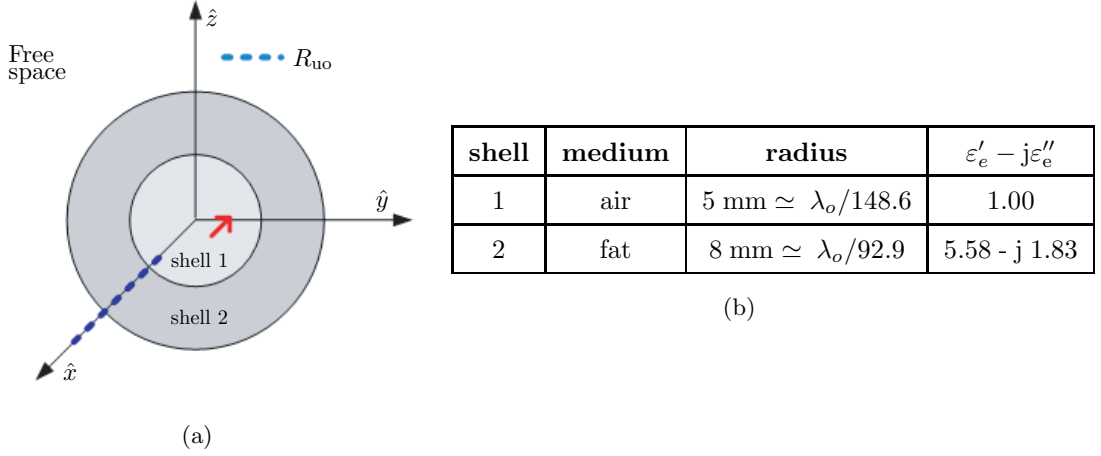

shell	medium	radius	$\varepsilon'_e - \mathrm{j}\varepsilon''_e$
1	air	5 mm $\simeq$ $\lambda_o/148.6$	1.00
2	fat	8 mm $\simeq$ $\lambda_o/92.9$	5.58 - j 1.83

(b)

(a)

Figure 3.11.: Description of the investigated electromagnetic problem for the numerical comparison with FEKO: (a) geometry and (b) environment properties (λ_o is the free space wavelength at 403.5 MHz). The Hertzian dipole, $\hat{\theta} = \pi/3$ and $\hat{\phi} = \pi/4$ oriented, is placed at x = 1, y = 1, z = 1 [mm].

(a)   (b)
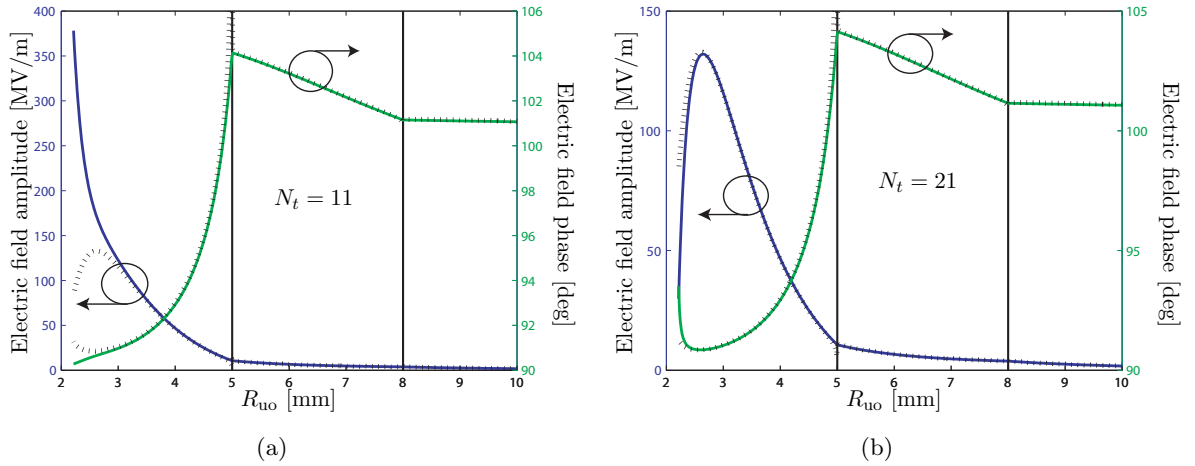
Figure 3.12.: Comparison of the $\hat{x}$ component of the electric field over R_{uo} (Fig. 3.11), between the MMT (solid line) code and FEKO (dotted line). Amplitude and phase are computed considering (a) $N_t = 11$ and (b) $N_t = 21$ which satisfy (3.29) for α equal to -140 and -70 dB, respectively. Vertical black lines indicate the shell boundaries.
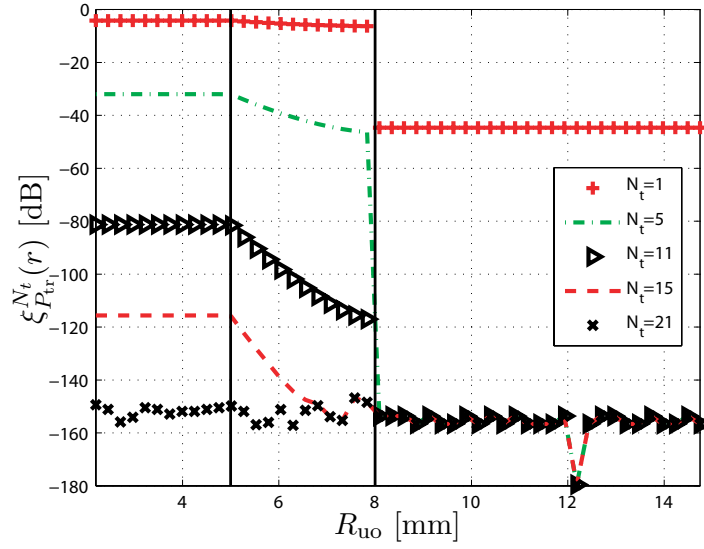
Figure 3.13.: Computation of the relative amount of truncated power, $\xi_{P_{\mathrm{tr}}}^{N_t}(r)$, over R_{uo} considering different values of N_t at 403.5 MHz for the problem described in Fig. 3.11.

The relative amount of truncated power $\xi_{P_{\mathrm{tr}}}^{N_t}(r)$ is plotted in Fig. 3.13 for different values of N_t. As expected, the number of modes is critical when getting closer to the source. To reach $\xi_{P_{\mathrm{tr}}}^{N_t}(r) \leq \alpha = $ -140 dB, $N_t = 21$ is thus required in shell number 1, whereas only 5 modes are sufficient from $r = 8$ mm (free space). For the far field description, $N_t = 1$ is enough, as depicted in Fig. 3.14. This is consistent with the classical recommendation $N_t = \lceil k_0 r_{\mathrm{ext}} \rceil$ [143, 144].
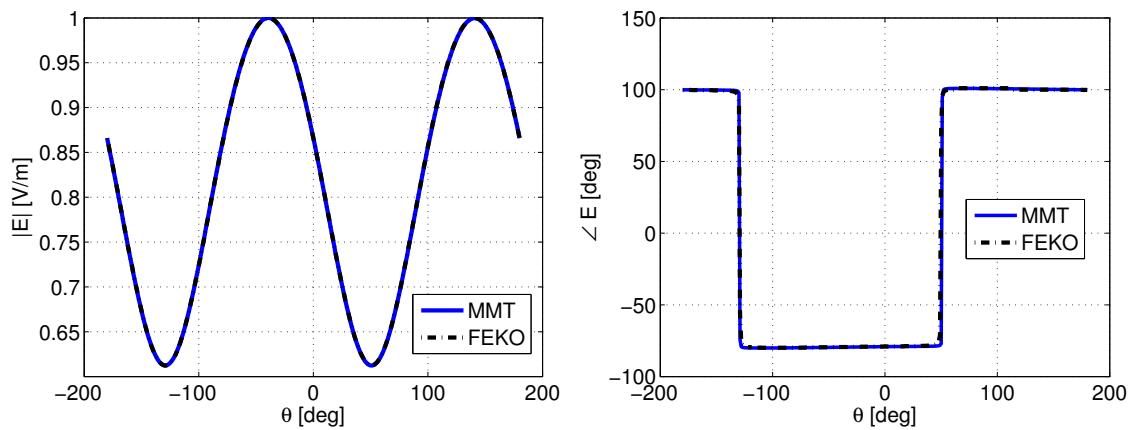

Figure 3.14.: Comparison between the MMT code and FEKO at 403.5 MHz considering $N_t = 1$ for the problem described in Fig. 3.11: (a) normalized $|\mathbf{E}|$ far field and (b) phase of E_θ both in the yz-plane.

3.4. Application of the Mathematical Model to the Physical Model

In this section, the mathematical model is applied to the physical model to investigate the power transmission enhancements that can be obtained with an internal and external insulations from an implanted source. Furthermore, the performed analysis also provides results for the attenuation of the EM wave propagation within the body.

To first assess the meaningfulness of the results evaluated in this section, it must be pointed out that our propagation results are in the same order of magnitude than those presented in [59, 65, 66, 78] -if the same working frequency, dielectric properties and loss definitions are set- where more complex body models are considered. Although this work is performed with a different modeling frame, our findings mostly match the conclusions of the aforementioned references. This confirms that the spherical model is indeed a good *average* of more complex geometries.

3.4.1. Internal Insulation: Numerical Results and Discussion

The effect of the internal biocompatible insulation is evaluated in this section. The results confirms and extends the discussions reported in [22, 54, 54, 92, 100] (obtained while investigating implantable radiators).

Table 3.1 reports the electrical (dielectric properties) and geometrical (shell radii) description of three investigated body phantoms. The radii of the equivalent human tissues are set as in [18].

Table 3.1.: Electrical and Geometrical Description of the Three Analyzed Body Models.

	Model	Dielectric properties		Radius
		$\varepsilon_e' - j\,\varepsilon_e''$	$\tan\delta$	[mm]
1	IEEE head model [83, p. 36]	43.50 - j 34.75	0.7989	90
2	Muscle tissue	57.10 - j 35.51	0.6219	90
3	Muscle tissue	57.10 - j 35.51	0.6219	82
	Fat tissue	5.58 - j 1.83	0.3280	86
	Dry skin tissue	46.70 - j 30.72	0.6578	90

All three body models were first analyzed in the presence of the electrical source. For the magnetic and the Huygens excitations, as presented in Section 3.3.2, only the most relevant case was considered. Five different biocompatible materials, described in Table 3.2, were investigated with thicknesses ranging from 1 to 4 mm. This range corresponds to $\lambda_o/743$ to $\simeq \lambda_o/190$, where λ_o is the free space wavelength at 403.5 MHz.

The dielectric properties of these shells are the same as real biocompatible materials. Since a discussion on chemical characteristics of bio-materials is out of the scope of this work, standard biocompatible insulations have been taken from [119] and [154]. For our application, that

requires electromagnetic power transmission, biocompatible insulation with high conductivity (such as gold or silver) are not appropriate. Thus, three polymers (polypropylene, PEEK -Polyetheretherketones, produced by [155]- and polyamide) and two ceramics (alumina and zirconia) have been selected. Their dielectric properties are reported in Table 3.2.

Table 3.2.: Internal Biocompatible Insulations.

Material	Dielectric Properties	
	$\varepsilon_e' - j\varepsilon_e''$	$\tan\delta$
Polypropylene	2.55 - j 0.0076*	0.003
PEEK	3.20 - j 0.0320*	0.010
Polyamide [156]	4.30 - j 0.0172	0.004
Alumina [156]	9.20 - j 0.0736	0.008
Zirconia (ZrO_2)[157]	29.0 - j 0.0507	0.002

* Measured values below 1 GHz.

The following characteristics were kept constant in the numerical analysis:

- working frequency of 403.5 MHz;

- the presence of 1 mm thick air insulation surrounding the excitation;

- radii of the human equivalent shells are fixed despite the insulation variations;

- the results are computed with a neglected power $\xi_{P_{tr}}(r)$ lower than $\alpha = -140$ dB. This gives exact results over the desired R_{uo} as the source is placed at the origin.

With these assumptions, if the diameter of the insulator is increased, then the thickness of the body model, through which the waves propagate, reduces. The result is obviously the reduction of the total loss, because a volume of highly lossy material is replaced by less lossy insulator each time the insulator thickness is increased. However, this variation is quantitatively negligible as shown in Section 3.4.1.

In order to asses the effect of the insulation layers, the net body loss η_b and the net insulation loss η_{ins} were defined as follows:

$$\eta_b = -10\log_{10}\frac{P_{\text{rad}}(r_b)}{P_{\text{rad}}(r_{\text{ins}})} \qquad \eta_{\text{ins}} = -10\log_{10}\frac{P_{\text{rad}}(r_{\text{ins}})}{P_{\text{rad}}(r_0)} \tag{3.30}$$

where r_b, r_{ins} and r_0 are the radii of the external body, the biocompatible insulation and the air shell, respectively, as illustrated in Fig. 3.15. The total power attenuation η_{tot}, due to the presence of the equivalent body model and the realistic internal insulation, is equal to $\eta_{\text{ins}} + \eta_b$. For a correct comparison, the power radiated by the source, $P_{\text{rad}}(r_0)$, is always normalized to 0 dBm.

The definition of the net body loss, η_b, is different from the one used in [65, 78] where $P_{\text{rad}}(r_b)$ is divided by the radiated power in free space. Our definition is not influenced by the dielectric loading of the surrounding tissue.
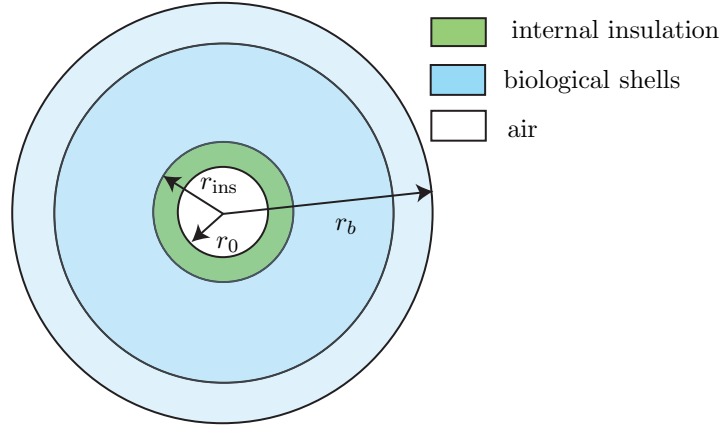
Figure 3.15.: Radii for the evaluation of the net body η_b and insulation η_{ins} losses.

The computed net body, insulation and total losses (i.e., η_{ins}, η_b and η_{tot}, respectively) are reported in Tables 3.3-3.5 when the implanted antenna is surrounded by the five biocompatible insulators. For a better understanding of the influence of the biocompatible materials, Tables 3.3-3.5 also report the no insulation (denominated "none") case. This happens when the model has no internal insulation layer, and it includes only the lossless air shell and the body equivalent spherical layers.

Electrical Excitation

Model 1-IEEE head model: the use of the insulation layer strongly reduces the power dissipated in the body. Let us compare, in Table 3.3, the η_b value of the none case (56.4 dB) with the results obtained by varying all the other insulators' thicknesses (i.e., 47.4, 42.2, 38.6 and 35.8 dB). A minimum improvement of 9 dB, and up to more than 20 dB, is found. Thus, the insulator is very useful to reduce the power absorbed by the body [92].

Table 3.3.: Power Loss [dB] for Different Internal Insulations with an Electric Dipole in Model 1 (IEEE head model).

Insulation	Thickness											
	1 mm			2 mm			3 mm			4 mm		
	η_{ins}	η_b	η_{tot}	η_{ins}	η_b	η_{tot}	η_{ins}	η_b	η_{tot}	η_{ins}	η_b	η_{tot}
Polypropylene	1.3		48.7	3.5		45.7	6.0		44.6	8.3		44.1
PEEK	2.9		50.3	6.4		48.6	9.5		48.1	12.2		48.0
Polyamide	1.1	47.4	48.5	3.1	42.2	45.3	5.3	38.6	43.9	7.5	35.8	43.3
Alumina	1.1		48.5	3.0		45.2	5.3		43.9	7.5		43.3
Zirconia	0.1		47.5	0.4		42.6	0.8		39.4	1.5		37.3
none	$\eta_{tot} = \eta_b = 56.4$											

Consequently, the presence of the insulator reduces the total attenuated power η_{tot}. With no insulation $\eta_{tot} = 56.4$ dB whereas for all insulation materials and thicknesses, η_{tot} is lower

than 50.3 dB. In particular the use of zirconia (4 mm thick) gives the best result with a 19 dB improvement (i.e., 56.4 - 37.3 = 19.1 dB) while PEEK (1 mm thick) provides only a 6 dB increase (i.e., 56.4 - 50.3 = 6.1 dB). This implies a noticeably larger efficiency (up to six times) for the implanted source.

Logically, and in agreement with [19, 22, 26, 92], increasing the thickness of the insulation reduces η_b and η_{tot}. This behavior also manifests in Fig. 3.16, where the computed radiated power is higher when the insulation thickness increases. For instance, in the case of zirconia,

(a)

(b)

Figure 3.16.: Computation of P_{rad} as a function of the radial distance at 403.5 MHz for the IEEE homogeneous head model with an electrical source considering different (a) polypropylene and (b) zirconia insulation thicknesses. Vertical black lines indicate the shell boundaries.

η_b and η_{tot} with a 4 mm thick insulation layer are around 12 dB and 10 dB lower than when a thinner layer is used.

However, this reduction highly depends on the insulation dielectric properties. There is indeed only a 2.3 dB reduction of η_{tot} when the PEEK thickness increases from 1 to 4mm (i.e., 50.3 - 48.0 = 2.3 dB) whereas 10.4 dB (47.5 - 37.3 = 10.2 dB) are gained in the case of zirconia as explained later on.

This result is very useful for the design of implanted antennas. In fact, as the volume of an implantable device is strictly limited, the radiator and the insulation dimensions have to be carefully chosen to optimize the radiation performances. Our values show that it is worth considering a thin PEEK insulation to allow the maximum volume for the antenna. On the contrary, in the case of zirconia, a relatively thicker insulation should be used. Moreover this dielectric material, due to its high ε'_e, facilitates the reduction of the real antenna dimensions.

The use of zirconia gives always the best results for η_b and η_{tot}. Clearly this material not only has the lowest $\tan\delta$, but also the ε'_e closest to the IEEE head model, thereby reducing the mismatch between the insulation and the body layer in agreement with [54]. Reversely, PEEK presents the worst performances, as it shows the highest $\tan\delta$ and a low ε'_e.

Finally, the use of alumina or polyamide is almost equivalent (less than 0.1 dB variation) despite the fact that the $\tan\delta$ of this ceramic doubles that of the polyamide. This is again explained by the improved matching due to the higher ε'_e of the alumina.

Model 2-Muscle model: all previous considerations, obtained with the IEEE head model, are still qualitatively confirmed when analyzing the muscle model, as reported in Table 3.4. The dissipated powers in muscle, η_b, are smaller (of around 2.5 dB) as this tissue presents a lower $\tan\delta$ than the IEEE head model (i.e., 0.6219 and 0.7989, respectively). On the contrary, the power attenuated in the insulation layer η_{ins} is always higher (of around 1 dB). This is due to the mismatch between insulation and body model, which is more important in the case of the muscle since its permittivity ε'_e is higher than the one of IEEE head model (57.1 instead of 43.5).

Table 3.4.: Power Loss [dB] for Different Internal Insulations with an Electric Dipole in Model 2 (Muscle).

Insulation	Thickness											
	1 mm			2 mm			3 mm			4 mm		
	η_{ins}	η_b	η_{tot}	η_{ins}	η_b	η_{tot}	η_{ins}	η_b	η_{tot}	η_{ins}	η_b	η_{tot}
Polypropylene	1.8		46.7	4.4		44.1	7.1		43.2	9.5		42.9
PEEK	3.7		48.6	7.6		47.3	10.9		47.0	13.5		46.9
Polyamide	1.5	44.9	46.4	3.9	39.7	43.6	6.4	36.1	42.5	8.7	33.4	42.1
Alumina	1.4		46.3	3.8		43.5	6.4		42.5	8.7		42.1
Zirconia	0.1		45.0	0.5		40.2	1.1		37.2	1.8		35.2
none	$\eta_{\text{tot}} = \eta_b = 53.8$											

This also implies that the choice of the biocompatible material has a deeper impact on the

η_{ins} and, thus, on the total lost power η_{tot}. For example, in the 1 mm case, we register a difference of 3.6 dB between PEEK and zirconia against the 2.8 dB value found in the IEEE head model. The same trend applies for all other thickness values.

Model 3-Multilayered model: the results in Table 3.5 are close to those in Table 3.4 (muscle model). The first body shell surrounding the excitation has indeed muscle equivalent properties in both models. The presence of the fat and dry skin layers changes the power losses (η_{ins}, η_b and η_{tot}) of less than 1 dB. This result is in agreement with [18], where also return losses of implanted antennas are very close when surrounded by these two body models.

Table 3.5.: Power Loss [dB] for Different Internal Insulations with an Electric Dipole in Model 3 (Multilayered).

Insulation	Thickness											
	1 mm			2 mm			3 mm			4 mm		
	η_{ins}	η_b	η_{tot}	η_{ins}	η_b	η_{tot}	η_{ins}	η_b	η_{tot}	η_{ins}	η_b	η_{tot}
Polypropylene	1.8		45.8	4.4		43.3	7.1		42.4	9.5		42.1
PEEK	3.7		47.7	7.5		46.4	10.8		46.1	13.5		46.1
Polyamide	1.5	44.0	45.5	3.8	38.9	42.7	6.4	35.3	41.7	8.7	32.6	41.3
Alumina	1.4		45.4	3.8		42.7	6.4		41.7	8.7		41.3
Zirconia	0.1		44.1	0.5		39.4	1.1		36.4	1.9		34.5
none	$\eta_{\text{tot}} = \eta_b = 53.0$											

Magnetic Excitation

The multilayered model with a 2 mm thick polyamide insulation is excited by a magnetic source. The choice of this insulation is justified as polymers are mechanically easy to manufacture and the polyamide has shown the best performances among them. Moreover, let us remind that polyamide presents performances very close to those of alumina, as shown in Section 3.4.1.

The power radiated through the body is compared in Fig. 3.17 for an electric and magnetic excitation. The magnetic source substantially reduces the absorbed power compared to the electric one ($\eta_{\text{ins}} < 0.1$ dB and $\eta_b = \eta_{\text{tot}} = 26.6$ dB instead of $\eta_{\text{ins}} = 3.8$, $\eta_b = 38.9$ and $\eta_{\text{tot}} = 42.7$ dB), for the same investigated model. Indeed, the radiation of the magnetic source through a body is more efficient in agreement with the early submarine and geophysical analysis discussed in Section 2.2 and with the results recently reported in [22, 26, 158]. The high magnetic near field does indeed not dissipate in the body since human tissues have no magnetic losses ($\mu_r'' = 0$). Finally, for a magnetic source, the dielectric characteristics of the real insulation layers have a negligible influence, in agreement with what shown in [158].

Huygens Source

The power radiated through the body is computed for a Huygens source in the same conditions as for the magnetic excitation. The level of the absorbed powers ($\eta_{\text{ins}} = 2.4$, $\eta_b = 29.6$ and

$\eta_{\text{tot}} = 32.0$ dB) is between those of the electric and the magnetic excitation, as shown in Fig. 3.17. Despite its 3 dB improved directivity, the radiation efficiency of the Huygens source is also between those of the electric and the magnetic dipoles. Indeed, it combines both sources. Therefore, the high electric near field coming from the electric dipole dissipates in the insulation and body layers, whereas the magnetic field is less affected.
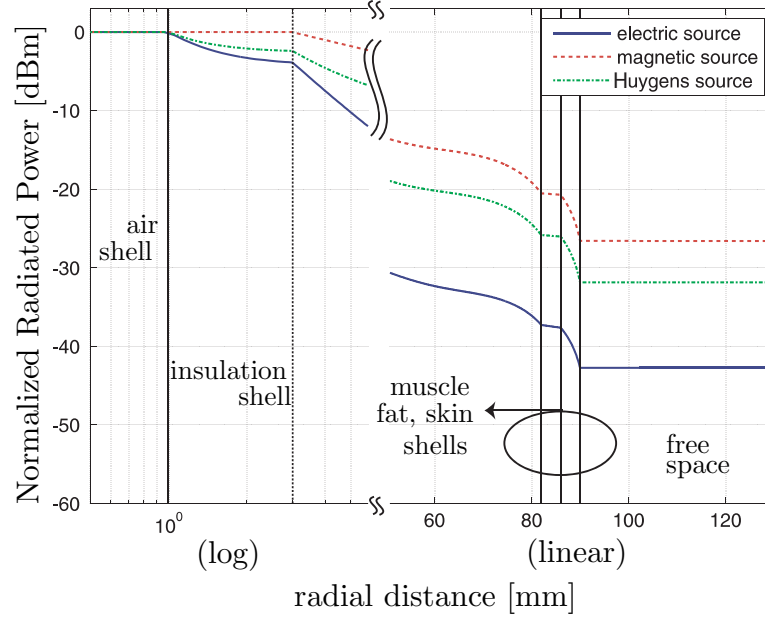

Figure 3.17.: Comparison of P_{rad} as a function of the radial distance at 403.5 MHz with the three different sources. The multilayered model is analyzed while considering the presence of an internal insulation made of polyamide 2 mm thick. Vertical solid lines indicate the shell boundaries.

Other Hypothesis

The values reported in Tables 3.3-3.5 show, for a constant external diameter of the body shell, that an increase in the thickness of the insulation layer results in lower power dissipation in the living tissue.

It is true that increasing the diameter of the insulator results in the reduction of the volume of the lossy media. The consequence is obviously the reduction of total loss, because a volume of highly lossy material is replaced by less lossy dielectric each time the insulator thickness is increased.

Nonetheless, the considerations previously presented hold true when different conditions for the body shell dimension are applied, such as constant volume [158] or thickness as confirmed by the results reported in the next paragraphs. It is worth reminding that previous work by the author [158] shows that the conclusions drawn in Section 3.4.1 are also confirmed when different power normalization and body phantoms are investigated.

Constant Volume: the effects of the internal insulating layer are evaluated for the model 1 (IEEE head model) with constant volume and considering an electrical excitation. The volume is fixed to 3053.623 cm^3 (corresponding to an external and internal radius of 9 cm and 1 mm,

respectively, when no insulation is considered). The head external radius changes according to the insulation dimensions when varying its thickness. The obtained values, reported below, confirm the conclusions drawn in the previous section. In fact, only a variation within 0.2 dB is appreciated for η_b.

Table 3.6.: Power Loss [dB] for Different Internal Insulations with an Electric Dipole in Model 1 (IEEE head model) with constant volume.

Insulation	Thickness											
	1 mm			**2 mm**			**3 mm**			**4 mm**		
	η_ins	η_b	η_tot	η_ins	η_b	η_tot	η_ins	η_b	η_tot	η_ins	η_b	η_tot
Polypropylene	1.3		48.7	3.5		45.7	6.0		44.6	8.3		44.1
PEEK	2.8		50.2	6.4		48.6	9.5		48.1	12.2		48.0
Polyamide	1.1	47.4	48.5	3.0	42.2	45.2	5.3	38.6	43.9	7.5	35.8	43.3
Alumina	1.1		48.5	3.0		45.2	5.3		43.9	7.5		43.3
Zirconia	0.1		47.5	0.4		42.6	0.8		39.4	1.5		37.3
none	$\eta_\text{tot} = \eta_b = 56.4$											

Constant Thickness: the effects of the internal insulating layer are evaluated for the model 1 (IEEE head model) with constant thickness considering an electrical excitation. The thickness is fixed to 89 mm (corresponding to an external and internal radius of 9 cm and 1 mm, respectively, when no insulation is considered). The head external radius changes according to the insulation dimensions when varying its thickness. The values of attenuations, presented in Table 3.7, are the same as in the previous case, except for a small variation of 0.2 dB in η_b. This confirms once more that the variation of attenuations is dependent on the insulation presence and not on the consequent modifications of the body phantoms.

Table 3.7.: Power Loss [dB] for Different Internal Insulations with an Electric Dipole in Model 1 (IEEE head model) with constant thickness.

Insulation	Thickness											
	1 mm			**2 mm**			**3 mm**			**4 mm**		
	η_ins	η_b	η_tot	η_ins	η_b	η_tot	η_ins	η_b	η_tot	η_ins	η_b	η_tot
Polypropylene	1.3		48.8	3.5		45.8	6.0		44.7	8.3		44.3
PEEK	2.9		50.4	6.4		48.7	9.5		48.2	12.2		48.2
Polyamide	1.1	47.5	48.6	3.1	42.3	45.4	5.3	38.7	44.0	7.5	36.0	43.5
Alumina	1.1		48.6	3.0		45.3	5.3		44.0	7.5		43.5
Zirconia	0.1		47.6	0.4		42.7	0.8		39.5	1.5		37.5
none	$\eta_\text{tot} = \eta_b = 56.4$											

Summary on the Effects of the Internal Insulations

Before proceeding with the SAR analysis and the investigations on the effect of external insulators, it is worth summarizing the main results obtained so far, namely:

- the presence of insulation reduces the power dissipation in the biological tissue and enhances the radiated power;

- the increase of the insulation thickness improves the benefit of its presence;

- the dielectric properties of the insulation affect the radiation performances;

- the electric source is the least efficient radiator when compared to magnetic and huygens sources.

Specific Absorption Rate

The peak SAR values were computed for the presented body models. It is well known that accurate and precise SAR values are strongly dependent on the human body representation, the implant locations and several biological phenomena as discussed in Section 2.2.5. Furthermore, unrealistically high values of the absolute electric field (therefore SAR) can be obtained when modeling ideal sources [133]. Nevertheless, despite the simplicity of the investigated body models, it is worth evaluating the peak SAR values, Table 3.8, in order to confirm the observations previously reported. These values are always found at the interface between the

Table 3.8.: Peak SAR [dBW/kg] with Different Internal Insulation Thicknesses for the Models described in Table 3.1.

Insulation	Model 1	Model 2	Model 3		
Thickness	Elec.	Elec.	Elec.	Magn.	Huy.
none	40.7	40.6	40.7	24.4	36.8
1 mm	17.5	17.5	17.5	10.9	16.5
2 mm	12.2	12.2	12.2	5.4	10.2
3 mm	8.4	8.4	8.4	1.5	5.5
4 mm	5.4	5.4	5.4	-1.5	1.8

internal biocompatible layer and the human body, and they are obtained when the acting source (i.e., a mathematical dipole source surrounded by an air shell) radiates 0 dBm at the 1 mm air shell interface. The mass density values can be found in [18]. Of course, the use of ideal sources provides unrealistically high values of the absolute electric field (therefore SAR) [133]. Thus, results are presented in [dBW/kg] so as better appreciate relative variations.

The dielectric properties of the insulation turn out to have a negligible effect on the obtained SAR values in the given spherical models; therefore, only results changing the insulation thickness are reported. Nonetheless, the variations of relative peak SAR value with respect to the type of source and insulation thickness enables to derive valuable information, as reported below.

In agreement with the results already reported, the presence of any insulation produces a large impact reducing SAR values by at least 14 dB compared to the case without insulation (none). In the case of an electric source excitation a difference of approximately 12 dB is found versus the insulation thickness, which is in perfect agreement with the η_b values reported in Tables 3.3-3.5.

As previously discussed, the presence of a magnetic source reduces the electric near field coupling in the biological tissue, consequently decreasing the SAR values with respect to the electrical excitation. The SAR obtained with the Huygens source is relatively closer to the electric one. This is in agreement with the results reported graphically in Fig. 3.17.

The effect of the insulation thickness is more remarked in the presence of the Huygens source. In fact, an improvement of approximately 15 dB is appreciable comparing the 1 mm to the 4 mm case, while 12 dB is obtained for the other two sources against the same thickness variation. Indeed, the increase of insulation thickness strongly reduces the coupling of the near field terms. Therefore, the far field component increases its relevance and the higher directivity inherent to the Huygens source, plays a positive role since it reduces the SAR values.

To better appreciate this effect, three dimensional polar plots are reported in Figs. 3.18-3.20 showing the distributions of SAR on a spherical surface just after the internal insulation/body interface for the electric dipole and the Huygens source, respectively. For a fair comparison,

(a)   (b)
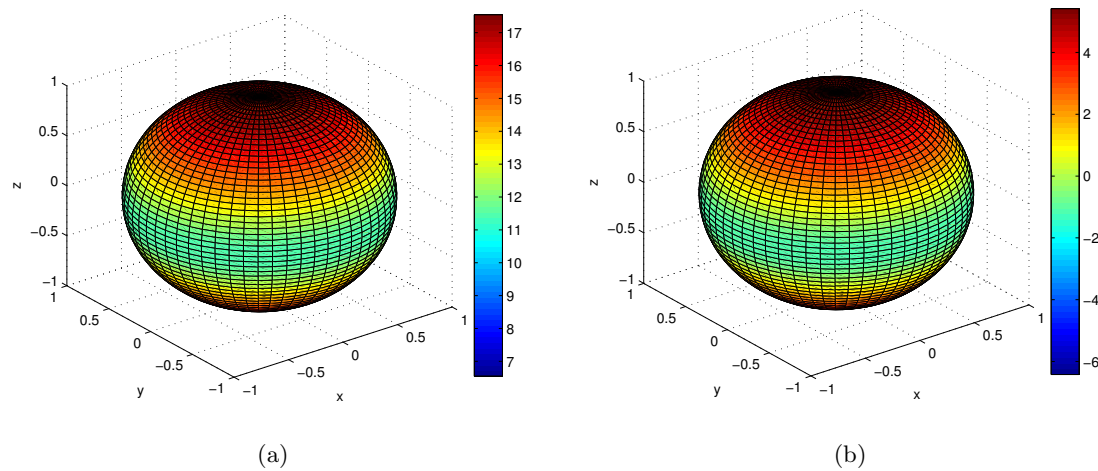
Figure 3.18.: SAR distributions on a spherical surface just after the internal insulation / body interface with an electric excitation in model 3: (a) 1 mm and (b) 4 mm thick internal insulation. Values in [dBW/kg].

the relative difference between the max value (dark red) and the minimum (dark blue) is always fixed to 11 dB. While no difference can be appreciated between the 1 mm and the 4 mm cases for the electric and magnetic excitations (Figs. 3.18-3.19 (a) and (b)), it is possible to note the improved focusing with the Huygens source (Figs. 3.20-(a) and (b)).

<center>(a)   (b)</center>
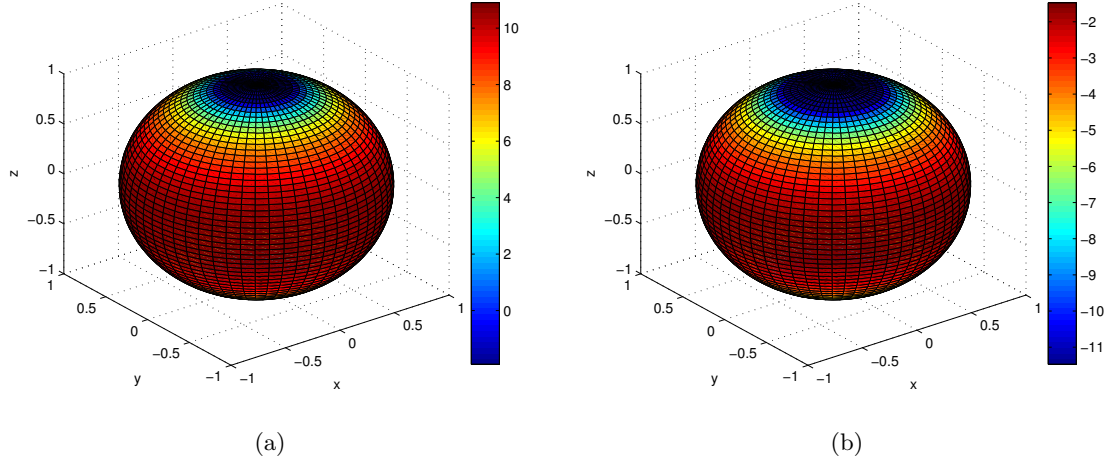
Figure 3.19.: SAR distributions on a spherical surface just after the internal insulation / body interface with an magnetic excitation in model 3: (a) 1 mm and (b) 4 mm thick internal insulation. Values in [dBW/kg].

<center>(a)   (b)</center>
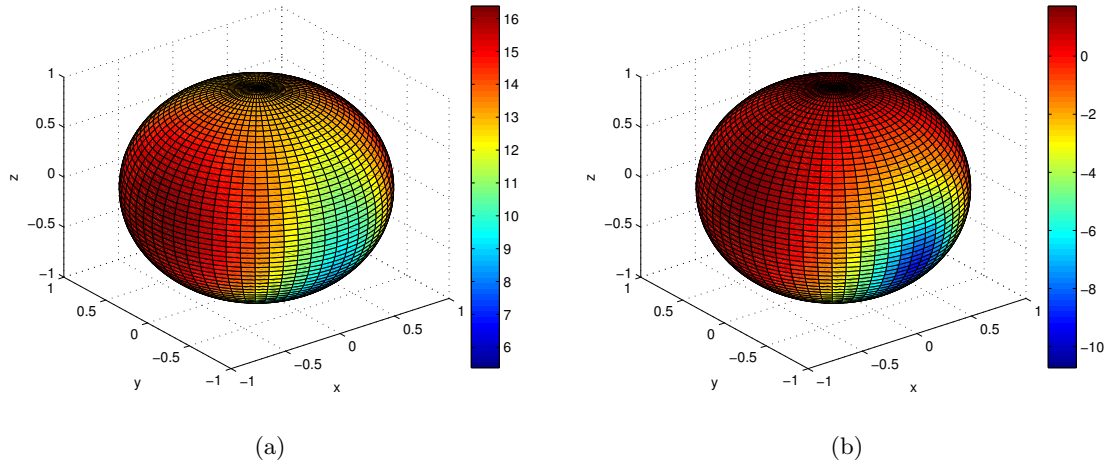
Figure 3.20.: SAR distributions on a spherical surface just after the internal insulation / body interface with a Huygens excitation in model 3: (a) 1 mm and (b) 4 mm thick internal insulation. Values in [dBW/kg]. The improved focusing toward the $\hat{z}$ axis (direction of max radiation for the chosen orientation of the source) can be appreciated.

3.4.2. External Insulation: Numerical Results and Discussion

Our previous analysis clearly pointed out the importance of the internal insulation layer. It is now logic to shift the attention towards the transition between the external body layer (skin) and the outer world (free space). For a practical wearable realization, can be imagined as an armband, a belt or a strap (for instance, as in tennis-elbow support).

A few types of external insulators are investigated. Those are: a polymer fiber, neoprene and silicon. Their dielectric properties are reported in Table 3.9, as well as the "ideal" case. The latter consists in the dielectric lossless shell that provides a perfect matching between the skin and the free space. The characteristics (permittivity and thickness) of this ideal matching layer are computed by analogy with the simple transmission line model [122].

Table 3.9.: External Biocompatible Flexible Insulations.

Material	Dielectric Properties	
	$\varepsilon_e' - j\varepsilon_e''$	$\tan\delta$
Fiber [132]	3.76 - j 0.0124	0.033
Neoprene [159]	6.50 - j 0.5850	0.090
Silicon (filled 67% TiO_2) [159]	8.50 - j 0.0085	0.001
ideal	7.90	0

External layers are modeled as spherical shells, whose thicknesses range from 5 to 20 mm, placed just after the body tissues, as shown in Fig. 3.2. For the numerical analysis, we considered the same characteristics listed in Section 3.4.1, with the Huygens source as the excitation, a 2 mm thick polyamide internal insulation and the multilayered body model.

The power attenuation in the internal 2 mm thick polyamide shell is $\eta_{ins} = 2.4$ dB (as in Section 3.4.1). Table 3.10 reports the power attenuation in the multilayered model and the external insulation (η_b and η_{ext}, respectively). Note that in this case η_{tot} is equal to $\eta_{ins} + \eta_b + \eta_{ext}$ with

$$\eta_{ext} = -10 \log_{10} \frac{P_{rad}(r_{ext})}{P_{rad}(r_b)} \tag{3.31}$$

where r_{ext} coincides with the radius of the external insulation shell, depicted in Fig. 3.2.

The cases of no external insulation (denoted "none") and the lossless matching layer (denoted "ideal") are also reported in Table 3.10.

The presence of the ideal insulation reduces η_{tot} in 7.9 dB compared to no insulation case (29.6 - 21.7 = 7.9 dB). This means establishing a communication almost three-times more efficient. Although not practically realistic (its thickness is approximately 71 mm) the ideal external insulation case is interesting to set the optimal value of the power transmission out of the skin tissue.

In agreement with [130], the presence of a thin external layer does not modify the η values as much as the internal insulator. For instance, the power transmission is enhanced of almost 2 dB by the presence of a 20 mm thick silicon layer. Although the investigated external insulations may not be the optimal ones, we showed that their influence is not negligible. Furthermore, a higher impact can be expected when considering subcutaneous implants. In this case, the external layer interacts with the near field terms of the electromagnetic radiation, as discussed

Table 3.10.: Power Loss [dB] for Different External Insulations with the Huygens Source in Model 3 (Multilayered) and a 2 mm Thick Polyamide as Internal Insulation.

Insulation	Thickness								
	5 mm			**10 mm**			**20 mm**		
	η_b	η_{ext}	η_{tot}	η_b	η_{ext}	η_{tot}	η_b	η_{ext}	η_{tot}
Fiber	29.3	< 0.1	31.7	29.1	< 0.1	31.5	28.7	< 0.1	31.1
Neoprene	29.2	0.3	31.9	29.0	0.5	31.9	28.3	0.8	31.5
Silicon	29.1	< 0.1	31.5	28.8	< 0.1	31.2	27.8	< 0.1	30.2
ideal	$\eta_b = 21.7$ and $\eta_{\text{tot}} = 24.1$ ($\simeq 71$ mm thick)								
none	$\eta_b = 29.6$ and $\eta_{\text{tot}} = 32.0$								

for the internal insulator.

3.5. Conclusion

This chapter analyzed the influence of the insulation layers in implanted antennas for biotelemetry applications in the MedRadio band. Body models composed of concentric spherical homogeneous shells excited by ideal sources were considered. The geometry of the structure allows to compute analytically the electromagnetic field with a Mode Matching Technique based on the Spherical Wave Expansion. The MMT has been numerically validated by comparison with a full-wave commercial software. Moreover, a convergence criterion has been defined to compute, with controlled accuracy, the power radiated at any radial distance, including the near field range.

Two homogeneous and one multilayered models have been investigated, considering both internal -surrounding the implanted radiator- and external -placed upon the human skin- insulations. The results obtained for the internal insulation provide guidelines for the selection of the biocompatible material, and for the implanted antenna design. Within the strictly limited volume available for the implanted device, the dimensions of the antenna and insulation thickness must be carefully chosen so as to optimize the radiation performances. For instance, a proper choice of the internal insulation leads up to a power transfer from the implanted source to the external receiver six-times more efficient.

The influence of the type of excitation (electric and magnetic dipole and Huygens source) has also been examined. As expected, since the body does not present any magnetic loss, the magnetic source is the most efficient.

We computed SAR values despite the limitations of the investigated body models. Our results confirm the effective role of internal insulation and the important effect related to the near field coupling is once more emphasized by the Huygens source analysis.

The external insulation has also been considered. An ideal matching layer, between the skin tissue and the air, increases the power transmission in almost 8 dB. The capability of a few low-loss, flexible materials has been analyzed in order to reduce the mismatch between

the body layer and the outer free space. Although far from the ideal case, around 2 dB can be gained with realistic external insulators.

The performed analysis finds its practical application in the next two Chapters. It has been shown that the use of a thick PEEK insulator is not an optimal solution to enhance the radiated power. However, this material presents excellent characteristic from the mechanical and bio-chemical points of view, thus it was selected for the design and the realization of the prototypes described in Chapters 4 and 5. In agreement with this numerical investigation, thin insulations are always chosen so as to consider the maximum available volume for the antenna design.

4. Guidelines for the Design of Implantable Antennas

4.1. Introduction

The antenna plays a key role to obtain robust communication links and a significant miniaturization of any implantable device with telemetry capabilities. Recently, the allocation of the MedRadio frequency spectrum, together with the ISM and UWB bands, boosted the research on this subject leading to the design of optimized implantable antennas, while previous works mainly used simple radiators (e.g., single turn loop [160]).

This part of the thesis aims at providing guidelines for the design of implantable antennas. In particular, the three main goals of this chapter are:

1. to present the challenges of the design of implantable antennas. This comprises the set of the general requirements of implanted device and the discussion of the solutions already presented in the literature;

2. to investigate various preliminary solutions to face some of the difficulties of the implantable antenna design in terms of:

    - design conception;

    - technological realization;

3. to formulate an efficient design strategy.

In order to reach these goals, this chapter is organized as follows: Section 4.2 presents the characteristics of implantable antennas focusing on the requirements and on the solutions that are already available. Four prototypes are described in Section 4.3. Design, realization and integration with the active components are here discussed, while the registered performances are compared with existing designs.

The analysis, realizations and measurements of these antennas allowed us to formulate a design strategy, that is presented in Section 4.5 to efficiently design an implantable radiator. The analysis presented here is built on the work presented in the previous chapters, and leads to the successful design and realization of an implantable antenna for in vivo application described in Chapter 5.

4.2. Specifications and Existing Solutions

The specifications of implantable antennas are first discussed in this section. This analysis is fundamental to then evaluate the qualities and limitations of the solutions proposed in the literature. The understanding of these aspects allows to investigate some preliminary implantable antennas and to formulate a design strategy.

4.2.1. General Requirements

In order to perform the design of an antenna for a complete active implantable system, several requirements, classified as physical constraints and electromagnetic characteristics, must be taken into account.

Physical Constraints

- The volume of the entire implant (including the antenna, insulation, electronics, batteries and bio-sensors) has to fit in a housing as small as possible that must have an ergonomic shape. Such a miniaturization requires a dense packaging, and a very efficient integration of all the components;

- a biocompatible insulation must surround the implantable device;

- the actual process of antenna manufacturing has to be taken into account in order to avoid extremely tight tolerances and to maximize the repeatability of the construction process itself.

Electromagnetic Characteristics

- The design of a miniature antenna, together with the choice of the MedRadio band ($\lambda_{air} = 0.7435$ m), results in an electrically very small radiator. This implies poor radiation performances such as narrow bandwidth and low efficiency. Correct assessment of the prototypes under test also arises because of the electrically small size of the radiators;

- the capability of dual band performances might be of great use, depending on the selected electronics, to reduce power consumption and extend life time;

- the antenna has to radiate in the presence of the human body. The latter is indeed a very complex environment with high inhomogeneity, frequency dependent properties, particular shape, and composed by lossy materials;

- the EM performance has to take into account the integration of the whole device, thus providing robust characteristics against the battery and electronics presence;

- the EM radiation has to comply with SAR requirements and emitted power regulations (EIRP).

4.2.2. State of the Art

Several implantable radiators with different characteristics and targeted applications have been recently presented. The performances of implantable antennas depend on the packaging of the whole device, the embedding insulation, and the modeled body phantoms. Therefore, comparing the radiators proposed in the literature is not straightforward because of the different characteristics, constraints, and environmental conditions that have been used. In order to better understand the challenges that apply to implanted antennas and the solutions that have been presented, a special effort was made to classify the reported radiators in the following groups:

- Miniaturized Antennas: radiators whose size reduction is achieved independently on the presence of any other components;

- Miniaturized Antennas with Packaging Considerations: radiators with biocompatible insulation for a more realistic implantation procedure and which take into account the allocation of the power supply and electronics;

- 3D Miniaturized Antennas with Packaging Considerations: three dimensional (3D) antenna designs which take into account the packaging and the insulation to optimize the radiating performances. At the same time, they minimize the volume occupation reaching the highest level of integration.

Radiation properties (directivity, efficiency, gain, bandwidth, SAR, etc.) are not discussed here as they would be irrelevant without a precise description of all the considered hypothesis. Finally, the presented implanted radiators are also classified according to the modeled body phantoms and their working frequency.

Miniaturized Antennas

Single layer spiral and meander planar typologies are the most common implantable radiators used in the MedRadio band; examples are depicted in Fig. 4.1. Indeed, their geometries with and without grounding pin facilitate miniaturization. These two typologies are investigated in [18, 161] and compared in [94]. Extensive analysis of these antenna typologies is also reported in [92] and [93], where the effects of different dimensions and materials, and optimization with genetic algorithms techniques are also included, respectively. Both antennas are suited for implantable applications, however the spiral design turns out to have a higher radiation efficiency.

| (a) | (b) |
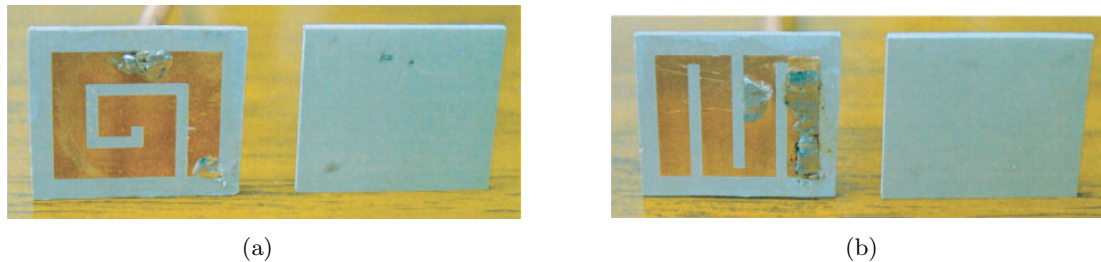
Figure 4.1.: Planar (single layer) antennas: the (a) spiral and (b) meander designs from [94]. Overall dimensions, including the biocompatible superstrate, shown on the right of each figure, are 20 x 24 x 2.5 [mm].

These works largely influenced the designs presented later on. For instance, the spiral radiator presented in [18] is also considered in [59, 60]. Moreover, a 19.5 x 10.8 x 2.5 [mm] meandered Planar Inverted-F Antenna (PIFA) is discussed in [98] for applications at 868 MHz.

More sophisticated planar designs are discussed in [162] and in [163] with and without superstrate, respectively. The metallization schemes of these solutions are optimized to reduce the size of the radiator and to obtain the desired performances.

Multilayered stacked design has proven to be useful to reduce the radiators size. Dimensions smaller than 10 x 10 x 1.9 [mm] are indeed achievable. Examples, depicted in Fig. 4.2, are

given in [95, 164–167] in the MedRadio frequency range. These radiators have a wide bandwidth behavior because of the strong interaction of the EM near field terms with the human tissues.

(a)   (b)
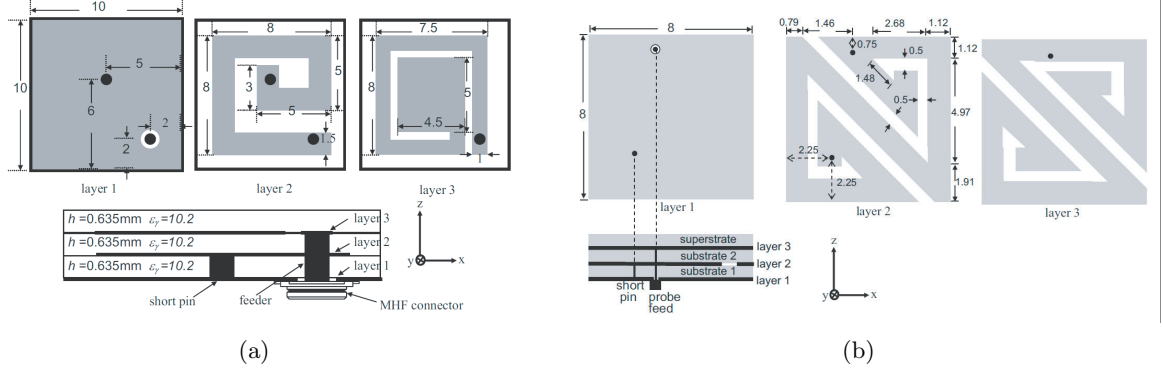
Figure 4.2.: Multilayered miniaturized antennas: (a) from [165] and (b) from [166]. Dimensions are in [mm].

Obviously, the selection of higher working frequencies facilitates the reduction of the radiator size. Antennas for retinal applications at 1.45 and 2.45 GHz (with dimensions smaller than 6 x 6 x 0.5 [mm]) are reported in [168]. Furthermore, radiation characteristics can be improved considering the vector alignment concept and space filling techniques as illustrated in [169].

Another possibility to achieve the desired performances and size requirements is the combination of fractal and inverted-F designs. An example, whose dimensions are 20 x 10 x 4.7 [mm], is given in [74] discussing an implantable antenna for GPS applications.

In order to efficiently use the available volume, three dimensional designs were also investigated. The comparison between two and three dimensional dipole antennas for retinal application at 1.41 GHz is reported in [170], while miniature cavity slot radiators working in the 2.45 GHz ISM band are discussed in [16, 84, 171]. The latter typology reaches dimensions as small as 1.6 x 4 x 2.8 [mm].

Higher frequency applications are also discussed in [172] at 6.7 GHz, and in [173] focusing on a 31 GHz radiator. However, the higher attenuation of the EM wave in the living tissues in these frequency bands deeply affects the working ranges of such solutions.

Considering a two bands solution increases the difficulty of the design. A dual band antenna, with dimensions equal to 22.5 x 22.5 x 2.5 [mm], is presented in [80] targeting the MedRadio and the 2.45 GHz ISM bands. Its subcutaneous in vivo implantation is discussed in [114, 174]. Although planar with sharp edges, as illustrated in Fig. 4.3, this radiator has a remarkable high gain, when inserted into a thin body phantom, thanks to the use of the particle swarm optimization method.

The two operating bands are also covered considering a Split Ring Resonator (SRR, $\simeq$ 13.5 x 13.5 x 5.1 [mm]) coupled to a spiral as presented in [103].

Magnetic sources are a preferable solution when the radiators are surrounded by lossy media. Loops and miniature spirals with a high number of turns are presented in [73, 175, 176]

(a)   (b)
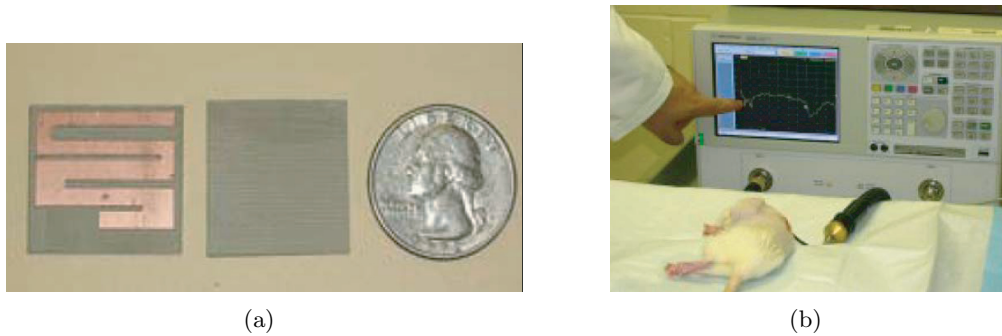
Figure 4.3.: Implantable dual band antenna: (a) antenna realization and (b) implantation in rats with a coaxial feeding cable. Pictures from [113] and [174], respectively.

and [177, 178], respectively. In particular, a loop (9 x 6 x $h^{\parallel}$[mm]) is compared over several frequency bands in [176]. This antenna typology (14 x 14 x 0.2 [mm]) is also used in [73] to characterize the RF transmission from an intracranial implant in the MedRadio range, and a loop and its matching circuit (no dimension given) are investigated in [175] for endoscopy applications at 1 GHz. The multi-turns spiral structure discussed in [178], with dimensions as small as 5 x 5 x 0.5 [mm], may be used for the integration of a complete device.

Finally, we must recall passive devices, with no battery and limited electronics, that are the only examples where the packaging of the whole device almost coincides with the packaging of the antenna itself. This is the case investigated in [101] and [179]. The former presents a single layer printed spiral design, with dimensions equal to 2.5 x 4 x 1.1 [mm], for pressure and temperature biotelemetry at 2.45 GHz; the latter considers a rounded PCB (circular, 20 x 3.54 [mm]) for RFID operation in the 865-956 MHz ISM band.

Miniaturized Antennas with Packaging Considerations

In order to realize a complete implantable device, the antenna must be integrated with all the other parts constituting the system. The necessity of considering packaging aspects may result in more stringent physical requirements or may ask for a specific design. For instance, a dense packaging of a chip antenna and all the components is presented in [180], while a PIFA spiral radiator is integrated in an intracranial implant in [100, 181] as illustrated in Fig. 4.4. Both antennas work in the 2.45 GHz ISM band.

A miniaturized spiral antenna is briefly discussed in [182]. This design takes into account the possible placement of the antenna in a biocompatible *capsule* with a diameter as small as 10.5 mm for endoscopy applications in the 400 MHz frequency range. For the same purpose, [183] presents a fat arm spiral radiator which is illustrated in Fig. 4.5.-(a).

The Normal Mode Helical Antenna (NMHA) is another well known typology for miniature antennas [184, 185]. This narrow band solution is investigated in [96] in the MedRadio band, as it can be easily integrated in a cylindrical *capsule*.

A printed loop, described in [186], is joined to a Low Temperature Co-fired Ceramic (LTCC)

$^{\parallel}$Height h not specified.
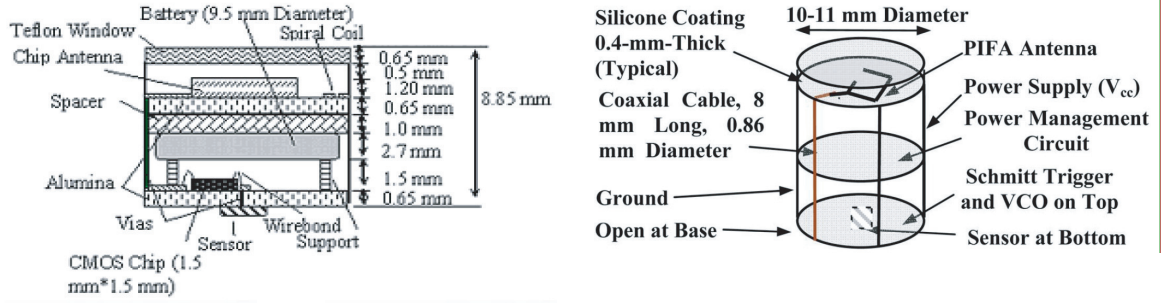
Figure 4.4.: Complete implantable devices: (a) a chip antenna is integrated with all other components from [180], and (b) a spiral PIFA is used in intracranial pressure implant from [181].

board in [187]. The resulting device has been used in the 2.45 GHz ISM band for transocular transmission as depicted in Fig. 4.5-(b).
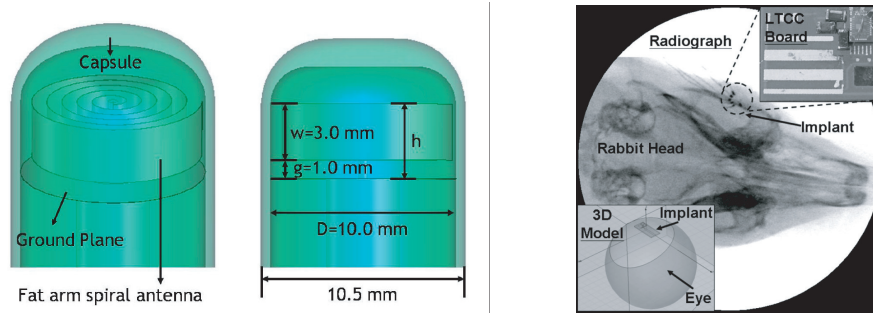
Figure 4.5.: Miniaturized antenna for the integration in a complete device: (a) the fat arm spiral radiator from [183] and (b) the printed LTTC loop from [187].

In many cases, packaging requirements get priority over the antenna requirements leading to the design of simple solenoid-like radiators. This is the case in [9, 188, 189], where an excellent integration is realized for gastrointestinal applications. The single layer loop antenna, illustrated in Fig. 4.6-(a) with dimensions are as small as 8 x 5 x 3 [mm], is designed and realized to resonate in the 400 MHz frequency range (or lower). Other examples are presented in [190] where only a short wire is used in the FM band for cortex biopotential recording applications, and in [191], where a multi-turns spiral (solenoid-like) is considered for transmission at 1.2 GHz from the gastrointestinal tract.

A multi-turns spiral is also the solution used in the complete implantable devices for wireless endoscopy presented in [7] and [192], at 433 MHz and 2.45 GHz, respectively. The radiator is indicated in Fig. 4.6-(b).

It must be pointed out that the need of sophisticated antenna designs depends on the targeted application and the requested working range. For instance, gastrointestinal and endoscopy applications set the external receiver in the close proximity of the body. Thus the very short distance over which the data transmission occurs relaxes the EM requirements, that can then be achieved with simple designs.
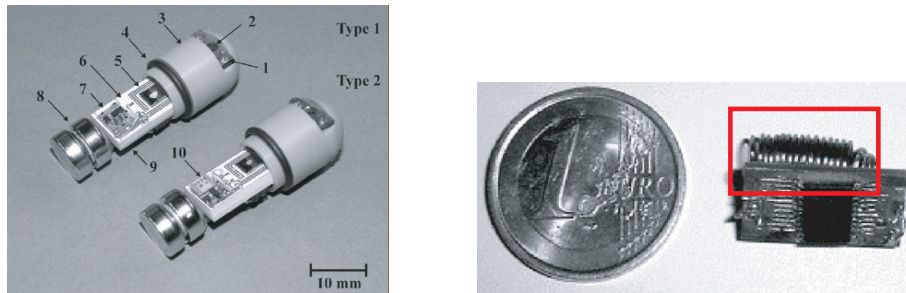
Figure 4.6.: Examples of designs where packaging requirements get priority over the antenna's ones: (a) the printed spiral, indicated by no. 5, from [188] and (b) the solenoid-like design, indicated in the red box, from [7].

As shown by the previous examples, the entire implantable device design usually consists in a miniaturized antenna that is subsequently stacked above the other components. However, other solutions are possible so as to optimize the volume allocation depending on the given requirements. For instance, three different packaging possibilities, depicted in Fig. 4.7-(a), are presented in [193]. These solutions consider the design of a *capsule* shaped printed antenna illustrated in Fig. 4.7-(b). This radiator aims at working in the 3.5-4.5 GHz band as described in [194]. Further results leading to a wider band behavior are discussed in [54].
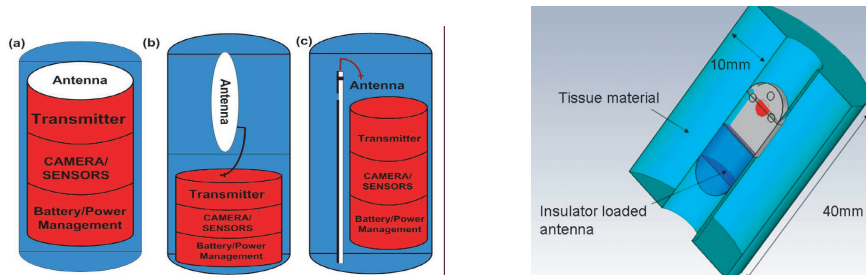
Figure 4.7.: Integration of a whole device: (a) three possible packaging solutions from [193] and (b) the *capsule* shaped printed antenna from [54].

3D Miniaturized Antennas with Packaging Considerations

Highest level of integration is achievable if the radiator takes advantage of the specific packaging of the targeted application. Such three dimensional solutions often following the shape of the power supply or/and the casing can minimize the radiator dimensions and improve its performances. For instance, a PIFA is investigated in [82] focusing on pacemaker applications in the MedRadio frequency range. In this case, a three dimensional ground plane is considered to allocate all the necessary electronics. For the same purpose, a similar solution is also investigated in [27]. Both designs are depicted in Fig. 4.8.

Considering endoscopy applications at 1.4 GHz, a conformal chandelier meandered dipole antenna is presented in [99]. This radiator, illustrated in Fig. 4.9-(a), follows the cylindrical semi-spherical *capsule* geometry and it cleverly uses the insulation as a supporting structure. A

Figure 4.8.: 3D Miniaturized antenna for pacemaker applications: (a) side view of the PIFA with a 3D ground plane from [82] and (b) the circular structure from [27].

complete device as a small as 11 x 26 [mm] is achievable with this typology. Following a similar idea, the feasibility of a design directly printed on the biocompatible insulation is presented in [195–197]. This interesting solution, depicted in Fig. 4.9-(b), completely frees the internal volume. However, the positive interaction of the radiator with the internal components and the external biological tissues is not demonstrated yet. That is why RFID applications (with no battery) were targeted in [198] and no SAR performances are discussed. The same problem may also apply to another clever conformal solution, a helical folded dipole antenna, described in [85].
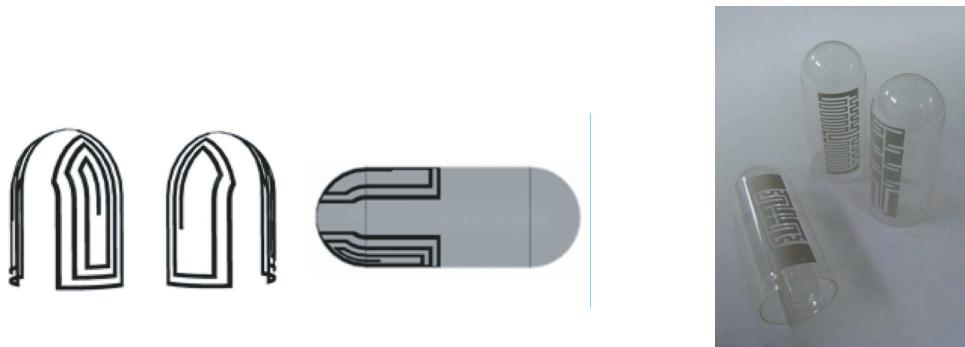
Figure 4.9.: 3D Conformal Miniaturized antenna: (a) the conformal chandelier meandered dipole antenna from [99] and (b) antennas whose metallizations are printed on the biocompatible insulation from [197].

Finally, we can consider the most extreme level of integration as when no antenna is specifically designed, and the radiator is just made up with the components that are already available. This is case of cardiovascular stent applications: these structures, depicted in Fig. 4.10 have been proven to be useful for short range communication in the 2.45 GHz ISM band in [62].

Other Classifications

Classification according to the Body Phantom: the implanted radiators are classified according to the body phantoms composition and geometry in Table 4.1 and Table 4.2, respectively. Different phantoms are often compared with the same radiator to better evaluate the influence of the human body on the characteristics of the investigated antennas.
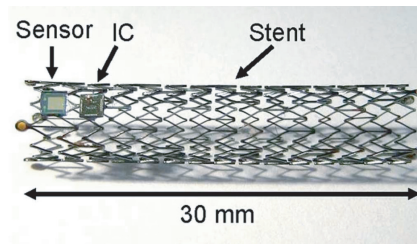
Figure 4.10.: Cardiovascular stents used as radiators for passive devices from [62].

Table 4.1.: Classification according to the Composition of the Body Phantoms.

Body Phantom Composition	References
Homogeneous	[18, 59, 60, 74, 92–95, 161–167, 178]
	[16, 80, 82, 84, 100, 101, 103, 113, 114, 170, 171]
	[9, 27, 54, 96, 99, 179, 182, 183, 186, 188, 190, 194]
Inhomogeneous (less than 7 tissues)	[18, 27, 74, 80, 84, 85, 98, 103, 161, 167, 173, 177]
Realistic (human or animal, above 7 tissues)	[18, 73, 74, 92, 101, 103, 161, 168, 169, 172, 174–176]
	[7, 27, 62, 99, 180, 181, 187, 189, 191, 192, 195, 196, 198]

Both the canonical inhomogeneous (less than 7 tissues) and the humanoid shape are very important when focusing on the radiation of subcutaneous implanted antennas. Quite surprisingly, these solutions are the least used for the design of implantable antennas.

Simple models are indeed preferred during the conception of the radiators because of their reduced computation requirements. Furthermore, their realization is easy for a practical measurement. On the contrary, realistic phantoms are necessary at the final stage of the design [92]. Therefore, intermediate steps such as canonical inhomogeneous (less than 7 tissues) and the humanoid shape are less considered as they increase the realization difficulties while still being quite far from the real-life scenario.

Table 4.2.: Classification according to the Geometry of the Body Phantoms.

Body Phantom Geometry	References
Canonical (box, cylinder or sphere)	[18, 74, 92–95, 98, 161–167, 172, 173, 177]
	[16, 54, 80, 82, 84, 100, 101, 103, 113, 114, 170, 171, 194]
	[9, 27, 96, 99, 179, 182, 183, 186, 188, 190]
Humanoid (combination of canonical geometries or similar)	[59, 60]
Realistic (simulated or measured human/animal models)	[18, 73, 74, 92, 101, 103, 161, 168, 169, 174–176, 180, 181]
	[7, 27, 62, 99, 187, 189, 191, 192, 195, 196, 198]

Classification according to the Working Frequency: Table 4.3 presents a classification according to the targeted frequency bands. While the majority of examples is found in the MedRadio and in the ISM at 2.45 GHz bands, others frequency range like the ISM at 915 MHz, the 1.2-1.6 GHz frequency range and the Ultra-Wideband spectrum (above 3 GHz) are becoming attractive for the realization of implantable devices with telemetry capabilities.

Table 4.3.: Classification according to the Working Frequency Range.

Frequency Range	References
lower than 400 MHz	[190]
401-406 MHz	[18, 27, 82, 92–96, 161–167, 175–178, 182]
433 MHz	[7, 9, 188, 189]
460-600 MHz	[183]
865-956 MHz	[98, 175, 176, 179, 195, 196, 198]
1.2-1.6 GHz	[74, 99, 168–170, 176, 191]
2.4-2.5 GHz	[16, 84, 101, 113, 168, 169, 171, 176, 180] [62, 85, 100, 181, 186, 187, 192]
3.1-5 GHz	[54, 193, 194]
Above 5 GHz	[172, 173]
Dual band 401-406 MHz and 2.4-2.5 GHz	[80, 103, 114, 174]

4.3. Preliminary Investigations of Implantable Antennas

Three implantable antennas were investigated, namely:

- Large Conformal Telemetry Device: integration of a conformal radiator (with dual band characteristics) with the selected transceiver and power supply relaxing the constraints on the physical dimensions;

- Miniature Dual Band Antenna: reduction of the antenna dimensions for a dual band radiator (in the MedRadio and ISM spectrum) with and without electronics. Particular attention is paid to the technological realizations aspects;

- Miniature Single Band Antenna: reduction of the antenna dimensions of a single band radiator (in the MedRadio spectrum). Free space analysis and human body presence are both taken into considerations.

Numerical analysis were performed with the commercial software High Frequency Structure Simulator (HFSS) [199].

For the telecommunication aspects, all antennas proposed in this thesis, including the radiator described in Chapter 5, target the integration with the Zarlink Semiconductors system [200, 201] that is presented below.

Zarlink System

The Zarlink Semiconductors system [200, 201] comprises the implantable Integrated Circuit (IC) ZL70101 [202] and an external module. The ZL70101 is an ultra low power, high performance transceiver which operates in the MedRadio and ISM bands. The system aims at providing data transmission over a minimum distance of 2 m (obviously depending on the performances of the antennas). A signal received in the ISM band wakes up the IC from its *sleeping* state; subsequently the bidirectional communication occurs in the MedRadio spectrum. This capability reduces the power consumption so as to extend the life time of implantable devices. Ultra-low power characteristics are also reinforced with a use of a *voltage step-up* matching (not conjugate) between the antenna and the IC.

MedRadio nominal characteristics of the implantable transceiver available in open literature [200, 201] are:

- a 500 Ω input impedance is required;

- the transmitted output power is programmable from -4.5 to -17 dBm;

- the receiver sensitivity is set according to the data rate. For instance, the minimum value equals to -99 dBm for a 200 kbps data rate.

Slightly different performances are achievable modifying some IC settings [202]. The Zarlink external module comprises the electronics for the transmission and reception and two omnidirectional monopole-like antennas (one for each working band) [202]. The characteristics of the external module and of the ISM band performances are not reported as they are not available in open literature.

4.3.1. Large Conformal Telemetry Device[†]

Design

We first proposed a Folded Inverted-F Antenna (FIFA) with a cylindrical cross section, which is illustrated in Fig. 4.11. This design allows for the housing all the electronics and power supply.
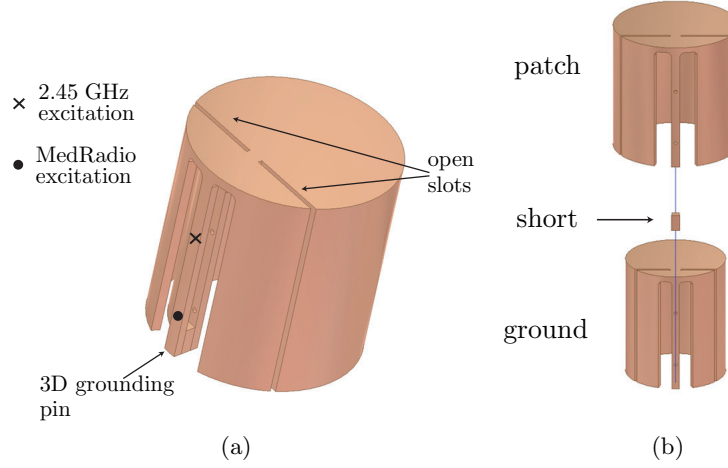
Figure 4.11.: FIFA final design: (a) complete structure identifying the excitation positions and a 3D grounding pin and (b) exploded view of the radiator. In (b), the "short" is a separate piece connecting the patch and ground parts.

Its working principle is similar to the one of a PIFA. In fact, a Planar Inverted-F Antenna was bent and extended on its three dimensions to reach the FIFA structure. The first steps of the design procedure are reported in Fig. 4.12, where the patch, ground and 3D grounding parts are clearly identified.
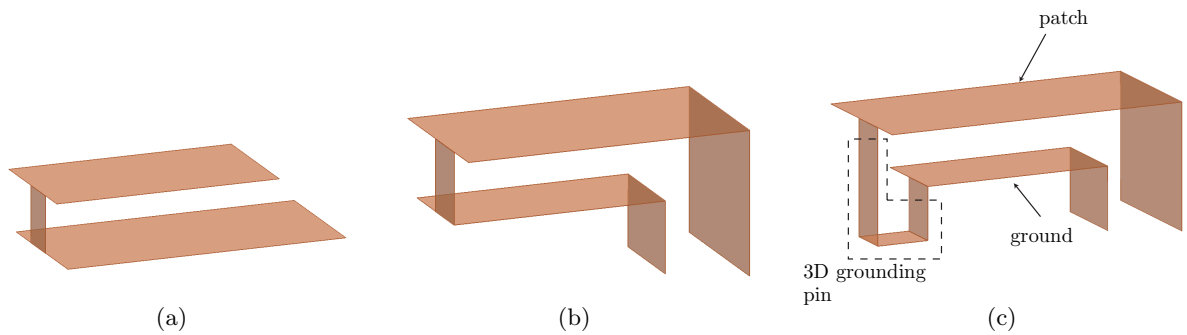
Figure 4.12.: Sketch of the design steps to reach the final FIFA: (a) PIFA, (b) PIFA with partially folded ground plane and (c) PIFA with folded patch and ground plane.

[†] -F. Merli, L. Bolomey, E. Meurville and A.K. Skrivervik, "Implanted antenna for biomedical applications," in *Proc. IEEE Antennas and Propagation Society Symposium (AP-S)*, San Diego (CA), USA, Jul. 4–12, 2008.

-F. Merli, L. Bolomey, E. Meurville and A.K. Skrivervik, "Implanted antenna for biomedical sensors," *Proc. European Electromagnetics (EUROEM 08)*, Lausanne, Switzerland, Jul. 21–25, 2008.

Finally, the structure was modified to follow a cylindrical geometry, and two open slots, see Fig. 4.11-(a) were added to reduce the resonance frequency and to obtain the desired dual band behavior. The detailed geometrical description, with dimensions, is reported in Appendix B.1.

The design was performed taking into account the surrounding media that are:

- the biocompatible insulation material: PEEK (thickness: 1 mm);

- the human body tissue: an homogeneous body phantom. The antenna was simulated at the center of a muscle equivalent sphere (radius: 45 mm) as indicated in Fig. 4.13.

The choice of of PEEK, despite its non optimal EM performances discussed in Chapter 3, has been mainly dictated by realization requirements, as it is very easy to manufacture and its biocompatibile characteristics are well established [188, 203]. Air is present between the ground and patch parts of the radiator. The antenna, including the casing of entire system, measures 32.0 x 33.8 [mm].
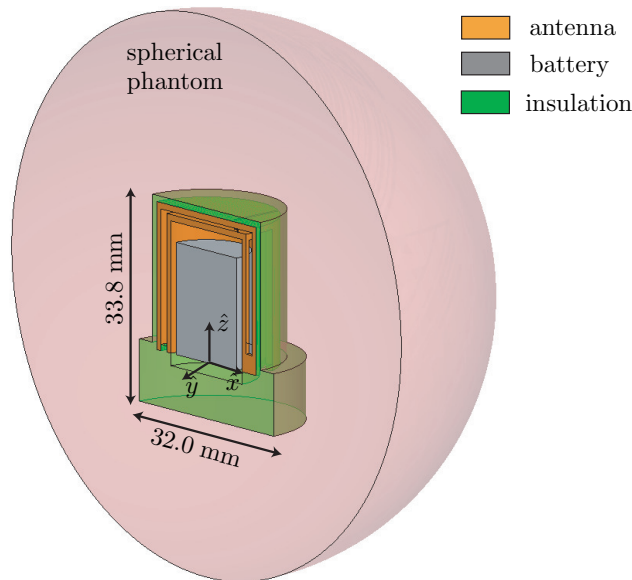
Figure 4.13.: Cutting view of the simulated model including the power supply, the biocompatible insulation and the spherical body phantom.

Simulated EM Characteristics

Current distributions are reported in Fig. 4.14. One can appreciate hot currents are present on the 3D grounding pin and around the open slots. Indeed, these two characteristics are the main responsible for the working behavior of the FIFA.

Fig. 4.15 illustrates the evaluated gain values. The MedRadio performances (gain = -29.2 dBi, $e_{\mathrm{rad}} = 0.053$ %) are comparable with previously reported works [82, 92] and they satisfy the I) ZL70101 requirements for indoor communication. Similar radiation characteristics (gain = -31.7 dBi, $e_{\mathrm{rad}} = 0.021$ %) were obtained in the higher frequency band.

Besides the homogeneous spherical muscle equivalent phantom, other models were numerically investigated to evaluate the performances of this radiator. These models are:
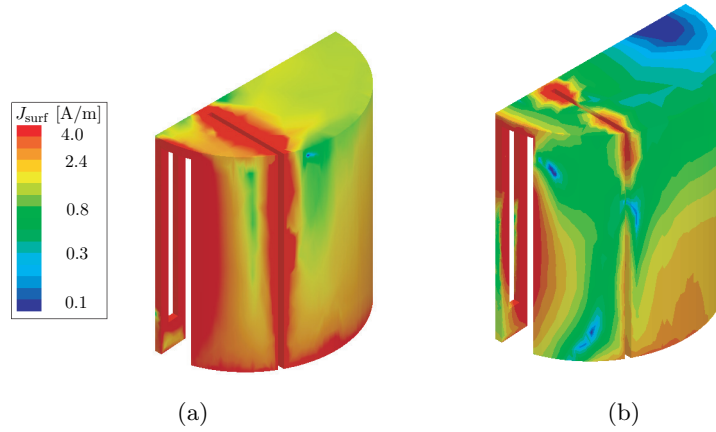
Figure 4.14.: Cutting views of simulated current distributions: (a) 405.6 MHz and (b) 2.445 GHz. Input power: 1 W.
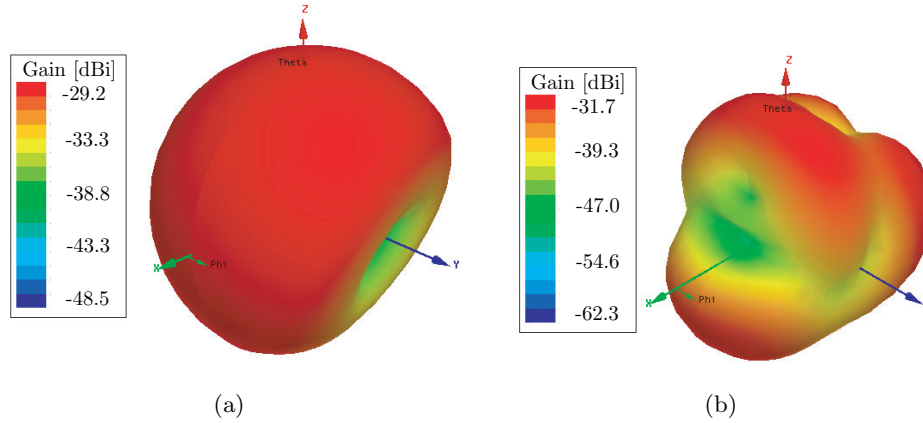
Figure 4.15.: Simulated 3D gain polar plots including body losses: maximum gain equals to (a) -29.2 dBi at 405.6 MHz and (b) -31.7 dBi at 2.445 GHz. Coordinate system is indicated in Fig. 4.13.

- homogeneous sphere with head equivalent properties (radius: 45 mm);

- larger homogeneous sphere with head equivalent properties (radius: 90 mm);

- homogeneous sphere with fat equivalent properties (radius: 45 mm);

The antenna was always placed at the center of the sphere. Dielectric properties of the biological tissues are given in Table 2.2.

The obtained results, reported in Fig. 4.16 and Table 4.4, illustrate that the matching of the proposed antenna is stable with respect of changes in the composition of the homogeneous phantom. In fact, the use of muscle or the equivalent head dielectric does not affect the FIFA matching characteristic. Furthermore, the resonant frequency is modified less than 1% when considering the fat phantom, which means a variation of about one order of magnitude of the dielectric properties with respect to the muscle case.

Radiation performances significantly depend on the chosen phantom. For instance, modeling a thick body phantom reduces the radiation efficiency of approximately ten times, while the
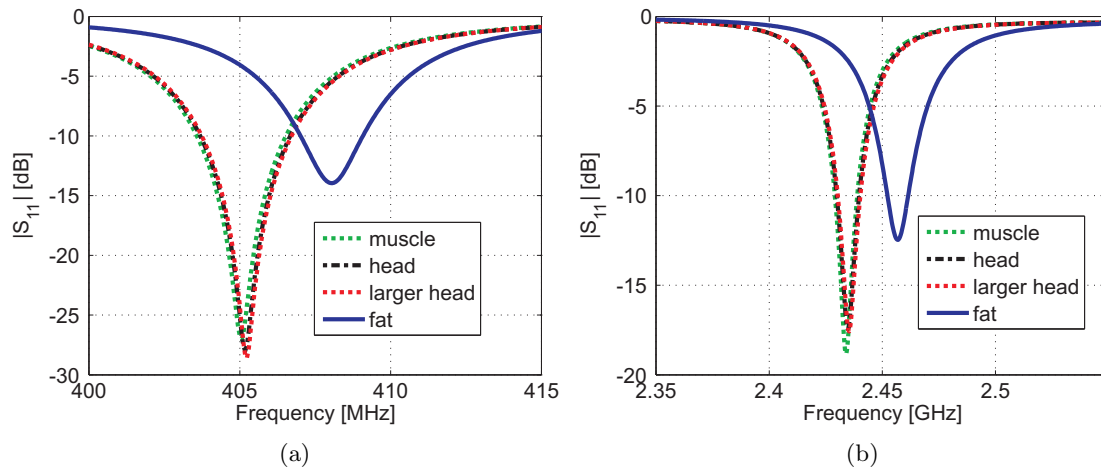
Figure 4.16.: Comparison of simulated $|S_{11}(f)|$ against frequency considering the FIFA inserted into different body phantoms in the (a) MedRadio and the (b) ISM bands. Matching is evaluated to the nominal IC ZL70101 input impedance requirements, and considering the IC matching capabilities.

Table 4.4.: Summary of the Simulated Radiation Results of the FIFA implanted in Different Body Phantoms. Maximum Values are reported for both Gain and Directivity.

Phantom	Frequency [MHz]	Gain [dBi]	Directivity [dBi]	e_{rad} [%]
muscle	405.6	-29.2	3.5	0.053
eq. head	405.2	-26.4	3.6	0.099
larger eq. head	405.1	-34.9	3.8	0.013
fat	408.6	-23.9	1.8	0.268
muscle	2445	-31.7	5.0	0.021
eq. head	2446	-34.7	4.9	0.011
larger eq. head	2447	-69.8	5.5	0.003e-3
fat	2469	-11.2	4.7	2.570

insertion in a lower lossy material (fat) implies the increase of the gain (+5.3 dB compared to the muscle phantom).

The analysis in the higher frequency band leads to similar considerations. Resonance is always within the targeted spectrum for all the investigated cases. Increasing the dimension of the spherical model results in a complete attenuation of the radiated signal (e_{rad} as low as 3e-6%). The latter characteristic is due to the electrical size, four λ_e, of the large equivalent head model.

Packaging and Realization

The efficient packaging of all components within the FIFA ground plane is illustrated in Fig. 4.17. This solution provided also a good shielding between the antenna and the electronics preventing any undesired coupling. The design and realization of all internal components was performed at LPM of EPFL by Dr. Bolomey [17]. Large power supply (height: 10.8 mm, diameter: 11.6 mm, capacity: 155 mA/h) were chosen in order to be able to carry out several measurements (31 hours of life with continuous transmission).
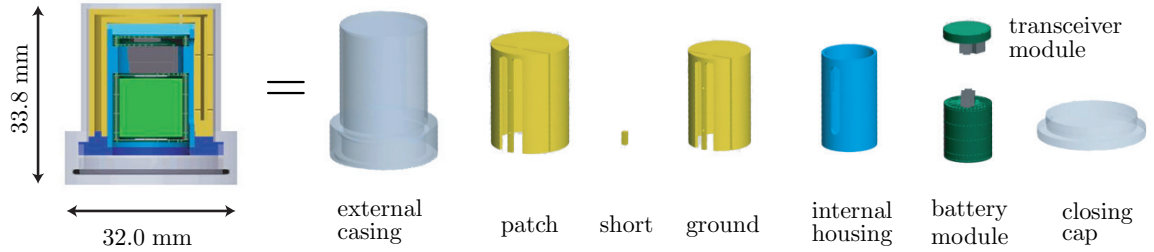
Figure 4.17.: Integration of all the components to realize a complete telemetry device with the FIFA.

The antenna was built by copper pieces 1 mm thick to facilitate the manufacturing process. This choice resulted in a structure as heavy as 46.84 g that is not suitable for real implantation. Both external and internal casings, identified in Fig. 4.17, are made of PEEK as for the numerical analysis. The realized antenna and all the pieces are shown in Fig. 4.18-(a). The electronics and the insertion of the battery module are illustrated in Fig. 4.18-(b)-(c), completing the final device.
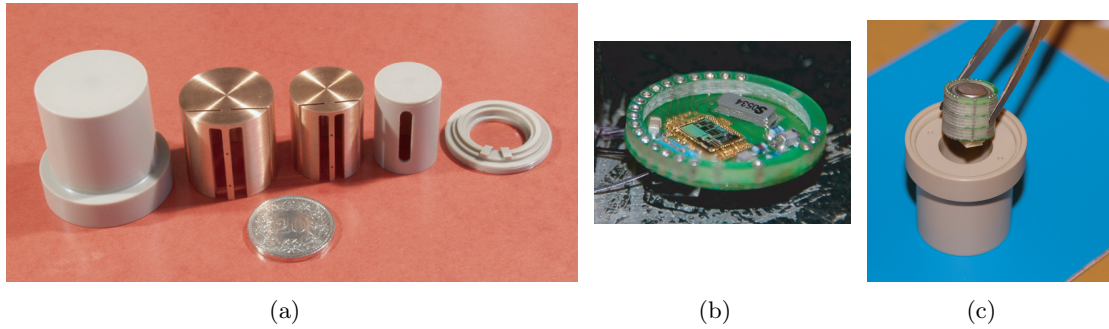
Figure 4.18.: Manufactured prototype: (a) FIFA parts including the biocompatible insulation, (b) transceiver module and (c) battery module insertion.

In Vitro Characterization

The device was immersed in a muscle equivalent solution contained in a cylinder. The antenna was entirely surrounded by roughly 1 cm of liquid, as shown in Fig. 4.19-(a). The communication performances were tested in an semi-anechoic chamber[†] using the Zarlink external module, as illustrated in Fig. 4.19-(b). Several distances, orientations and liquid quantities were verified showing a maximum range of about 4 m. The MedRadio communication distance specified by Zarlink, i.e., 2 m was observed in all cases. Tests were run as well for the *wake-up* signal in the

---

[†]This chamber belongs to the Electromagnetic Compatibility Laboratory at EPFL.

ISM band; in this case only distances almost up to 1 m were found to work properly. The measurements of the complete system show acceptable radiation characteristics and demonstrate the feasibility of a first prototype, given the preliminary knowledge of the IC requirements and of its capabilities.

(a)   (b)
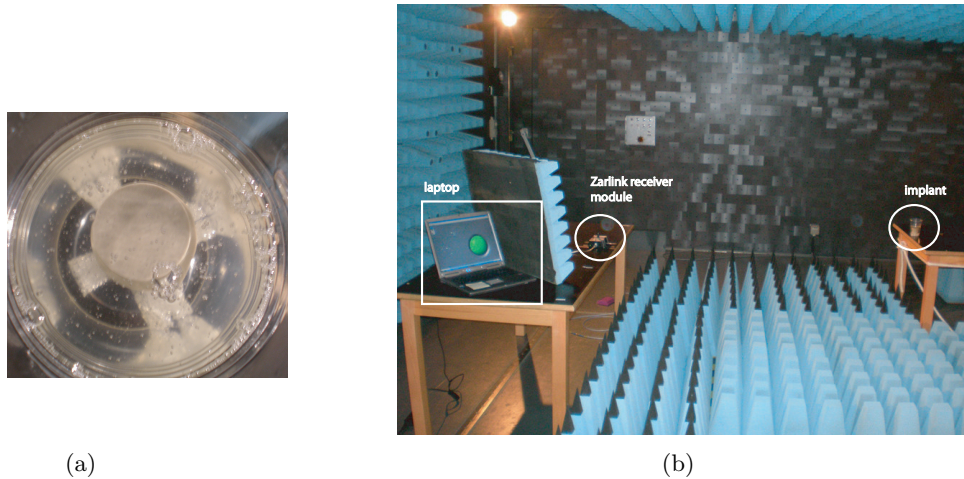
Figure 4.19.: Measurement setup: (a) FIFA immersed in the liquid phantom, and (b) complete system, including the Zarlink external module, in the semi-anechoic chamber. The green light on the laptop screen identifies a successful communication.

4.3.2. Miniature Dual Band Antennas

After the successful realization of a complete implantable telemetry device, our investigations focused on the miniaturization of the radiator. Indeed, the conformal antenna presented in the previous section is too large and heavy for a realistic implantation. The reduction of the size of the antenna implies stricter requirements from the technological/fabrication point of view. Thus, 50 Ω input impedances were always considered to evaluate the matching behavior of the antennas without increasing the complexity of the measurement.

Design

Further miniaturization was achieved by considering a dielectric material with a high dielectric constant. The ECCOSTOCK HIK 500F substrate ($\varepsilon'_e = 25$, $\tan \delta = 0.0015$, [204]) was used to realize a partially cylindrical hollow structure. Fig. 4.20 illustrates a sketch of the model. The biocompatible insulation (material and thickness) and equivalent spherical body phantom were chosen as for the FIFA. This radiator shares the same conception of the FIFA; the metallic design comprises the same three main elements (patch, 3D grounding pin and ground, as indicated in Fig. 4.20-(b). However, open slots where not required to reach the targeted performances. The use of the dielectric between the ground and the patch resulted in a reduction of dimensions by more than a factor of two. In order to minimize the circuitry, dual band capability was obtained with a single feeding.
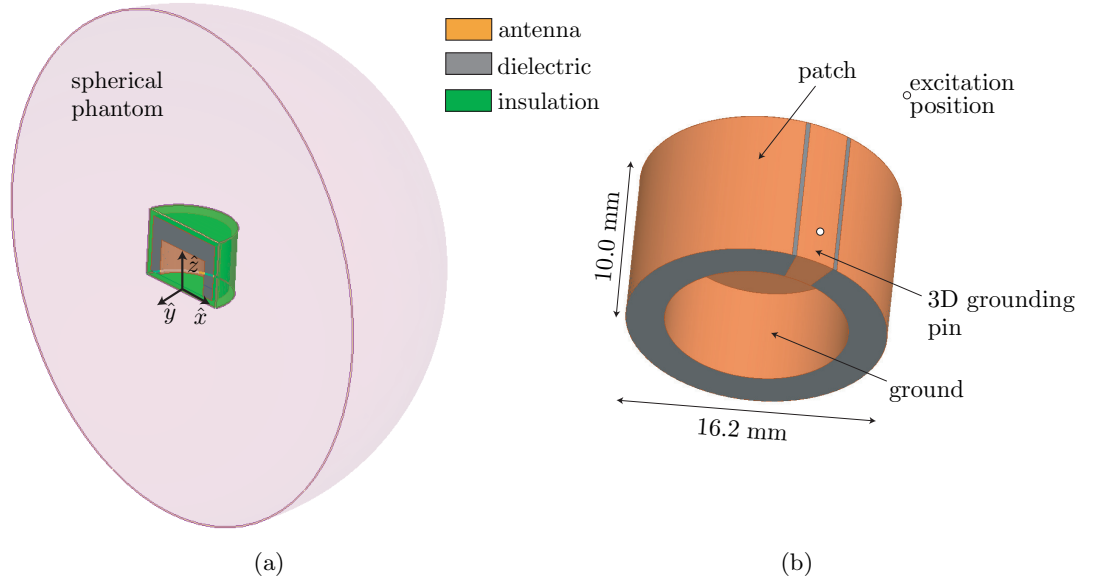
Figure 4.20.: Sketches of the simulated model: cutting view including the biocompatible insulation and the spherical body phantom and (b) radiator. Power supply is not illustrated (although considered) for clarity reason.

Simulated EM Characteristics

The EM performances in the MedRadio and in the ISM bands are reported in Fig. 4.21 and Fig. 4.22. Despite the size reduction, generally implying a lower e_{rad} [34], it can be noted
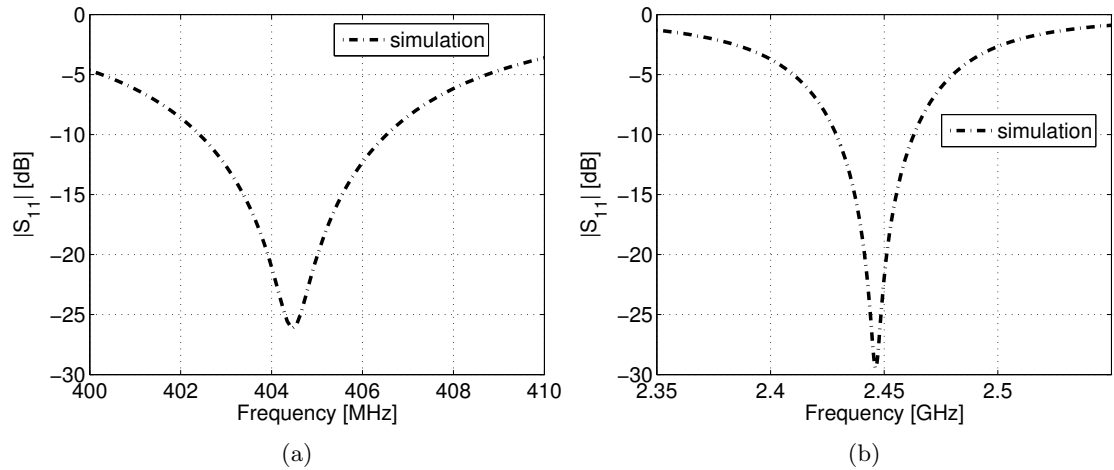
Figure 4.21.: Simulated reflection coefficients, $|S_{11}(f)|$, against frequency: (a) MedRadio and (b) ISM bands.

that this radiator is as efficient as the FIFA. The reasoning behind this is that the dielectric increases the electrical distance between the patch and the ground parts of the antenna. This results in a more constructive combination of the radiation of the surface currents. Indeed,

(a)   (b)
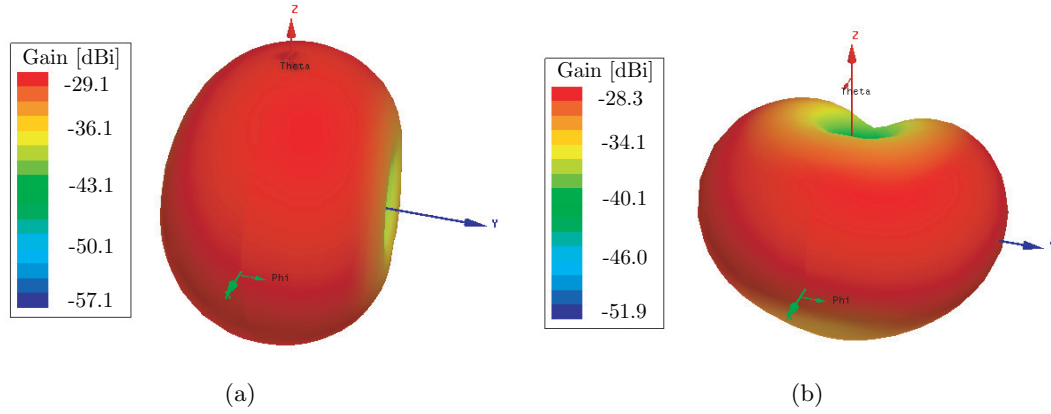
Figure 4.22.: Simulated 3D gain polar plots including body losses: maximum gain equals to (a)
-29.1 dBi at 404.4 MHz and (b) -28.3 dBi at 2.446 GHz. Maximum Directivity (e_{rad}) is
2.3 dBi (0.072%), and 2.6 dBi (0.081%), respectively. Coordinate system is indicated in
Fig. 4.20.

one can appreciate the $|\mathbf{E}|$ distributions of this antenna antennas (with ECCOSTOCK HIK
500F) and the one of the FIFA (without any dielectric) reported in Fig. 4.23.

(a)   (b)
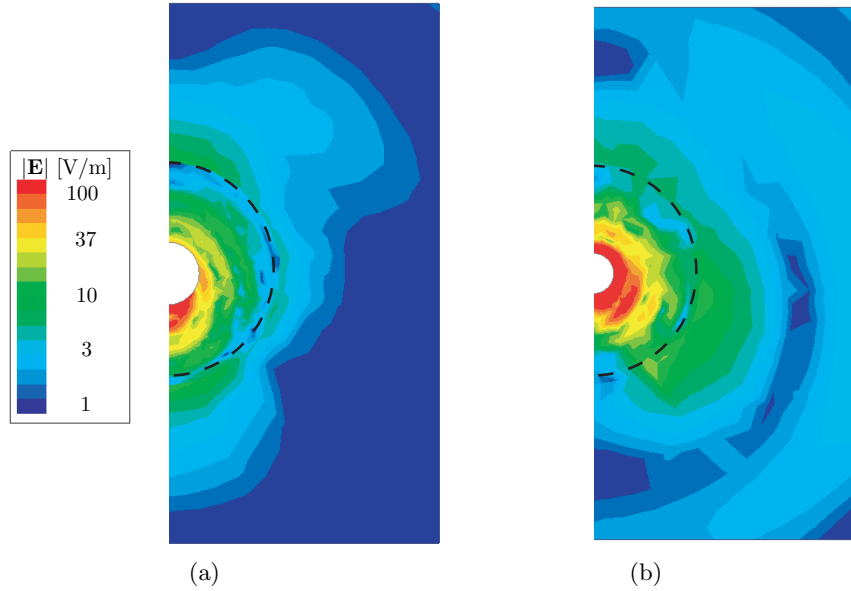
Figure 4.23.: Top view of simulated electric field, $|\mathbf{E}|$, at the excitation position when antennas are fed
with 1 W input signal in the ISM band: (a) FIFA at 2.445 GHz and (b) radiator with
ECCOSTOCK HIK 500F dielectric at 2.446 GHz. Higher radiation can be appreciated
in the latter case. Solid dashed line indicates the spherical phantom, while the radiators
are in white color.

Packaging and Realization

A sketch all the active components fitting within the antenna ground plane are reported in Fig. 4.24. These components were designed by Dr. Bolomey [17].
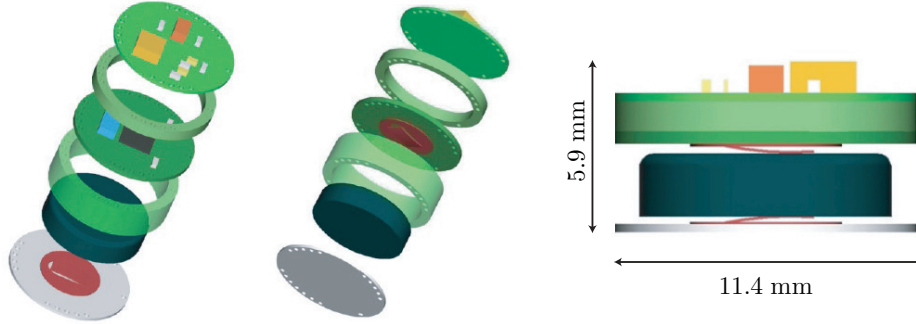
Figure 4.24.: Module stack of all the active components fitting the volume within the ground plane of the proposed antenna.

The antenna was realized at the *Atelier d'électromécanique* (AEM workshop) of EPFL. The manufacturing of the ECCOSTOCK HI-K 500F was not an easy task as this ceramic is very hard, and it is built of different grains requiring diamond tools (drill).

Two different metallizations were considered:

- silver based paint (this realization is denominated "Painted FIFA"). The detailed geometrical description, with dimensions, is reported in Appendix B.2;

- 0.5 mm thick brass foil (this realization is denominated "Brass FIFA"). The detailed geometrical description, with dimensions, is reported in Appendix B.3.

The two realized prototypes are depicted in Fig. 4.25 and Fig. 4.26, respectively.

(a)   (b)
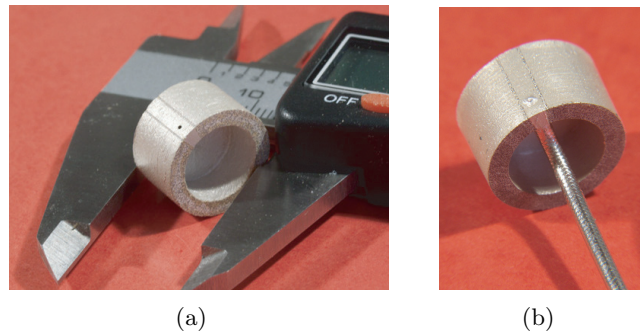
Figure 4.25.: Manufactured prototype: (a) Painted FIFA with ECCOSTOCK HI-K 500F dielectric and (b) radiator connected to a coaxial feeding cable for testing purposes.

The metallic design of the Brass FIFA was modified so as to obtain the desired resonances in free space (without the body phantom and the biocompatible insulation). This choice was taken in order to validate the selected technological realization without adding to the
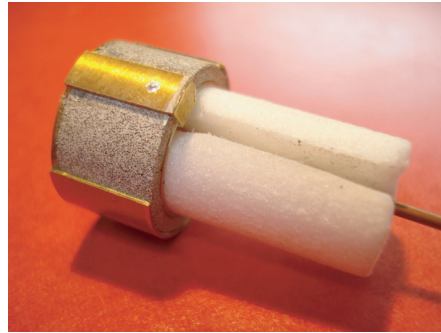
Figure 4.26.: Realized prototype considering the ECCOSTOCK HI-K 500F dielectric and brass met-
allization. White material (foam plastic) is present only as a mechanical support for
the feeding cable.

complexity related to the presence of the human body. The Brass FIFA prototype presented
two issues illustrated in Fig. 4.27 :

- air gaps presence between the brass metallization and ECCOSTOCK HI-K substrate;

- dielectric cracks.

(a)   (b)
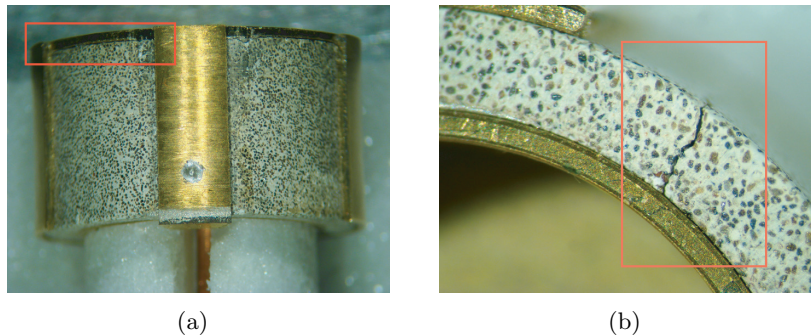
Figure 4.27.: Details of the realization of the Brass FIFA antenna with ECCOSTOCK HI-K 500F:
(a) air gaps presence and (b) dielectric cracks. The different grain composition of the
dielectric is visible in (b).

Free space Characterization

In order to asses the performance of the realized prototypes, we first tested them in a free
space environment. Obviously, this choice modifies the EM characteristics of the Painted
FIFA: higher resonance frequencies are expected without the dielectric loading effect of the
body phantom and of the biocompatible insulation. Nonetheless, this choice did allow us to
have standard and very reproducible measurement conditions$^{\parallel}$. The measured performances
did not match with the expected characteristics for both realized prototypes as illustrated in
Fig. 4.28 and Fig. 4.29.

$^{\parallel}$As matter of fact the $|S_{11}(f)|$ measurements considering the body presence gives rise to additional problems
that are discussed in Chapter 7.
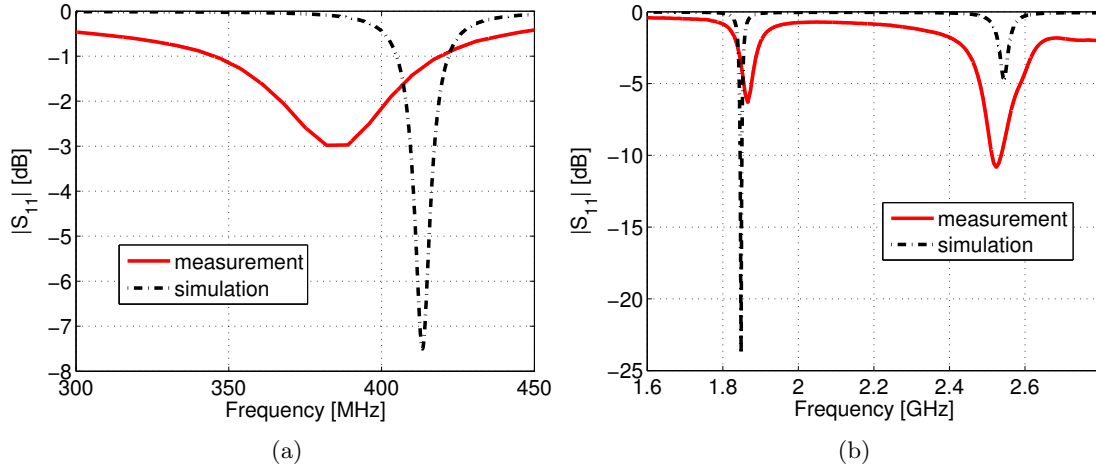
Figure 4.28.: Comparison of simulated and measured $|S_{11}(f)|$ of the Painted FIFA in a free space environment without the biocompatible insulation: (a) MedRadio and (b) ISM bands.
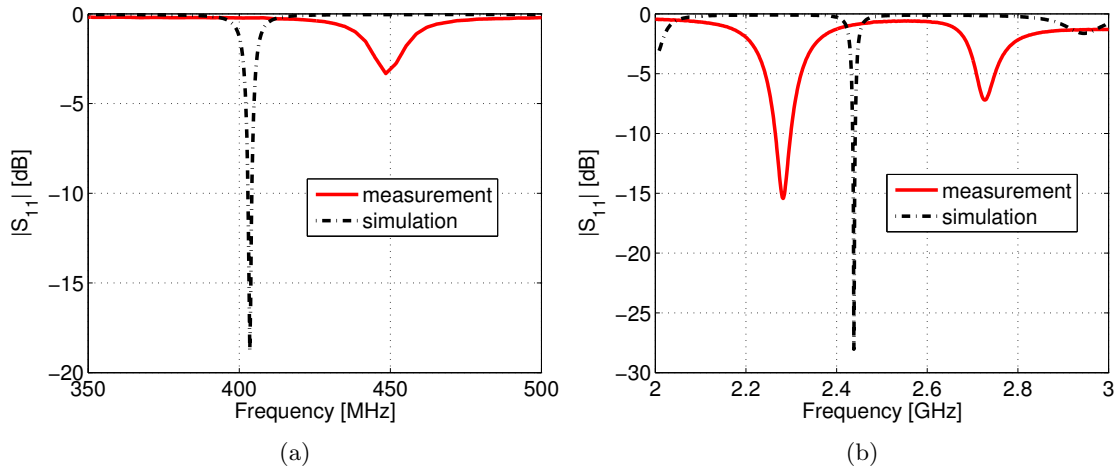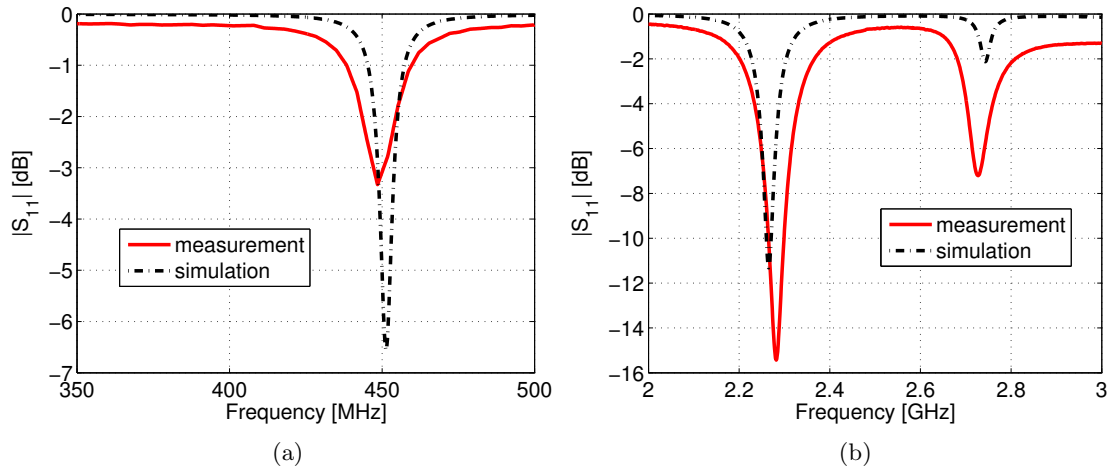

Figure 4.29.: Comparison of simulated and measured $|S_{11}(f)|$ of the Brass FIFA with dielectric material in free space without the biocompatible insulation: (a) MedRadio and (b) ISM bands.

An extensive numerical analysis was performed to identify the main reasons behind the observed disagreement:

- Painted FIFA: besides the building tolerances, the low conductivity of the used paint was identified being the principal source of the undesired measured behaviors. In fact, the numerical results reported in Fig. 4.28 were obtained setting the conductivity of the metallic part as equal as silver ($\sigma'_e = 61e6$ S/m). Closer agreement was found between the simulated and measured results, as illustrated in Fig. 4.30, by considering $\sigma'_e = 10.5e4$ S/m;
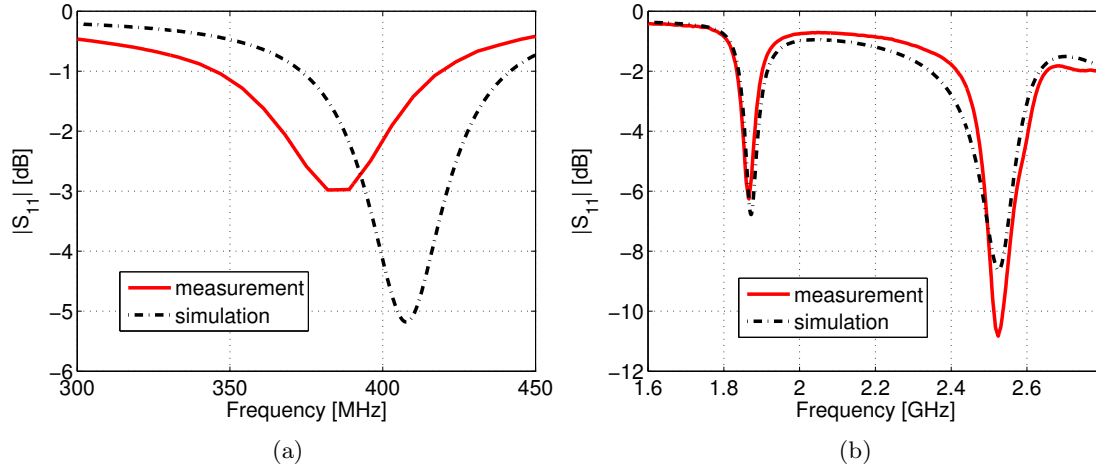
Figure 4.30.: Comparison of simulated and measured $|S_{11}(f)|$ of the Painted FIFA considering $\sigma'_e = 10.5\text{e}4\,\text{S/m}$ in a free space environment without the biocompatible insulation: (a) MedRadio and (b) ISM bands.

- Brass FIFA: the building details pointed out in Fig. 4.27 were included in the numerical analysis to a certain extent. Thus, it has been possible to obtain a closer agreement between simulated and measured matching performances in both working bands as illustrated in Fig. 4.31.

Figure 4.31.: Comparison of simulated and measured $|S_{11}(f)|$ of the Brass FIFA with dielectric material in free space without the biocompatible insulation including building errors: (a) MedRadio and (b) ISM bands.

In conclusion, the proposed FIFA designs with the use of dielectric manifested promising EM performances with dimensions as small as 10 x 16.2 [mm]. However, the realization of such an antenna typology requires technological tolerances and competencies beyond what was available to the author. Thus, this choice was no longer considered in the following of this thesis without further need of in vitro tests.

4.3.3. Miniature Single Band Antenna[†]

After the design of conformal dual band radiators, we decided to deeper investigate the miniaturization techniques such as dielectric loading, grounding pin, slots or meanders, spirals and 3D design, etc. [34] so as to obtain the most efficient radiator given the available volume in the MedRadio band. For this purpose, the presence of the transceiver, electronics and power supply was momentarily put aside.

Design

Previous investigations showed that designing an antenna from scratch, taking into account the body and its losses, is a tedious process as the simulation time involved may be be very large. Thus, in a first step, an antenna was analyzed in free space aiming at a maximum gain value higher than -20 dBi since body absorption losses were not present. As a starting point for the design procedure, the volume occupation was initially limited to 10 cm^3, which corresponds to a cube with a side measuring 2.15 cm.

PIFA and NMHA radiators were considered as inspiring models. Fig. 4.32 shows the first design steps, starting from a planar model to a three dimensional radiator and finally showing the structure with a double dielectric substrate and a 3D-spiral metallization. The ground plane is on the back side of the first dielectric, while the spiral metallization is wound around the upper substrate. This design is denominated "Folded Rectangular Helix" (FRH) in the following of this thesis.
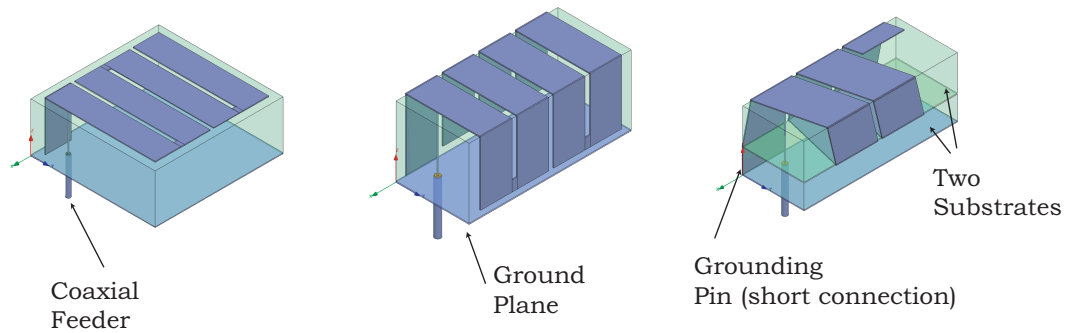
Figure 4.32.: First design steps (in free space) leading to a 3D-spiral structure.

To achieve optimal performances, an iterative miniaturization method was undertaken. This method consisted of performing a series of optimizations that led to the maximum volume reduction while still obtaining the desired electromagnetic behavior of the antenna. The sketches, dimensions and design parameters of both the starting and final radiator are illustrated in Fig. 4.33.

[†] -J. Abadia, F. Merli, J.-F. Zürcher, J.R. Mosig and A.K. Skrivervik, "3D-spiral small antenna for biomedical transmission operating within the MICS band," in *Proc. 3$^{\text{rd}}$ European Conference on Antennas and Propagation (EuCAP 2009)*, Berlin, Germany, Mar. 23–27, 2009.
    -J. Abadia, F. Merli, J.-F. Zürcher, J.R. Mosig and A.K. Skrivervik, "3D-Spiral Small Antenna Design and Realization for Biomedical Telemetry in the MICS band," *Radioengineering*, vol. 18, num. 4, pp. 359–367, Dec. 2009.

First, each of the three main dimensions bounding the antenna volume (xg, yg, h in Fig. 4.33) were reduced keeping constant the resonant frequency of 400 MHz with a tolerance of $\pm$ 2 %. This allowed for a fair comparison of the different results.

Subsequently, a complete optimization was performed by analyzing several spiral configurations. All the parameters, indicated in Fig. 4.33, were modified while still maintaining the desired resonance frequency.

The last step of the procedure included the choice of the dielectric material. Since the design calls for the use of two separate substrates, several possibilities combining Teflon ($\varepsilon'_e = 2.1$, $\tan \delta = 0.001$) and a ceramic material (ECCOSTOCK HI-K500 [204], $\varepsilon'_e = 11$, $\tan \delta = 0.0015$) were analyzed. As expected, simulation results showed that the use of the highest relative permittivity for both substrates led to a smaller, yet still efficient, antenna. Hence, the ceramic substrate was chosen. Once the iterative procedure was finished, the antenna dimensions are $14 \times 14 \times 15$ [mm] as illustrated in Fig. 4.33-(b).
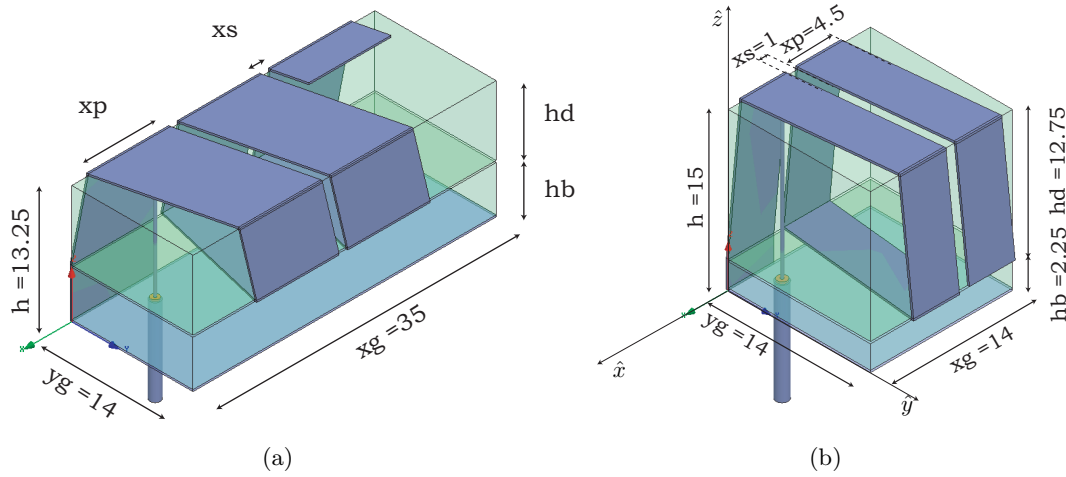
Figure 4.33.: Geometry and main dimensions in [mm] of the (a) starting and (b) final structure obtained via the miniaturization method in free space.

The radiator shows a maximum gain of -17.6 dBi (e_{rad} 1.805%) and 0.75 % relative bandwidth centered at 402 MHz. As the antenna is electrically very small, the radiation pattern is omnidirectional. In summary, Table 4.5 shows the initial and the final 3D-spiral antennas' characteristics. The total volume was successfully reduced by 55 %, while only losing 1.4 dB on gain and maintaining the bandwidth during the optimization process.

After the optimization of the radiator in free space, the biocompatible insulation and the human body model were introduced. As for the previous radiators, PEEK was chosen as the biocompatible layer. The antenna was placed at the center of a homogeneous cylinder with dielectric properties similar to those of a real muscle tissue. The cylinder has a radius of 4 cm, which correspond to a body thickness of approximately 30 mm, with a height of 10 cm. These dimensions are set based on the model of the human arm presented in [16].

Due to the presence of muscle and PEEK, the EM performances of the antenna changed, but the knowledge acquired during the optimization procedure in free space facilitated the necessary corrections. Thus, only the relocation of the feed and a variation of the substrates' thicknesses, hb and hd, were required, while considering the same volume. The detailed geo-

Table 4.5.: Antenna's Characteristics Before and After the Optimization Procedure Performed in Free
Space.

Characteristics	Initial	Final
Dimensions	35×14×13.25 [mm]	14×14×15 [mm]
Volume	6.49 cm^3	2.94 cm^3
Bandwidth	0.75%	0.75%
Gain	-16.2 dBi	-17.6 dBi
Directivity	1.2 dBi	1.3 dBi
e_{rad}	1.820%	1.288%
Frequency	399 MHz	402 MHz
$\min |S_{11}(f)|$	-31.14 dB	-25.15 dB

metrical description, with dimension, is reported in Appendix B.4.

Simulated EM Characteristics

The effects of the variation of the insulation thickness *hpeek* ranging from 1 to 4 mm were
analyzed versus the bandwidth performances. The optimum value of *hpeek* was found equal
to 1.5 mm, as illustrated in Fig. 4.34. With this dimension, the gain attains a maximum value
of -28.5 dBi ($e_{\mathrm{rad}} = 0.068\%$) and the resonant frequency is located at 405 MHz, with a -10 dB
bandwidth of 225.5 MHz (55.7 %). This large bandwidth is related to the introduction of the
equivalent muscle medium. In fact, the lossy material absorbs most of the incident power
reducing considerably the reflected one.
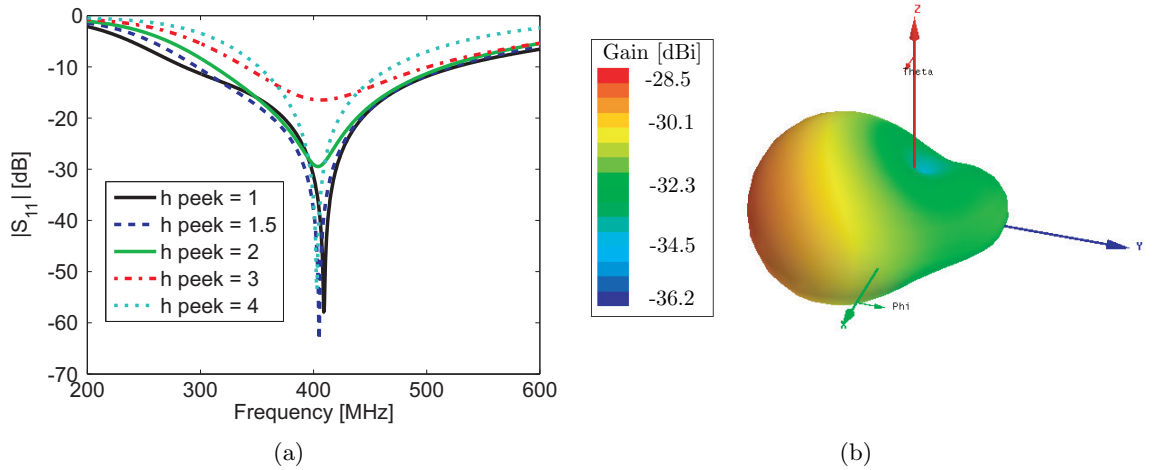
Figure 4.34.: Simulated performances: (a) $|S_{11}(f)|$ variation due to different insulation (*hpeek*) thick-
nesses in [mm] and (b) 3D gain polar plot including body losses of the final design at
405 MHz; maximum gain equals to -28.5 dBi.

An additional glue layer ($\varepsilon_r = 3$, $\tan\delta = 0.001$, to be used during the building process) was

included in the numerical analysis. This extra layer is in contact with the metallic and dielectric materials, thus it is important to take its influence into account. Fig. 4.35-(a) shows the reflection coefficients, $|S_{11}(f)|$, obtained for different glue layer thicknesses. As expected, the thicker the glue layer is, the more the resonant frequency shifts, and the higher the mismatch becomes. The wide band behavior of the radiator tolerates this variation but, if desired, the metallization of the antenna could be slightly adjusted to take this shift into account.
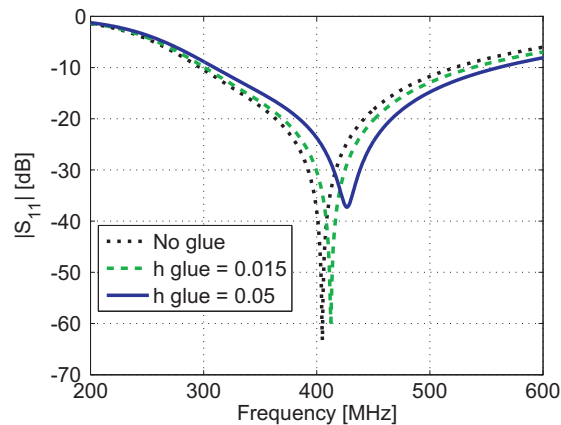
Figure 4.35.: Simulated $|S_{11}(f)|$ considering different glue layer thicknesses in [mm] with the radiator inserted into the homogeneous muscle phantom.

Besides the homogeneous cylindrical muscle equivalent phantom, two other models (with the same geometrical dimensions) were numerically investigated to evaluate the performances of radiator. The characteristics of these models are:

- homogeneous cylindrical with head equivalent properties;

- homogeneous cylindrical with fat equivalent properties.

Dielectric properties of the biological tissues are given in Table 2.2.

Radiation performances at resonance are reported in Table 4.6. The "fat" row is intensionally left empty to underline the absence of a matched resonance when considering this tissue. Simulated reflection coefficients against the frequency, are shown in Fig. 4.36.

Table 4.6.: Summary of the Simulated Radiation Results of Folded Rectangular Helix in Different Body Phantoms with Glue Thickness equal to 0.05 mm. Maximum Values are reported for both Gain and Directivity.

Phantom	Frequency [MHz]	Gain [dBi]	Directivity [dBi]	e_{rad} [%]
muscle	429.5	-28.1	3.4	0.071
eq. head	438.0	-28.7	3.0	0.068
fat	–	–	–	–

The FRH shows a quite stable behavior versus the selection of homogeneous phantoms. In fact, the use of muscle or the equivalent head model does not noticeably affect its matching
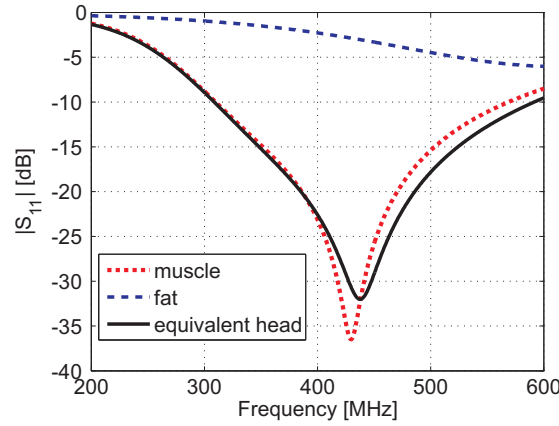
Figure 4.36.: Simulated $|S_{11}(f)|$ considering different body phantoms with glue thickness equal to 0.05 mm.

characteristic. A change of around 25% in the dielectric constant only modifies the resonant frequency of 2%. However, this behavior has its limits and it no longer applies to the fat case where the large dielectric variation (around of 1 order of magnitude smaller with respect to the other models) results in a complete mismatch.

The Specific Absorption Rate in the homogeneous muscle equivalent phantom was also computed so as to get an idea of the power absorbed by the body model. Maximum SAR values are distributed in close proximity of the feeding cable. Providing the antenna with a 1 W input signal, the peak spatial-average (1 g) SAR distribution over the yz-plane (at the excitation position) is depicted in Fig. 4.37. In order to satisfy the IEEE recommendation [14] (1.6 W/kg per 1 g averaging), the power delivered to the antenna should be decreased to 5.9 mW (7.7 dBm). It is worth noting that the input power of the entire system previously used with the FIFA is less than 0 dBm thus, complying with SAR requirements.
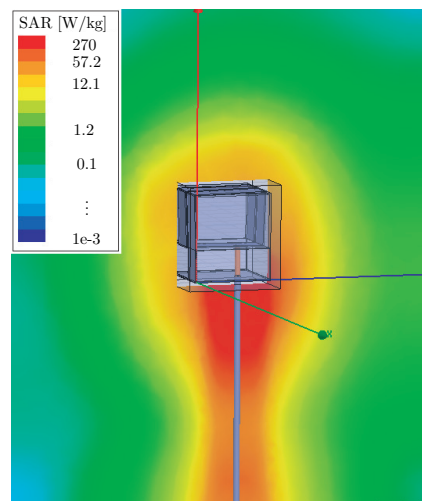
Figure 4.37.: Simulated surface peak spatial-average (1 g) SAR distribution over the yz-plane (at the excitation position) at 405 MHz. Input power: 1 W.

Packaging and Realization

A prototype, shown in Fig. 4.38, was built in order to validate the numerical analysis. Even if the structure is rather complex, only a simple construction procedure was required since the metallization is folded around the two dielectric pieces. This prevented also all the metallization problems experienced in the prototyping of the FIFAs with the dielectric substrates. The antenna is composed of a 200 μm thick copper-beryllium metallization, two ECCOSTOCK HI-K500 ceramic substrates, and it is covered by PEEK. As for the other presented prototypes, all the dielectric materials have been characterized by measurements.

(a)   (b)
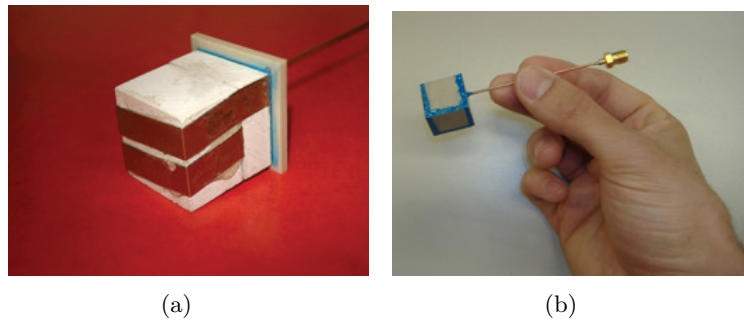
Figure 4.38.: Realization of the FRH prototype: (a) intermediate and (b) final structure.

In Vitro Characterization

The measurement setup is shown in Fig. 4.39. Matching experimental results with the use of a coaxial feeding cable confirmed the simulated performances, as shown in Fig. 4.39-(b).

(a)   (b)
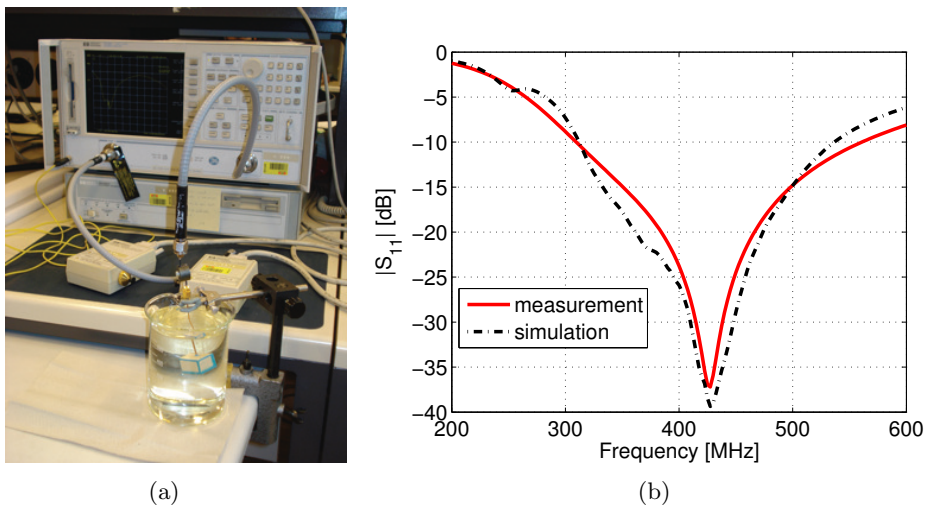
Figure 4.39.: Measurement setup (a) and comparison of the simulated (glue thickness: 0.05 mm) and measured $|S_{11}(f)|$ for the realized prototype (b) with the realized antenna performance in the equivalent body medium.

4.4. Comparison of Implantable Antennas

The characteristics of the radiators proposed in this chapter and a selected choice of designs from open literature are discussed. Characteristics are reported in Table 4.7 and Table 4.8 for the MedRadio and the ISM band, respectively. Basic information, such as dimensions, body phantom and implant depth are given for each antenna. Only gain values are presented as other information are not always provided in the selected references.

Table 4.7.: Comparison of Different Implantable Radiators in the MedRadio Band.

Antenna	Dimension with insulation [mm]	Body Phantom			Implant depth [mm]	Gain [dBi]
		ε'_e	σ'_e	dimension [mm]		
Spiral based on [18]	38.0 x 42.0 x 4.0 = 6384.0	49.60	0.51	50 x 40 x 20	5	-30.6
Spiral PIFA [92]	17.0 x 27.0 x 6.0 = 2754.0	42.80	0.64	50 x 40 x 20	7	-35.0
Meandered PIFA [80]	22.5 x 22.5 x 2.5 = 1265.6	46.70	0.68	103 x 103 x 8.5	3	-24.9
Stacked PIFA [167]	3.6^2 x π x 0.7 = 28.5	46.70 / 13.1 / 57.4	0.69 / 0.09 / 0.74	100 / 95 / 90	$\simeq 2$	-55.6
PIFA with 3D ground plane [82]	40 x 30 x 13.2 = 15600.0	38.10	0.53	100 x 100 x 50	4	-28.0
FIFA	$\simeq 16^2$ x π x 33.8 = 27184.0	57.10	0.79	90	$\simeq 18$	-29.2
Painted FIFA	6^2 x π x 18.2 = 2058.4	57.10	0.79	90	$\simeq 34$	-29.1
FRH	17 x 17 x 18 = 5202.0	57.10	0.79	80 x 100	$\simeq 20$	-28.5

*[mm]. Three values are for box geometries, two for cylindrical (diameter x height),

and one for spherical (diameter).

Looking at the dimension column in Table 4.7 of the first four antennas, it can be appreciated that the Inverted-F typology (either Planar or Folded) is the most used and effective way to reduce the size of the radiator. Indeed, the dimensions the Spiral PIFA [92] (17.0 x 27.0 x 6.0 [mm]) and of the meandered PIFA presented in [80] (22.5 x 22.5 x 2.5 [mm]), are much smaller than the ones of the spiral inspired from [18] (38.0 x 42.0 x 4.0 [mm]). Further miniaturization is then achievable combing stacked planar metallization, as in [167]. However, if dimensions are reduced till less than 30 mm^3, a drastic reduction of the radiation performance occurs (gain = -55.6 dBi) .

Taking a more global view to the characteristics reported in Table 4.7, one understands that dimensions, body phantom and gain values are all interconnected and cannot be discussed singularly. For instance, the meandered PIFA proposed in [80] shows the best performances. However, the reduced depth of the antenna, 3 mm, and the very small thickness of the investigated body model, 8.5 mm, do affect the obtained results. As a matter of fact, spiral designs are found to be slightly more effective then meandered ones in [92, 94]. As a second example, the FRH maximum gain value (-28.5 dBi) is observed when modeling a noticeably deeper depth ($\simeq 20$ [mm]).

Among the eight considered radiators, only the PIFA with 3D ground plane [82], the FIFA, and its painted version take into account the presence of any active components and power supply. On the one hand, this fact implies a larger volume occupation, if compared to the optimized designs reported in [80, 92, 167]. For instance, the FIFA has the largest dimensions of the reported radiator. On the other hand, the design of 3D ground planes enhances the EM radiation. Indeed, these three radiators present comparable gain values although being surrounded by larger body phantoms and/or being deeper implanted. In particular, the Painted FIFA solution shows promising EM performances (gain = -29.1 dBi) with dimensions as small as 12 x 18.2 [mm] and considering the deepest implantation depth. However, the realization of this antenna typology requires technological tolerances and competencies beyond to what available to the author. This is the reason why this choice was no longer considered in the following of this work.

The use of the 2.45 GHz higher frequency facilitates the size reduction of the radiators as one can appreciate from the characteristics reported in Table 4.8. For instance, the PIFA presented in [100] occupies only 161.6 [mm]. Furthermore, considering optimized solutions (such as the cavity slot [16], the double helix [85] and the spiral dipole [101]) volumes smaller than 25 [mm] are achievable. In particular the latter radiator shows a extremely reduced volume occupation, i.e. 11 mm mm^3. Only when the antenna has also to resonate in the MedRadio band, as for the FIFA and painted FIFA, and Meander PIFA from [80], volume larger than 1000 mm^3 are observed.

As a drawback, the higher attenuation of the EM wave in the lossy media in the ISM band makes the radiation very much dependent on the size of the body model and the depth of the implanted antenna. That is why gain values range from -8.5 to -34.0 dBi for the compared radiators.

A closer look to the gain values shows, despite the different body phantoms, that the radiation performances of the radiators proposed in this chapter are not optimal (gain <-24 dBi). Higher gain, even with smaller dimensions, are attained by the Cavity slot proposed in[16], by the Double Helix described in [85] and by the Meandered PIFA presented in [80]. The reason behind this is twofold. First, the design procedure always preferred the MedRadio band, as the requirements in terms of electrically dimension are stricter in this frequency range. Second, higher EIRP limit are allowed in the ISM band, thus relaxing the required RX capability of the implantable antennas.

Table 4.8.: Comparison of Different Implantable Radiators in the ISM Band.

Antenna	Dimension with insulation [mm]	Body Phantom			Implant depth [mm]	Gain [dBi]
		ε'_e	σ'_e	dimension [mm]		
Cavity slot antenna [16]	1.6 x 4 x 2.8 = 17.9	35.15	1.60	180 x 60 x 60	4	-22.3
Double Helix [85]	0.6^2 x π x 17.7 = 20.1	38.00 / 5.30 / 52.70	1.50 / 0.10 / 1.70	180 x 60 x 60 / 180 x 56 x 56 / 180 x 48 x 48	2	-14.0
Spiral Dipole [101]	2.5 x 4 x 1.1 = 11.0	52.00	1.74	50 x 50 x 50	25	-34.0
Meandered PIFA [80]	22.5 x 22.5 x 2.5 = 1265.6	38.06	1.44	103 x 103 x 8.5	3	-8.5
PIFA [100]	$\simeq 5.5^2$ x π x 1.7 = 161.6	saline** and 50.0	2.20	152 x 152 x 20 / 80 x 50 x 8	$\simeq 8$	-24.8
FIFA	$\simeq 16^2$ x π x 33.8 = 27184.0	52.73	0.24	90	$\simeq 18$	-31.7
Painted FIFA	6^2 x π x 18.2 = 2058.4	52.73	0.24	90	$\simeq 34$	-28.3

**Dielectric properties are not specified.

4.5. Conclusion: Formulation of a Design Strategy

This chapter described the main physical constraints and electromagnetic characteristics of implantable antennas facilitating the understanding of the existing solutions in open literature. Based on this knowledge, four new designs were investigated via numerical analysis and measurements. These antennas differ in conceptions, dimensions, materials and fabrication. these studies allowed us to analyze the importance of the antenna typology, its numerical analysis (performed with HFSS [199]) comprising the human body presence, and the possible technological realizations. The Folded Inverted-F Antenna was conceived in order to realize a complete device. In fact, its conformal geometry allows for the placement of all the active components and power supply within its ground plane. Following the same concept Painted and Brass PIFA explored different metallization techniques so as to miniaturize the radiator. A specific optimization procedure was undertaken to design the single band Folded Rectangular Helix. This realization allowed us to systematically appreciate the variation of the EM performances versus the reduction of the dimensions.

The presented investigations were performed in different body phantoms in terms of compositions and shapes. Numerical analysis in free space were also carried out to better understand the modification because of the surrounding lossy media. Preliminary evaluation

of SAR provided us the first ideas about the power budget requirements meeting with safety requirements. Biocompatibility was also taken into account and analyzed so as to improve the radiators characteristics. In agreement with the conclusions drawn in Chapter 3, thin layers of PEEK were selected letting the maximum available volume to the antenna design.

Taking advantage of previous investigations and considerations, we propose an efficient design strategy for implanted antennas. Such a strategy targets a design yielding the best possible power transfer from the implanted device to the Base Station, while reducing the computational requirements. This design strategy comprises the following steps:

1. fix the external geometry, the maximum volume for the whole telemetry device, and any other specific physical requirements for the targeted application;

2. perform a first design in a homogeneous lossless medium so as to select the most performing antenna typology. Consider a medium having a dielectric permittivity representative of the tissue surrounding the implant or equal to free space. Different antenna typologies can therefore be investigated; the final choice will depend on the required bandwidth, the selected packaging and the available technological realizations;

3.   a) make a proper choice of the dielectric material, of the insulation layer and of the body phantom, and include them in the numerical analysis;

     b) set the excitation area so as to minimize the assembly complexity, once the precise volume dedicated for each components constituting the implantable device is defined, and consequently arrange the chosen antenna typology;

     c) optimize the radiator given its new surrounding environment;

4. evaluate the performances of the antenna in different body phantoms (from rough approximations to more detailed models). If required, modify the design starting from point 3.

The analysis in a homogeneous lossless medium, point 2, may seem awkward as the coupling of the near field in the lossy tissues is not taken into account from the very beginning of the design procedure. However, the computer time requested is orders of magnitude smaller with such a choice than when all details of the surrounding medium are taken into account. Moreover, considering a lossless medium around the antenna (but keeping the conducting and dielectric losses of the antenna itself) allows the optimization of the radiation efficiency following the current vector alignments concept [169, 205, 206]. Furthermore, it is important to ignore the body losses at this step in order not to optimize the antenna bandwidth by just increasing the power lost in the body. This analysis gives also insight into the radiating performances of the radiator which will be a great use for the tuning and optimization of the antenna itself, point 3. Finally, the proper selection of the insulation properties gives the antenna engineer a certain control on the coupling between the near field and the biological tissues. Thus, the desired working behavior can be preserved to a certain extent when a lossy medium is added to the model.

This strategy will be applied to design and realize an implantable antenna in the following chapter. Although mainly focusing on the MedRadio performances, results will show that acceptable dual band capabilities can also be achieved proving the usefulness of the proposed strategy.

5. Design, Realization and In Vitro Characterization of an Implantable Antenna[†]

5.1. Introduction

The strategy formulated at the end of the previous chapter is applied to design and realize an implantable antenna. In order to clearly present all the characteristics of this radiator, this part of the thesis focuses on the antenna alone, while the packaging of the radiator oriented to the making of a complete Body Sensor Node (BSN) [17] is discussed in the next chapter.

The four main goals of this chapter are:

1. to apply the formulated design strategy to design an implantable antenna for a real life application;

2. to realize and to characterize the radiator;

3. to perform numerical analysis in a realistic body phantom;

4. to discuss the versatility of the design and its possible further evolutions.

In order to reach these goals, this chapter is organized as follows: the design procedure is applied in Section 5.2. First, we present the specific physical constraints, the EM characteristics, and the overall packaging of the complete BSN. Then, the investigations in free space are described. Finally, the insulation and a body phantom are included in the modeling. Section 5.3 describes the realization of the proposed radiator, while its in vitro characterization and improvements are discussed in Section 5.4.

Advanced numerical analysis are presented in Section 5.5, comprising the investigation considering a realistic body phantom, and the versatility of the design. The latter answers to different requirements, in terms of power supply or monitoring devices, and facilitates a possible further miniaturization. Finally, conclusions are drawn in Section 5.6.

5.2. Application of the Design Strategy

The design strategy formulated at the end of the previous chapter is applied to design an implantable antenna for a real life application. In agreement with this strategy, specific requirements are illustrated in Section 5.2.1, while the Section 5.2.2 presents the performed analysis in free space. The chosen Multilayered Spiral Antenna is optimized in Section 5.2.3

[†] -F. Merli, L. Bolomey, J.-F. Zürcher, G. Corradini, E. Meurville and A.K. Skrivervik, "Design, realization and measurements of a miniature antenna for implantable wireless communication systems," *IEEE Trans. Antennas Propag.*, in press.

considering the presence of the biocompatible insulation and a homogeneous body phantom. Finally obtained performances are presented in Section 5.2.4.

5.2.1. Specific Requirements

Physical constraints and EM characteristics are presented to target a real subcutaneous application for monitoring purposes. In addition to these requirements, we introduce also the versatility aspect as detailed below.

Physical Constraints

- The volume of the entire implant (i.e., the antenna, insulation, electronics, batteries and biosensors) must fit in a biocompatible cylindrical housing. A maximum external diameter of 10 mm is set to allow subcutaneous implantation in rats [207] or pigs;

- a dense packaging is required to reduce the implant volume [208], hence the feeding of the antenna is placed in a small predefined area (3×3 mm^2) to minimize the circuitry complexity.

An example of the dense packaging is illustrated in Fig. 5.22 showing the *Pillcam* system for near field data communication [209].
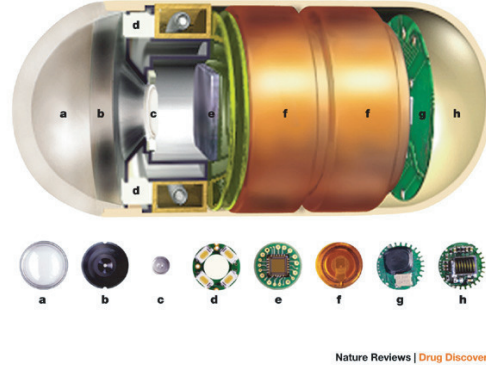
Figure 5.1.: Pillcam [209] is an example of small dimensions (11×26 [mm]) and dense packaging for a near field data communication implantable system for endoscopy applications.

Electromagnetic Characteristics

- Dual band capability must be obtained to operate with the transceiver ZL70101 (presented in Section 4.3). This capability minimizes power consumption as the sensor can be awoken from *sleeping* state by receiving a signal in the 2.4-2.5 GHz band. Subsequently, data transmission occurs only in the MedRadio frequency range;

- a single antenna feeding point is targeted to minimize the assembly complexity;

- antenna gains higher than -30 and -20 dBi are targeted in the MedRadio band and the ISM band, respectively. Note that these gain values include both the antenna radiation characteristics and the simulated body phantom presence. The corresponding radiation

efficiencies are rather small, but they provide operational ranges wider than 10 m in the MedRadio and 5 m in the ISM bands, with the use of the Zarlink transceiver and external module. These performances ensure excellent communication in the targeted 2 m distance;

- the antenna has to preserve its working behaviors with different surrounding conditions. This means to conceive a radiator with EM characteristics robust to the implant location in the human body.

Versatility

- The design aims at realizing an versatile implantable antenna for a general purpose BSN. The radiator should withstand the variation of some physical constraints (different casings, power supply and monitoring sensor), while keeping adequate electromagnetic characteristics.

5.2.2. Selection of the Antenna Typology in Free Space

The overall BSN concept is depicted in Fig. 5.2. It has a cylindrical volume (diameter: 10 mm, height: 32 mm). The battery and two circuitry placements, indicated in Fig. 5.2, are off-centered with respect to the cylinder axis.
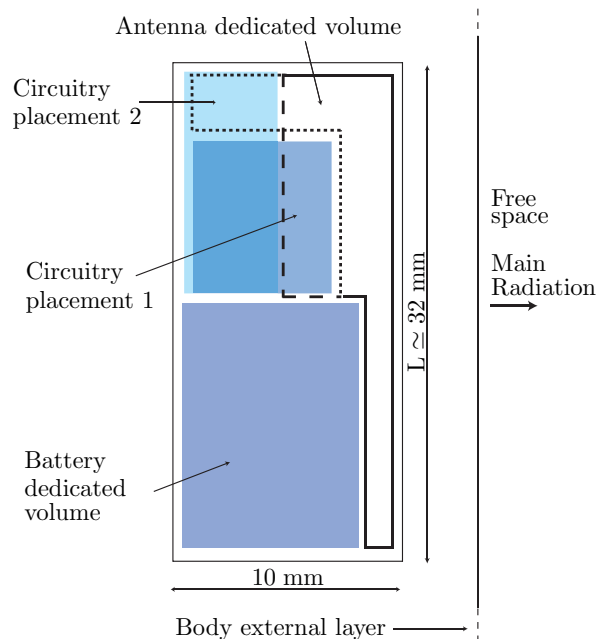
Figure 5.2.: Implanted sensor conception. Maximum dimensions are indicated. Placements of battery and electronics are indicated to estimate the overall volume occupancy; two possible geometries of the circuitry (in light colors), and consequently of the antenna (solid-dashed lines), are shown.

In order to reduce the interference due to the active components on the antenna's behavior, we considered a ground plane made of a rectangular planar section and a half hollow cylinder part (both depicted in light color in Fig. 5.3). This solution, with its off-centered

design that results in an eccentrically insulated radiator, also enhances the directivity of the radiator towards the desired out-of-the body direction, and it has the advantage of reducing the power absorbed by the biological tissues. For an easier understanding, the half hollow cylinder part has been referred to as "conformal ground plane" in the following sections.

The four different typologies depicted in Fig. 5.3 were investigated: spherical (conceived for the circuitry placement 1 in Fig. 5.2), spiral, meander and multilayered spiral (for the circuitry placement 2 in Fig. 5.2). All designs have a ground connection to further reduce the resonant frequency.

planar
ground
plane

conformal
ground
plane

(a)   (b)   (c)   (d)
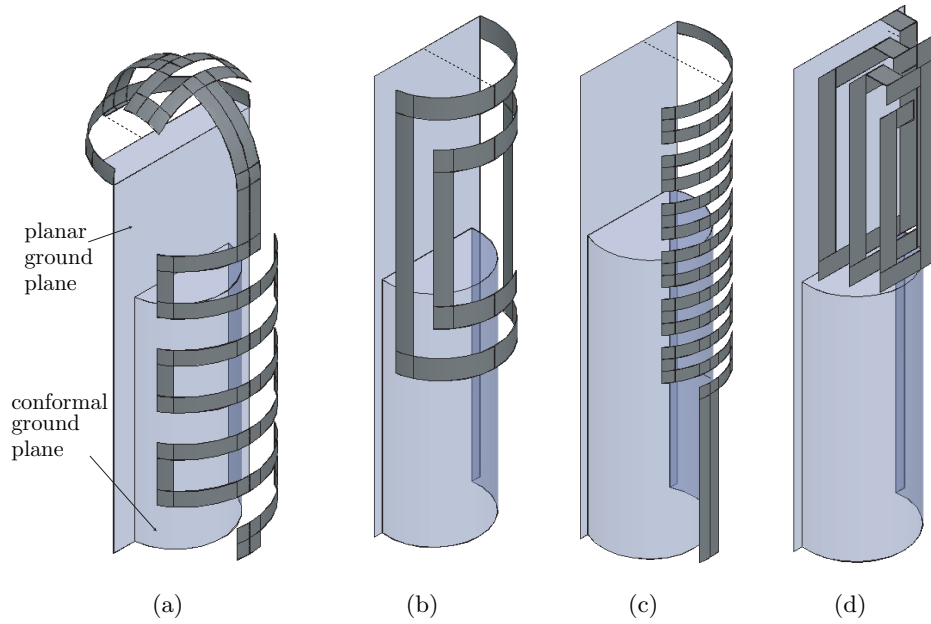
Figure 5.3.: First investigated typologies in free space: (a) spherical, (b) spiral, (c) meander and (d) multilayered spiral. The ground plane (in light color), always consists of a rectangular section and a conformal part (half hollow cylinder), as indicated for the (a) case. Delta-gap excitations are indicated with dashed lines.

An extensive study of the indicated typologies was performed to choose an efficient antenna structure, given the available volume, in free space. Radiation characteristics and the current vector alignments concept [169, 205, 206] were considered to improve the performances of each typology.

Table 5.1 reports the simulated results of these four typologies[*]; only one result per typology, that can be considered as a reference for all the evaluated designs, is given. The single resonant frequency is chosen at around 1 GHz. The dielectric loading effect (due to the presence of dielectric substrates, biocompatible insulation and body phantom that are considered in the second step of the design procedure) will consequently shift the resonant frequency towards

---

[*]Given the importance of the radiation efficiency, values with three decimal digits are reported in this thesis while gain and directivity are always rounded to one decimal in [dB]. That is the reason why different values than what reported can be obtained making the ratio between the gain and the directivity could be evaluated.

lower frequencies, close to the MedRadio band. Only ohmic losses are taken into account (copper 17 μm thick).

Table 5.1.: Comparison of the Radiation Performances for Four Antenna Typologies in Free Space. Maximum Values are Reported for both Gain and Directivity.

Typology	**Frequency** [GHz]	**Gain** [dBi]	**Directivity** [dBi]	e_{rad} [%]
Spherical	1.035	-7.6	1.2	12.882
Spiral	1.029	-3.8	1.8	27.173
Meander	1.038	-7.9	1.3	11.841
Multilayered Spiral	1.058	-1.8	1.8	43.515

The spherical case provides a more accentuated omnidirectional radiation (lowest directivity), without any noticeably efficiency. Thus, we considered the other three typologies, sharing the same antenna dedicated volume indicated in Fig. 5.2, so as to facilitate the radiation in the desired direction.

The spiral design increases the radiation efficiency and directivity compared to the meander case, in agreement with [92, 94, 168]. However, both metallizations of these two typologies (depicted in dark gray in Fig. 5.3) reach over the region dedicated to the battery housing. The very small distance between the ground plane and the metallizations does not facilitate the radiation. On the contrary, the multilayered spiral solution achieves the desired resonance by utilizing only the uppermost part of the volume. This aspect, combined with the spiral conception, provides the most performing typology, both in directivity and efficiency, for the targeted application. Furthermore, the multilayered structure presents the simplest realization process; therefore this typology was selected for the making of the design.

5.2.3. Optimization with Insulation and Body Phantom

The Multilayered Spiral Antenna (MSA) consists in a *pyramidal* assembling to comply with the physical constraints. The structure, illustrated in Fig. 5.4-(a), is made of four stacked dielectric substrates. Roger TMM 10 (alumina) with 35 μm copper metallization was chosen because of its high relative dielectric constant ($\varepsilon'_e = 9.2$) and low loss ($\tan\delta = 0.0022$). The *pyramidal* structure is united with the conformal ground plane, depicted in Fig. 5.4-(b). The latter consists of a metallized half hollow cylinder made of PEEK. As for the previous investigations, the choice of this material was mainly dictated by practical requirements.

At this stage of the design procedure, the antenna was integrated with the biocompatible insulation and inserted into the body phantom. The former is made of PEEK because of its bio-compatibility and excellent mechanical, thermal and chemical resistance. Its thickness was set to just 0.8 mm to maximize the volume for the antenna design, in accordance with the considerations given in Chapter 3. The latter is a cylindrical homogeneous body phantom (diameter: 80 mm, height: 110 mm) with muscle equivalent dielectric properties; dimensions are set based on the model of the human arm presented in [16]. To mimic the targeted subcutaneous implantation, the antenna placement in the cylindrical body phantom was off-centered, as illustrated in Fig. 5.5.

Once the excitation area was set by the physical constraints, we tuned (with a trial and error procedure) the dimensions of the multilayered spiral metallization in order to achieve the desired performance. Fig. 5.6 depicts the final radiator, including its biocompatible housing.

The four substrates are illustrated in Fig. 5.7, while Table 5.2 reports the values all the geometrical parameters. The excitation area is indicated in Figs. 5.6 and 5.7-(a).
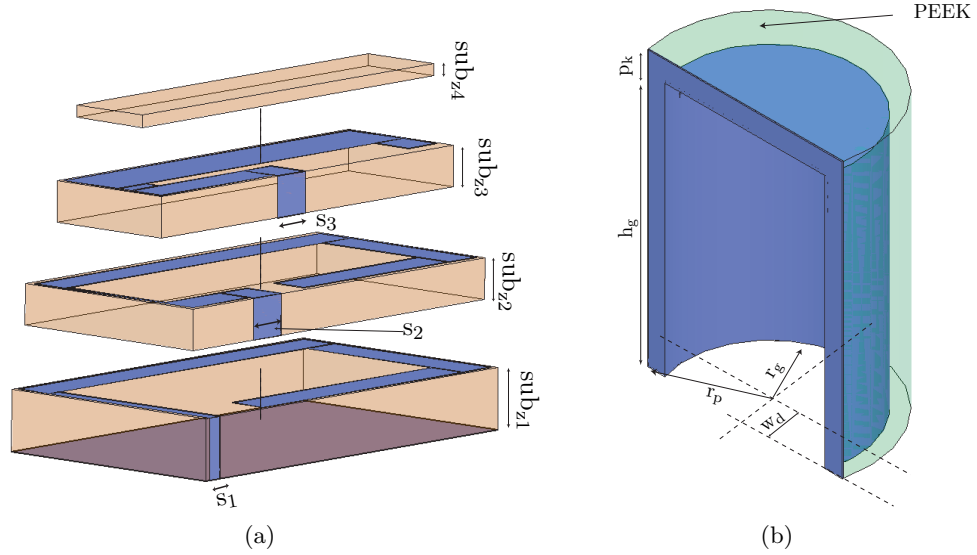

(a)   (b)

Figure 5.4.: Sketch of the main part of the MSA: (a) *pyramidal* assembly, and (b) conformal ground plane. In (a) the metallization is shown in dark color. $s_{1,2,3}$ are the widths of the vertical metallizations whose dimensions are given in Table 5.2. The four substrates are separated for a better comprehension. In (b), half hollow cylindrical structure to house the batteries. Metallization of the PEEK piece is made of copper foil 0.05 mm thick (dark color). Dimensions are given in Table 5.2.
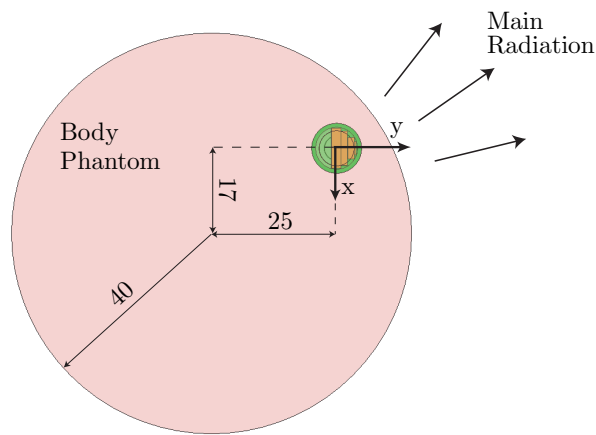
Figure 5.5.: MSA off-centered placement in the homogeneous cylindrical body phantom (at the middle of its height) to mimic subcutaneous implantation. Dimensions in [mm].
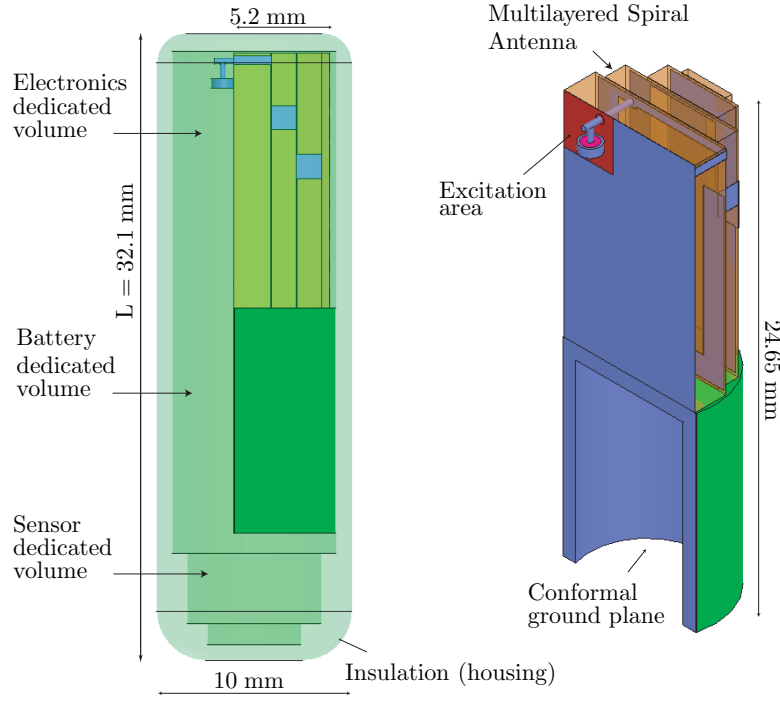
Figure 5.6.: Design of the proposed prototype. The conformal antenna and its housing allow for the placement of all the necessary components for the sensor control, data processing, communication and power supply.
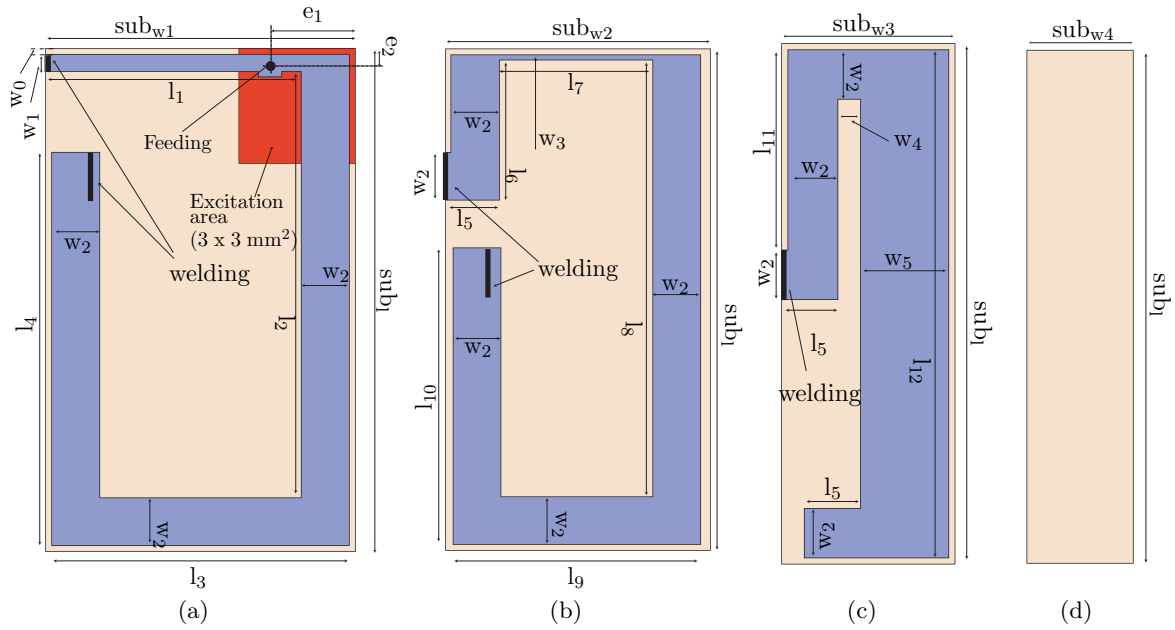
Figure 5.7.: Top view of Roger TMM substrates: (a) first (double layer) with the excitation area, (b) second (single layer), (c) third (single layer) and (d) fourth (no metallization). Metallic lines are depicted in dark color (blue). Parameter dimensions are given in Table 5.2. Thick black lines indicate where the welding (with the vertical metallizations) occurs.

Table 5.2.: Values of the Design Parameters indicated in Figs. 5.4 and 5.7.

Parameter	Value [mm]	Parameter	Value [mm]	Parameter	Value
sub_{w1}	8.000	w_5	2.200	l_6	3.650
sub_{w2}	6.900	l_1	6.617	l_7	4.000
sub_{w3}	4.300	l_2	11.100	l_8	11.400
sub_{w4}	2.7	l_3	7.700	l_9	6.450
sub_{z1}	1.905	l_4	10.250	l_{10}	7.750
sub_{z2}	1.270	l_5	1.400	l_{11}	5.050
sub_{z3}	1.270	w_4	0.550	l_{12}	12.800
sub_{z4}	0.381	e_1	2.200	e_2	0.450
sub_l	13.100	h_g	10.750	p_k	0.800
w_1	0.450	r_p	5.000	r_g	3.500
w_2	1.250	w_d	1.000	w_0	0.150
w_3	0.150	s_1	0.450	$s_{2,3}$	1.250

The overall volume of the implantable device is equal to 2477 mm^3; only approximately 24% of it is allocated to the radiator. This results in an electrically very small antenna in the MedRadio band ($\lambda/13$ referring to the insulation dielectric properties [19, chapter 5]).

5.2.4. Simulated EM Characteristics

Several results, including the analysis of different body phantoms, are presented in the following paragraphs. For an easier understanding, Table 5.3 summarizes the obtained performances.

Matching, Design Robustness against the Batteries and Electronics Presence and Radiation

Reflection coefficients versus frequency, $|S_{11}(f)|$, are plotted in Fig. 5.8. It can be noted that, while the antenna is well matched in the MedRadio frequency range (with a 2.3% relative band), the higher resonance at 2.387 GHz is slightly lower than the targeted 2.45 GHz. Nevertheless, the simulated $|S_{11}(f)|$ shows a wide working band (6% at -10 dB points), that includes a sufficient part of the desired ISM frequency spectrum.

The volumes allocated to the batteries and the circuitry placement "2", depicted in Fig. 5.2, were filled with dielectric and metallic materials [99]. A FR-4 substrate (with microstrip lines) and a copper cylinder were included in the model to mimic the presence of the electronics and power supply. Matching performances are reported in Fig. 5.8. Only 0.5% and 0.17% frequency shifts resulted in the two working bands, with realized gain variations limited to 0.2 dB. These performances confirm the validity of the design, and they are satisfying for the integration of the whole BSN.
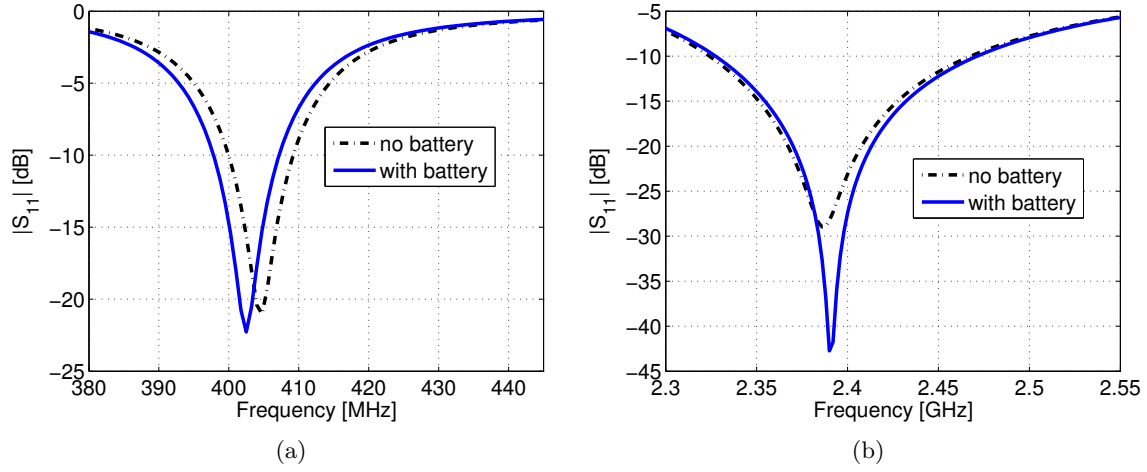
Figure 5.8.: Simulated $|S_{11}(f)|$ against frequency. The effect of the presence of the battery (and electronics) is compared with the reference design (no battery): (a) MedRadio and (b) ISM bands.

3D gain polar plots, without battery, are reported in Fig. 5.9. The maximum gain values are, taking the body phantom into account, -28.8 and -18.5 dBi in the MedRadio and ISM bands, respectively. Despite the higher attenuation of the electromagnetic field in the muscle tissue at higher frequency, the radiator is much more efficient in the ISM band, as its size is electrically larger than in the MedRadio range.
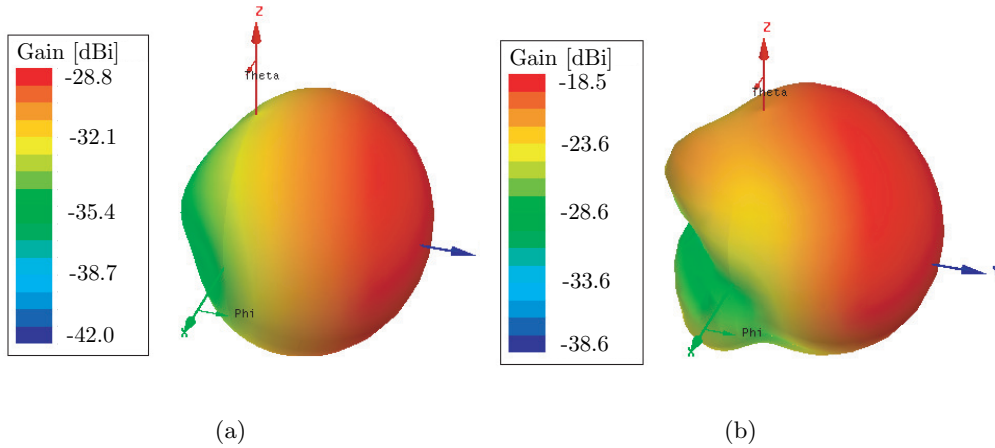
Figure 5.9.: Simulated 3D gain polar plot at: (a) 404.5 MHz and (b) 2.387 GHz. Radiation efficiencies e_{rad} are 0.058 % and 0.530 %, respectively. Coordinate system is the same as in Fig. 5.5.

Surface current distributions are illustrated in Fig. 5.10; as expected, almost the whole multilayered spiral structure is relevant in the MedRadio range while some cold zones (especially on the ground plane) can be identified in the ISM band when the antenna dimensions are electrically larger.
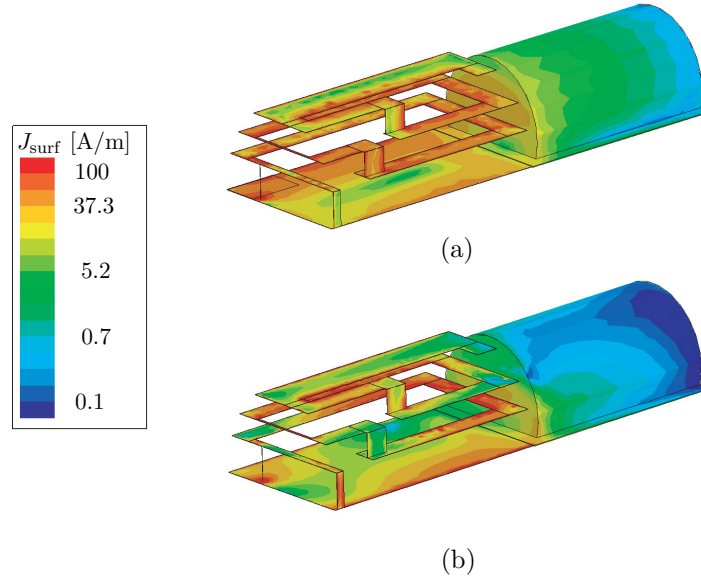
Figure 5.10.: Surface current distributions at (a) 404.5 MHz and (b) 2.387 GHz. Input power: 1 W.

Analysis with Different Body Phantoms

In order to obtain insights about the sensitivity of the proposed design versus different implant locations, two cylindrical body phantoms with the following characteristics were additionally investigated:

- height: 110 mm;

- homogeneous composition with equivalent head model dielectric properties (see Table 2.2) and radius equal to 40 mm;

- 3-layered structure made of muscle-fat-skin (dry) based on[18, 80], whose radii are 32, 36, and 40 mm, respectively. Dielectric properties are reported in Table 2.2.

As the cylindrical body phantom dimensions might be too small for a correct assessment of the performance of the radiator in the MedRadio range, a muscle rectangular cuboid (box) phantom with dimensions based on [18] (i.e., 286 x 584 x 320 [mm]) was considered. In this case the antenna was also placed at the middle of the phantom height and off-centered, 5 mm away from the external surfaces. This antenna location, modeling a targeted placement in the human torso above the hips, is depicted in Fig. 5.11. Electromagnetic performances are reported in Figs. 5.12-5.13 and summarized in Table 5.3.

Despite the variation of the analyzed phantoms, only a difference of 2.3% on the resonant frequency is observed in the MedRadio band, as seen in Fig. 5.12-(a). We also computed the realized gain, i.e, $(1 - |S_{11}(f)|^2) \cdot$ gain, at 404.5 MHz. Values of -28.8, -30.4 and -31.3 dBi were found for the muscle, head and multilayered phantoms, respectively. The 2.5 dB reduction in the multilayered case is mainly due to the resonant frequency shift. Giving explanation for the decreased radiation efficiencies in the two latter models is not an easy task, especially when the radiator is electrically very small. In fact, e_{rad} substantially depends on the nearest surrounding of the antenna (near field coupling), and the transition between the body and the
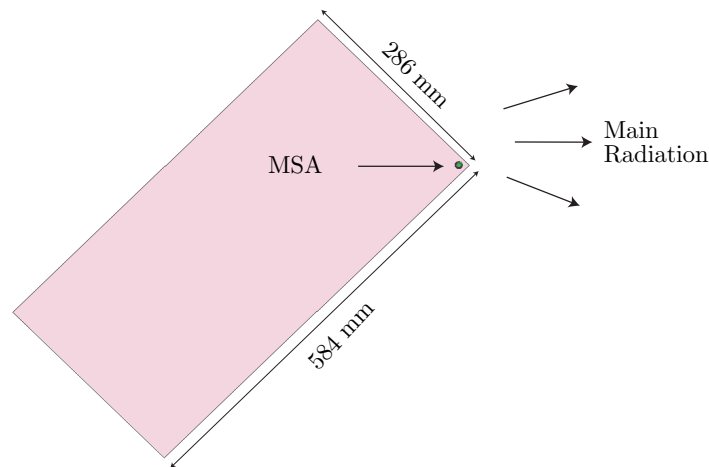
Figure 5.11.: MSA off-centered placement in the homogeneous large box body phantom (at the middle of its height) to mimic subcutaneous implantation. Coordinate system is the same as in Fig. 5.5.
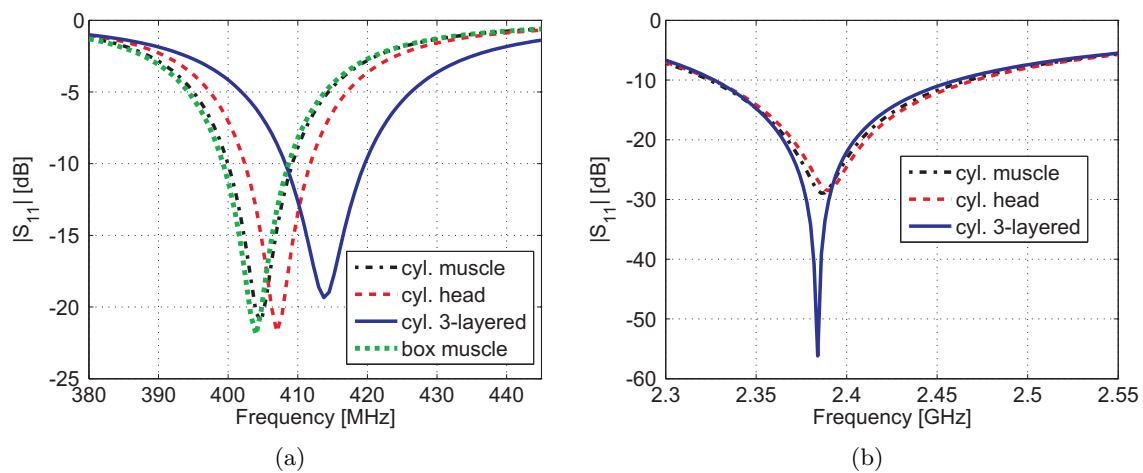
Figure 5.12.: Comparison of simulated $|S_{11}(f)|$ against frequency considering the antenna inserted into different body phantoms in the (a) MedRadio and the (b) ISM bands.

free space as discussed in Chapter 3.

The antenna size is electrically larger in the ISM band compared to the MedRadio case. This involves a lower coupling of the near field with the lossy tissues, which results in a reduced sensitivity to the surrounding environmental conditions; the resonant frequency variation is within 0.3% as shown in Fig. 5.12-(b). Realized gains attain -18.5, -17.7, -16.3 dBi for the muscle, head and multilayered phantoms, respectively. Explanation about the improvement of realized gain versus different body phantoms for the ISM frequency range can be obtained by paying attention to the dielectric characteristics of the investigated models. First of all, dielectric losses: note that the maximum realized gain (and highest efficiency) is found for the multilayered model when the antenna is in close contact with fat tissue that presents the lowest $\tan\delta$ among the selected tissues [20]. Second, let us consider the fixed distance between

the antenna and the external free space (≈ 5 mm). Given a constant resonant frequency (i.e., 2.387 GHz), this distance is electrically smaller when considering the head and multilayered models, as they are constituted by materials with lower permittivities. Thus, the radiated wave undergoes minor attenuation. As previously mentioned, these considerations are not true for the proposed radiator in the MedRadio range, where the higher near field coupling is the main responsible factor of the radiation efficiency.

Only small differences in directivity (-1 dB) and radiation efficiency (+0.02%) are found between the box and the cylindrical body phantoms. A similar realized gain (0.4 dB variation) and pattern (especially in the desired direction of radiation) are obtained between the two different modeled geometries as appreciable in Fig. 5.13. It is worth noting that the numerical analysis of the cylindrical body phantom is six times more efficient than the large box case.
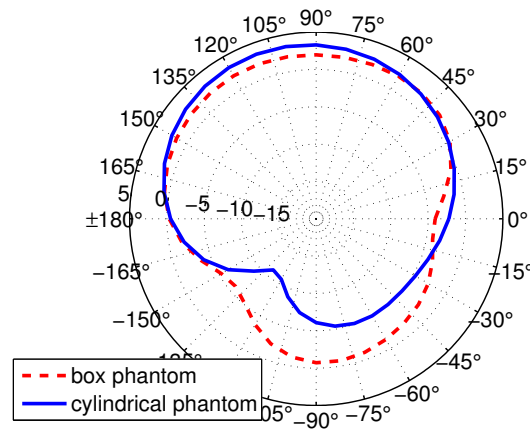
Figure 5.13.: Simulated radiation patterns in [dBi] on the horizontal plane when the radiator is inserted into the box and cylindrical body phantoms at 404.5 MHz. The origin of the coordinate system, shown in Fig. 5.5-(a), is always placed at the center of the antenna [25].

These results show the satisfactory robustness of the design versus the variation of the surrounding environmental conditions, as well as the suitability of the chosen cylindrical phantom dimensions for the targeted application. Hence, quite stable performances can be expected for realistic implant locations of the whole integrated telemetry system.

The Specific Absorption Rate was computed at the transmitting frequency, i.e, in the MedRadio band. With a mass density equal to $1.04\ 10^3$ kg/m^3 [18], we evaluated the peak spatial-average 1 g SAR at the resonance frequency of 407 MHz in the equivalent head phantom, in accordance with [86]. The obtained value, with a 1 W input power, is 289 W/kg. This implies that the antenna can be fed with signal up to 5.5 mW (7.4 dBm) and still meet the IEEE recommended value of 1.6 W/kg per 1 g averaging [14]. This analysis, although obtained in rough approximation of the human body, gives a preliminary idea on the power levels that are acceptable for the MSA. It is worth noting that the input power of the entire system is less than 0 dBm, thus complying with safety requirements.

Table 5.3.: Summary of the Simulated Results of the Proposed Radiator in Different Body Phantoms. Maximum Values are Reported for both Gain and Directivity.

Phantom at 404.5 MHz	Real. Gain [dBi]	Directivity [dBi]	e_{rad} [%]
cyl. muscle	-28.8	3.6	0.058
cyl. muscle & battery	-28.6	3.6	0.060
cyl. head	-30.4	3.5	0.040
cyl. 3-layered	-31.3	3.6	0.041
box muscle	-28.4	2.6	0.078
at 2.387 GHz			
cyl. muscle	-18.5	4.2	0.530
cyl. muscle & battery	-18.6	4.3	0.507
cyl. head	-17.7	4.2	0.647
cyl. 3-layered	-16.3	4.2	0.883

5.3. Realization

Figs. 5.14-5.15 show the built MSA and its housing. The manufacturing of ROGER TMM substrates followed standard microstrip fabrication procedures. The assembling (stacking) of the *pyramidal* geometry of Fig. 5.4, connected by vertical copper-beryllium pieces, was ensured by a two-component epoxy adhesive. The resonance frequency of the antenna is affected by the adhesive ($\varepsilon'_e = 3$, $\tan \delta = 0.001$, thickness: 35 μm) [210]; the presence of this material was included in the numerical analysis previously presented. The same glue
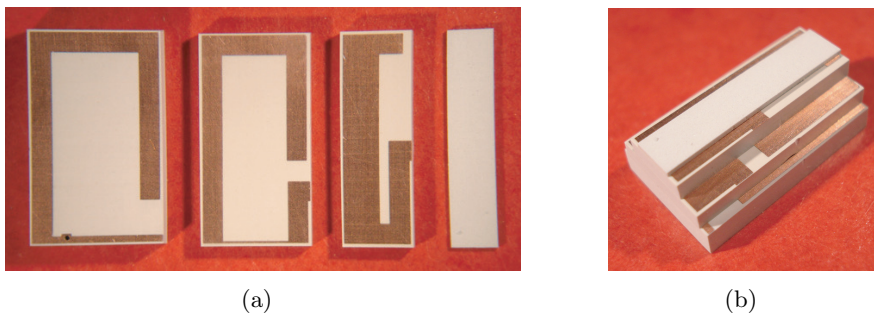
Figure 5.14.: Manufactured prototype: (a) four substrates with the desired metallic lines and (b) multilayered spiral assembly.

was used to fix the multilayered spiral structure to the conformal ground plane. The latter consists of a coated PEEK piece with the use of a copper foil 50 μm thick. The whole construction process is rather delicate but it does still allow good repeatability, as discussed in Section 5.4.2. The prototype, including housing and without batteries, weights 2.54 g.

The realization of the electronics components and the packaging of the complete BSN is presented in the next chapter.

(a)   (b)

(c)
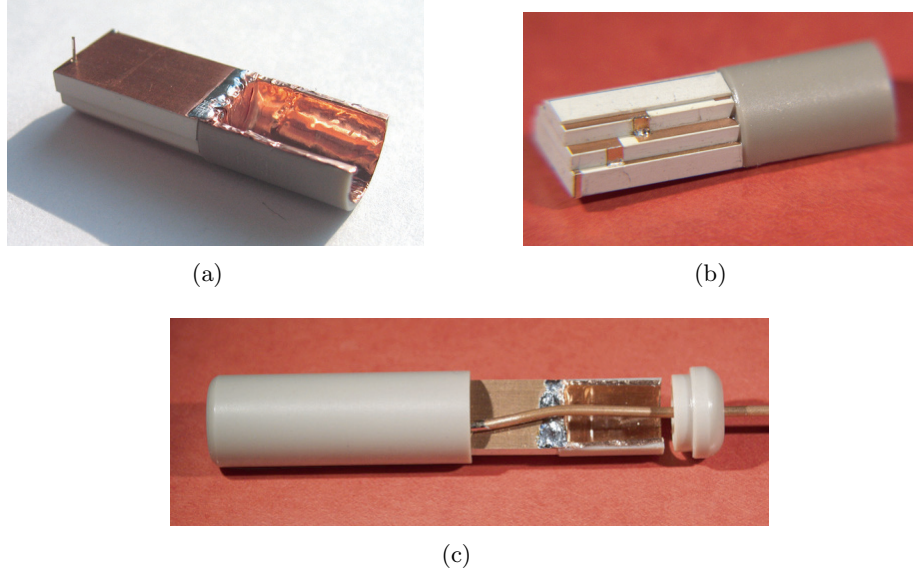
Figure 5.15.: Manufactured prototype: (a)-(b) the conformal ground plane and (c) final prototype assembling including housing and closing cap. The coaxial feeding cable is present only for testing purposes.

5.4. In Vitro Characterization

Experimental results of realized antennas are described in this section. The radiators, inserted into the cylindrical homogeneous phantom, were measured in the absence of the active components. After the realization and characterization of the first prototype, another radiator was built to improve the calibration of the electromagnetic simulation and, consequently, the EM performance of the model itself.

5.4.1. First Prototype

Fig. 5.16-(a) depicts the satisfactory match between prediction and experiment in the MedRadio band. On the contrary, the comparison between simulated and measured performances in the ISM band presents a remarkable difference, as illustrated in Fig. 5.16-(b). Nonetheless, the experimental result shows how the frequency behavior is still useful ($|S_{11}(f)|$ equals to -10 dB at 2.40 GHz) As presented in the next section, the discrepancy is mainly caused by the difference between the dielectric properties of simulated and actually used materials.

The exact placement of the antenna inside the body phantom, the coaxial feeding cable, and the liquid phantom itself do influence and increase the difficulty of radiation measurement in the anechoic chamber. Therefore, only the measurement of the horizontal radiation pattern was performed in the ISM band, as reported in Fig. 5.17, obtaining an acceptable agreement with the theoretical predictions.
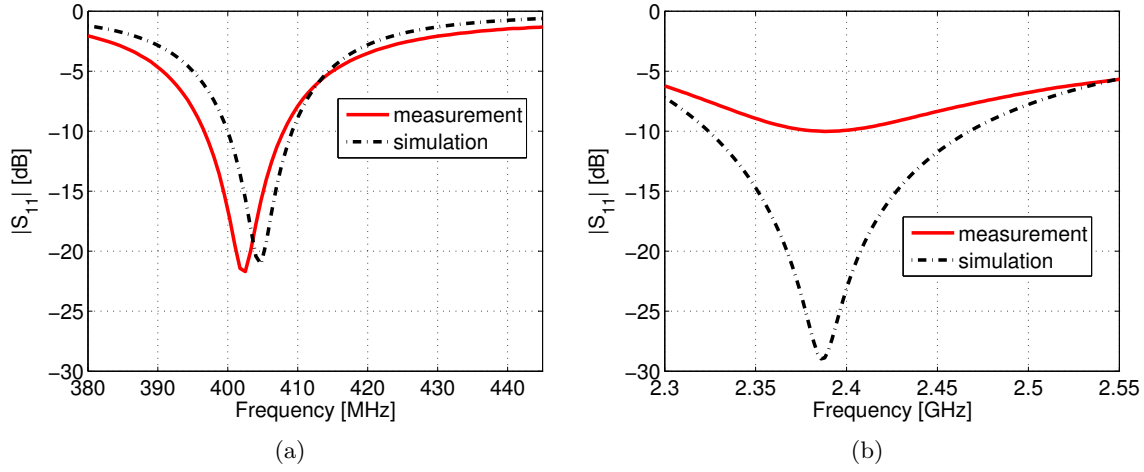
Figure 5.16.: Simulated and measured $|S_{11}(f)|$: (a) MedRadio and (b) ISM bands. Measurement in the MedRadio band considers the de-embedding of the feeding cable effect discussed in Chapter 7.
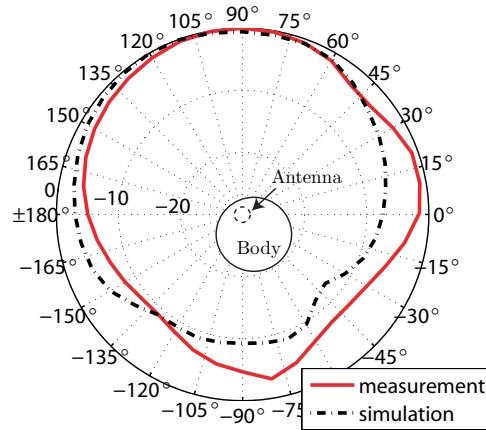
Figure 5.17.: Simulated and measured normalized radiation patterns [dBi] on the horizontal plane (vertical polarization) at the measured resonant frequency (i.e., 2.3945 GHz). Maximum value corresponds to 4.2 dBi. The cylindrical body phantom and the antenna relative positions are indicated at the center of the diagram.

5.4.2. Improved Prototype

The first experimental results allowed the improvement of the calibration of the EM simulation. The numerical analysis was modified as follows: first, different adhesive dielectric properties ($\varepsilon'_e = 4$, $\tan\delta = 0.001$, thickness: 30 μm) were considered in the ISM band; second, the conductivity of vertical copper-beryllium metallizations (see Fig. 5.4) was set to $\sigma'_e = 14 \cdot 10^6$ S/m, while copper conductivity was reduced to $29 \cdot 10^6$ S/m. Furthermore, some geometrical modifications were considered for both the simulated and realized prototype, that are reported in Table 5.4. The final design has a total length of 32.1 mm.

Table 5.4.: Values of the Parameters, indicated in Figs. 5.4-5.7, that Differ from the Ones in Table 5.2 for the Improved Prototype.

Parameter	Value [mm]	Parameter	Value [mm]
sub_{w4}	2.9	h_g	10.650
s_1	1.600	r_g	3.550

Simulated and measured $|S_{11}(f)|$ are reported in Fig. 5.18. Maximum frequency deviations of less than 1% are found in both the MedRadio and the ISM bands. The desired matching, that is better than -10 dB, is achieved for the two working frequencies. The close match found in the ISM band shows the importance of the aforementioned modifications. The new design differs only slightly from the first one (gain = -29.4, -17.7 dBi directivity = 3.5, 4.4 dBi, e_{rad} = 0.051, 0.605% in the MedRadio and ISM band, respectively) , hence results about radiation performances, robustness against of the presence of batteries and effect of different body phantoms are not reported to avoid redundancy.

(a)   (b)
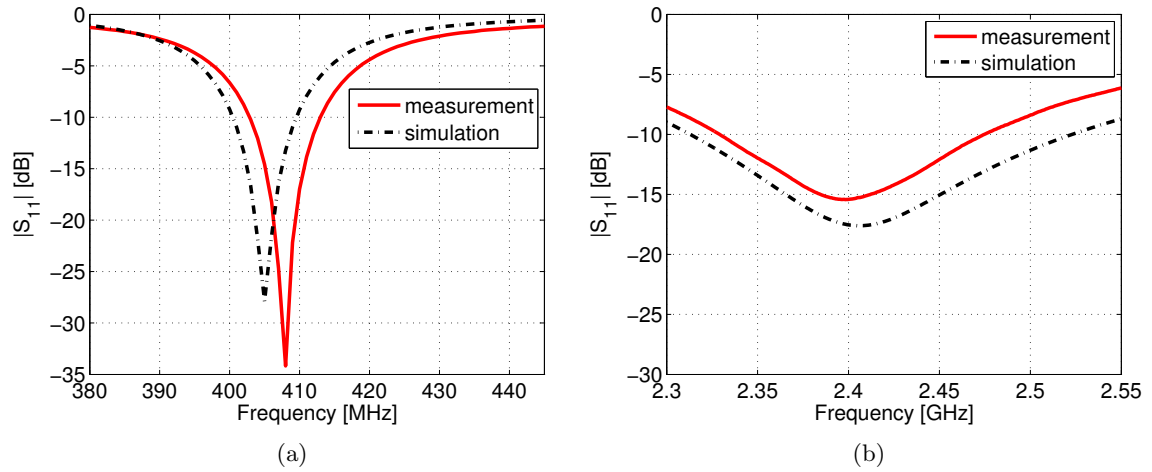
Figure 5.18.: Simulated and measured $|S_{11}(f)|$ for the improved MSA: (a) MedRadio and (b) ISM bands.

5.4.3. Tunability

The MSA presents a broad band behavior in the ISM range, but only a 2.3% bandwidth (at -10 dB) is available in the MedRadio spectrum. Therefore, it is useful to identify a simple way to fine tune the performances in the lower frequency range to withstand fabrication tolerances or inaccuracies. The simulated results illustrated in Fig. 5.19 show that varying the width of the 4th substrate (sub_{w4}, indicated in Fig. 5.7) does affect the MedRadio band resonance without modifying the higher frequency characteristic. It can be appreciated that the presence of the 4th substrate shifts the lower resonance down of around 1 MHz / 0.2 mm. Moreover, this substrate is easily accessible, and it is added at the last step of the fabrication process. This makes the modification of its width possible to counterbalance undesired inaccuracies, so as to obtain the sought-after performances. In agreement with the previous considerations, we realized two prototypes with only three substrates constituting the *pyramidal* structure.
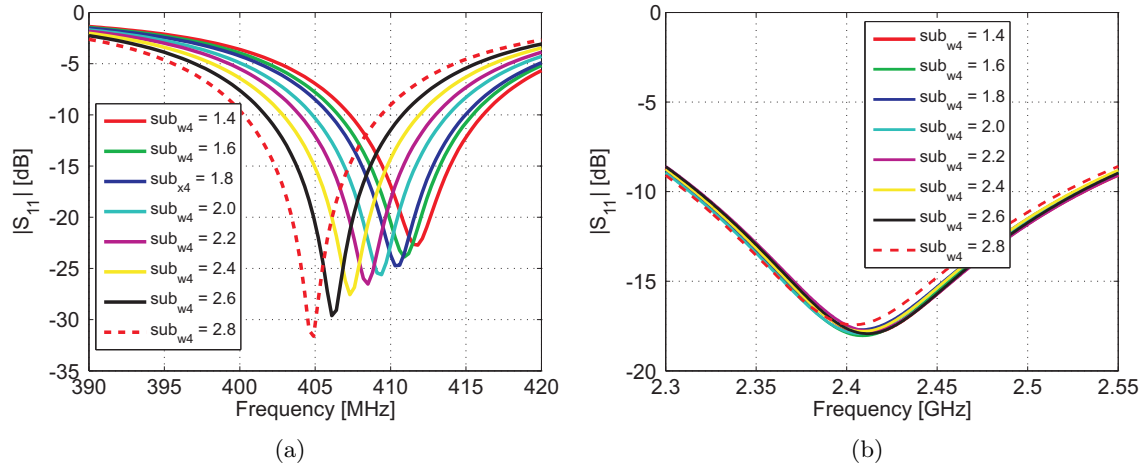
Figure 5.19.: Simulated $|S_{11}(f)|$ varying sub$_{w4}$ (values in [mm]) when the radiator is inserted into the cylindrical homogeneous body phantom: (a) MedRadio and (b) ISM bands.

Obviously, this choice implies a higher resonant frequency, but this intermediate step allowed us to verify the quality of the fabrication procedure. Fig. 5.20-(a) reports the comparison among the simulated and measured matching performance in the MedRadio band. It can be noted that both prototypes do not match the predicted results, as they presents lower resonant frequencies (of 9 MHz) than the expected one. Keeping in mind the results reported in Figs. 5.19-(a) and 5.20-(a), the 4th substrate was then added with sub$_{w4}$ equal to 2.2 mm. This value aimed at shifting the resonance frequencies in the middle of the MedRadio band. The agreement between targeted and measured results illustrated in Fig. 5.20-(b) confirmed the selected choice.
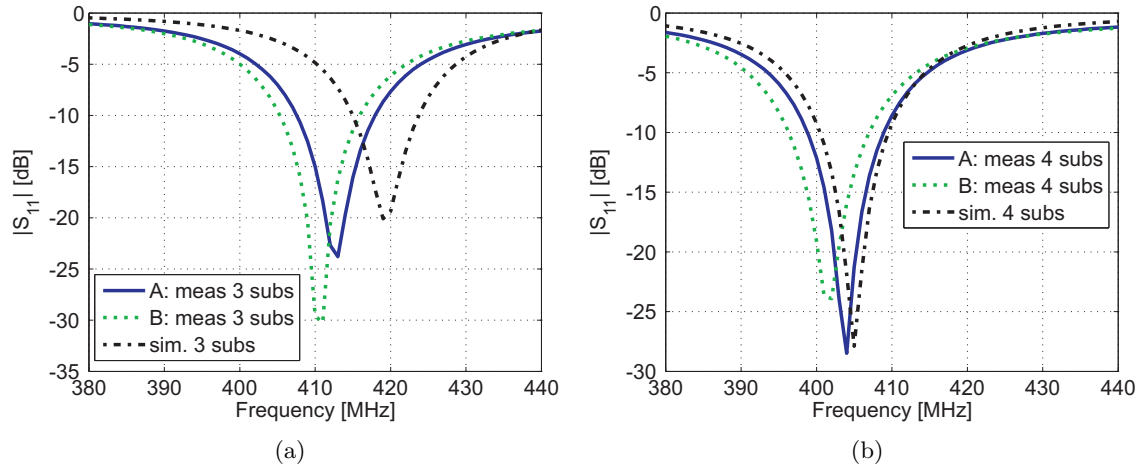
Figure 5.20.: Simulated and measured $|S_{11}(f)|$ considering (a) three and (b) four substrates in the *pyramidal* assembling in the MedRadio band. Simulated and measured results in (b) are obtained with sub$_{w4}$ equal to 2.7 and 2.2 mm, respectively. The radiators are inserted into the cylindrical homogeneous body phantom.

Despite the fact that some fabrication inaccuracies affected also the ISM behavior, adequate performances were still obtained in the higher targeted frequency, as illustrated in Fig. 5.21.
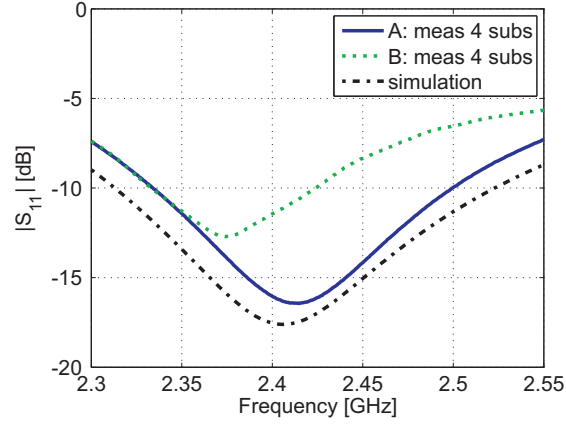
Figure 5.21.: Measured $|S_{11}(f)|$ considering all four substrates in the *pyramidal* assembling in the ISM band when the radiators are inserted into the cylindrical homogeneous body phantom

5.5. Advanced Numerical Investigations

The design of the improved MSA was further numerically investigated to evaluate its performances in a real human body model and to show the versatility of its conception.

5.5.1. Virtual Family

The performances of the MSA were investigated considering the *Duke* model belonging to the Virtual Family [49, 50]. This numerical analysis was performed with the commercial software SEMCAD X [79].

Figure 5.22.: Virtual Family models [49, 50]. Image from http://www.itis.ethz.ch/research/virtual-population/virtual-population-project/.

The MSA was first simulated by SEMCAD X with the same cylindrical homogenous phantom for two main reasons. First, to validate the SEMCAD analysis against the HFSS result (thus to also appreciate the differences between the two software). Second, a fair comparison between the different body phantoms, calls for the use of the same software as unavoidable discrepancies are present due to different solving, meshing techniques, etc.

Details of the comparison are given in Appendix C.

The MSA made of PEC (as explained in Appendix C) was implanted in *Duke*. The antenna was located in the human torso above the hips, as depicted in Fig. 5.23.
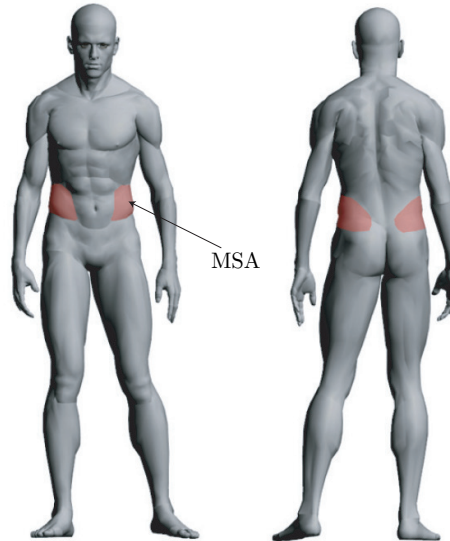
Figure 5.23.: Targeted implantation site (in red) for the MSA.

For an easier understanding of the implantation site, cutting views along the tree main axis are reported in Figs. 5.24 and 5.25. These images allow to appreciate the variety of tissues modeled in *Duke*. Two different positions were considered: intra-muscular (*Duke* 1) and subcutaneous (*Duke* 2) locations, as depicted in Fig. 5.24-(c). One can appreciate that the radiator is completely surrounded by muscle tissue in Fig. 5.24-(c).*Duke* 1, while fat and skin tissues are present in the closest proximity of the antenna in Fig. 5.24-(c).*Duke* 2.
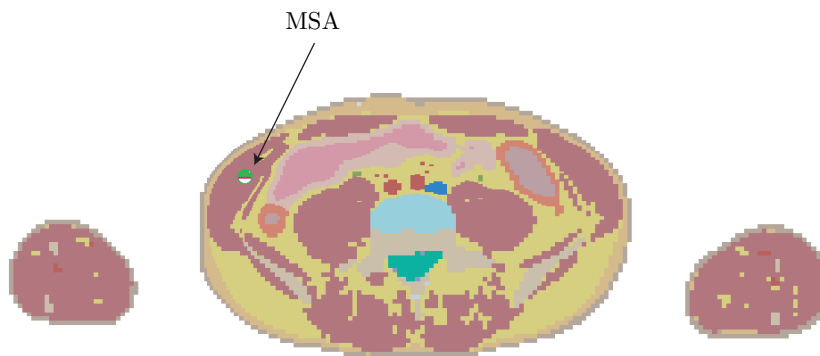
Figure 5.24.: Top cutting view of the *Duke* model at the MSA location. The whole phantom is voxeled with a 3 mm precision, and the accuracy is increased to 1 mm in the close proximity of the radiator. Parts of the phantom are not depicted as not intersected by the cutting plane.
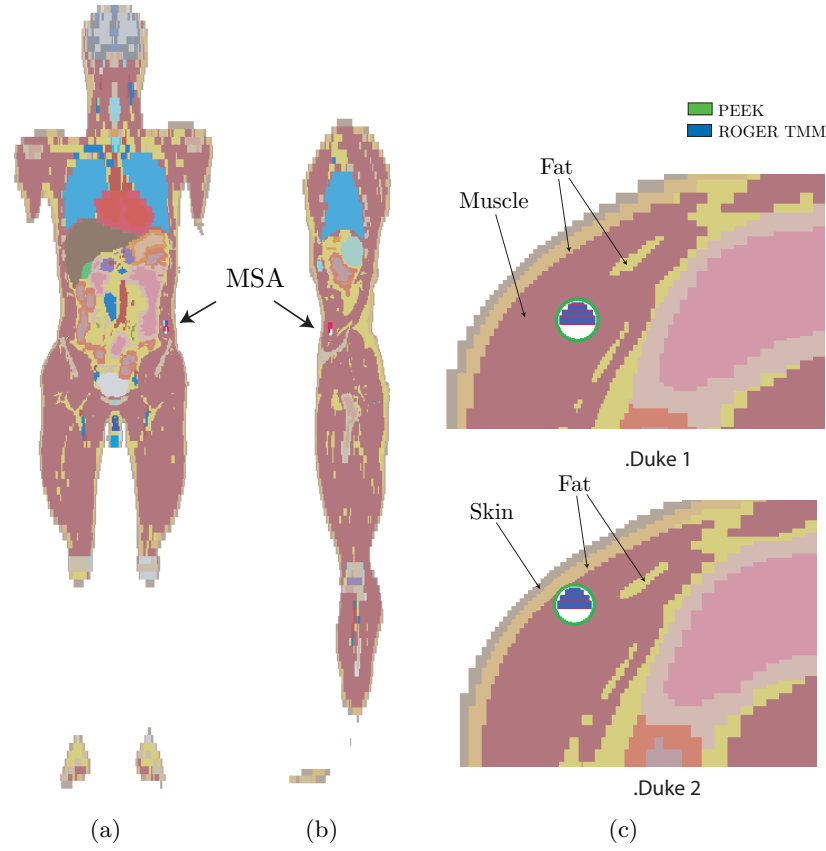
Figure 5.25.: Cutting views of the *Duke* model at the MSA locations: (a) front and (b) side. Details are depicted in (d); the antenna depth is $\simeq 12$ mm and $\simeq 5$ mm in (c).1 and (c).2, respectively.

The obtained reflection coefficients, considering the intra-muscular location (*Duke* 1) and the homogenous phantom are reported in Fig. 5.26. The results are almost superimposed in the MedRadio range, while a resonant frequency variation smaller than 1% is registered in the ISM band. These performances confirm the validity of the choice of the cylindrical homogeneous phantom for the targeted realistic location.

The matching results between when the MSA is implanted in the *Duke* 2 location and the multilayered cylindrical phantom are slightly further apart, as illustrated in Fig. 5.27. However, the registered differences, within 1.5% in both working bands, still confirm the effectiveness of the simplified models also for such an implantation site.
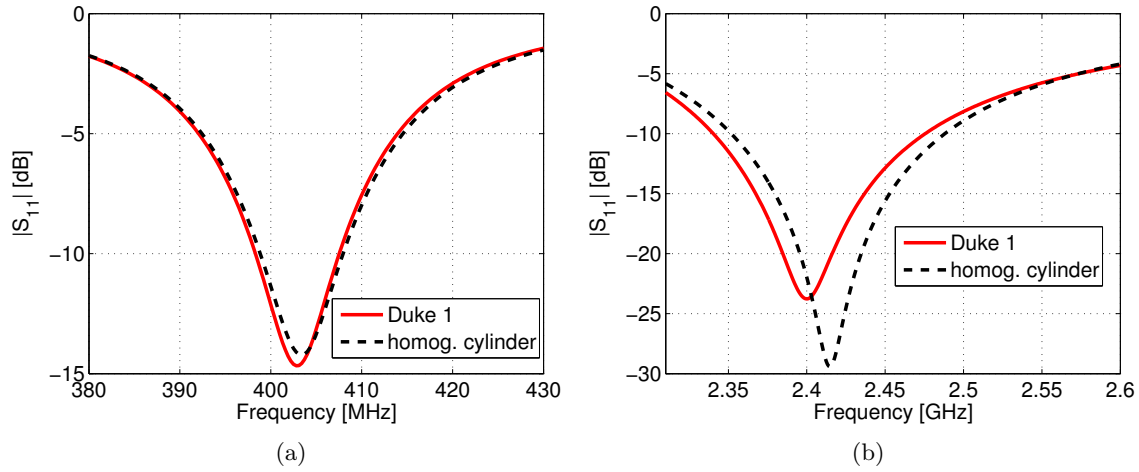
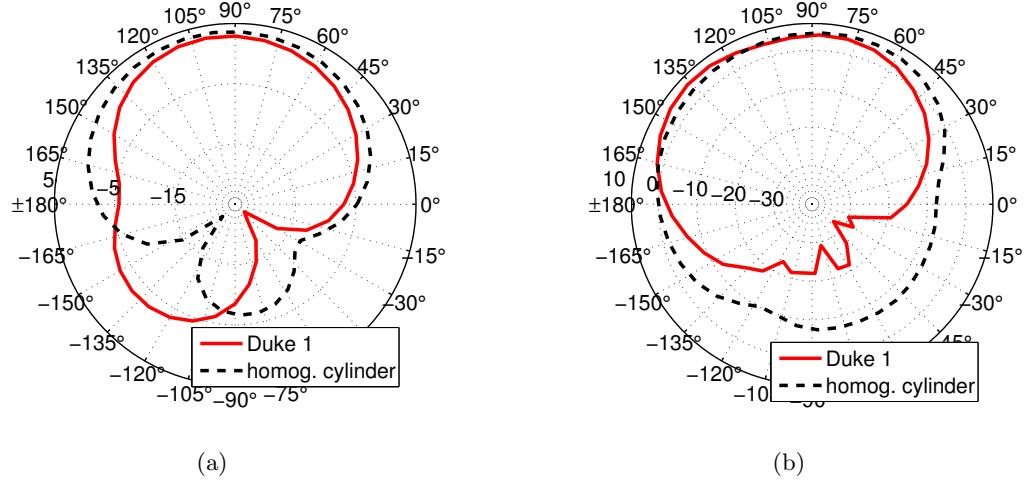**Figure 5.26.:** Simulated $|S_{11}(f)|$ by SEMCAD X in the homogeneous cylindrical body phantom and at the intra-muscular location (*Duke* 1) : (a) MedRadio and (b) ISM bands. All analysis consider non dispersive properties of the tissues in the investigated bands.
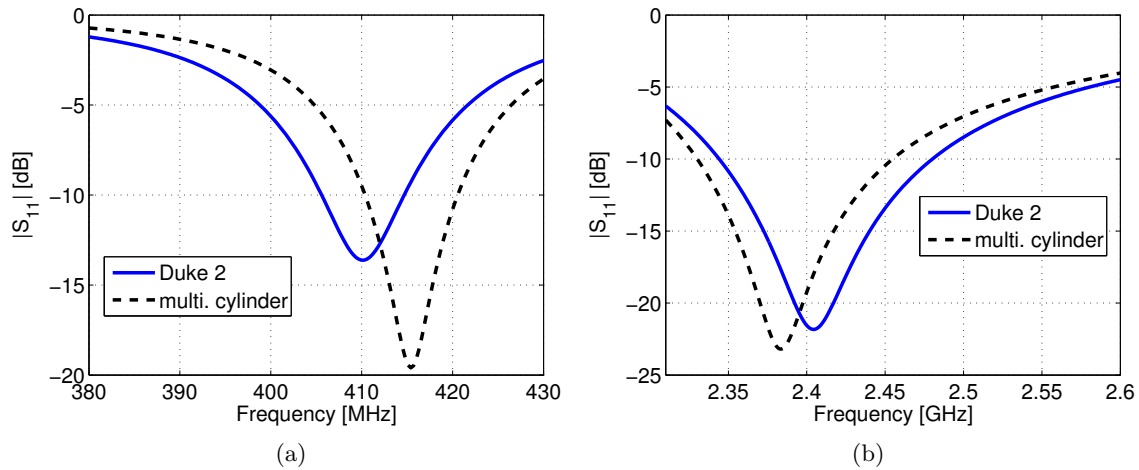
Figure 5.27.: Simulated $|S_{11}(f)|$ by SEMCAD X in the multilayered cylindrical body phantom and at the subcutaneous location (*Duke* 2) : (a) MedRadio and (b) ISM bands. All analysis consider non dispersive properties of the tissues in the investigated bands.

As expected, larger discrepancies are found when focusing on the radiation performances. The polar diagrams of the directivity on the horizontal planes are reported in Figs. 5.28 and 5.29 for both locations. Maximum values always differ of only 0.1 and 1.2 dB in the MedRadio and ISM band, respectively, but dissimilar back scatterings are registered because of the shadowing of the real model. Focusing on the backward radiation, i.e., towards the body, differences up to 20 dB are found.

(a)   (b)

Figure 5.28.: Simulated radiation patterns in [dBi] by SEMCAD X in the homogeneous cylindrical body phantom and at the intra-muscular location (*Duke* 1) : (a) 402.8 MHz and (b) 2399.2 MHz.

(a)   (b)
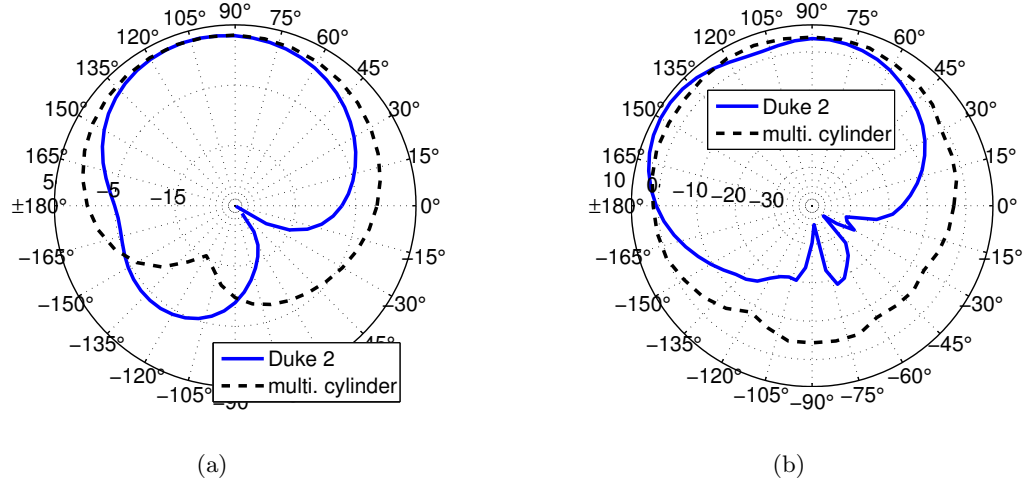
Figure 5.29.: Simulated radiation patterns in [dBi] by SEMCAD X in the multilayered cylindrical body phantom and at the subcutaneous location (*Duke* 2) : (a) 410.2 MHz and (b) 2404.0 MHz.

Table 5.5 summarizes all the radiation performances evaluated with the *Duke* model, while 3D gain graphs are depicted in Fig. 5.30 for the intra-muscular implantation site. Maximum gain values equal to -30.2 and -17.2 dBi in the MedRadio and ISM bands, respectively, are

registered for the intra-muscular location. As expected, the minor depth considered for the subcutaneous location results in higher gain values (+1.5 and +2.9 dB, respectively). In agreement with what observed previously observed via the radiation pattern analysis and in Chapter 2 (Section 2.3), the presence of the realistic model is confirmed to affect the directivity of the implanted antenna. That is why high directivity values are noticed, especially in the ISM band, in Table 5.5.

In conclusion one can appreciate that, despite the differences among patterns and radiation efficiencies, maximum gain values in the desired off-body directions are comparable with the results obtained in the simplified body phantoms. It is worth reminding that the EM performances, taking also into account the fact that the numerical analysis considers PEC, do still guarantee a robust operation in the targeted 2 m range.

Table 5.5.: Simulated Radiation Results of the Multilayered Spiral Antenna obtained with SEMCAD X. Maximum Values are Reported for both Gain and Directivity.

Phantom	Frequency [MHz]	Gain* [dBi]	Directivity* [dBi]	e_{rad}* [%]
Duke 1	402.8	-30.2	4.7	0.032
Duke 2	410.2	-28.7	4.8	0.044
Duke 1	2399.2	-17.2	7.0	0.390
Duke 2	2404.0	-14.3	7.1	0.734

*All these values are obtained with the MSA made of PEC.

(a)   (b)
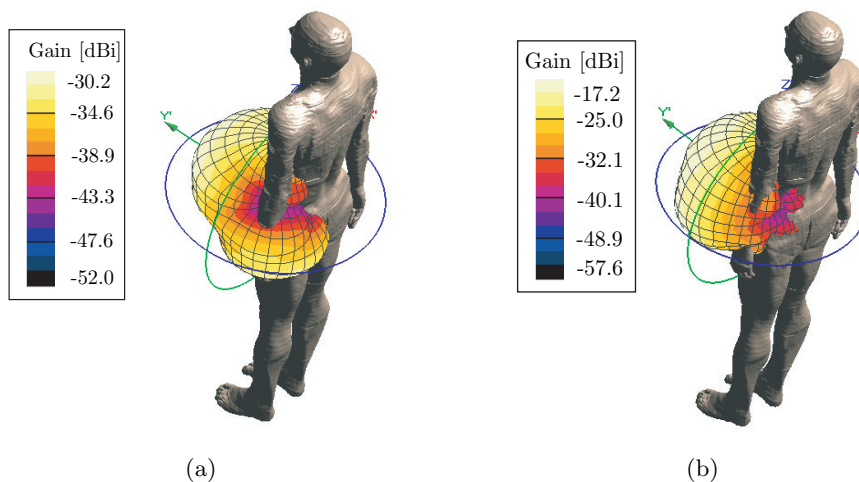
Figure 5.30.: Simulated 3D gain polar plots including body losses for the intra-muscular location (*Duke* 1): maximum gain equals to (a) -30.2 dBi at 402.8 MHz and to (b) -17.2 dBi at 2399.2 MHz. Similar 3D plot are obtained for the subcutaneous placement (*Duke* 2); in this case maximum gain equals to (a) -28.7 dBi at 410.2 MHz and to (b) -14.3 dBi at 2404.0 MHz.

The Specific Absorption Rate was computed with the MSA implanted in the *Duke* model.

The highest value was registered for the subcutaneous location (*Duke* 2). The peak spatial-average (1 g) SAR, with a 1 W input power, is 189 W/kg. This implies that the antenna can be fed with signal up to 8.5 mW (9.3 dBm) and still meet the IEEE recommended value of 1.6 W/kg for 1 g averaging [14]. We note that the prediction in the homogeneous phantom provides higher SAR values (289 W/kg), confirming that the analysis with a homogeneous model tends to overestimate the SAR [102].

5.5.2. Versatility[†]

The MSA dimensions can be ulteriorly reduced, hence showing the versatility of the design vs. different size/packaging requirements. The MSA consists in a design assembled in a *pyramidal* structure (made of four substrates), and a conformal ground plane strictly related to the battery presence. As the multilayered structure is the most active part of the antenna, shortening the conformal ground plane -h_g in Fig. 5.31- has relatively small effects on the resonant characteristics.
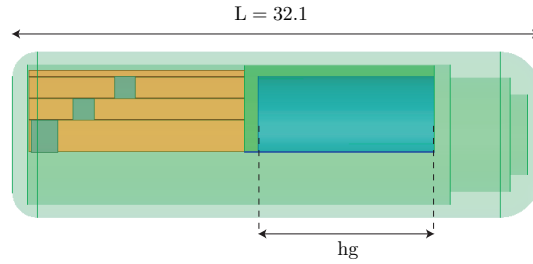
Figure 5.31.: Sketch of the MSA antenna indicating the L and hg parameters. Dimensions in [mm].

Simulated reflection coefficients, $|S_{11}(f)|$, and evaluated performances when reducing h_g are reported in Fig. 5.32 and Tables 5.6 and 5.7, respectively.
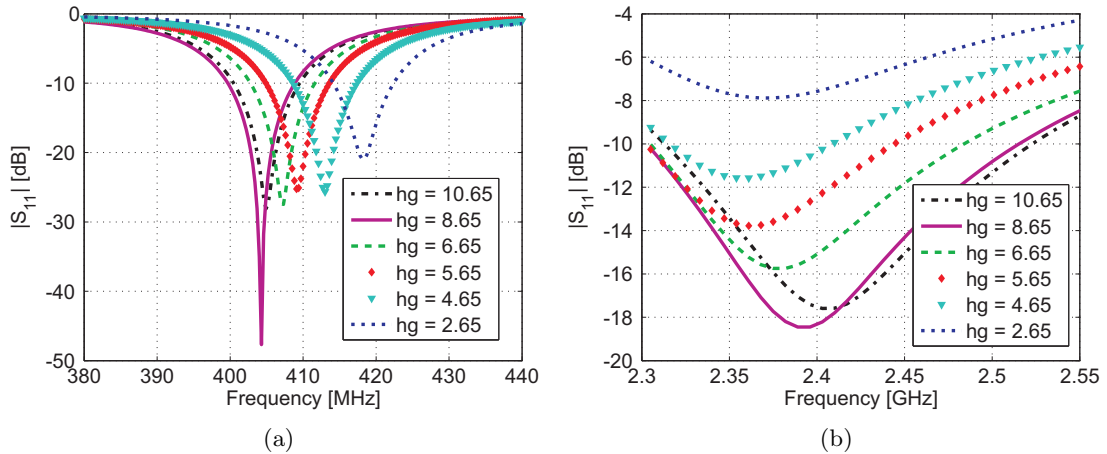
Figure 5.32.: Simulated $|S_{11}(f)|$ reducing h_g (values in [mm]) while the radiator is inserted into the cylindrical homogeneous body phantom: (a) MedRadio and (b) ISM bands.

[†]- F. Merli, L. Bolomey, J. F. Zürcher, E. Meurville and A.K. Skrivervik, "Versatility and tunability of an implantable antenna for telemedicine," in *Proc. 5*[th] *European Conference on Antennas and Propagation (EuCAP 2011)*, Rome, Italy, Apr. 11–15, 2011.

One can notice that resonance frequencies variations (within 4%) are around one order of magnitude smaller than the corresponding geometrical variation. Moreover, the ground plane reduction has no relevant effect on the matching values in the lower frequency spectrum $(\min |S_{11}(f)|$ always lower than -20 dB).

Table 5.6.: Electromagnetic Performances versus h_g and L reduction in the MedRadio Frequency Range. Relative Variations refer to the L = 32.1 mm case.

h_g [mm]	L [mm]	var.	Frequency [MHz]	var.	Gain [dBi]	Directivity [dBi]	e_{rad} [%]
10.65	32.1	0%	404.9	0%	-29.4	3.5	0.051
8.65	30.1	-6%	404.3	-0.1%	-30.3	3.4	0.042
6.65	28.1	-12%	407.3	+0.6%	-30.8	3.3	0.038
5.65	27.1	-15%	409.1	+1.0%	-31.1	3.3	0.037
4.65	26.1	-18%	413.0	+2.0%	-31.2	3.2	0.036
2.65	24.1	-25%	418.1	+3.3%	-31.5	3.0	0.036

Table 5.7.: Electromagnetic Performances versus h_g and L reduction in the ISM Frequency Range. Relative Variations refer to the L = 32.1 mm case.

h_g [mm]	L [mm]	var.	Frequency [GHz]	var.	Gain [dBi]	Directivity [dBi]	e_{rad} [%]
10.65	32.1	0%	2.406	0%	-17.7	4.4	0.605
8.65	30.1	-6%	2.391	-0.6%	-18.2	4.7	0.506
6.65	28.1	-12%	2.379	-1.1%	-19.7	4.6	0.373
5.65	27.1	-15%	2.363	-1.8%	-20.7	4.5	0.302
4.65	26.1	-18%	2.358	-2.0%	-21.7	4.4	0.242
2.65	24.1	-25%	2.371	-1.5%	-23.5	4.5	0.158

A different behavior occurs in the ISM band. In fact, minimum reflection coefficients are obtained towards lower frequencies while shortening h_g, and $|S_{11}(f)|$ increase up to -8 dB as illustrated in Fig. 5.32-(b). The reason behind this is that the decrease of h_g implies a reduction of the real part of the input impedance in the ISM band as appreciable in Fig. 5.33). Consequently, the best matching occurs towards the closest anti-resonance, at 2.19 GHz, characterized by a steep increase of the input resistance [211].

These results show that the conception of the proposed MSA allows for different packaging and power supply requirements. Indeed, the reduction of 25% of its length can be afforded without jeopardizing its working behavior. Thus, only minor modifications are necessary to counterbalance such a modification. Furthermore, it is worth reminding that the dedicated volume for the bio-sensors or actuators makes the use of the MSA for several applications possible.
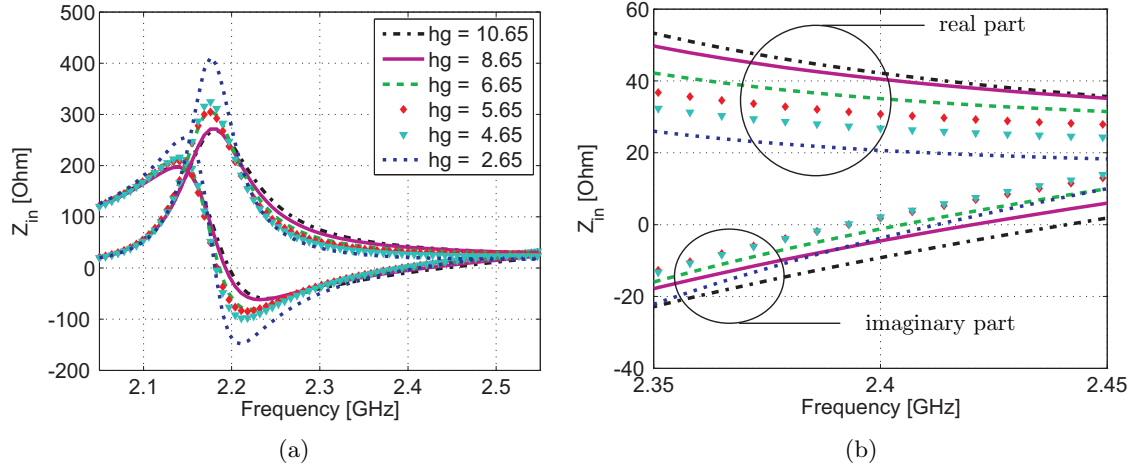
Figure 5.33.: Simulated input impedances against frequency in the ISM band reducing h_g (values in [mm]) while the radiator is inserted into the cylindrical homogeneous body phantom: in (a) it can be appreciated the anti-resonance at around 2.19 GHz while a zoomed detail is reported in (b) focusing on the 2.35-2.45 GHz frequency spectrum.

Further Miniaturized Design

To confirm the previous consideration, we modified the MSA to reach overall dimensions as small as 10 x 8.8 x 20 [mm], including the biocompatible casing. Minor modifications of the metallic strips in the *pyramidal* structure, extensions of the ground plane with vertical parts, and the movement of the excitation point are all that are necessary to reach the desired performances with the shortened antenna, with the feeding position still within the area that was set by the physical constraints -indicated in Fig. 5.7- and a casing able to house the developed electronics[††]. The presence of the vertical ground plane parts is mandatory from the EM point of view, as they counterbalance the decrease of the real part of the input impedance in the ISM band due to the shortening of the ground plane. The new design is depicted in Fig. 5.34.
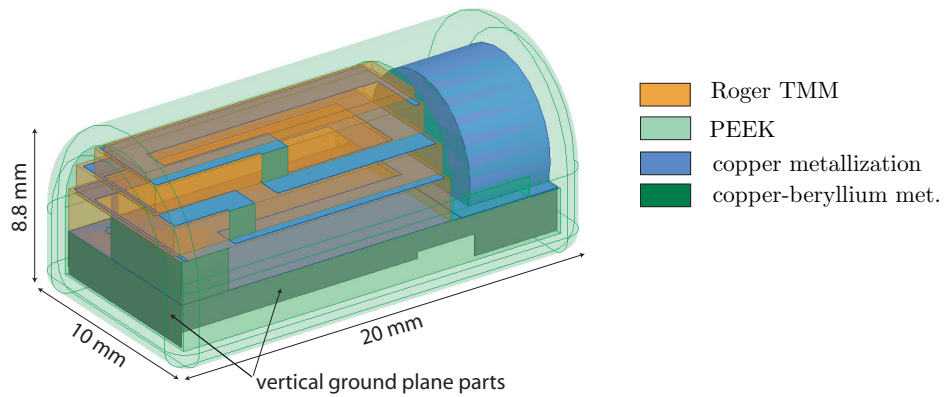
Figure 5.34.: Sketch, materials and main dimensions of the further miniaturized MSA implantable dual band antenna. A modified casing (with a planar bottom surface) can be noted.

[††]The electronics to form a complete BSN are described in Chapter 6.

Simulated matching and radiation performances are reported in Fig. 5.35 and Table 5.8, respectively. The numerical results, although not confirmed by a physical realization, show that an acceptable matching is obtained in both working frequencies (at -10 dB) while the low radiation efficiencies are still sufficient for a 2 m operating range.
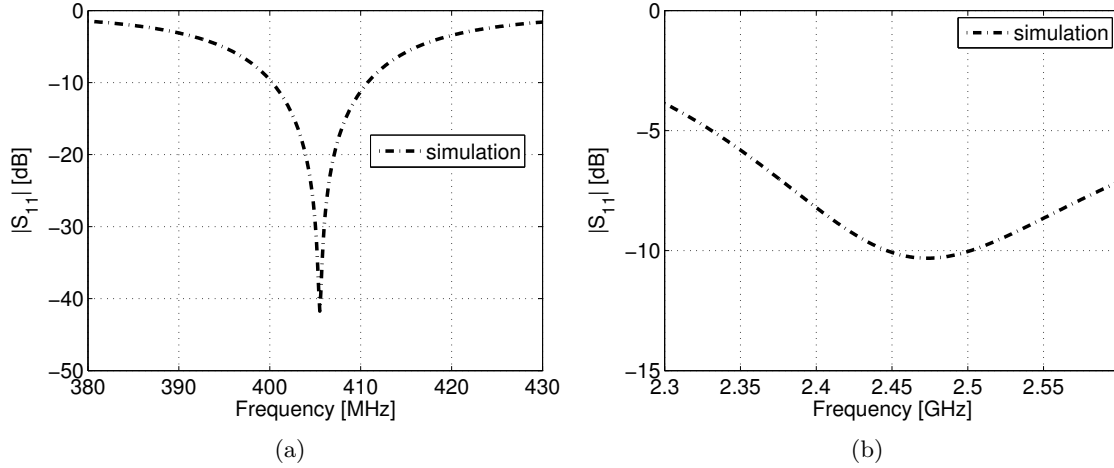

(a)   (b)

Figure 5.35.: Simulated $|S_{11}(f)|$ for the further miniaturized radiator (overall dimensions 10 x 8.8 x 20 [mm]). Results are obtained when the antenna is inserted into the cylindrical homogeneous body phantom: (a) MedRadio and (b) ISM bands.

Table 5.8.: Radiation Performances of the Further Miniaturized Design. Maximum Values are Reported for both Gain and Directivity.

Frequency [GHz]	Gain [dBi]	Directivity [dBi]	e_{rad} [%]
405 MHz	-32.6	3.2	0.026
2.473 GHz	-20.1	4.5	0.345

Wireless Power Transfer: given the new MSA dimension and casing, it is necessary to consider a single battery with rechargeable capability. This would have the great advantage of making a dual band implantable device with dimensions as small as 8.8 x 10 x 20 [mm] feasible. Accordingly, a solenoid capable of capturing the electromagnetic energy via inductive link must be carefully designed to achieve such a result.

For this purpose, as a preliminary investigation, we designed ad realized a three layered solenoid. The solenoid is printed on three faces of two substrates (ROGER TMM 10: $\varepsilon'_e = 9.2$, $\tan\delta = 0.0022$, thickeness = 0.381 mm) that are connected by metallic vias. In order to fit into the miniaturized MSA, the overall dimension of the solenoid are 14.13 x 8.38 x 0.762 [mm]. Fig. 5.36 depicts the realized prototype.

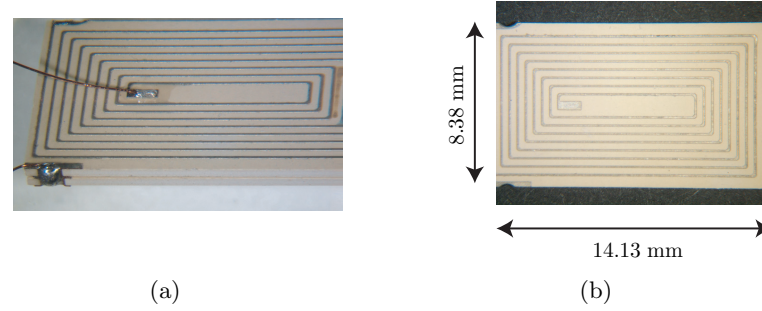(a)   (b)

Figure 5.36.: Realized multilayered solenoid: (a) perspective and (b) top views. In order to improve the performances, all sharp edges have been chamfered.

The solenoid is supposed to be placed at the bottom of the biocompatible casing as shown in Fig. 5.37 to facilitate the connections with the circuitry. However, such a choice is not optimal for the power transfer, as the solenoid is further away from the external free space reducing the power transfer range [212–214]. Nonetheless, it is important to place the solenoid below the antenna in order not to interfere with the functioning of the radiator itself.

multilayered   MSA   conformal
solenoid   ground plane
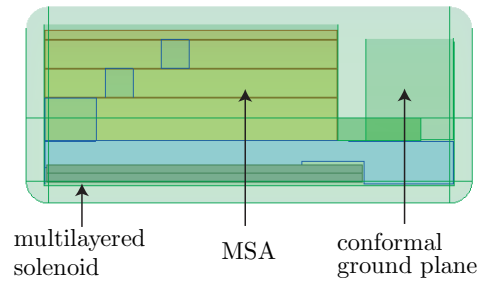
Figure 5.37.: Sketch of the multilayered solenoid placement underneath the miniaturized MSA.

The solenoid aims at having the highest inductance and quality factor Q given the limited available volume. Simulated results are illustrated in Fig. 5.38, where it can be appreciated that the maximum Q occurs in proximity of the targeted working frequency of 13.56 MHz. Special care was also paid to obtain self resonance above 30 MHz (more than double of the working frequency). Finally, once can appreciate that the proposed packaging solution does not noticeably change the solenoid behavior as shown by the simulated results in Fig. 5.38.

The realized prototype was preliminarily tested showing the capability of intercepting a magnetic field (as in transformer) in order to power a battery. However, further investigations are necessary focusing on the design of the receiving circuit and on the external transmitter (both solenoid and circuitry).
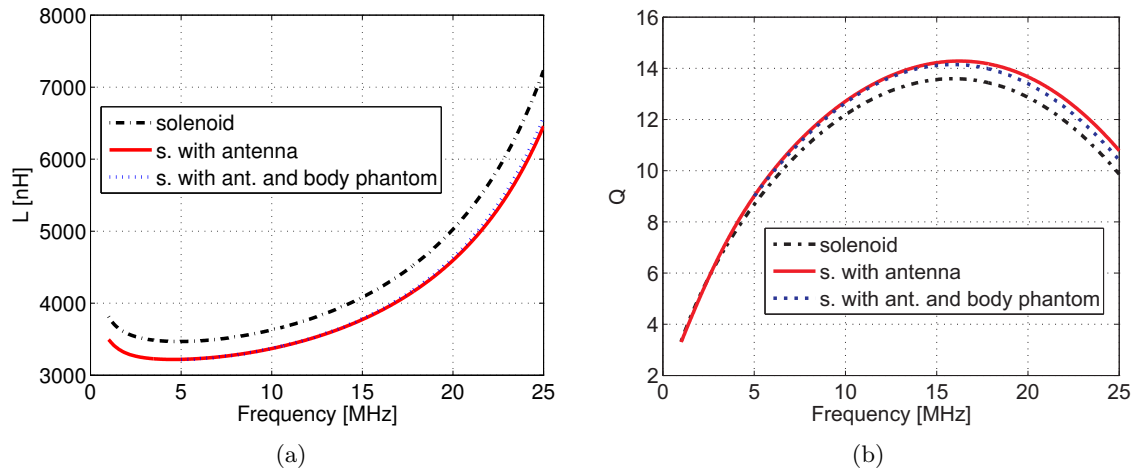
Figure 5.38.: Simulated (a) inductances in [nH] and (b) Qs for the proposed multilayered solenoid in the 13.56 MHz frequency range. The presence of the multilayered antenna and the homogeneous cylindrical body phantom does not disturb the solenoid behavior.

5.6. Conclusion

Following the design strategy formulated in the previous chapter, the design, realization and characterization of the miniature Multilayered Spiral Antenna for implantable telemetry applications were described. The MSA has dual band capability working in both the MedRadio and the ISM bands. Specific physical constraints, EM requirements and versatility were discussed in order to set the targeted goals.

The MSA consists in a conformal design that aims at high system integration while optimizing the EM radiation. Its housing includes a specific volume for the monitoring sensors, or bio-actuators. The impact of the presence of active components was computed confirming the robustness of the design. Its performances were investigated in different conditions including the implantation in a human male model (Duke) belonging to the Virtual Family. Results validated the proper choice of simplified phantoms during the design procedure.

Fifty Ohms input impedances were targeted for both working frequencies. Different values could be selected, at the early stage of the design procedure to match specific IC requirements. Obviously, this would call for a re-arrangement of the chosen antenna design.

Radiation performances (maximum gain equal to -29.4 and -17.7 dBi in the MedRadio and the ISM band, respectively) fulfill the initial requirements, and thus providing a robust communication for a real applications targeting a minimum working range of 2 m.

Building issues and software calibration aspects were described. A first realization allowed the improvement of the model. Furthermore, a solution to tune the radiator matching characteristic was identified and successfully used. Finally, the versatility of the MSA was proven showing that a further miniaturization and different power supply could be considered without the necessity of starting a new design from scratch.

The packaging of four MSAs and the realization of four corresponding BSNs is discussed in the following chapter presenting its in vitro characterization and in vivo experiments.

6. Packaging, Realization, In Vitro Characterization and In Vivo Experiment of a Body Sensor Node[†]

6.1. Introduction

After the successful design of the MSA, we realized a complete Body Sensor Node (BSN) for data telemetry. The BSN comprises all the components necessary for data transmission from an implant to an external Base Station (BS). This realization has been performed in close collaboration with Dr. Bolomey [17] from LPM of EPFL.

The proposed integration, with a dedicated volume to the bio-sensors or actuators, results in a versatile device. Indeed, different bio-sensors (temperature, pH, glucose, etc.) can be joined to the BSN so as to answer the requirements of different applications or purposes.

The work performed in this part of the thesis aims at realizing a complete implantable system for remote monitoring telemedicine. In particular, the three main goals of this chapter are:

1. to present the packaging and realization of a complete BSN;

2. to characterize its performances in vitro validating the expected performances;

3. to perform in vivo experiments with remote monitoring capabilities in a real life application.

In order to reach these goals, this chapter is organized as follows: the realization and packaging of the BSN is presented in Section 6.2. Active electronics, matching, power supply and sensors are presented here. The complete implantable device was tested in vitro as reported in Section 6.3. The measurements confirmed the feasibility of the BSN and allowed us to validate its capabilities.

Section 6.4 presents the in vivo experiments that were performed in a porcine animal. These experiments were carried out in collaboration with F. Gorostidi from the *Laboratoire de Dynamique des Cellules Souches* (LDCS) of EPFL-UNIL-CHUV directed by Professor Y. Barrandon.

[†]- L. Bolomey, F. Merli, E. Meurville, J.-F. Zürcher, and A.K. Skrivervik, "Telemetry system for sensing applications in lossy media," International Request PCT/IB2011/050991 for the Swiss Patent Application: 00335/10, 11th Mar. 2010.

- F. Merli, L. Bolomey, E. Meurville, and A.K. Skrivervik, "Dual band antenna for subcutaneous telemetry applications," in *Proc. IEEE Antennas and Propagation Society Symposium (AP-S)*, Toronto, Ontario, Canada, July 11–17, 2010.

6.2. Packaging and Realization

The BSN is encapsulated by a biocompatible casing (length: 32.1 mm, diameter: 10 mm). This casing houses the four main components of the entire system, namely:

- the Multilayered Spiral Antenna (MSA);

- the Electronics Assembly: a flexible Printed Circuit Board (PCB) including the IC ZL70101 [202], Digital Signal Processor (DSP) unit and the matching circuit;

- the Power Supply: four batteries to guarantee the desired the life time (1 year, depending on the application);

- the Bio-sensors (or -actuators): monitoring devices for glucose, pH, temperature, pressure, etc.

as depicted in Fig. 6.1. The MSA was presented in the previous chapter, thus the remaining three components, and their integration, are discussed in the following sections.

(a)

(b)
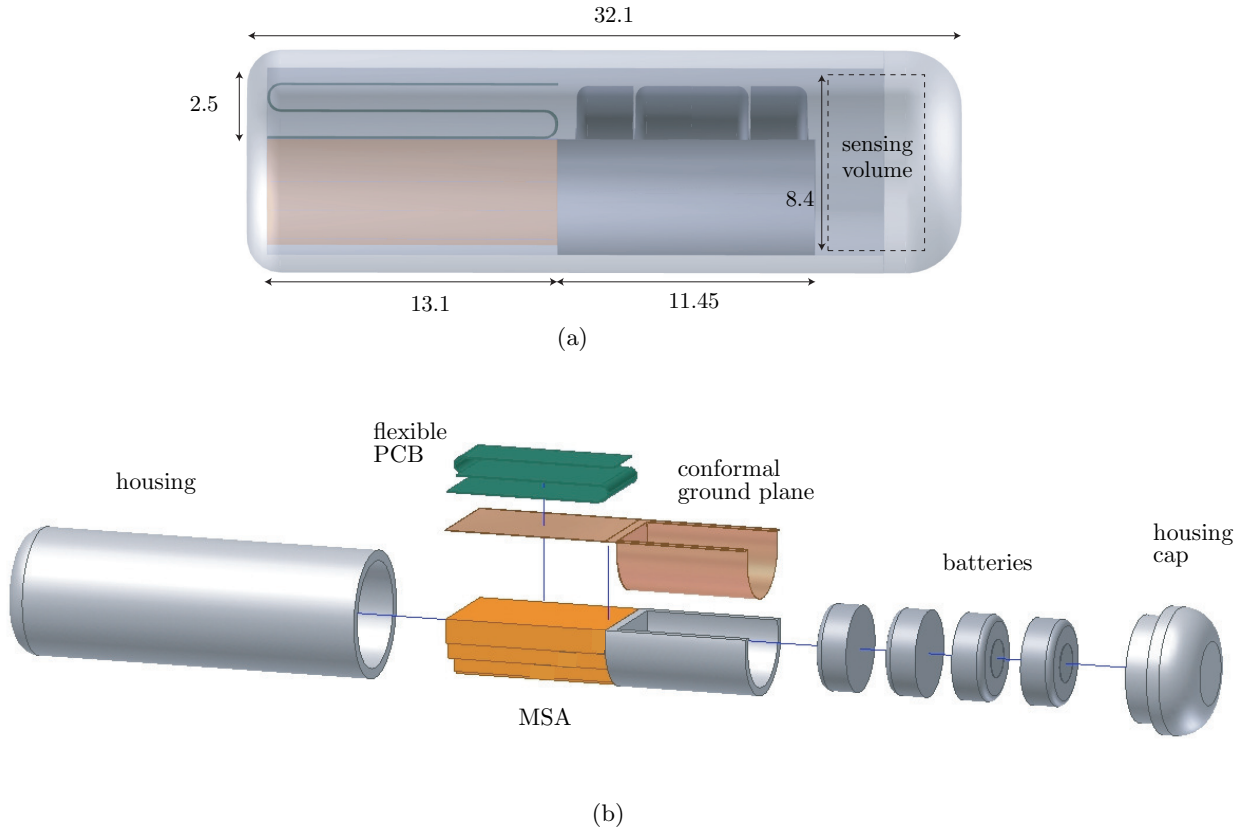
Figure 6.1.: Complete packaging of the BSN: (a) integrated and (b) exploded views. Dashed line in (a) identifies the volume dedicated to the bio-sensors. Dimensions in [mm].

6.2.1. Electronics Assembly

The electronic components to drive the BSN were assembled on a flexible PCB. The two stages board is depicted in Fig. 6.2. PCB routing was performed using a 70 μm track width

and spacing, and a 70 μm via hole diameter. In order to reduce the radius of curvature in the bending area, copper and solder masks were removed from the opposite side of the track. The PCB assembly was performed in two steps:

1. all the components of the flexible PCB (excepted for the IC and the matching PCB) were mounted and soldered on the board;

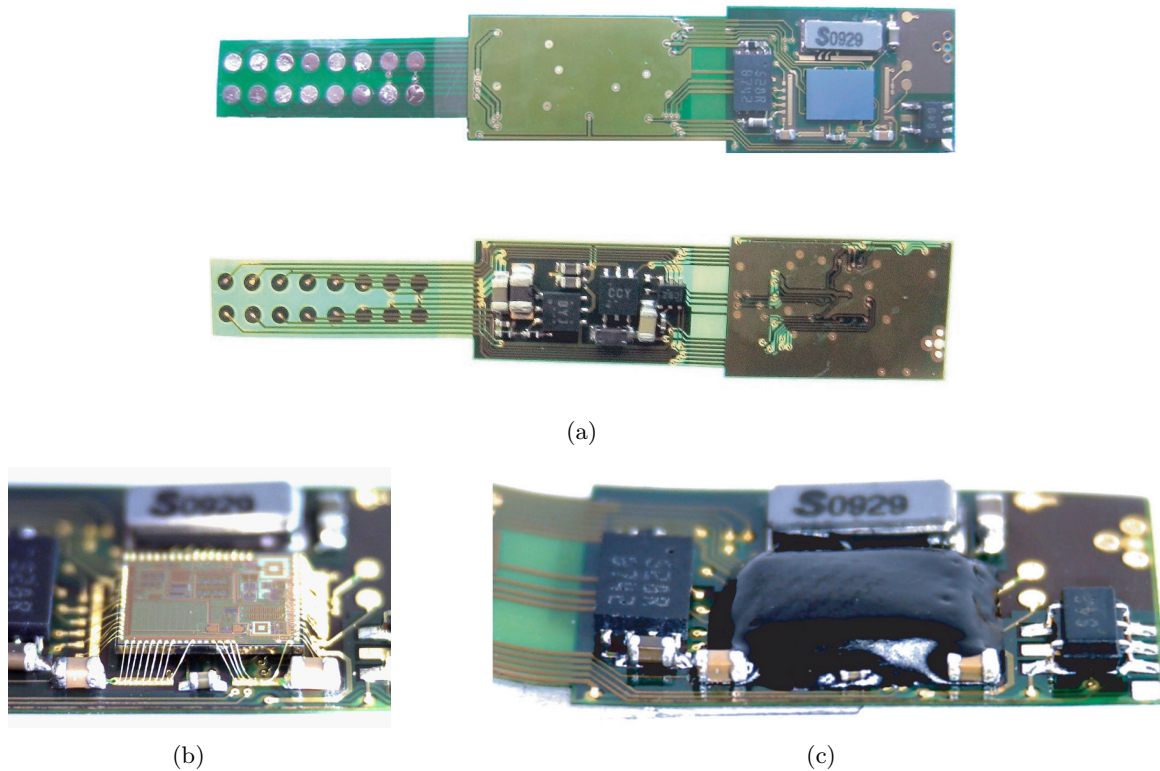2. the ZL70101 IC is glued on the DSP and bonded. The bonding was protected by a layer of EPOTEK H6243 epoxy[‡].

(a)

(b)

(c)

Figure 6.2.: Realized electronics on a flexible PCB: (a) flexible board (top and bottom views), (b) IC bonding, and (c) bonding protection with EPOTEK H6243.

Matching PCB

Matching the MSA radiator to the ZL70101 IC requirements (Section 4.3) was not an easy task. Besides the problems related to the presence of the flexible PCB and its connections, and the necessity of voltage step-up matching, it is worth reminding that uncertain values are provided about the IC input impedances (especially in the higher frequency range).

A separate board was realized to allow for different trials, as illustrated in Fig. 6.3-(a). Once discrete components were soldered here, the matching board was subsequently glued and connected to the flexible PCB. Several attempts were performed so as to characterize the IC and optimize the matching circuit both via numerical and experimental analysis. Finally, a

---

[‡]Produced by Epoxy Technology, Inc. : www.epotek.com.

cut-and-try approach was considered for the concluding optimization. The discrete components and the connection to the IC are given in Fig. 6.3-(b)-(c), while Fig. 6.4 illustrates the realized matching board glued on the flexible PCB. As confirmed by the results measured during in vitro experiments, the obtained overall performances closely matched the expected values.
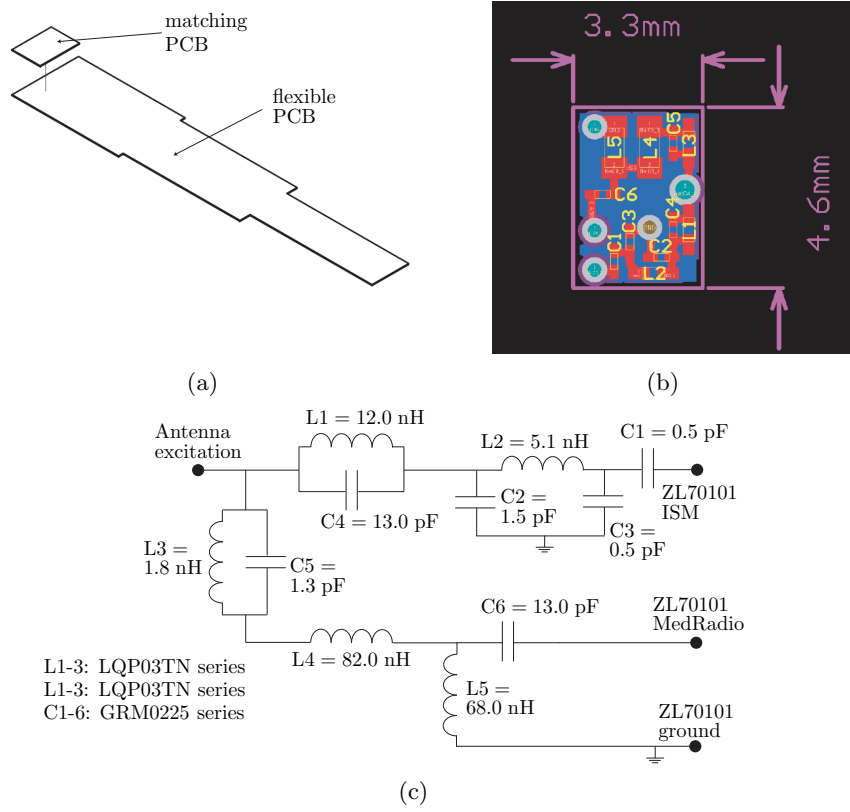

Figure 6.3.: Matching circuit PCB: (a) sketch of the matching board and its position on the flexible PCB, (b) top view with dimensions [mm] and position of each component, and (c) schematics identifying the discrete elements (produced by Murata Manufacturing Co., Ltd.).
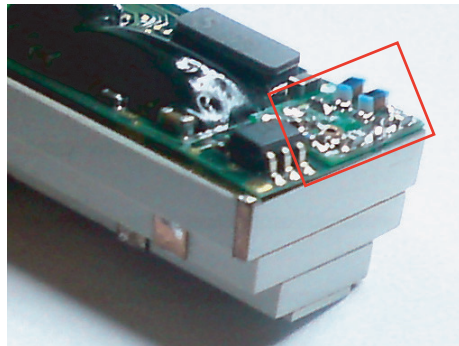
Figure 6.4.: Realized matching circuit board glued on the flexible PCB below the MSA ground plane.

6.2.2. Power Supply

In order to realize a BSN capable of driving the glucose microviscometer investigated in [215, 216], four coin type 377 batteries, manufactured by Energizer, were selected. These batteries were packed together with a conductive glue. The assembled batteries pack is illustrated in Fig. 6.5 with the ground in the middle of the pack and the positive voltage on both edges connected together. The three wires ensures the connection to the flexible PCB. This solution ensures a life time of 281 days with the glucose microviscometer.
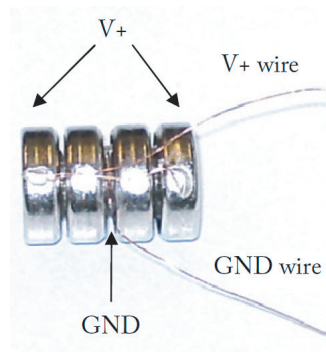
Figure 6.5.: Realized battery pack.

6.2.3. Bio-sensors

The conception of the complete BSN gives a broad freedom regarding the monitoring device or bio-actuator to be included. As an example, Fig. 6.6 illustrates the presence of the front-end electronics and the rotor that were developed to drive the glucose microviscometer.

Different instruments for the monitoring of other physiological data can be integrated, thus showing the versatility of the BSN for different applications. For instance, a potentionstat[||] for electrochemical sensor is showed in Fig. 6.8-(b).
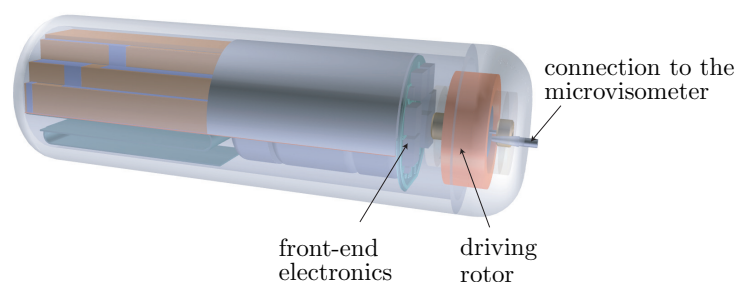

Figure 6.6.: Sketch of the BSN including the driving rotor for the glucose microviscometer described in [215, 216]. Details about the driving rotor are given in [17].

[||]A potentionstat identifies the electronic hardware required to control a three electrode cell and run most electroanalytical experiments (http://en.wikipedia.org/wiki/Potentiostat).

6.2.4. Complete BSN

All the realized components were integrated to realize the complete BSN. Fig. 6.7 depicts several views of the built prototype. The volume occupations and weights are reported in Table 6.1.
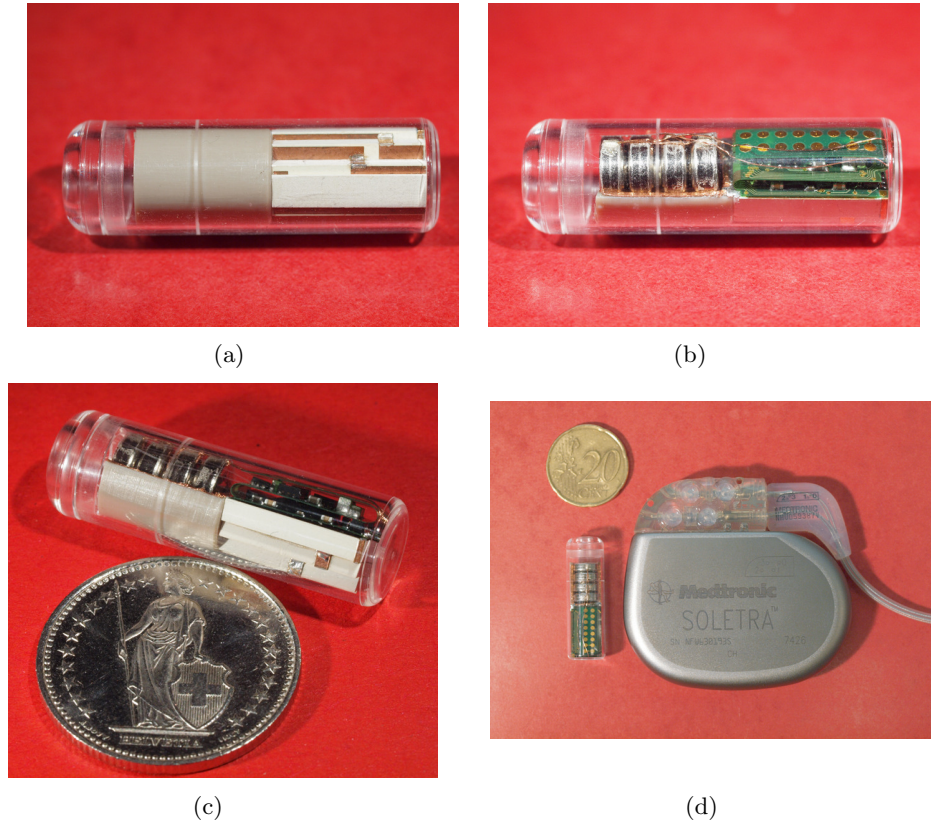

(a)

(b)

(c)

(d)

Figure 6.7.: Different views of the realized BSN. For clarity reason, PEEK is substituted by a Poly(methyl methacrylate) (PMMA). The BSN is compared to a deep brain stimulator device in (d).

Table 6.1.: Volume and Weights of the realized BSN.

BSN Component	Volume		Weight	
	[mm^3]	[%]	[g]	[%]
MSA	600	24	1.367	31
Flexible PCB	254	10	0.305	7
Power supply	424	17	1.543	35
Sensing	307	13	–	–
Housing	892	36	1.176	27
Total	2477	100	4.391	100

No weight information is given about the sensing part as this depends on the targeted application. The proposed BSN includes all the necessary components in a volume as small

as 2477 mm^3 and its weight is less than 5 g. This volume occupation is similar to the one of a 000 capsule§ commonly used in medicine.

Finally, as an example of the versatility of the complete BSN, Fig. 6.8-(a) depicts the top view of the driving rotor for a glucose microviscometer, while the realization including a potentionstat for glucose and dopamine bio-sensors is shown in Fig. 6.8-(b). The latter is currently being used by C. Boero at the Laboratoire des Systèmes Intégrés (LSI) at EPFL.
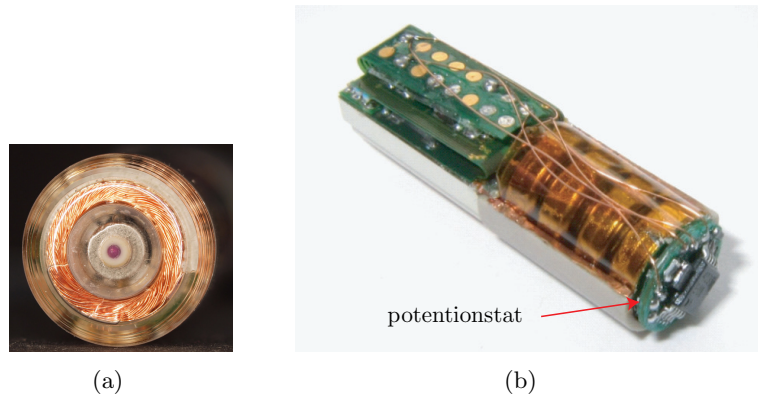

(a)   (b)

Figure 6.8.: Different application of the realized BSN depending on the devices allocated in the available sensing volume: (a) top view of the driving rotor for a microviscometer and (b) potentionstat.

6.3. In Vitro Characterization

In vitro tests were performed in order to check the functioning of the realized device and validate the MSA radiation characteristic. Fig. 6.9 depicts the BSN inserted into the liquid phantom. This choice provided stable conditions for the evaluation of the BSN performances.

Figure 6.9.: In vitro setup: BSN inside a cylindrical body phantom. The cylinder measures 80 mm in diameter and 110 mm in height as the phantom used for the numerical analysis.

---

§Information available in www.erowid.org/archive/rhodium/pdf/gelcap.sizechart.pdf.

The system behavior was assessed with the use of the Zarlink external module in different working environments.

6.3.1. MedRadio Indoor Tests

The BSN MedRadio transmission range was first evaluated in a laboratory room. The experimentation set up is depicted in Fig. 6.10. In this environment the transmission range was far beyond four meters. Despite the randomness of the multi-path propagation that occurs in an indoor environment with several metallic objects, this experiment was very useful to verify all the functionalities of the system. Furthermore, it gave us the first idea of the working ranges considering a realistic scenario, as MedRadio devices are supposed to be used indoor.

Figure 6.10.: Indoor communication tests. Yellow and Red boxes identify the BSN and the external module, respectively.

6.3.2. MedRadio Outdoor Tests

Given the preliminary indoor working distances, outdoor tests were carried out to identify the maximum communication ranges. The measurements were taken on a green place were no obstacles were present, as shown in Fig. 6.11. The body phantom and the external module were elevated about 1 m over the ground.

To assess the maximum range of the MedRadio communication link, the BSN was set to transmit the maximum output power and to receive with the highest sensitivity. Four realized prototypes (A-B-C-D) were measured.

Several sub-bands, i.e., channels, within the MedRadio band were tested. Table 6.3 reports the registered performances (channels 0 and 9 correspond to 402 and 405 MHz, respectively). All prototypes largely surpassed the primary requirement of 2 m, while the best performances reached as far as 14 m. Such capabilities ensure a reliable link even for a non optimal position of the BS and the implant. For example, a successful communication was achieved up to 3 m rotating the body phantom (and the BSN) of 180°deg. This provides an unfavorable condition given the main direction of radiation of the MSA. Finally, considering the BSN placed in the
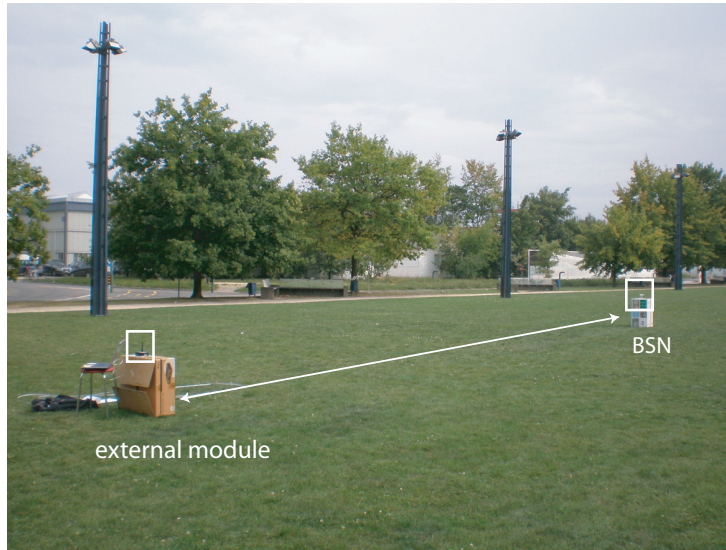
Figure 6.11.: Outdoor communications tests.

middle of the body phantom, i.e., surrounded by 35 mm of liquid, we still registered a working range of 10 m for the BSN D.

Table 6.2.: Summary of the Maximum Registered Ranges during the Outdoor Tests in the MedRadio band for a 200 kbit/s bi-directional data telemetry.

BSN	MedRadio Channel	Maximum Range [m]
A	0	6.0
	4	12.0
	9	9.0
B	0	6.0
	4	8.0
	9	8.5
C	0	8.0
	4	9.0
	7	11.5
	9	9.5
D	0	7.0
	4	14.0
	9	14.0

6.3.3. ISM Anechoic Chamber Tests

The *wake-up* transmission distance in the ISM band was assessed in an anechoic chamber[†]. Working ranges are reported in Table 6.3, while the measurement setup is illustrated in Fig. 6.12. We successfully woke-up all the prototypes with the external module placed at 2.4 m from the implant and radiating an EIRP of 14 dBm. This is equivalent to transmitting at two times the distance, i.e. 4.8 m, with the maximum allowed EIRP of 20 dBm. The *wake-up* bandwidth of the four BSNs ranged from 2.43 to 2.49 GHz, as reported in Table 6.3.

These performances were obtained with the maximum bias current in the low noise amplifier of the transceiver. The frequency tuning facilities of this amplifier was also assessed. Default values were found to offer on average the best performance.

Table 6.3.: Summary of the Registered Working Ranges during Anechoic Chamber Tests in the ISM band with 14 dBm EIRP.

BSN	Working Band [GHz]	Working Range [m]
A	2.45-2.49	2.4
B	2.45-2.49	2.4
C	2.43-2.48	2.4
D	2.45-2.49	2.4
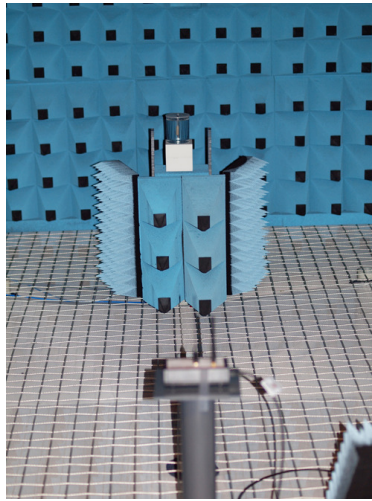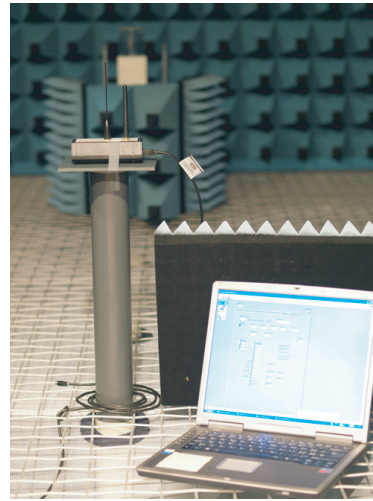
(a)   (b)

Figure 6.12.: Measurement setups inside the anechoic chamber. The driving laptop, shown in (b), was masked to reduce any possible interference.

6.3.4. Summary on the In Vitro Characterization

In vitro tests allowed us to verify the feasibility and characteristics of the proposed BSN. Four prototypes were realized and measured. Despite the differences among the prototypes

---

[†]This chamber belongs to the Laboratory of Electromagnetics and Acoustics at EPFL.

(for instance, maximum distances ranging from 8.5 to 14 m in the MedRadio band), all BSNs performed successful communications far beyond the minimal targeted 2 m range in both working frequencies.

These tests confirmed the simulated performances of the MSA. Considering the power link budget characteristics of the IC ZL70101 and the Zarlink external module[¶], the maximum registered ranges correspond to antenna gain values equal to -30.5 and -18.6 dBi in the MedRadio and ISM band respectively. These performances, which take into account the mismatch and the losses within the electronics assembly, closely match with the predicted characteristics, i.e., -29.4 and -17.7 dBi.

6.4. In Vivo Experiments

In order to assess the performances of the realized BSNs in a real scenario, two devices were implanted in a porcine animal. In vivo tests imply challenges that go far beyond the electromagnetic aspects of a system for data telemetry. Thanks to a collaboration with the LCDS laboratory, we were able to perform such tests in accordance to all ethical considerations and the regulatory issues related to animal experiments.

6.4.1. Purpose and Method

The LDCS team is currently investigating the influence of the temperature on the healing process of a deep wound operated in the skin of animals. Particular attention is paid to the effect of temperature on the skin stem cells behavior, as they might find application in the healing of burned skin of humans [217]. Porcine animals (Göttingen minipigs) are selected for the resemblance of their tissues to the human ones. Therefore, a temperature sensor was inserted into the BSN to answer to the LCDS interest.

Two in vivo experiments were performed. The first one lasted fifteen days, while the second took place over a period of five weeks.

In vivo experiments comprise the following aspects:

- implantation process at the hospital;

- Base Station setup to perform telemedicine with remote monitoring capability from a farm.

Implantation Process

The BSN must undergo a sterilization procedure to be implanted. Common techniques requires high temperature ($>100°$ C). Since the realized prototypes have a maximum operating temperature of $60°$ C, because of the embedded batteries, a chemical sterilization with gas (ethylene oxide gaz) was performed.

The MSA and the whole packaging of the BSN were conceived to facilitate the radiation in the off-body radiation given a fixed position of the system. However, implants can move within

---

[¶]Detailed description of the link budget characteristics between the IC ZL70101 and the Zarlink external module is not reported as not available in open literature.

the body if not properly fixed. In order to solve this issue, we fixed the BSN onto a plate during the first in vivo test. The plate was subsequently stitched to the surrounding tissues. The plate was realized in PMMA, a biocompatible material, and it was glued on the BSN housing with a medical grade glue (Loctite M-21HP). Fig. 6.13 illustrates the final casing.
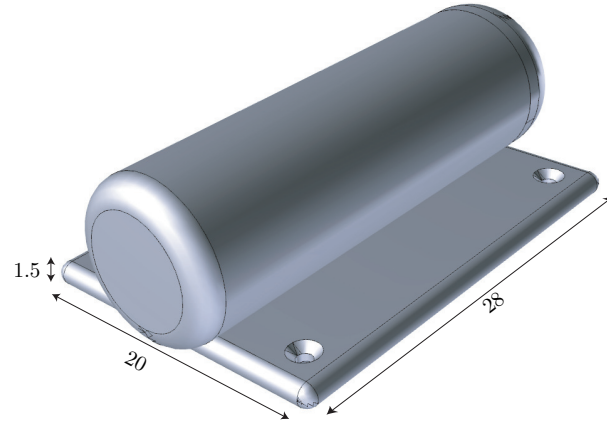

Figure 6.13.: BSN glued onto a plate to ensure its position when implanted for the first in vivo experiment. Dimensions in [mm].

In order to reduce the invasiveness of the implantation process, the casing was modified for the second experiment. Fig. 6.14 illustrates the new design.
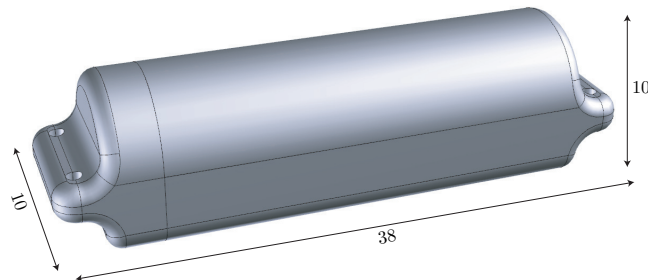

Figure 6.14.: BSN casing for the second in vivo experiment. Dimensions in [mm]. The design still allows its stitching to the surrounding tissues to prevent any BSN movement.

Two BSNs were implanted in the back of a porcine animal as shown in Fig. 6.15; each one was located at different depths: subcutaneous placement at $\simeq 5$ mm and intra-muscular one at $\simeq 28$ mm. Details of the BSN positions are given in Fig. 6.16.
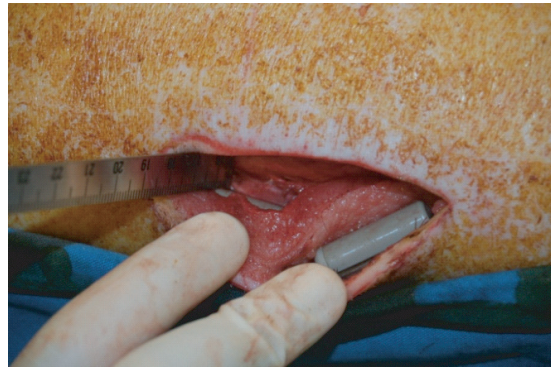
Figure 6.15.: Implantation of two BSNs at different depths.

Epidermis

Dermis

Hypodermis

intra-muscular   subcutaneous
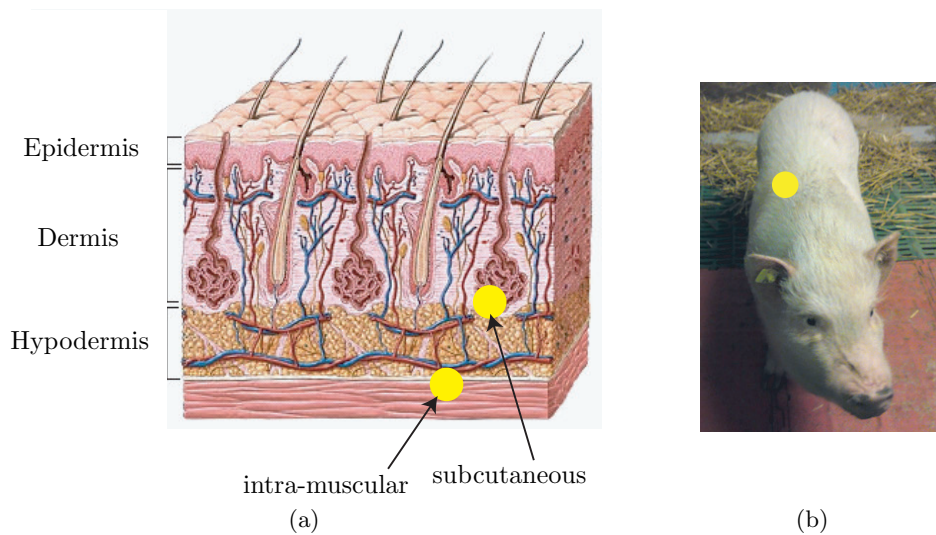
(a)   (b)

Figure 6.16.: Schematics of the BSN implantation sites. Yellow spots identify the BSNs, so as to understand their placements in living tissues (a) -in reality the hypodermis is much ticker than the dermis- and their location on the back of the animal (b).

Base Station Setup

During the in vivo experiments the pig was kept in a farm. Check-ups at the hospital occurred every two days. In fact, skin growth experiments were also carried out while the two BSNs were implanted.

In order to realize a telemedicine system with remote monitoring capabilities, the Base Station comprised:

- - the Zarlink receiver module;

- - an antenna for each working band;

- - an image acquisition system;

- - a 3G USB modem;

- a laptop to drive the entire system and to store the measurements.

While being at the farm, the animal position was restrained to a cage surface, depicted in Fig. 6.17. The BS was placed in attic above the room cage, as illustrated in Fig. 6.17. This choice protected the BS from the cage cleaning, movement of animals and people and other actions that daily occur in the cage room. The attic is approximately 2.50 m above the cage, thus meeting our transmission requirements.
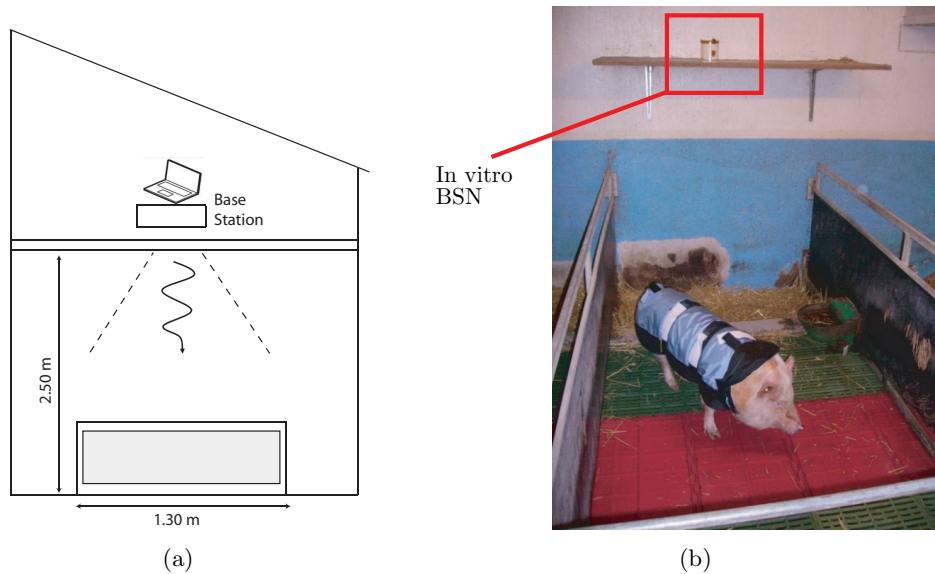

Figure 6.17.: Farm location: (a) cutting view (b) and pig in the cage. An in vitro BSN is placed in the same room to monitor the room temperature. The cage measures 1.3 x 2.7 [m].

Given the fixed orientation between the BS and the cage, a cavity-backed double patch radiator [218] and a helix were used in the MedRadio and ISM bands, respectively. These radiators, maximum gain of 7-8 dBi, substituted the omnidirectional antennas of the Zarlink receiver module. As the animal is free to move within the cage, which modifies the relative orientation between the MSA and the BS antennas, the latter radiators have circular polarization.

In order to monitor the pig position, we implemented an image acquisition system triggered at each temperature measurement. The uCam module from 4D Systems59, depicted in Fig. 6.18-(a), was connected to the laptop via Bluetooth.

The laptop was connected to a 3G USB modem to enable a remote desktop connection. Fig. 6.19 shows the graphical user interface, implemented by Dr. Bolomey, when remotely accessing the laptop. Finally, to protect it from dust and other environment hazards, the entire Base Station was enclosed in plastic boxes as depicted in Fig. 6.18-(b).
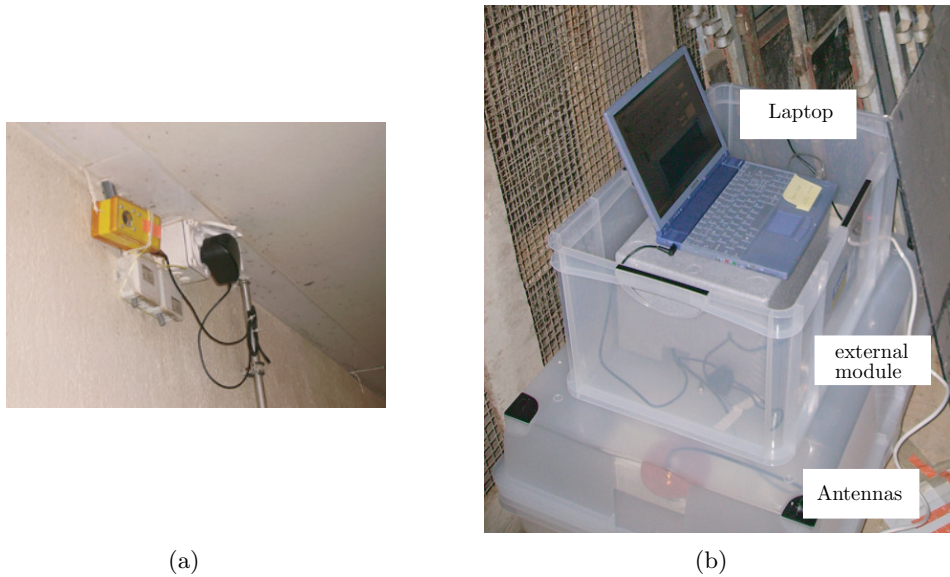
(a)   (b)

Figure 6.18.: Base Station components: (a) wireless camera placed in front of the animal cage (b) laptop, Zarlink external module and antennas all enclosed in plastic boxes.
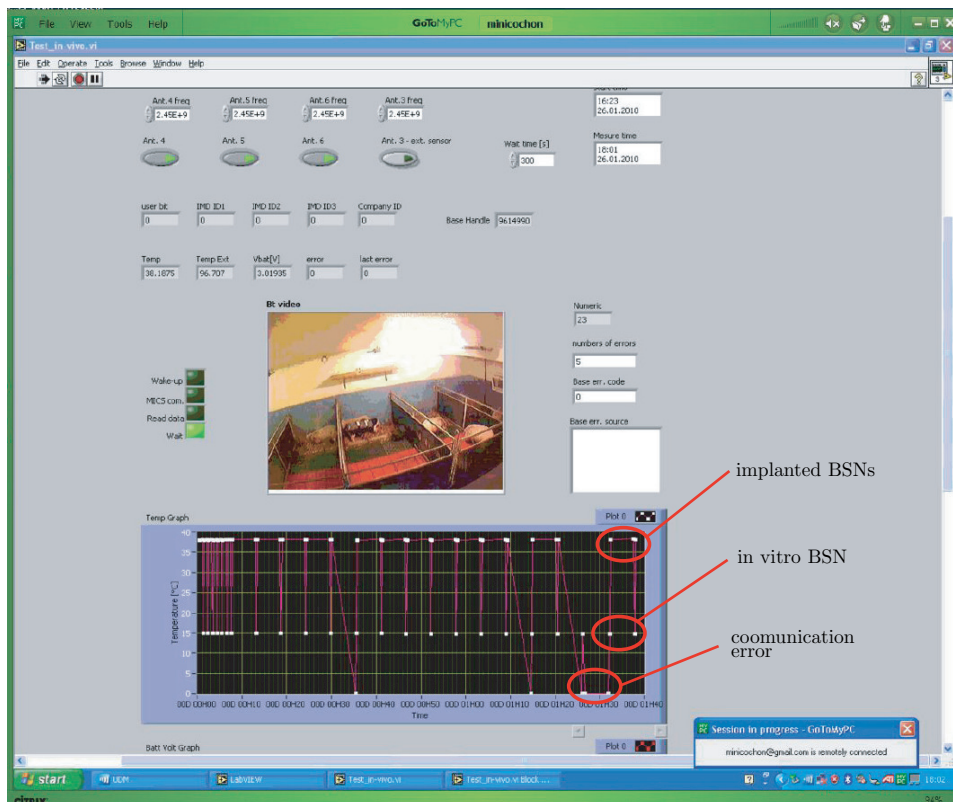

Figure 6.19.: LabView graphical user interface when remotely connected. Temperature values of the three BSNs (two implanted, one in vitro) are recorded and displayed. The picture at the center illustrates the pig position.

6.4.2. Telemetry: Results and Discussion

In order to to appreciate and evaluate the performances recorded during the in vivo tests, results are classified in the following sections:

- Temperature Remote Monitoring: presentation and discussion of the recorded temperature data;

- Histology: analysis of the reaction of immune system;

- Wireless Communication Reliability: presentation and discussion of the wireless link performances.

Temperature Remote Monitoring

The first in vivo trial lasted fifteen consecutive days. The local temperature values, graphically depicted in Fig. 6.20, were measured every five minutes by both implanted BSNs. The time lag between each temperature was set in agreement with the LCDS team.

At first sight, one can appreciate that the intra-muscular implant recorded always a higher temperature (0.2° C). The circadian rhythm of the pig is also observable. The lowest temperature occurred around 5-6h, while the pig was sleeping, and the highest around 18-19h.
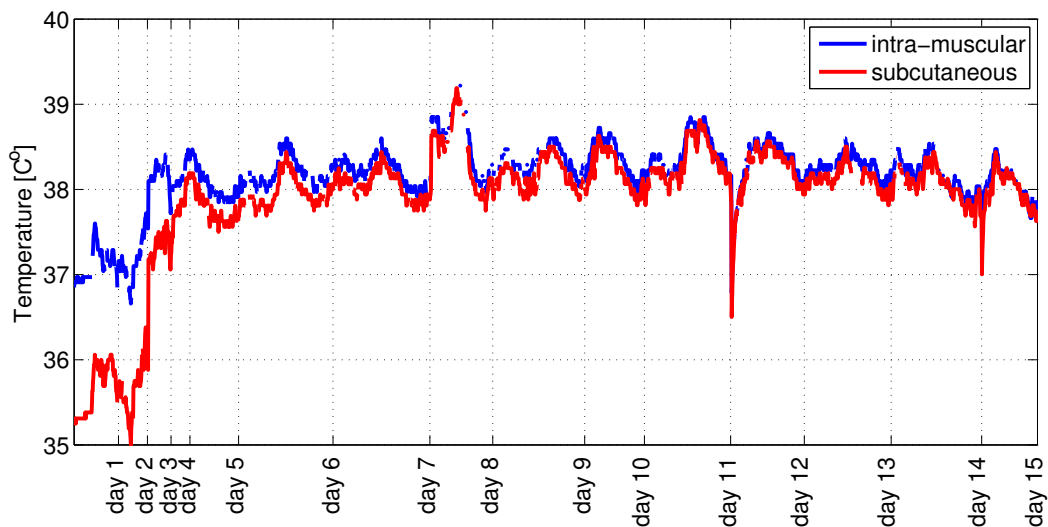

Figure 6.20.: Measured temperature over fifteen days from the implanted BSNs. Timeline is not constant as different number of measurements were taken during each day.

Some particular values merit specific explanations: Fig. 6.21 reports particularly low and high recorded values. Low temperature values occur any time the animal is brought to the hospital. Cleaning the wound implies a decrease of the local temperature; this cooling was still appreciable when the animal was back at the farm, as shown in Fig. 6.21-(a). A local increase of temperature was recorded on the days 7-8, as reported in Fig. 6.21-(a). This increase was caused by the biological reaction of the tissues (inflammation) due to the not
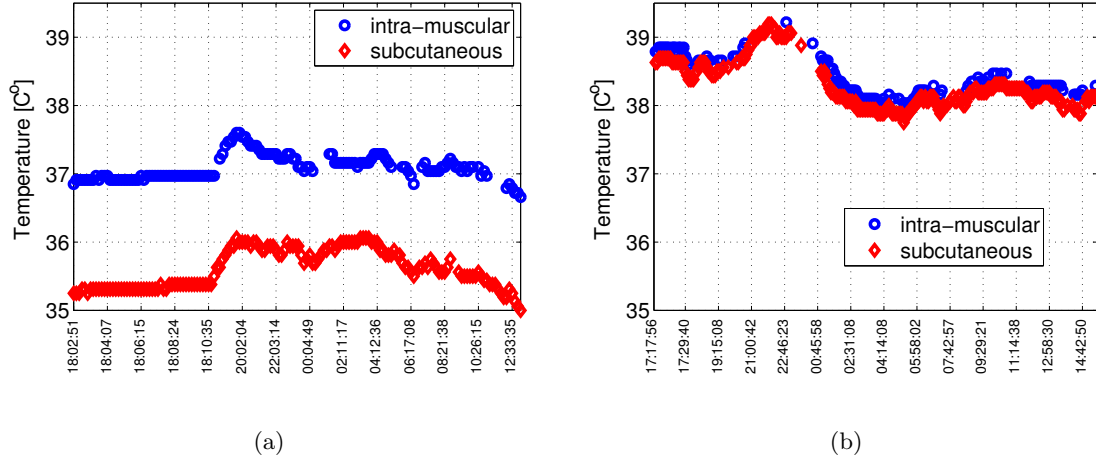
optimal suturation of the incision.

(a)   (b)

Figure 6.21.: Temperature values that differ from the standard average 37-38° C: (a) low values and (b) high values.

The temperature was also monitored within the hospital while the animal was anesthetized, as reported in Fig. 6.22. A rectal probe was used to measure the internal temperature. As expected, the values recorded by the two BSNs are lower than the ones measured by the rectal probe due to the more external positions of the BSNs and because of the cleaning of the wound.
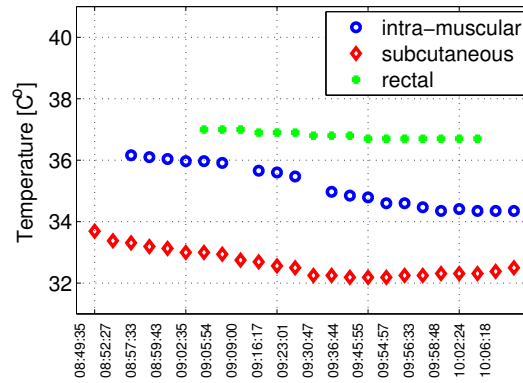

Figure 6.22.: Measured temperature values at the hospital.

The second in vivo trial lasted five consecutive weeks. Measurements, reported in Fig. 6.23, were taken every seven minutes in agreement with the LDCS team. Conclusions are similar to the ones drawn from the first experiment, thus no further details are reported to avoid redundancy. An average higher temperature, compared to the previous experiment, was recorded because of a longer cicatrization with a longer lasting inflammation[‡].

[‡]The observed inflammations have always been caused by the suturation procedures and they were not related
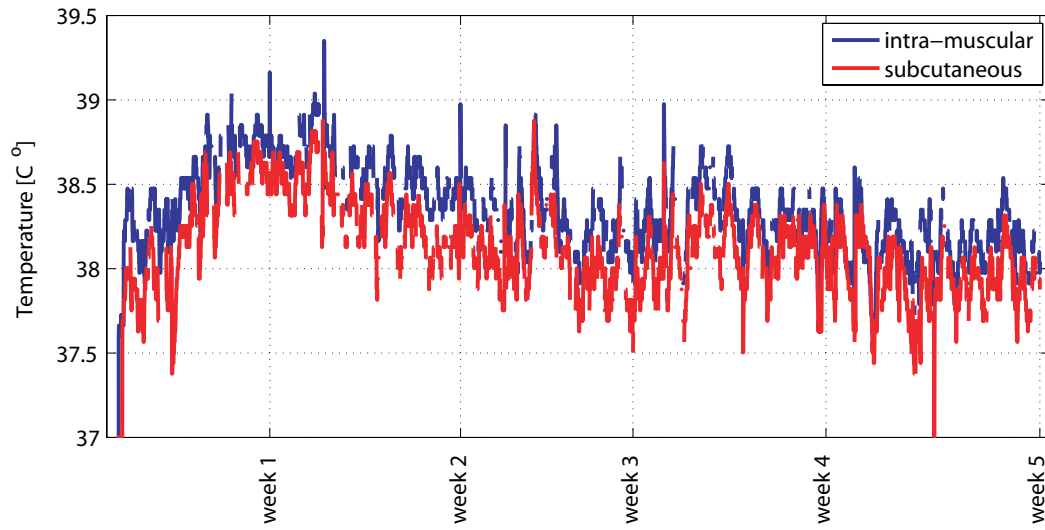
Figure 6.23.: Measured temperature over five weeks from the implanted BSNs.

Histology

Histology, i.e., the study of microscopic anatomy of cells, was performed by examining a thin slice of tissue close to the BSNs. The results of the investigations, carried out by F. Gorostidi, are depicted in Fig. 6.24. The denser and darker cells clearly identify the inflammation generated by skin bacteria that entered the living tissues because of the non optimal suturation.
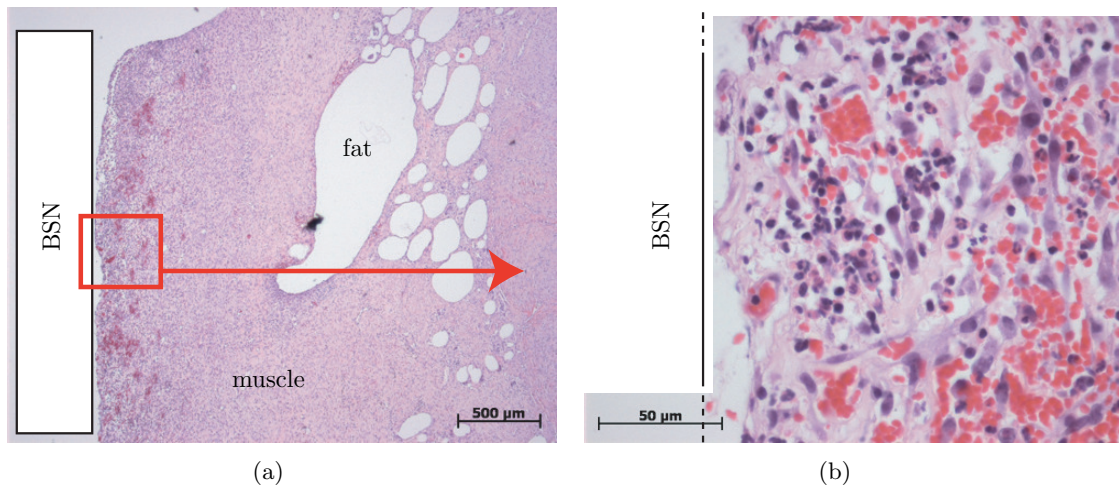

(a)

(b)

Figure 6.24.: Histological specimen of the tissue below the BSN: (a) large view and (b) zoom on the inflammation area (red and dark blue cells).

___

to the biocompatibility of PEEK.

Wireless Communication Reliability

During the fifteen days experiment, we performed 2696 data acquisitions per BSN. Each measurement includes the complete wireless communication cycle: *wake-up* of the implants with a 2.45 GHz signal, bi-directional data transmission in the MedRadio band and return of the BSNs to the *sleeping* state.

Several parameters influence the communication performances such as the position of the animal and of the Base Station, the selection of the channel in both MedRadio and ISM bands,and the physiological recovery of the animal skin. Fig. 6.25 reports the number of relative errors for the periods of continuous observation during the first in vivo experiment. The RF problems have been classified according to the working frequency (MedRadio, ISM), while malfunctioning of the driving software is identified by "firmware".
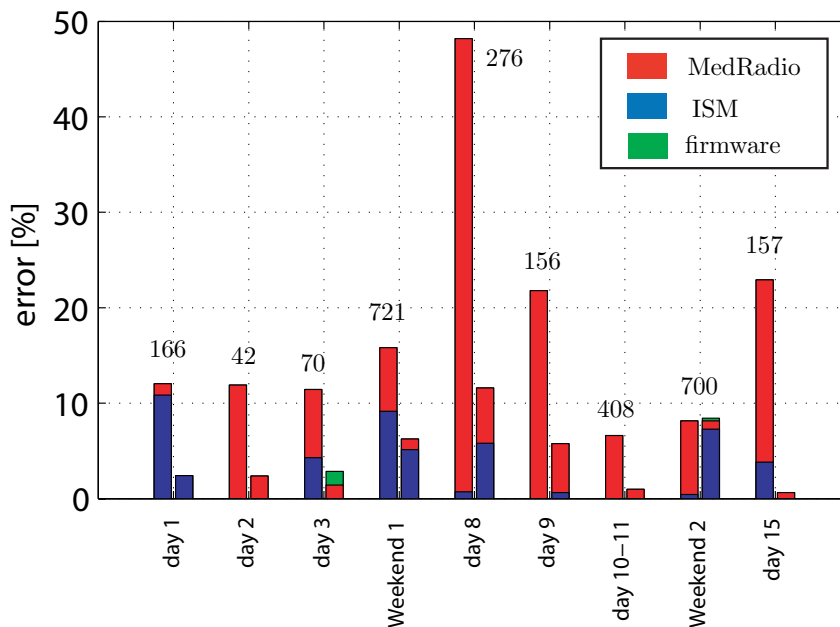

Figure 6.25.: Relative communication errors of the wireless communication over the fifteen days implantation: first column always identifies the intra-muscular BSN, while the second column relates to the subcutaneous one. Relative values are always calculated with respect to the number of measurements (reported above each set of columns) of each continuous period.

ISM *wake-up* was the principal problem recorded during the first day, thus the Base Station position and the channel for the 2.45 GHz signal were modified. These modifications had a positive effect for all the rest of the experiment, although ISM errors still occurred. Two positions of the animal, depicted in Fig. 6.26, were identified as always preventing the ISM communication.

Since the day 2, MedRadio errors became predominant. The Worst performances, reaching almost 50% of failure, were recorded during the day 8 for the intra-muscular BSN. Explana-
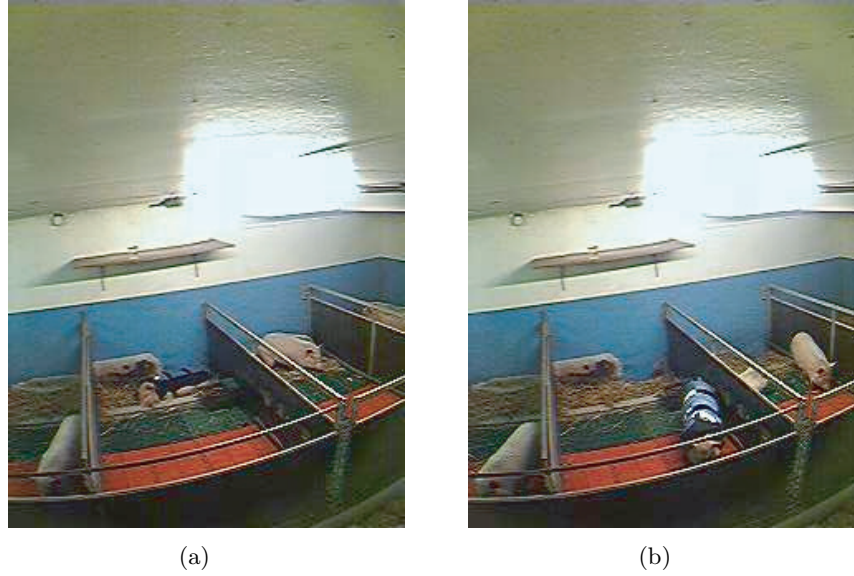
(a)   (b)

Figure 6.26.: Identified positions that were unfavorable for the wireless communication: (a) the pig
is sleeping on the BSNs side and (b) the pig at the frontal extremity of the cage.

tion was found by the local inflammation that occurred. The infection modified the electric
characteristics of the tissues, thus this implied a shift of the MSA resonant frequency. Varying
the channel for the data transmission and treating the infection resulted in an improvement
of the performances for the subsequent days. However, MedRadio errors increased again at
the end of the second week, as skin bacteria had still the possibility to penetrate the tissues
because of the non optimal suturation.

The subcutaneous BSN had a higher reliability (less errors) than the intra-muscular one.
Indeed, its less deep implantation facilitated the RF transmission.

Despite the presence of a high number of errors during some days, the overall performances,
reported in Table 6.4, are satisfying: the relative error over all the measurements, err_{tot}s, are
below 20% and 10% for the intra-muscular and subcutaneous BSNs, respectively.

Table 6.4.: Communications Performances for the Two Weeks In Vivo Test.

BSN	Number of meas.	$err_{MedRadio}$ [%]	$err_{firmware}$ [%]	err_{ISM} [%]	err_{tot} [%]
intra-muscular	2696	12.46	0.00	3.63	16.09
subcutaneous	2696	1.67	0.11	4.04	5.82

During the second in vivo experiment we acquired 6922 and 6931 data from the intra-
muscular and the subcutaneous BSNs, respectively. Relative errors are illustrated in Fig. 6.27.
The acquired knowledge during the first experiment allowed us to increase the robustness of
the communication protocol and of the driving interface. Indeed, MedRadio and firmware
problems became almost negligible

On the contrary, ISM *wake-up* showed an increased number of errors reaching relative values,
err_{ISM}, as high as 32% for the intra-muscular BSN during the week 3. The main reason behind

this decrease of reliability was the BS position. In order to obtain a full coverage of the cage so as to follow the pig daily movement -including the position indicated in Fig. 6.26-(b)- the BS was moved towards the frontal end of the cage. Consequently, it radiated a weaker signal towards the back of the cage where the animal rested. Consequently, many attempts to establish the communication failed while the pig was asleep.

The overall performances, reported in Table 6.4, show the improvement for the MedRadio and firmware performances ($err_{MedRadio}$ and $err_{firmware}$ <0.5%), if compared to the values reported in Table 6.4. On the contrary ISM *wake-up* communication must be improved, modifying the BS coverage, to obtain a more reliable monitoring.
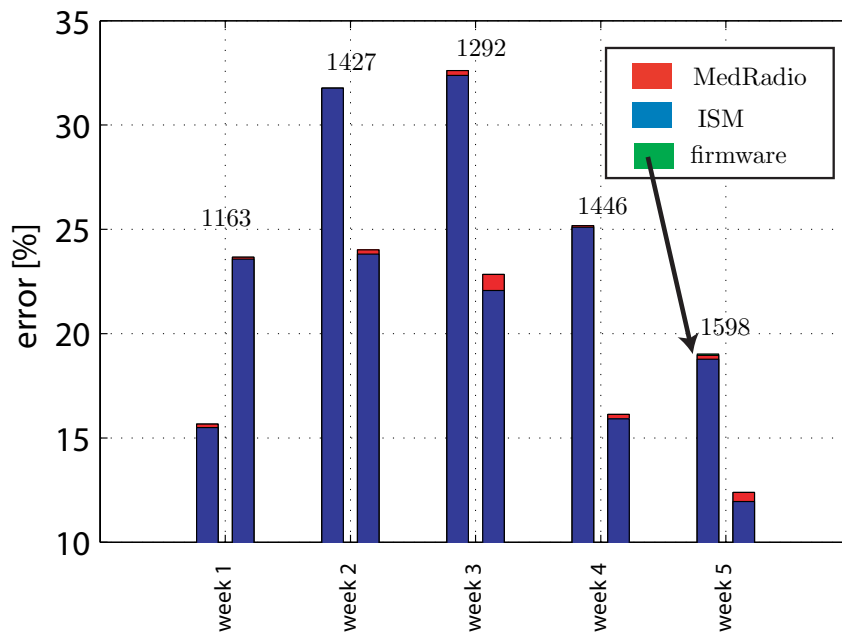

Figure 6.27.: Relative communication errors of the wireless communication over the five weeks implantation: first column always identifies the intra-muscular BSN, while the second column relates to the subcutaneous one. The only firmware error is indicated. Relative values are always calculated with respect to the number of measurements (reported above each set of columns) performed during each week.

Table 6.5.: Communications Performances for the Five Weeks In Vivo Test.

BSN	Number of meas.	$err_{MedRadio}$ [%]	$err_{firmware}$ [%]	err_{ISM} [%]	err_{tot} [%]
intra-muscular	6922	0.13	0.01	24.74	24.89
subcutaneous	6931	0.34	0.00	19.05	19.40

6.5. Conclusion

This chapter presented the packaging and realization of a generic Body Sensor Node. This node comprises all the necessary electronics, power supply and bio-sensor to form a versatile implantable device. All the components perfectly integrate with the Multilayered Spiral Antenna presented in the previous chapter.

In vitro experiments were performed confirming the MSA predicted results. Working ranges far beyond the initial 2 m requirements were always accomplished by the four realized BSNs for both working frequencies and in different environments. The characterization and the experiments reported here focused on the performances of the whole system. The next chapter will present some considerations on the correct assessment of the matching properties of implantable antennas at the component level.

Two BSNs were implanted in a porcine animal for in vivo tests during two separate periods. The sterilization process and the biological responses were investigated, while an ad hoc Base Station with image acquisition capabilities and remotely accessible was set up. This solution realized a complete system for telemedicine.

In vivo experiments showed that many more challenges are present in a real life application compared to the analysis in simplified body phantoms. The robust performances measured via in vitro tests were found to be necessary so as to allow good reliability of system. Overall relative errors during the two in vivo tests ranged from a minimum of 5% to a maximum of 25%. The main sources of errors were discussed identifying the necessary improvements in terms of the implantation process (reducing the adverse responses of the immune system) and of the optimization of the BS (position and antennas).

7. Antenna Measurements for In Vitro Characterization†

7.1. Introduction

Measured results of several implantable antennas have been presented in previous chapters. The measurement setups and the encountered issues while performing these in vitro characterizations are now discussed.

The matching performances of the investigated radiators were evaluated through a coaxial cable, which is an unbalanced feed. This choice may provide erroneous results, such as frequency shifts (larger than 25%) and different matching levels. Thus, it is mandatory to take into account the presence of the feeding cable in order to obtain correct proof of the desired performances. The work performed in this part of thesis aims at identifying, and possibly mitigating, any undesired effects related to the feeding cable for the in vitro characterization of implantable antennas. In particular, the two main goals of this chapter are:

1. to state the problem under investigation;

2. to propose solutions for a correct assessment of the matching performances of electrically small implantable radiators inserted into a body phantom.

In order to reach these goals, this chapter is organized as follows: Section 7.2 presents the measurement issue, while solutions, experimentally and numerically validated, are given in Section 7.3. Finally, conclusions are drawn in Section 7.4.

7.2. Statement of the Problem

Before targeting in vitro tests, it is worth reminding three aspects, namely:

- the measurement of implantable antennas fed by a coaxial cable is very interesting, as it avoids complex and costly system measurements;

- implanted radiators are often electrically very small antennas in the MedRadio frequency range;

- a phantom surrounds the radiator to mimic the human body presence.

The combination of these aspects increases the challenges of the in vitro characterization of implantable antennas. The two main consequences of the presented aspects are illustrated in Fig. 7.1.

---

†- F. Merli and A.K. Skrivervik, "Design and measurement considerations for implantable antennas for telemetry applications," in *Proc. 4*$^{\text{th}}$ *European Conference on Antennas and Propagation (EuCAP 2010)*, Barcelona, Spain, Apr. 12–16, 2010.

First, Electrically Small Antennas (ESA) are well known to interact with an unbalanced feeding [34, 219]. Current distributions are usually present on the back side of the antenna ground plane and they can flow on the external surface of outer conductor of the feeding cable as shown in Fig. 7.1-(a). This phenomenon affects the antenna characterization. For instance, the low radiation efficiency of the ESA can be hidden by the radiation of such currents. This is why no experimental radiation characteristics were reported in previous chapters in the MedRadio range. Indeed, validation of the simulated performances has been proven only with a system approach (Section 6.3.4).

Second, in the case of an implantable ESA, the currents on the cable couple with the highly lossy materials constituting the modeled biological tissues, as in Fig. 7.1-(b). This coupling, leading to a dissipation of energy, can modify not only the radiation properties but even the matching characteristics of the radiator under test.
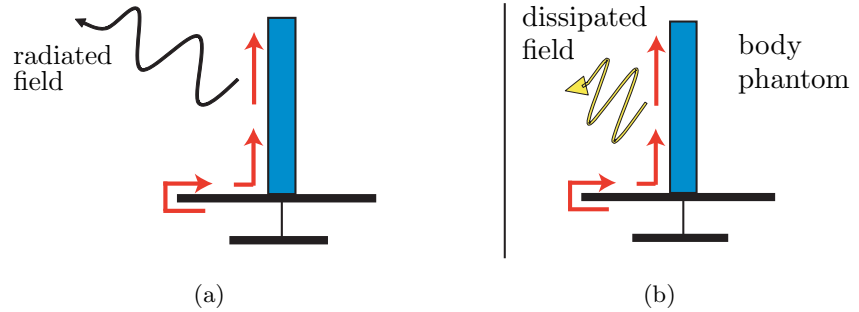

(a)   (b)

Figure 7.1.: Sketches of the interactions between a coaxial feeding cable and the current distribution (red arrows) of an ESA: (a) in free space the currents on the cable contribute to the radiated field (black arrow), while in (b), when a body phantom surrounds the antenna, such currents dissipate in the biological tissue (yellow arrow).

These aspects are not clearly addressed in the literature of implantable antennas for data telemetry. In fact, classical implantable antenna measurements (see Fig. 7.2), are carried out as illustrated in Fig. 7.1-(b).
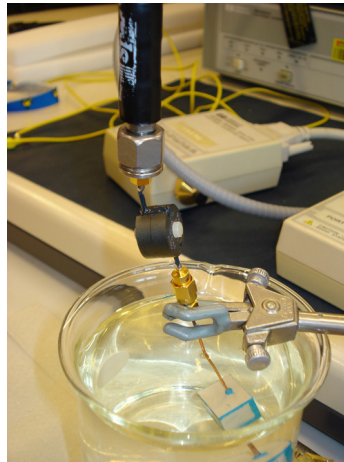

Figure 7.2.: Classical implantable antenna measurement setup: the antenna and the cable are directly inserted into a body phantom while a choke is used to reduce currents reaching the network analyzer.

Particular solutions are considered only in [179] and, as detailed in the following sections, in this thesis. On the contrary, several investigations and answers can be found in microwave hyperthermia applications [220–225]. Such applications consider the cable not only for testing purposes, but as a part of the heater. Special feeders have been developed for this specific application. These solutions reduce the interaction between the coaxial outer conductor and the living tissue to focus the electromagnetic radiation on the targeted zone. Fig. 7.3 illustrates the cable specifically designed in [225].
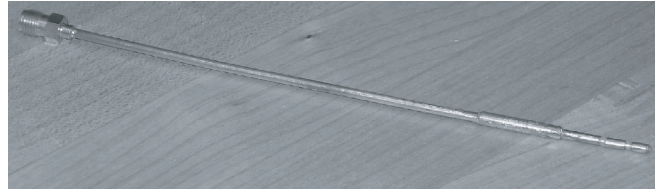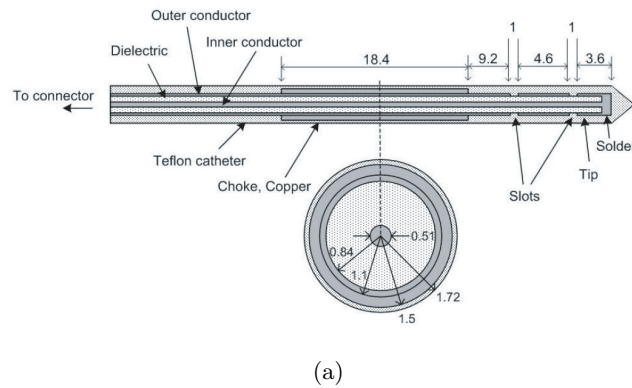

(a)

(b)

Figure 7.3.: Example of a modified coaxial cable in microwave hyperthermia applications from [225]: (a) schematic and (b) realized prototype. Dimensions in [mm].

7.3. Solution: New Measurement Setups

In order to overcame the problem presented above and still carry out in vitro measurements with a coaxial feeding cable, we propose to carry out measurements in accordance with different measurement setups illustrated in Fig. 7.4, namely:

- setup 1: direct contact between the cable and the body phantom (most popular choice);

- setup 2: presence of a vacuum shell (thickness s_{tk}) around the cable;

- setup 3: reduction of the implant depth in the body phantom.

(a) setup 1

(b) setup 2

(c) setup 3
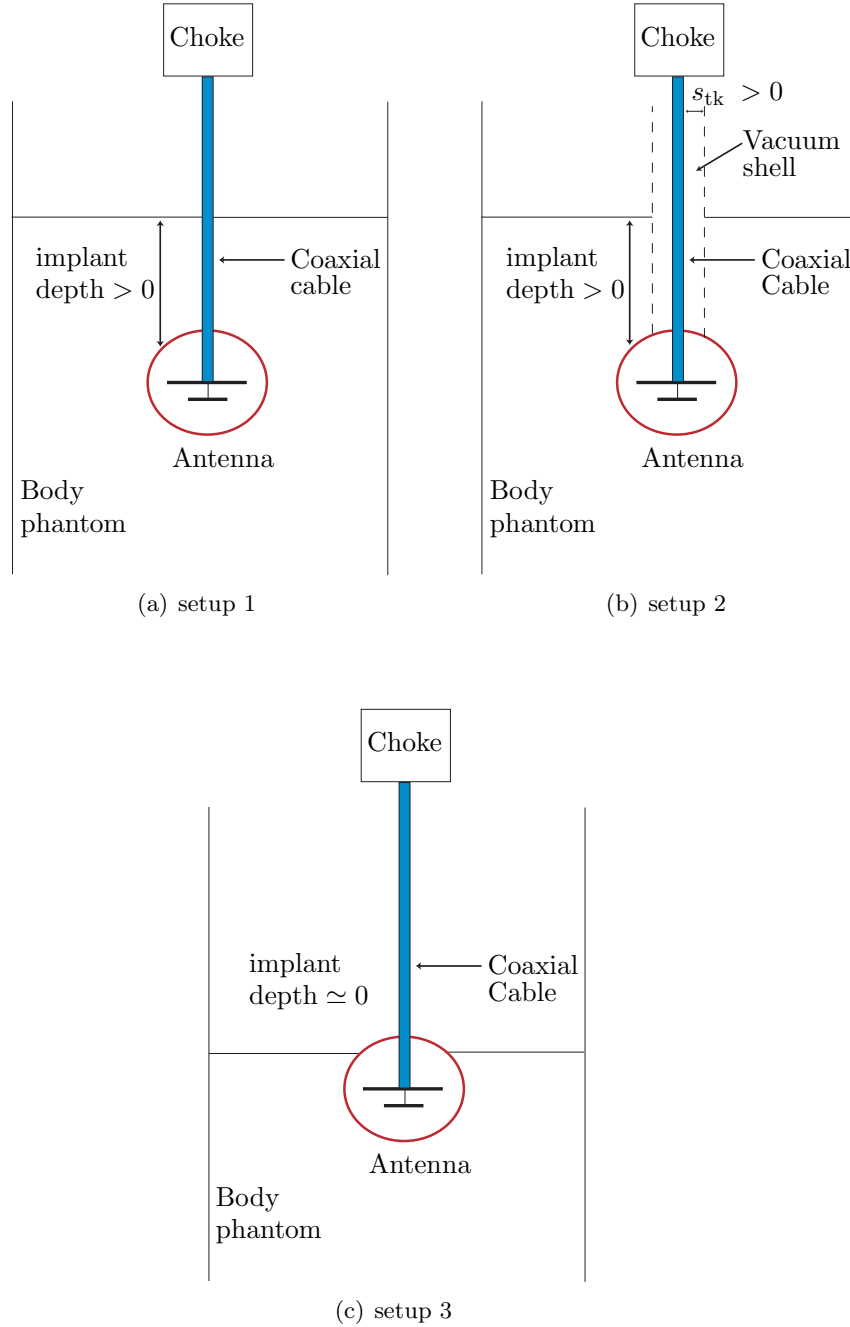
Figure 7.4.: Description of the investigated setups to verify and avoid interference between the feeding cable and the antenna/body phantom. The red solid line indicates the biocompatible insulation, and dashed line identify the vacuum shell surrounding the coaxial feeding cable. A ferrite bead choke was always considered between the slim coaxial cable feeding the antenna and the network analyzer.

Comparing the performances obtained with these different setups, and evaluating their numerical counterparts allow the antenna engineer to identify any cable effects. More specifically, setup 2 and 3 reduce the coupling of the currents present on the external surface of the coaxial cable with the equivalent biological tissues.

These setups are easy to implement from both a practical and the numerical modeling point of view. Comparing the experimental and simulated performances in these different conditions leads to the correct validation its functioning as if implanted. The latter case is reminded in Fig. 7.5, where no cable is present. This setup can be used during the measurements if dedicated wide band electronics are realized and characterized as shown in [219].
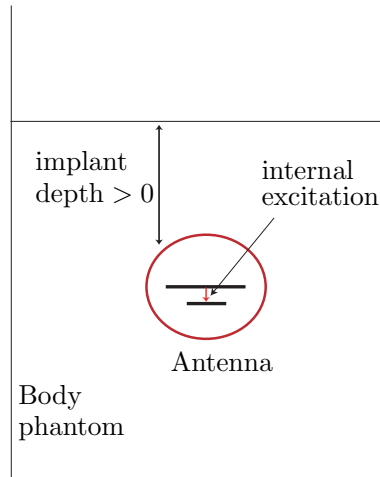
Figure 7.5.: Sketch of the targeted internal excitation for an implantable antenna inserted into a homogenous phantom. The red solid line indicates the biocompatible insulation.

7.3.1. Application to Realized Prototypes

The measurement setups presented in Fig. 7.4 are applied to the in vitro characterization of the Folded Rectangular Helix (FRH) and Multilayered Spiral Antenna (MSA), illustrated in Fig. 7.6.
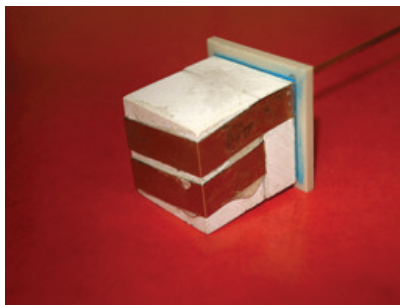
(a)
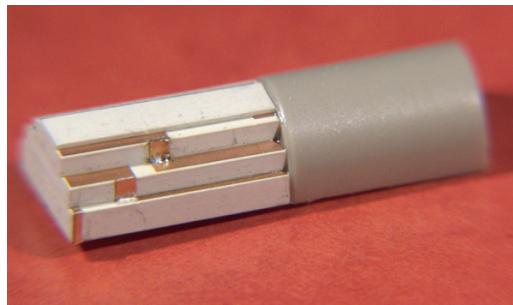
(b)

Figure 7.6.: Realized prototypes: (a) FRH -before adding the biocompatible insulation- and (b) MSA.

Folded Rectangular Helix

Fig. 7.7-(a) shows the close match between the numerical and experimental in vitro character-
ization of the FRH antenna. These performances are obtained considering the direct contact
between the outer conductor and the lossy body phantom, i.e., setup 1, for both the simulated
and experimental values.
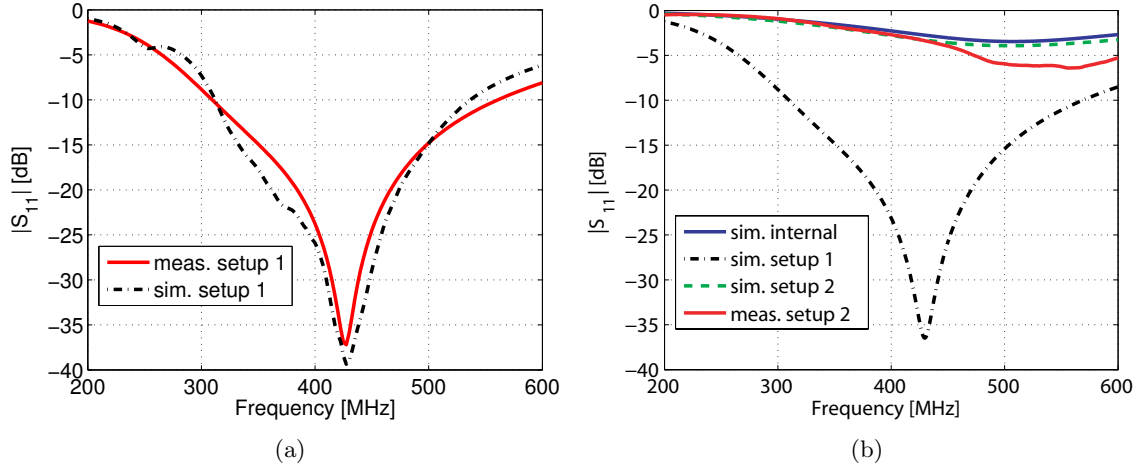
Figure 7.7.: Reflection coefficients $|S_{11}(f)|$: simulations and measurements of the different setups and
numerical analysis with the internal excitation.

Fig. 7.7-(b) shows the measured performances for setup 2, and the simulated results con-
sidering setup 1, setup 2 and the internal excitation (condition depicted in Fig. 7.5). Looking
at these results, one can notice two aspects. First, eliminating the direct contact between the
feeding cable and the body phantom modifies the registered performance of the FRH; indeed,
the measured results considering setup 2 are significantly different from the results of setup 1.
Second, both numerical and experimental results in the presence of the vacuum shell around
the cable (setup 2, obtained with $s_{\text{tk}} = 0.9$ mm) provide the same performance as the one with
the internal excitation. Therefore, it is clear that the simulated and measured performances
reported in Fig. 7.7-(a) are biased by the presence of the feeding cable, as confirmed by the
significant current distributions observed in Fig. 7.8.

Figure 7.8.: Current distributions of significant magnitude are present on the coaxial feeding cable
for the FRH (setup 1). Input power: 1 W.

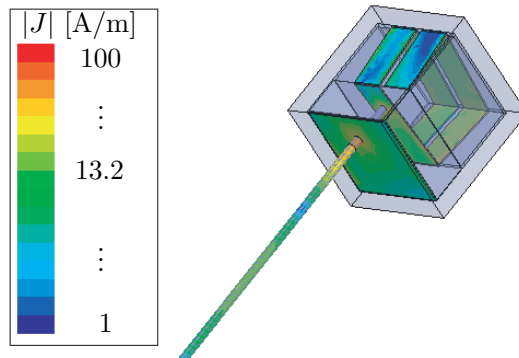The experimental results do still validate the numerical analysis and the technological realization, but the matching behavior is different from what would be obtained if the radiator were fed by an internal power supply as shown in Fig. 7.7-(b)(sim. internal).

Multilayered Spiral Antenna

While the FRH was designed considering the coaxial feeding cable, the MSA has been conceived and realized with its biocompatible casing so as to have an internal power supply. Thus, the identification, and the mitigation, of any effect related to the feeding cable used for testing purposes, is of uppermost importance. The three setups considering this specific antenna are illustrated in Fig. 7.9.
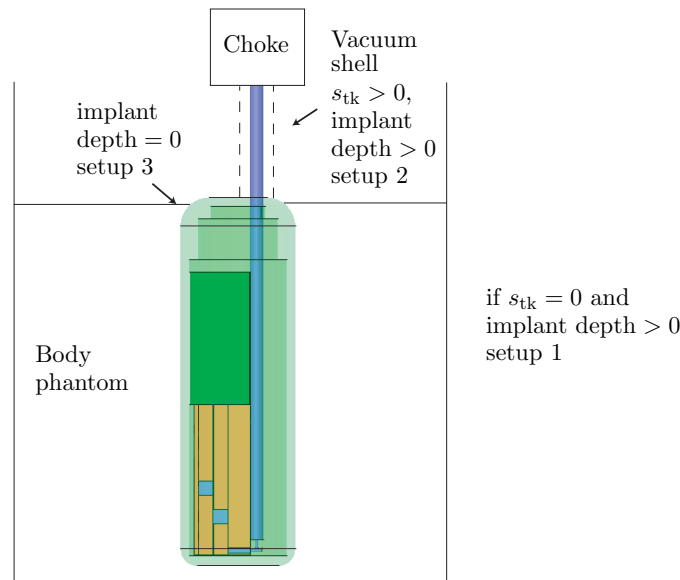
Figure 7.9.: Description of setups 1, 2 and 3 considering the Multilayered Spiral Antenna.

Simulated reflection coefficients for the three setups and the internal excitation are reported in Fig. 7.10-(a). These results show, as for the FRH antenna, that the presence of a coaxial feeding cable modifies the matching of the radiator. By inserting the antenna and the cable directly into the lossy tissue , simulated results (sim. setup 1) are far from the targeted performance (sim. internal). The large coupling between the currents flowing on the cable and the body phantom, is verified by experimental data. Indeed, close match is registered between the simulated and measured performances in accordance with setup 1, as illustrated in Fig. 7.10-(b). Although manifesting results far from the MedRadio range, setup 1 is still useful to prove the validity of the technological realization, and to show that the numerical analysis models well the presence of the cable.

Analyzing the numerical results depicted in Fig. 7.10-(a), it is possible to identify the correct setup to properly characterize the performance of the radiator. In fact, one can appreciate that the simulation obtained reducing the implant depth (sim. setup 3) is in close agreement with the one of the targeted internal excitation (sim. internal); indeed the measurements reported in Section 5.4 and Section 5.4.3 do consider this condition. It is, however important, to underline

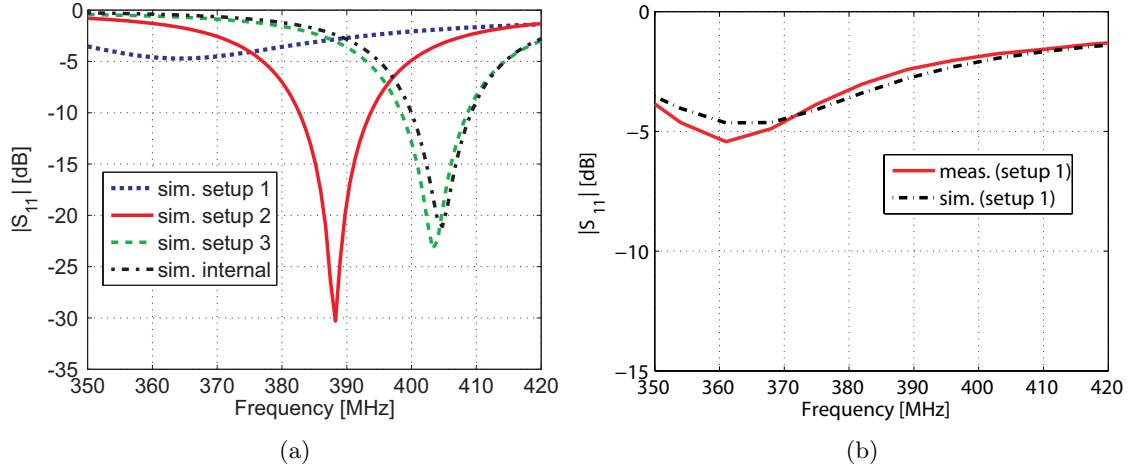**Figure 7.10.:** Reflection coefficients of the MSA: (a) simulation for setups 1, 2, and 3 and the internal excitation, and (b) measurements and simulation for setups 1. In the case of setup 2, the feeding cable is surrounded by a vacuum cylinder with $s_{\text{tk}} = 0.3$ mm.

that the use of setup 3 has been proven to be useful for the considered Multilayered Spiral Antenna only. Indeed, its particular packaging allows to reduce the implant depth without affecting the working behavior of the antenna.

Summary on the Analysis of Realized Prototypes

The analysis performed on the Folded Rectangular Helix radiator and the Multilayered Spiral Antenna showed that different conditions may be used to mitigate the cable effects. For the FRH, setup 2 (i.e., presence of a vacuum shell around the cable) provides close agreement with an internal excitation, while setup 3 (i.e., reduction of the implant depth in the body phantom) gives correct result considering the MSA.

7.3.2. Application to Existing Designs

Every electrically small antenna has its own characteristics, and it may be affected in different ways by the presence of a feeding cable. To confirm the validity of the setups previously discussed, we numerically investigated three implantable antennas respectively based on the designs presented in Kim [18], Karacolak [114] and Lee [164]. Structures as close as possible to the originals were modeled.

These three radiators, depicted in Fig. 7.11, where chosen as they have different characteristics: Kim - single layer spiral, Karacolak - single layer meander PIFA and Lee - multilayered circular PIFA. Regarding the human models, Kim and Lee antennas are implanted in a homogenous phantom with human skin properties, while rat skin properties are considered for the Karacolak radiator. Implant depth (phantom dimension) is 4 mm (72 x 80 x 16 [mm]) for Kim, 4 mm (40 x 30 [mm]) for Lee, and 3 mm (103 x 103 x 30 [mm]) for Karacolak. Fig. 7.12 shows the simulated reflection coefficients resonating in the MedRadio band in agreement with the performances reported in [18, 114, 164].
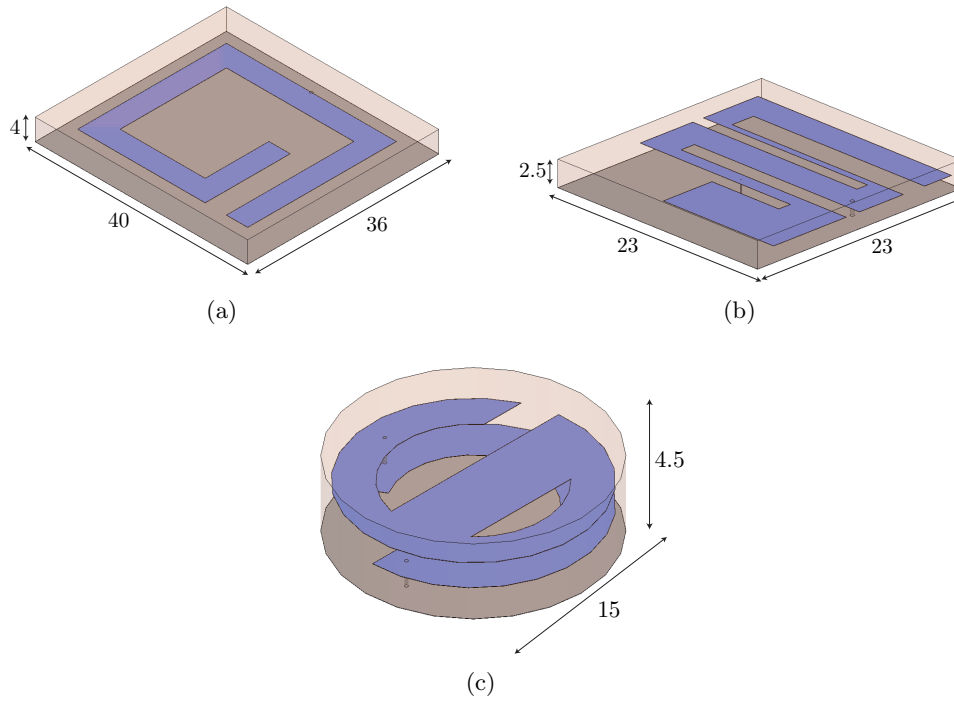
Figure 7.11.: Sketches of the three selected reference antennas: (a) Kim (b) Karacolak and (c) Lee. Substrates are depicted in light pink, dark gray indicates ground planes, while blue represents copper metallizations. All antennas present a superstrate to isolate the copper metallization from the biological tissues. Dimensions are in [mm].
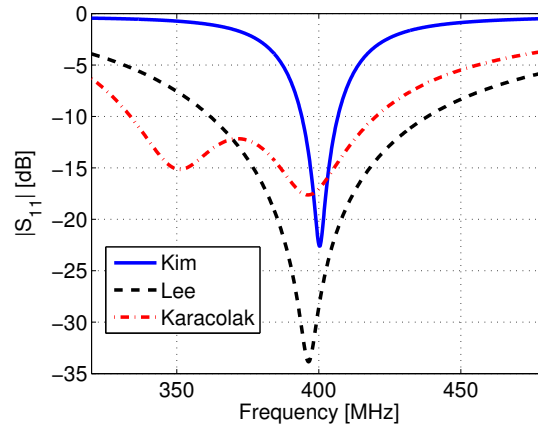
Figure 7.12.: Simulated reflection coefficients of the implantable antennas based on [18, 114, 164] with internal ideal excitations. Satisfactory agreements are found with the results given in the references.

The numerical investigations of the different setups previously presented are reported in Fig. 7.13. These results suggest that the performances of these radiators do not suffer from any cable effects; indeed, minimal variations are registered among setup 2, setup 3 and the internal excitation.

(a)

(b)

(c)
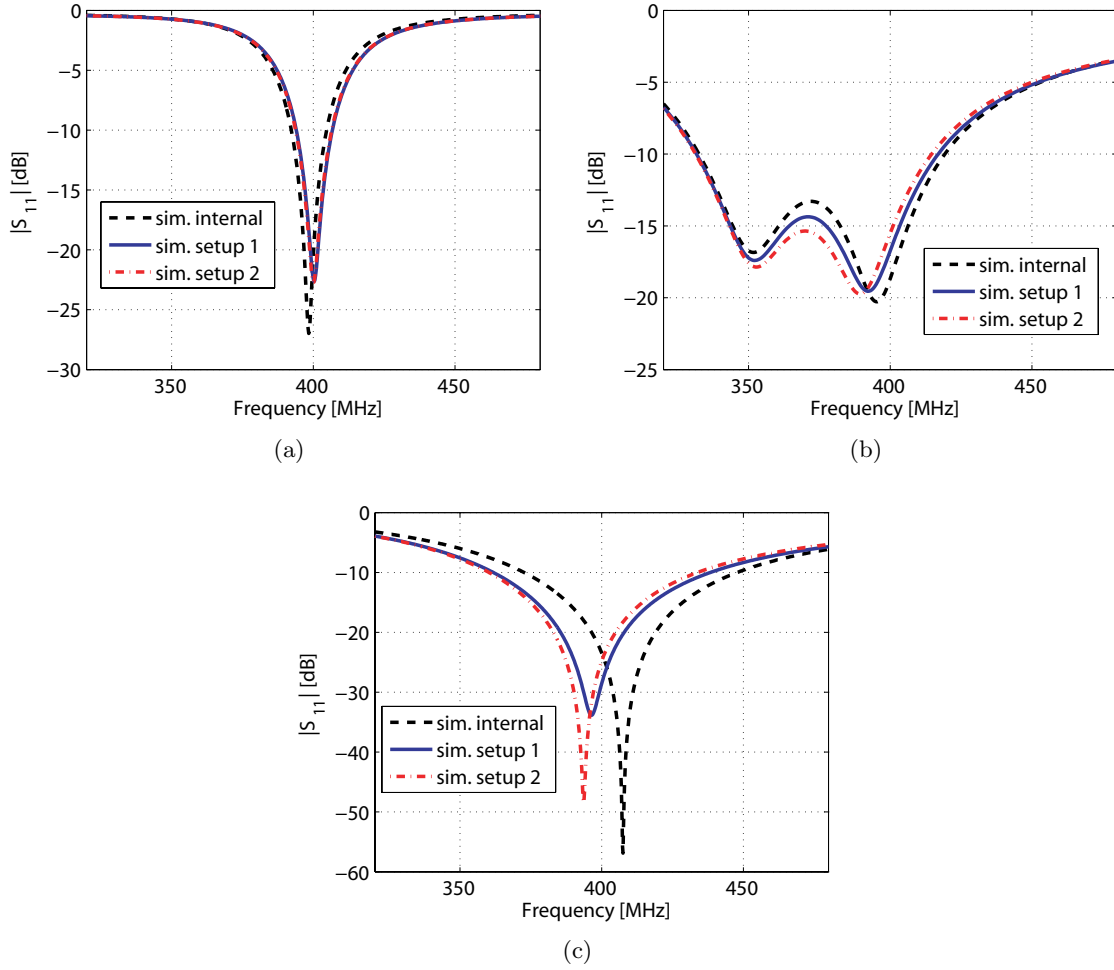
Figure 7.13.: Simulated reflection coefficients, $|S_{11}(f)|$, considering different setups and the internal excitation: (a) Kim (with $s_{\mathrm{tk}} = 2.2$ mm for setup 2), (b) Karacolak ($s_{\mathrm{tk}} = 0.9$ mm for setup 2) and (c) Lee antenna (with $s_{\mathrm{tk}} = 3.4$ mm for setup 2). As for the FRH, setup 3 is not considered as it leads to results that are not linked to a meaningful modeling of the body phantom.

As these results are in contradiction with what has found for the FRH and the MSA radiators, it is worth focusing on the main difference between the realized prototypes and the antennas chosen from the literature. The radiators from [18, 114, 164] consider only a superstrate over the antenna to be isolated from the body, whereas FRH and MSA are completely encapsulated by a biocompatible plastic. As a consequence, the lower/back side of the ground planes of the antennas from [18, 114, 164] are in direct contact with the body phantom. Thus, the currents present there dissipate in the biological tissue and become almost negligible on the feeding cable, as indicated in Fig. 7.14-(a). This is the reason why small variations (in same cases almost negligible) are found considering the conditions for the antennas from [18, 114, 164]. On the contrary, this dissipation does not occur when completely encapsulating the radiator, currents reach the coaxial feeding, and, thus, cable effects are most likely to be present, Fig. 7.14-(b).
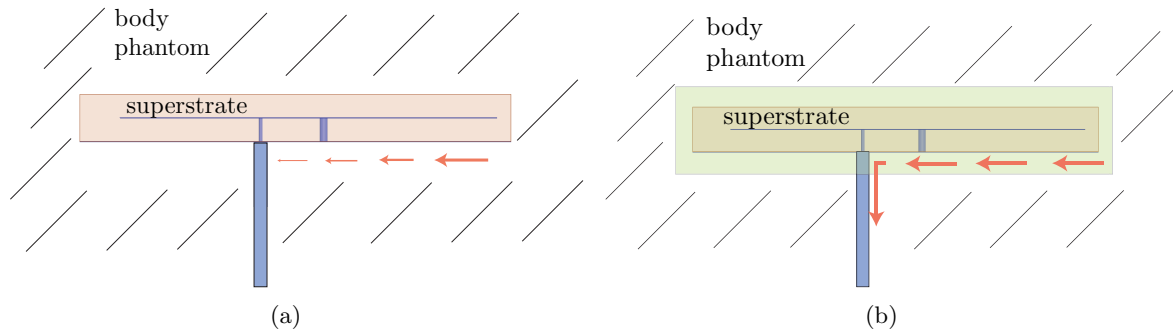
Figure 7.14.: Sketch of the coupling between the currents on the back side of the ground plane and the body phantom considering the Karacolak radiator: (a) without insulation the currents dissipate, thus becoming negligible on the coaxial cable, (b): the presence of a low lossy biocompatible insulation reduces the dissipation into the surrounding lossy medium, thus currents of significant amplitude can reach the cable.

Numerical Results in the Presence of the Biocompatible Insulation

To verify the validity of the previous reasoning, the three antennas were modeled adding completely surrounding insulations. As for the realized prototypes, we chose PEEK (thickness: 1 mm). The insulation presence modifies the electromagnetic behavior of the radiators (resonant frequency shifts towards higher frequencies due to the decreased dielectric loading effect of the body phantom), but this phenomenon is of secondary importance here, as the main focus is on the effect of the feeding cable. First, we investigated the current distribution present on the back side of the ground plane of the antennas and on the feeding cable. The numerical analysis confirmed that the presence of the biocompatible insulation modifies such current distributions. For instance, differences are appreciated in Fig. 7.15 showing the current distributions of the Karacolak antenna with and without insulation. In the absence
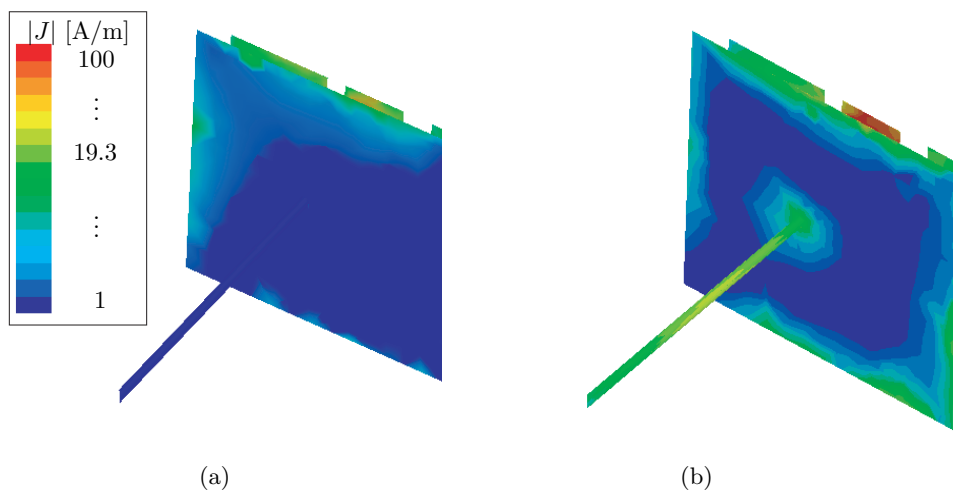
Figure 7.15.: Current distributions at resonance for the Karacolak radiator feed by a coaxial cable in direct contact with the body phantom (setup 1): (a) without and (b) with a PEEK biocompatible insulation completely encapsulating the antenna. Input power: 1 W.

of the insulating material -Fig. 7.15-(a)- negligible currents are present on the outer side of
the coaxial feeding, as almost complete dissipation occurs just after the ground plane edges.
On the contrary, in the model with the PEEK insulator, significant currents reach the coaxial
cable, as shown in Fig. 7.15-(b).

As a second analysis, we focused on the matching performances obtained considering setup
1, setup 2 and the internal excitation. In agreement with the results registered for the realized
prototypes, one can appreciate significant differences when numerically analyzing the different
setups and the internal excitation for the Karacolak and Lee antennas, Fig. 7.16-(b)-(c).
Looking at the results in these two figures, one can notice two aspects. First, the presence of
a vacuum shell surrounding the coaxial cable (setup 2) is confirmed to be an effective way
to mitigate the cable effects for the Karacolak antenna. Second, the Lee radiator is strongly
dependent on the cable itself (even avoiding the contact with the body phantom). Therefore
additional techniques should be considered for the correct assessment of this antenna such as
the use of a balun integrated in the coaxial cable as in [221–223].

(a)   (b)

(c)

Figure 7.16.: Simulated reflection coefficients, $|S_{11}(f)|$, considering different excitations in the pres-
ence of PEEK insulation: (a) Kim with $s_{tk} = 2.2$ mm, (b) Karacolak with $s_{tk} = 0.9$ mm
and (c) Lee with $s_{tk} = 3.4$ mm.

Minimal differences are only found for the Kim antenna, as shown in Fig. 7.16-(a). The fact is explained by the different electrical size of the three radiators. As each antenna is designed considering a different body phantom, we express the electrical size in terms of the free space wavelength λ_0 (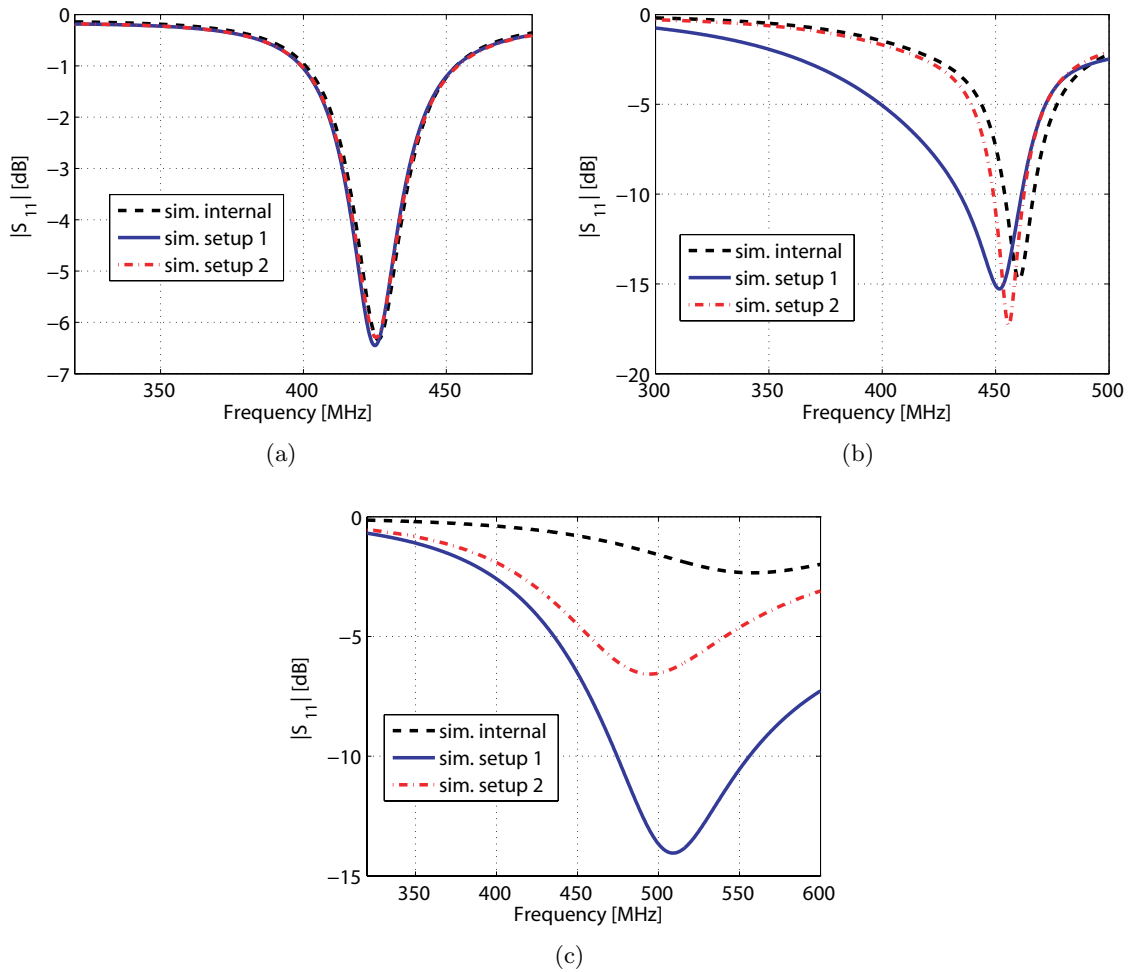74.3 cm at 403.5 MHz) to have a common reference. The Kim radiator is noticeably electrically larger, $\lambda_0/18$, whereas the Karacolak and Lee antennas dimensions are $\lambda_0/32$ and $\lambda_0/49$, respectively.

7.4. Conclusion

This chapter discussed the in vitro characterization of implantable antennas. This work provided information to understand the validity of the experimental results in the MedRadio band reported in the previous chapters.

We showed that the well known feeding cable problems of electrically small antennas can be amplified or hidden by the presence of the body phantom. In order to clearly identify and possibly mitigate any undesired effects related to the presence of a feeding cable, we proposed three simple measurement setups. Two of them were proposed to avoid any disturbance from the cable while still considering its presence. These two solutions are:

- setup 2: presence of a coaxial cable surrounded by a vacuum shell;

- setup 3: reduced implant depth in the body phantom.

The remaining solution (setup 1: direct contact between the cable and the body phantom, which is the most popular measurement condition), is however found useful. Although results could not represent the real working condition of an implantable antenna, it does find a valuable application in order to validate the technological realization.

The coupling between currents on the cable and the body phantom is linked to the electrical size of the radiator. Thus, five different radiators were considered. As expected, the electrically largest investigated radiator is found not to be affected by the cable, while the electrically smallest one requires the use of special solutions as in microwave hyperthermia applications.

The disturbances of the cable do also depend on the presence of the biocompatible insulation. This material affects the coupling between the current on the ground plane of the radiators and the equivalent biological tissues. Two opposite conditions were identified.

First, if prototypes with ground planes in direct contact with the body phantom are considered, the currents dissipate in the lossy matter and small (negligible) cable effects could be expected. In this case the antenna engineer should pay attention only to the conductive material choice; for instance titanium provides excellent biocompatible characteristics, while copper could induce aggressive immune response even when gold plated [120].

Second, if a biocompatible plastic insulation encapsulates the whole device, cable effects must be solved to allow the prototyping of implantable antennas at the component level.

Solutions for the in vitro characterization of the radiating performances (pattern, gain, efficiency) of implantable antennas fed by a cable were not discussed in this chapter because of two open issues.

First, the low radiation efficiency of such radiators ($<1\%$) makes them to be hidden by any perturbing component used during the test. For instance, any minimal current on the cable connecting to a network analyzer (despite the presence of chokes or baluns) is most likely to radiate more than the antenna. Second, as discussed in Chapter 2 and Section 5.5.1, realistic body phantoms are necessary to carefully evaluate the radiation parameters.

Further investigations are necessary to provide solutions to these aspects so as to allow the complete and correct assessment of the characteristics of implantable antennas.

8. Conclusions and Future Work

The work performed in the framework of this thesis aims at paving the use of telemedicine with the use of wireless implantable devices. In fact, despite the great academic and industrial interest on the topic, still few applications make use of such a technology. Besides the pacemaker, the state of the art of implantable sensors commercially available can be represented by the *GlucoDay S*[*] and the *Pillcam*[¶] systems for glucose monitoring and endoscopy, respectively. The former, illustrated in Fig. 8.1.-(a), is a wearable device with a pervasive micro-fibre capable of measuring the glucose concentration from the interstitial liquid. The latter, shown in Fig. 8.1.-(b) provides images from the digestive tract over a very short distance (receivers are stitched on the skin of the patient). Both solutions, although extraordinarily improving the medical diagnosis, do not answer to the request of a healthcare monitoring system as "transparent" as possible to the patient.

(a)   (b)

Figure 8.1.: Examples of commercially available implantable monitoring devices: (a) *GlucoDay S* and (b) *Pillcam*.

In order to extend the working range and reducing the use of pervasive components, this thesis tackled the wireless transmission of information from inside the body. Keeping into account a wide range of technical and medical concerns, the focus has been concentrated on the antennas, one of the most challenging elements of an implantable device targeting far field data telemetry. In addition to the classical antenna problems, such as miniaturization and its consequent decrease of radiation efficiency, we paid particular attention to the coupling of the EM field with the biological lossy tissues. Furthermore, biocompatibility, physical requirements and the tight coexistence among all the components present in an entire sensor have been taken into account.

The performed investigations provided a better understanding of the working characteristics of implantable antennas, and led to the realization of Body Sensor Node for far field data telemetry. This node was used to investigate the influence of the temperature on the healing process of a deep wound operated in the skin of animals and to monitor glucose and dopamine. Realizing such a BSN required the study of several aspects, and the next section precisely recalls the assessments of this thesis in the general optic of an entire wireless implantable system for healthcare monitoring applications.

---

[*]http://www.glucomen.co.uk/
[¶]http://www.givenimaging.com/en-us/Pages/GivenWelcomePage.aspx

8.1. Thesis Assessment

Among the salient aspects of a wireless implantable system, identified in Fig. 1.2, the achievements of this thesis can be classified according to the following topics:

- Human Body (and lossy matter in general);

- Insulations;

- Implantable Antennas;

- Characterization and Experiments.

The main assessments associated with each part are summarized and discussed below.

Human Body (and lossy matter in general)

In Chapter 2, we discussed the impact of the presence of the human body. To understand the physical consequences of such a presence, the theory of antennas in lossy matter has been revisited in the light of our purposes. This analysis, supported by numerical investigations, was fundamental to identify the challenges of the design of antennas in lossy matter before targeting practical implantable realizations.

The focus has then been shifted on the complicated, dispersive and highly lossy (for the EM propagation) characteristics of the human body. Thus, we reviewed and discussed the available phantoms in terms of modeling and physical realizations.

This analysis does not fully constitute an original contribution, but rather consists in revisiting and extending some existing knowledge for the design of antennas surrounded by lossy biological tissues, thus providing a solid base for the work presented further on.

Insulations

In order to reduce and control the coupling between the EM field and the lossy biological tissues, we investigated the effect of insulating layers in Chapter 3. We first identified the main phenomena in which insulations layers play a role, and consequently A specifically oriented physical and mathematical models were presented. Accordingly, we proposed a numerical tool to analyze and quantify these phenomena. We described the analytical development and numerical implementation based on the Mode Matching Technique of the Spherical Wave Expansion of the EM field. Three different body models and three different sources were taken into account. For instance, a proper choice of the internal biocompatible insulation leads up to a power transfer from the implanted source to the external receiver six-times more efficient. Although the goal was to consider sources deeply implanted, the analytical formulation and the numerical issues related to the subcutaneous analysis are also discussed.

The extensive analysis confirmed and extended the comprehension of the beneficial effects of the insulating layers. The results, for the first time, clearly identify the trade-off that the antenna engineer should make between the volume available for the radiator and the biocompatible casing of an implantable device.

Implantable Antennas

The specificity of the implantable antenna design was addressed in Chapter 4. Solutions proposed in the literature have been revisited to identify the main characteristics and the open issues in the implantable antenna field. This analysis led to some preliminary investigations that focused on different aspects, such as dual band performance, miniaturization techniques, technological realizations, integration and packaging with all the components of a complete device. Based on the acquired knowledge, the formulation of an efficient design strategy was proposed.

This strategy was applied in Chapter 5, where the miniature, conformal, dual band, versatile Multilayered Spiral Antenna is presented. This design fulfills all implantable antenna requirements allowing real life applications. Different design steps and body models (from rough approximations to most realistic ones) were reported first to show the usefulness of the proposed strategy, and, second, to provide complete understanding of the performances of the radiator. Specific technological and numerical issues were also addressed to underline all the aspects that the antenna engineer must take into account.

Characterization and Experiments

The in vitro characterization and in vivo experiments of an entire Body Sensor Node for telemedicine were detailed in Chapter 6. The novel MSA was integrated and packaged with all the active components to form a functioning implantable device. This work bridged the starting approaches of the antenna and system engineers.

Two in vivo experiments were carried out performing the realization of an entire telemedicine system remotely accessible. Challenges, solutions and issues far beyond the EM aspects, were presented and detailed to provide a further step towards the use of telemedicine in real life.

Particular attention has been paid to the in vitro characterization of the antenna alone in Chapter 7. The well known problems of measuring electrically small antennas fed by coaxial cables were revisited from the implantable antenna point of view. For the first time, the interaction between a feeding cable -used for testing purposes- and the body phantom was investigated. Simple, but mandatory, solutions were presented and applied to several radiators.

8.2. Perspectives

In this thesis, several aspects related to the implantable antennas have been addressed. However, there are improvements and open issues that should be further investigated.

Body Centric EM Propagation: the propagation of EM waves from inside the body to an external or wearable Base Station is of great importance. The understanding of all the phenomena (such as multi-path, excitation of surface waves, etc.) is given a lot of attention but it does still requires further investigations to make telemedicine a reality. This aspect encompasses the design of specific antennas for the Base station, either off- or on-body placed.

Body Phantoms and In Vitro Characterization: while models of excellent precision are numerically available to mimic the human body, their use and practical realization are still field of active research. On the one hand, the analysis of such detailed models require computational power that often cannot be afforded during the design process of implantable

antennas. On the other hand, radiation characteristics should be evaluated considering the geometry of the human body as it does contributes to the EM wave. Therefore, engineered solutions must be identified to model and realize the human body while preserving the accuracy required to efficiently design and characterize the radiators (at the system and the component levels). Regarding the latter point, it is important to remind the undesired effects that might occur when considering the presence of a coaxial feeding cable, as shown in Chapter 7. As the proposed solutions depend on the characteristics of the antenna under test (electrical size, insulation, etc.), measurements with an optical fiber shall be taken in the future.

Bioelectromagnetism: this thesis focuses on the EM radiation from an implanted antenna towards an external Base Station. For this purpose, the human body is modeled by a series of dielectric materials. However, interaction of the EM field on the biological characteristics and functioning of the cells/organs is of great interest. Considering this point of view would also allow the analysis of the biological hazards of EM field, and its Specific Absorption Rate surrogate, which is very relevant in the case of implantable antennas.

EM Compatibility and Privacy: the presence and capabilities of implantable devices have great potential to improve the healthcare system. However, the presence of such devices has to be compatible with the use of other well established EM diagnostic tools, for instance the Magnetic Resonance Imaging. Furthermore, the wireless transmission of private physiological data -which is a very sensitive information- and the remote control of implantable devices, introduce potential vulnerabilities to adversaries that can result in life-threatening situations as well as compromises of privacy. Therefore both aspects need to be carefully investigated.

Performances and Miniaturization - Always Ask for More: there are two opposite demands from the doctor's and the patient's perspective to any implantable device. First, more and more capabilities and performances are requested to improve the healthcare system. Second, only extreme miniaturization (dimensions as small as a grain of rice!) would considerably reduce the physical and psychological invasiveness of an implant. Thus, there is an endless need of improving the characteristics of an implant (including its antennas) to answer to these opposite requests.

Wireless Power Transfer: in order to extend the life time of an implant and reduce its volume, wireless data transmission can include, or work side by side with, power transfer. This capability calls for the design of antennas that share different working functionalities or coexist with different EM systems. The realization of implantable device with both data and power transfer technologies is one of the present and future research line in medical implantable devices.

A. Appendix: Mathematical Model

A.1. Spherical Wave Basis Functions Orthogonality Properties

The spherical modal vectors $\mathbf{M}_{mn}^{vs}$ and $\mathbf{N}_{mn}^{vs}$ have several orthogonality properties. The ones used to get the radiated power formula (3.10) are:

$$\oint_{S_r} \left(\begin{array}{c} \mathbf{M}_{mn}^{vs} \\ \mathbf{N}_{mn}^{vs} \end{array} \times \begin{array}{c} \overline{\mathbf{M}_{m'n'}^{v's'}} \\ \overline{\mathbf{N}_{m'n'}^{v's'}} \end{array} \right) \cdot \vec{dS} = 0 \tag{A-1}$$

and

$$\oint_{S_r} \left(\mathbf{M}_{mn}^{vs} \times \overline{\mathbf{N}_{m'n'}^{v's'}} \right) \cdot \vec{dS} = \cdots \tag{A-2}$$

$$\frac{\lambda_{mn}^v}{|k|^2} |z|^2 Z_n^s(z) \overline{K_n^{s'}(z)} \delta_{v,v'} \delta_{m,m'} \delta_{n,n'}$$

S_r is a sphere centered at the origin and δ is the Krönecker symbol.

A.2. Spherical Wave Basis Functions Asymptotic Properties

A.2.1. Large values of N

For $z \neq 0$, $n \to +\infty$, following [140, eq. 9.3.1] (where $Z_n^1(z) = j_n(z)$ and $Z_n^4(z) = h_n^{(2)}(z)$) and[226], we obtain:

$$\left\{ \begin{array}{c} Z_n^1(z) \\ \\ K_n^1(z) \end{array} \right\} = \left\{ \begin{array}{c} \sqrt{\dfrac{1}{2z(2n+1)}} \left(\dfrac{ez}{2n+1} \right)^{(n+1/2)} \left(1 + O\!\left(1/|n| \right) \right) \\ \\ \dfrac{1}{\sqrt{2e}} \left(\dfrac{ez}{2n-1} \right)^n - \dfrac{1}{2n+1} \sqrt{\dfrac{e}{2}} \left(\dfrac{ez}{2n+1} \right)^n \left(1 + O\!\left(1/|n| \right) \right) \end{array} \right\} \tag{A-3}$$

$$
\left\{
\begin{array}{c}
Z_n^4(z) \\
\\
K_n^4(z)
\end{array}
\right\}
=
\left\{
\begin{array}{c}
j\sqrt{\dfrac{2}{z(2n+1)}}\left(\dfrac{ez}{2n+1}\right)^{(-n-1/2)}\left(1+O\!\left(1/|n|\right)\right) \\
\\
j\dfrac{\sqrt{2e}}{2n-1}\left(\dfrac{ez}{2n-1}\right)^{-n}-j\dfrac{n}{z^2}\sqrt{\dfrac{2}{e}}\left(\dfrac{ez}{2n+1}\right)^{-n}\left(1+O\!\left(1/|n|\right)\right)
\end{array}
\right\}
\qquad \text{(A-4)}
$$

A.2.2. Small Argument

As $|k|r \to 0$ we introduced asymptotic values [140, eqs. 10.1.4-5] for $n = 1, 2, \dots$:

$$
\left\{
\begin{array}{c}
Z_n^1(z) \\
K_n^1(z)
\end{array}
\right\}
\rightarrow
\left\{
\begin{array}{c}
\dfrac{z^n}{(2n+1)!!} \\
z^{n-1}\dfrac{n+1}{(2n+1)!!}
\end{array}
\right\}
\qquad \text{(A-5)}
$$

which, evaluated at the origin, give:

$$
\left\{
\begin{array}{c}
Z_n^1(0) \\
K_n^1(0)
\end{array}
\right\}
=
\left\{
\begin{array}{c}
0 \\
2/3 \text{ for n} = 1, \ 0 \text{ otherwise}
\end{array}
\right\}
\qquad \text{(A-6)}
$$

The functions Z_n^4, K_n^4 have the following asymptotic behavior, given in [140, eqs. 10.1.4-5], as $|k|r \to 0$ and for $n = 1, 2, \dots$:

$$
\left\{
\begin{array}{c}
Z_n^4(kr) \\
K_n^4(kr)
\end{array}
\right\}
\rightarrow
\left\{
\begin{array}{c}
\dfrac{1}{(2n+1)!!}(kr)^n + j\,(2n-1)!!\,(kr)^{-(n+1)} \\
\dfrac{n+1}{(2n+1)!!}(kr)^{n-1} - j\,n(2n-1)!!\,(kr)^{-(n+2)}
\end{array}
\right\}
\qquad \text{(A-7)}
$$

Please note that $K_n^4(z)$ in (A-7) is obtained with the following development (taking advantage of [140, eqs. 10.1.19]):

$$
\begin{aligned}
K_n^4(z) &= \frac{1}{z}\frac{d}{dz}\left(z Z_n^4(z)\right) && \text{(A-8)} \\
&= Z_{n-1}^4(z) - \frac{n}{z} Z_n^4(z) \\
&= j_{n-1} - j\,y_{n-1} - \frac{n}{z}(j_n - j\,y_n) \\
&= j_{n-1} - j\left(\frac{2n+1}{z}\,y_n - y_{n+1}\right) - \frac{n}{z}\,(j_n - j\,y_n)
\end{aligned}
$$

and substituting the expression of j_n and y_n given in [140, eqs. 10.1.4-5].

A.2.3. Large Argument

The asymptotic expressions of the spherical Hankel functions $|z| \to \infty$ [140, eqs. 9.2.1]:

$$\left\{ \begin{array}{c} Z_n^4(z) \\ K_n^4(z) \end{array} \right\} = \left\{ \begin{array}{c} \mathrm{j} \\ 1 \end{array} \right\} \mathrm{j}^n \frac{e^{-\mathrm{j}z}}{z} + O\big(1/|z|^2\big) \tag{A-9}$$

A.3. Ideal Excitations in a Bounded Lossy Medium

A Hertzian dipole radiating in an unbounded lossy medium must be supplied with infinite power, which is not physically meaningful, as shown in [133]. This still applies for a dipole placed in a bounded lossy spherical shell. Equation (3.10) can be rewritten:

$$P_{\text{rad}}(r) = \frac{r^2}{2|\zeta|^2} \text{Re}\Big\{ \mathrm{j}\zeta \sum_{n,m,v,s} \gamma_{mn}^{vs}(kr) \Big\}, \tag{A-10}$$

where ζ and k are complex values in a lossy shell. γ_{mn}^{vs} is a product of spherical modal coefficients and Bessel functions. If one lets r approach zero in (A-10), it can be easily shown that P_{rad} becomes infinite. One term of (A-10) is indeed proportional to $\mathrm{j}r^2 Z_n^4(kr)\overline{K_n^4(kr)}$ which has a dominant $(kr)^{-(2n+1)} + O(kr^{-2n+1})$ dependency when r tends toward zero [140, eqs. 10.1.4-5]. It is important to note that the $(kr)^{-(2n+1)}$ component does add to the real radiated power when k is complex while its contribution is purely imaginary (i.e., null) in a lossless case. This result, valid also for the magnetic dipole and Huygens source, confirms and extends the demonstration given in [133].

A.4. Diffracted Spherical Coefficients for Concentric Spheres

The analytical formulation of the diffracted coefficients a_{mn}^{dvs} - b_{mn}^{dvs} is presented. All the coefficients expressed here are diffracted unless explicitly indicated. In fact, the superscript d is dropped and substituted with p to identify the shell in which the given expression is valid.

A.4.1. Source in the Innermost Shell

If the excitation is placed in the innermost shell ($p = 1$), considering the model depicted in Fig. 3.5, the following conditions are true

$$\left[\begin{array}{c} a_{mn}^{1v,4} = a_{mn}^{iv,4} \\ b_{mn}^{1v,4} = b_{mn}^{iv,4} \end{array} \right] \text{ and } \left[\begin{array}{c} a_{mn}^{q+1v,1} = 0 \\ b_{mn}^{q+1v,1} = 0 \end{array} \right] \tag{A-11}$$

Substituting (A-11) into (3.26) and (3.27) and keeping in mind the considerations presented by Wilcox [139], it is possible to explicitly obtain the diffracted coefficients as

$$p = 1 : \left\{ a_{mn}^{1v,1} = -\frac{T_{q,n_{12}}^a}{T_{q,n_{11}}^a}\, a_{mn}^{iv,4}\, , \, b_{mn}^{1v,1} = -\frac{T_{q,n_{12}}^b}{T_{q,n_{11}}^b}\, b_{mn}^{iv,4} \right. \tag{A-12}$$

$$2 \leq p \leq q : \begin{cases} a^{pv,1}_{mn} = \left[\dfrac{(T^a_{p-1,n_{11}})(-T^a_{q,n_{12}})}{T^a_{q,n_{11}}} + T^a_{p-1,n_{12}} \right] a^{iv,4}_{mn} \\[2em] b^{pv,1}_{mn} = \left[\dfrac{(T^b_{p-1,n_{11}})(-T^b_{q,n_{12}})}{T^b_{q,n_{11}}} + T^b_{p-1,n_{12}} \right] b^{iv,4}_{mn} \\[2em] a^{pv,4}_{mn} = \left[\dfrac{(T^a_{p-1,n_{21}})(-T^a_{q,n_{12}})}{T^a_{q,n_{11}}} + T^a_{p-1,n_{22}} \right] a^{iv,4}_{mn} \\[2em] b^{pv,4}_{mn} = \left[\dfrac{(T^b_{p-1,n_{21}})(-T^b_{q,n_{12}})}{T^b_{q,n_{11}}} + T^b_{p-1,n_{22}} \right] b^{iv,4}_{mn} \end{cases} \tag{A-13}$$

$$p = q + 1 : \begin{cases} a^{q+1v,4}_{mn} = \left[\dfrac{(T^a_{q,n_{21}})(-T^a_{q,n_{12}})}{T^a_{q,n_{11}}} + T^a_{q,n_{22}} \right] a^{iv,4}_{mn} \\[2em] b^{q+1v,4}_{mn} = \left[\dfrac{(T^b_{q,n_{21}})(-T^b_{q,n_{12}})}{T^b_{q,n_{11}}} + T^b_{q,n_{22}} \right] b^{iv,4}_{mn} \end{cases} \tag{A-14}$$

A.4.2. Source in an Intermediate Shell

If the excitation is placed in an intermediate shell ($p = s$ with $1 < s \leq q$) of the model depicted in Fig. 3.5, the following conditions apply

$$\left[\begin{array}{c} a^{1v,4}_{mn} = 0 \\ b^{1v,4}_{mn} = 0 \end{array} \right] \text{ and } \left[\begin{array}{c} a^{q+1v,1}_{mn} = 0 \\ b^{q+1v,1}_{mn} = 0 \end{array} \right] \tag{A-15}$$

Substituting (A-15) into (3.26) and (3.27) we obtain:

$$p = 1 \begin{cases} a^{1v,1}_{mn} = \dfrac{a^{iv,1}_{mn} - \dfrac{T^{s,a}_{q,n_{12}}}{T^{s,a}_{q,n_{11}}} a^{iv,4}_{mn}}{T^a_{s-1,n_{11}} + \dfrac{T^{s,a}_{q,n_{12}}}{T^{s,a}_{q,n_{11}} T^a_{s-1,n_{11}}} T^a_{s-1,n_{21}}} \\[3em] b^{1v,1}_{mn} = \dfrac{b^{iv,1}_{mn} - \dfrac{T^{s,b}_{q,n_{12}}}{T^{s,b}_{q,n_{11}}} b^{iv,4}_{mn}}{T^b_{s-1,n_{11}} + \dfrac{T^{s,b}_{q,n_{12}}}{T^{s,b}_{q,n_{11}} T^b_{s-1,n_{11}}} T^b_{s-1,n_{21}}} \end{cases} \tag{A-16}$$

$$2 \leq p \leq s - 1 : \begin{cases} a^{pv,1}_{mn} = T^a_{p-1,n_{11}} a^{1v,1}_{mn} \ , \ b^{pv,1}_{mn} = T^b_{p-1,n_{11}} b^{1v,1}_{mn} \\[1em] a^{pv,4}_{mn} = T^a_{p-1,n_{21}} a^{1v,1}_{mn} \ , \ b^{pv,4}_{mn} = T^b_{p-1,n_{21}} b^{1v,1}_{mn} \end{cases} \tag{A-17}$$

$$p = s : \begin{cases} a^{sv,1}_{mn} = -\dfrac{T^{s,a}_{q,n\,12}}{T^{s,a}_{q,n\,11}}\,(a^{iv,4}_{mn} + a^{sv,4}_{mn}) \;,\; b^{sv,1}_{mn} = -\dfrac{T^{s,b}_{q,n\,12}}{T^{s,b}_{q,n\,11}}\,(b^{iv,4}_{mn} + b^{sv,4}_{mn}) \\[2mm] a^{sv,4}_{mn} = T^{a}_{s-1,n\,21}a^{1v,1}_{mn} \;, \qquad\qquad\quad b^{sv,4}_{mn} = T^{b}_{s-1,n\,21}b^{1v,1}_{mn} \end{cases} \tag{A-18}$$

$$s+1 \le p \le q : \begin{cases} a^{pv,1}_{mn} = T^{s,a}_{p,n\,11}a^{sv,1}_{mn} + T^{s,a}_{p,n\,12}(a^{sv,1}_{mn} + a^{iv,1}_{mn}) \\[2mm] b^{pv,1}_{mn} = T^{s,b}_{p,n\,11}b^{sv,1}_{mn} + T^{s,b}_{p,n\,12}(b^{sv,1}_{mn} + b^{iv,1}_{mn}) \\[2mm] a^{pv,4}_{mn} = T^{s,a}_{p,n\,21}a^{sv,1}_{mn} + T^{s,a}_{p,n\,22}(a^{sv,1}_{mn} + a^{iv,1}_{mn}) \\[2mm] b^{pv,4}_{mn} = T^{s,b}_{p,n\,21}b^{sv,1}_{mn} + T^{s,b}_{p,n\,22}(b^{sv,1}_{mn} + b^{iv,1}_{mn}) \end{cases} \tag{A-19}$$

$$p = q+1 : \begin{cases} a^{q+1v,4}_{mn} = T^{s,a}_{q,n\,21}a^{sv,1}_{mn} + T^{s,a}_{q,n\,22}(a^{sv,1}_{mn} + a^{iv,1}_{mn}) \\[2mm] b^{q+1v,4}_{mn} = T^{s,b}_{q,n\,21}b^{sv,1}_{mn} + T^{s,b}_{q,n\,22}(b^{sv,1}_{mn} + b^{iv,1}_{mn}) \end{cases} \tag{A-20}$$

where $T^{s,a}_{q,n} = \prod_{i=q}^{s} M^{a,i}_{n}$ and $T^{s,b}_{q,n} = \prod_{i=q}^{s} M^{b,i}_{n}$.

A.4.3. Source in the Outer Space

If the excitation is placed in the outer space ($p = q+1$ shell) of the model depicted in Fig. 3.5, the following conditions are true

$$\begin{bmatrix} a^{1v,4}_{mn} = 0 \\ b^{1v,4}_{mn} = 0 \end{bmatrix} \text{ and } \begin{bmatrix} a^{q+1v,1}_{mn} = a^{iv,1}_{mn} \\ b^{q+1v,1}_{mn} = b^{iv,1}_{mn} \end{bmatrix} \tag{A-21}$$

Substituting (A-21) into (3.26) and (3.27) and keeping in mind the considerations presented in [139], the diffracted coefficients are expressed as

$$p = 1 : \begin{cases} a^{1v,1}_{mn} = \dfrac{1}{T^{a}_{q,n\,11}}\,a^{iv,1}_{mn} \;,\; b^{1v,1}_{mn} = \dfrac{1}{T^{b}_{q,n\,11}}\,b^{iv,1}_{mn} \end{cases} \tag{A-22}$$

$$2 \le p \le q : \begin{cases} a^{pv,1}_{mn} = \dfrac{T^{a}_{p-1,n\,11}}{T^{a}_{q,n\,11}}\,a^{iv,1}_{mn} \;,\; b^{pv,1}_{mn} = \dfrac{T^{b}_{p-1,n\,11}}{T^{b}_{q,n\,11}}\,b^{iv,1}_{mn} \\[3mm] a^{pv,4}_{mn} = \dfrac{T^{a}_{p-1,n\,21}}{T^{a}_{q,n\,11}}\,a^{iv,1}_{mn} \;,\; b^{pv,4}_{mn} = \dfrac{T^{b}_{p-1,n\,21}}{T^{b}_{q,n\,11}}\,b^{iv,1}_{mn} \end{cases} \tag{A-23}$$

$$p = q+1 : \begin{cases} a^{q+1v,4}_{mn} = \dfrac{T^{a}_{q,n\,21}}{T^{a}_{q,n\,11}}\,a^{iv,1}_{mn} \;,\; b^{q+1v,4}_{mn} = \dfrac{T^{b}_{q,n\,21}}{T^{b}_{q,n\,11}}\,b^{iv,1}_{mn} \end{cases} \tag{A-24}$$

B. Appendix: Geometries of the Preliminary Investigated Implantable Antennas
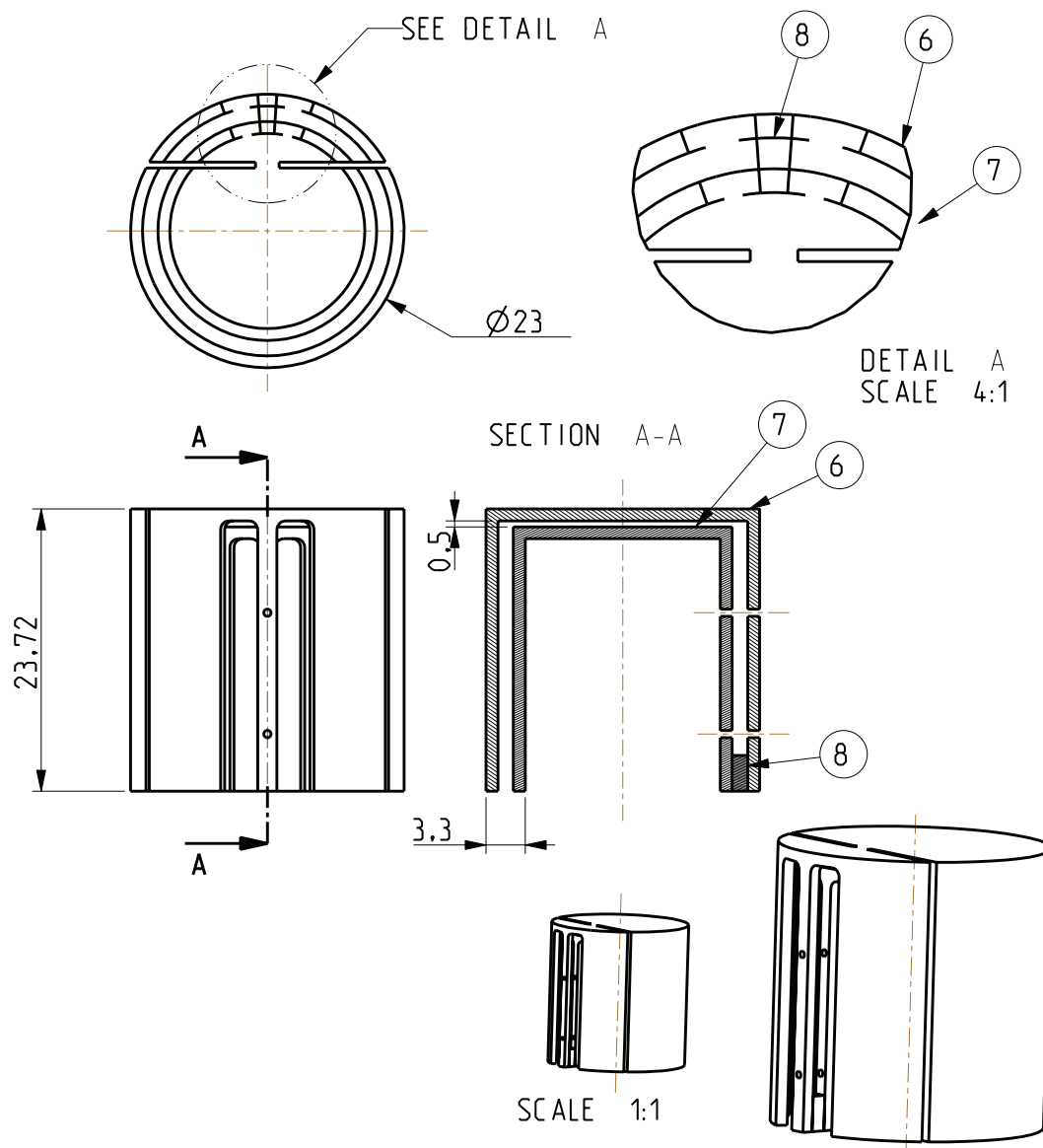
B.1. Folded Inverted-F Antenna

Figure B.1.: FIFA.Dimensions in [mm].
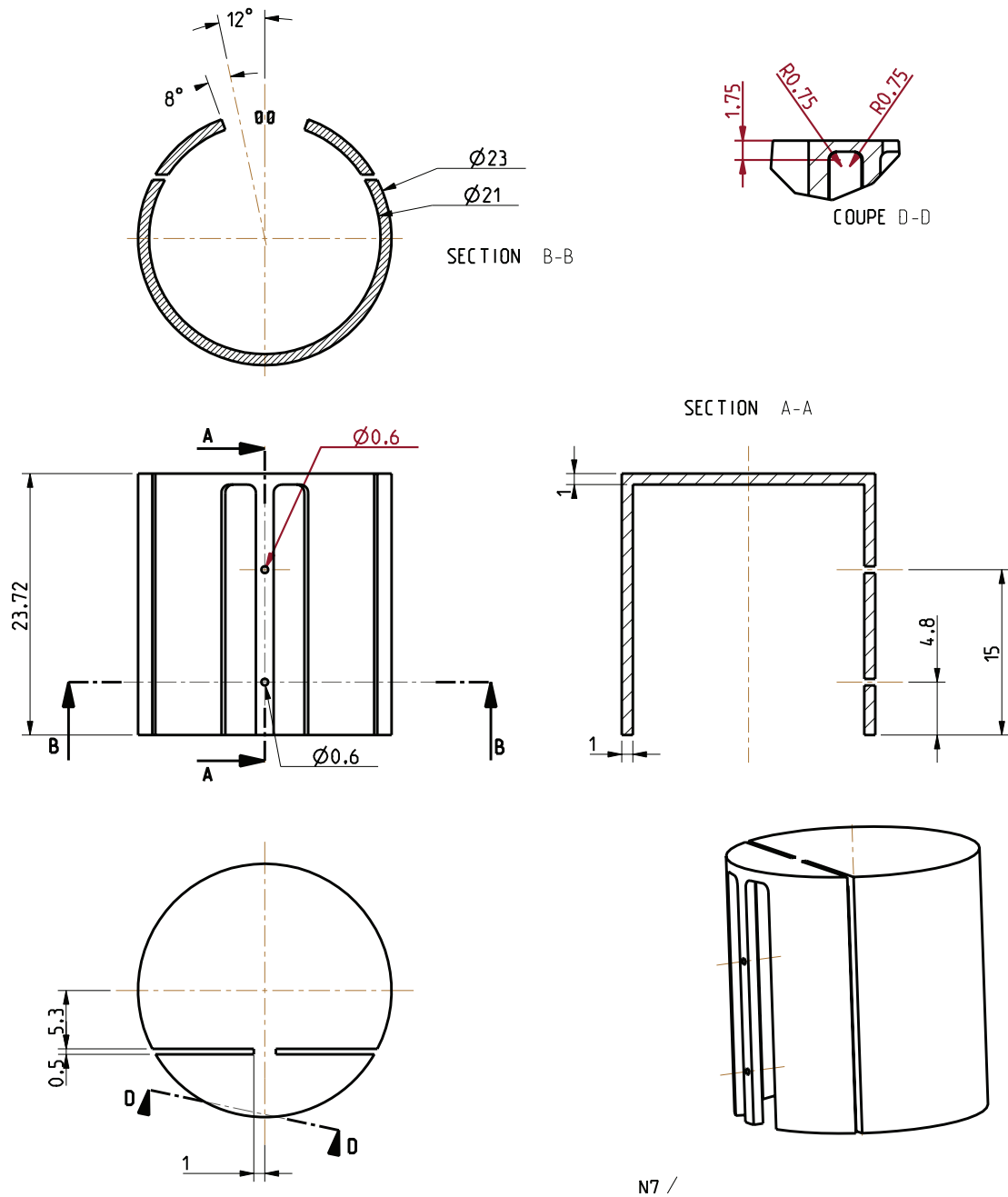
Figure B.2.: FIFA patch piece (copper). Dimensions in [mm].
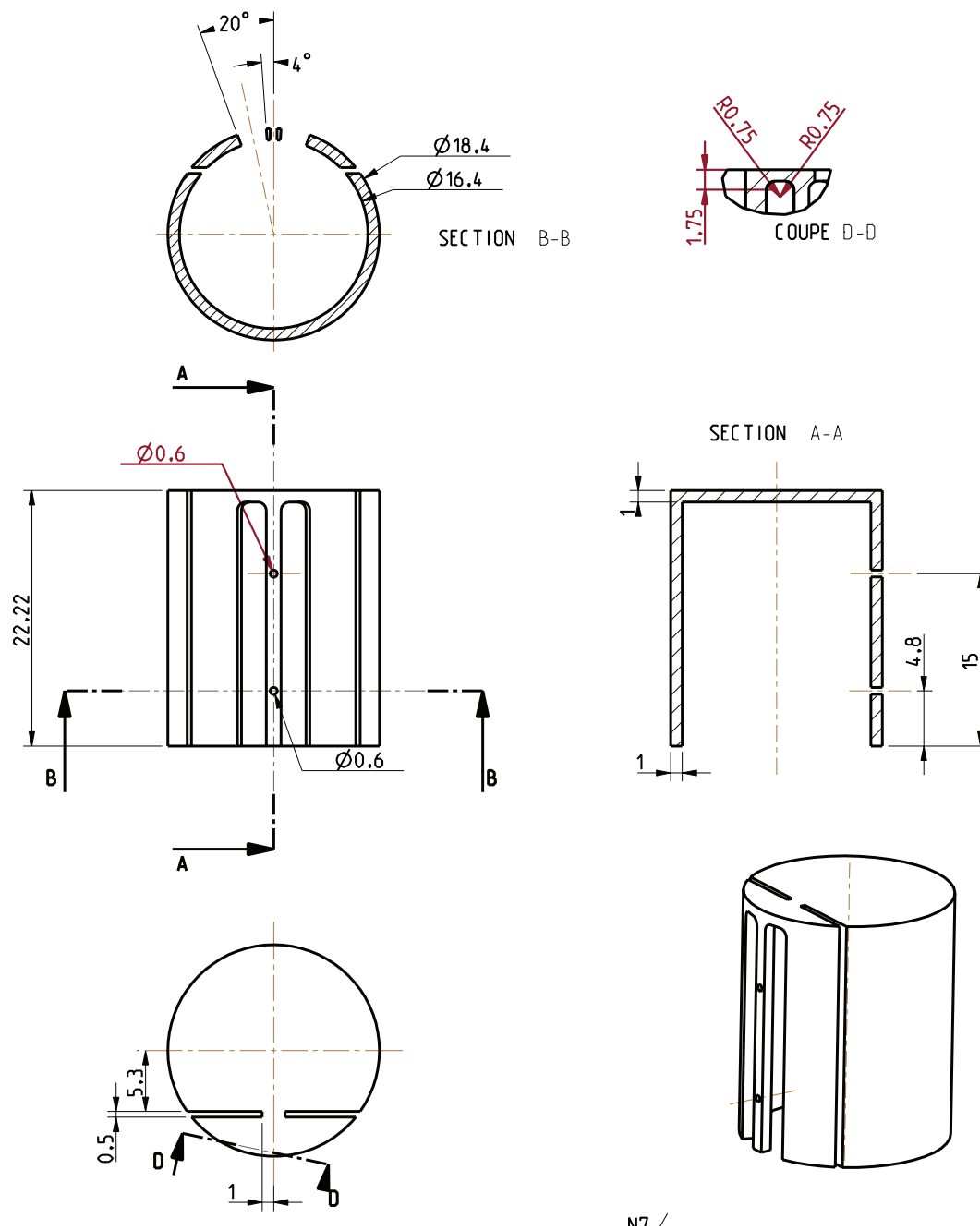
Figure B.3.: FIFA ground piece (copper). Dimensions in [mm].

(a)

(b)

(c)
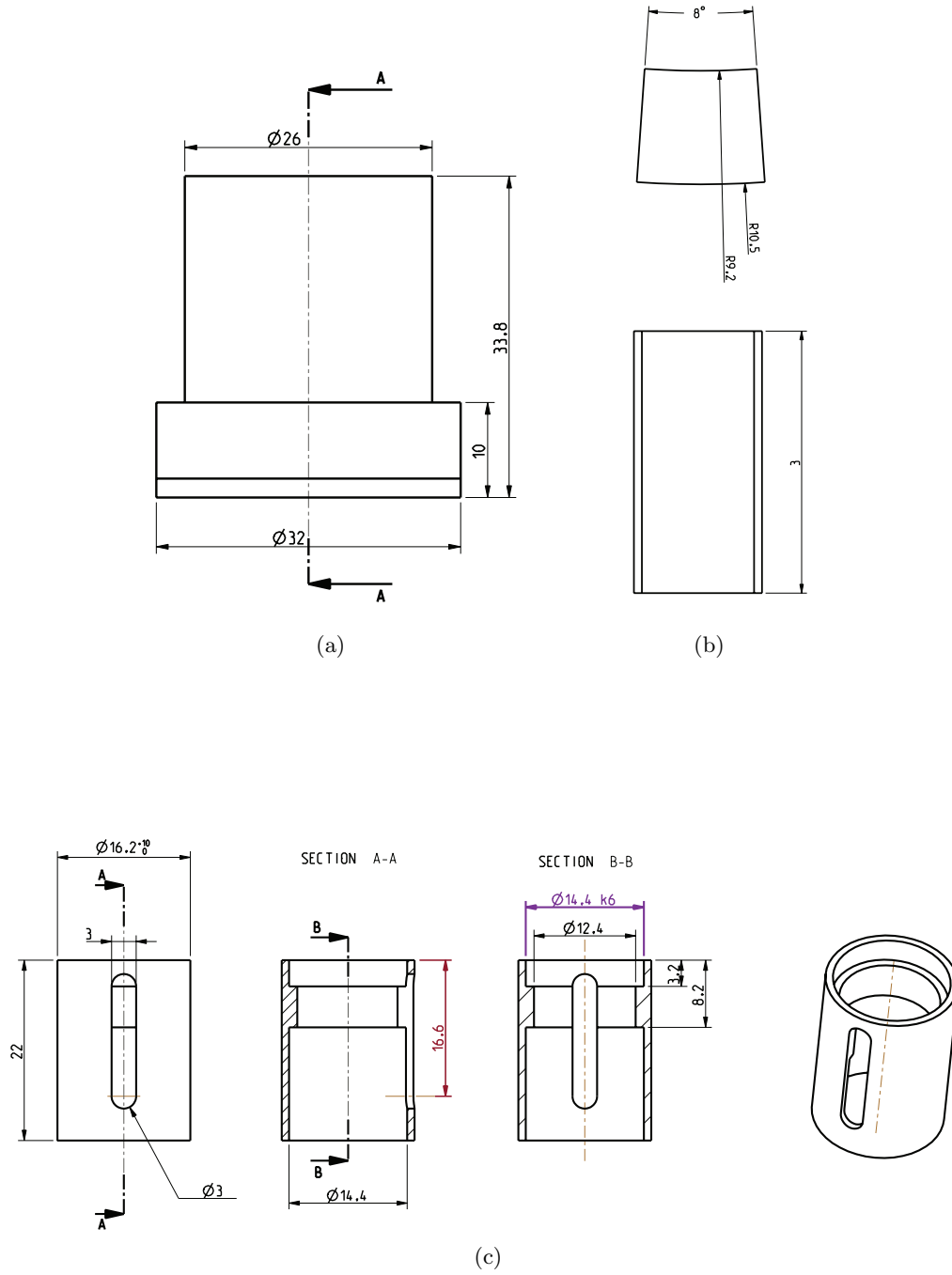
Figure B.4.: FIFA: (a) external biocompatible casing (PEEK, $\varepsilon'_e = 3.2$), (b) short (copper), and (c) internal housing (PEEK). Dimensions in [mm].

B.2. Painted Folded Inverted-F Antenna
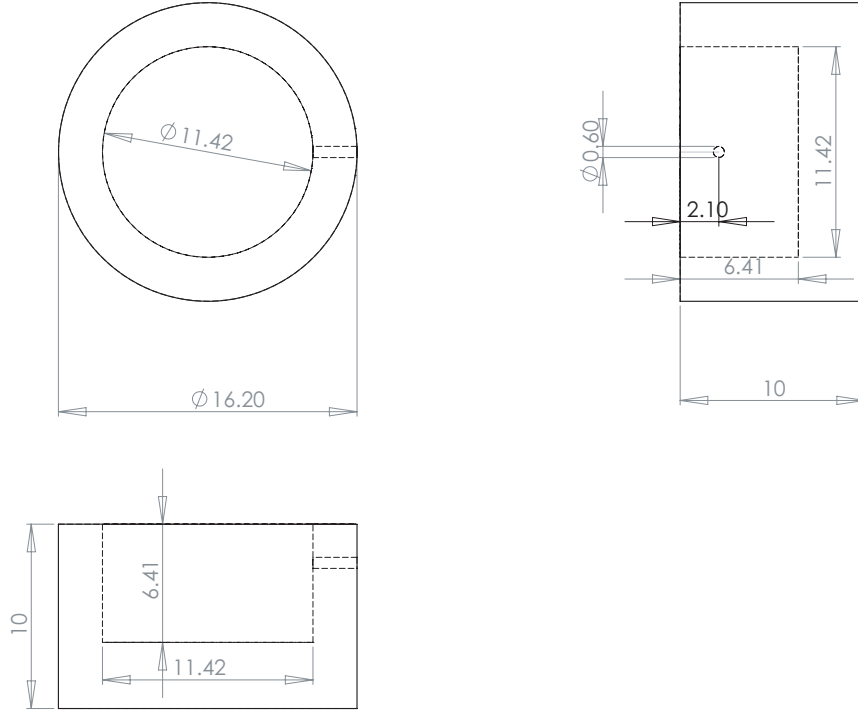
Figure B.5.: Painted FIFA dielectric piece (ECCOSTOCK HI-K500, $\varepsilon'_e = 25$). Dimensions in [mm].
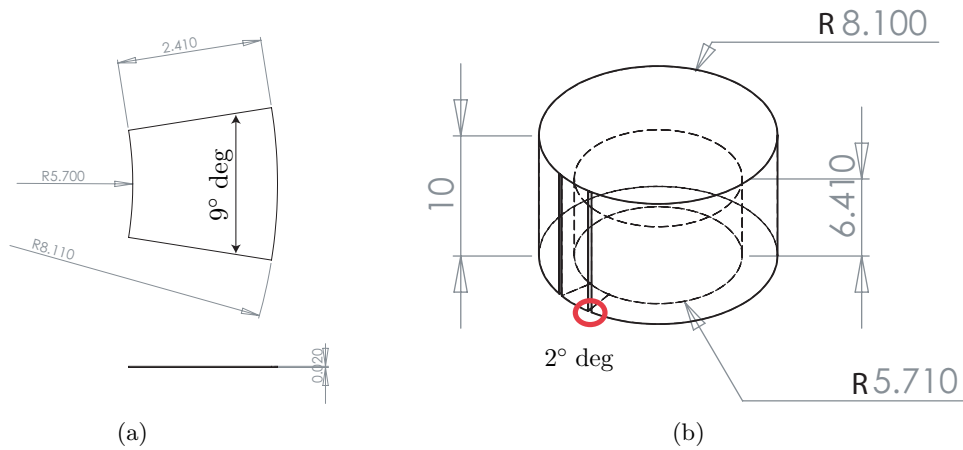
Figure B.6.: Painted FIFA metallizations: (a) short and (b) patch part. The internal surface of the hollow concluder is completely metallized realizing the ground part. Dimensions in [mm].
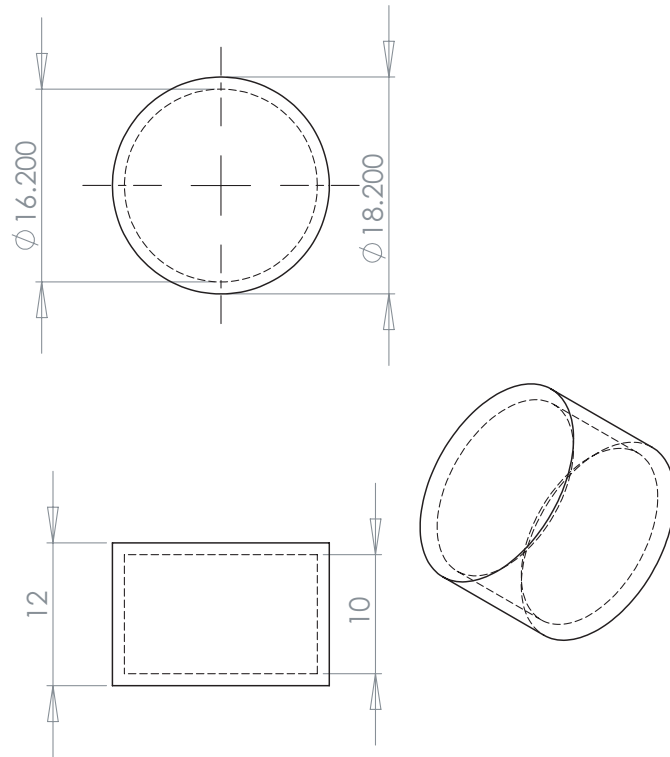
Figure B.7.: Painted FIFA biocompatible casing (PEEK, $\varepsilon'_e = 3.2$). Dimensions in [mm].

B.3. Brass Folded Inverted-F Antenna

(a)

(b)
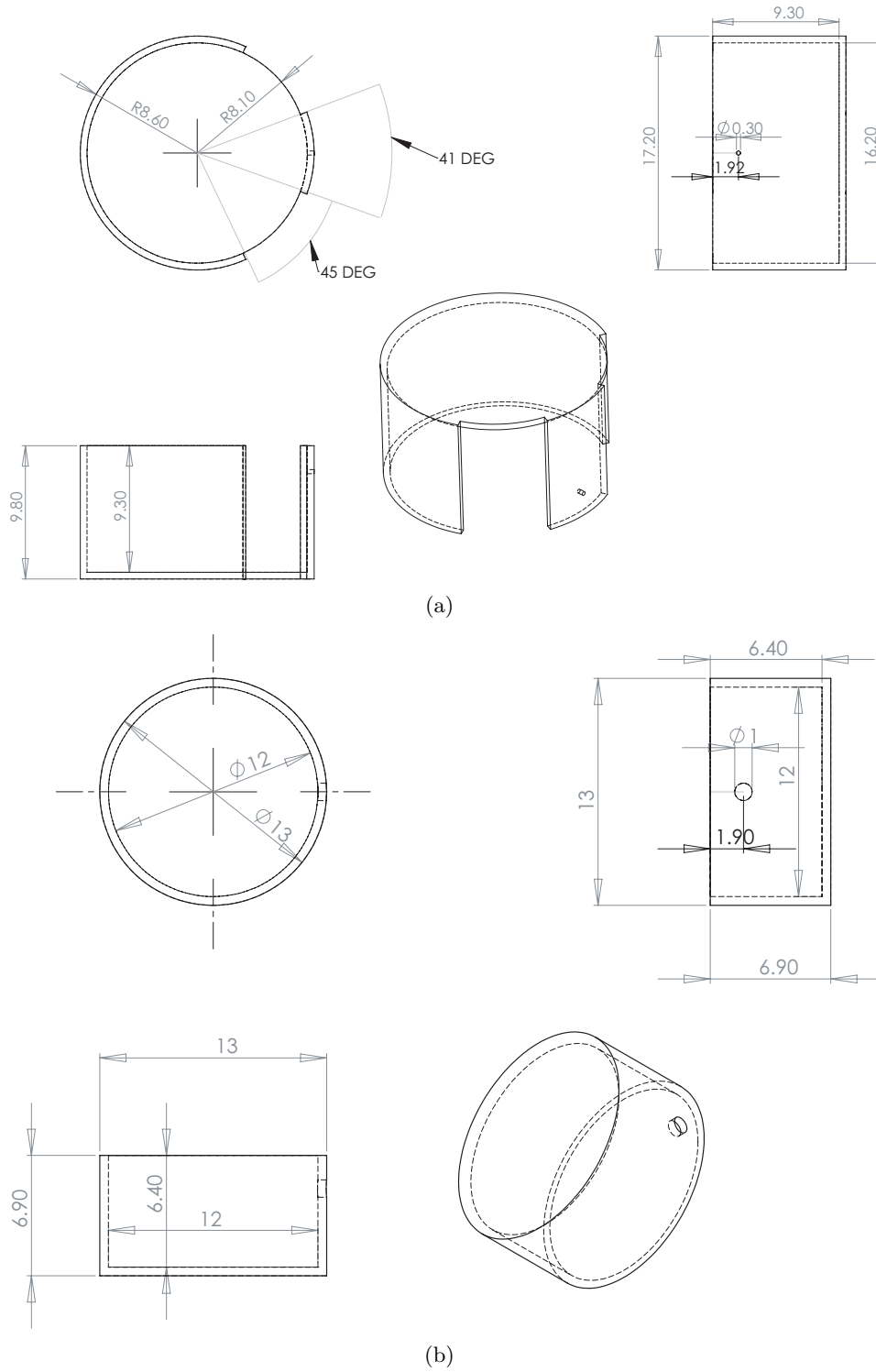
Figure B.8.: Brass FIFA: patch (a) and ground (b) metallizations. Dimensions in [mm]. The dielectric piece ((ECCOSTOCK HI-K500, $\varepsilon'_e = 25$) is the same as in Fig. B.5.
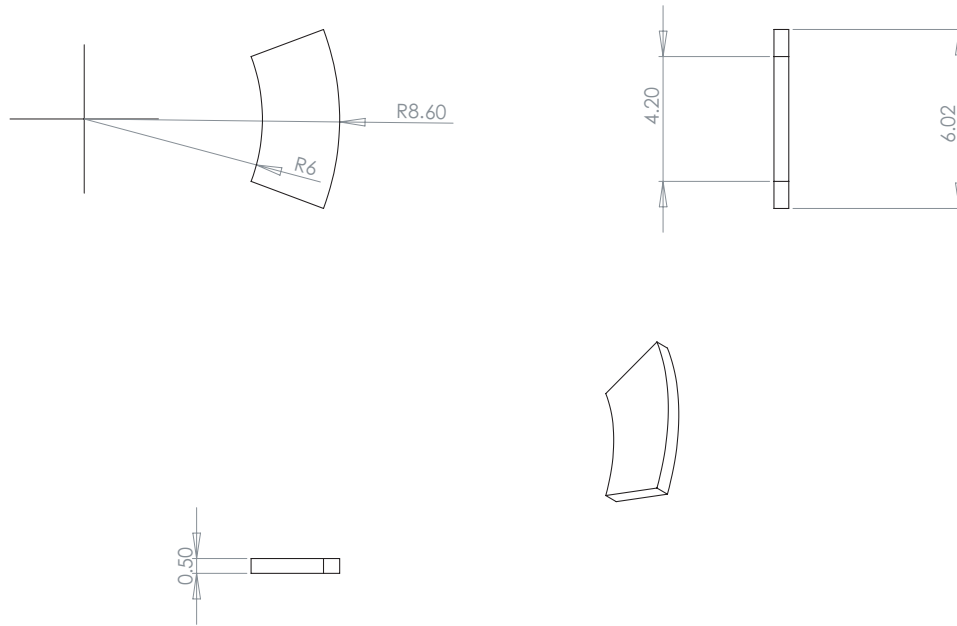
Figure B.9.: Brass FIFA short metallization. Dimensions in [mm].

B.4. Folded Rectangular Helix
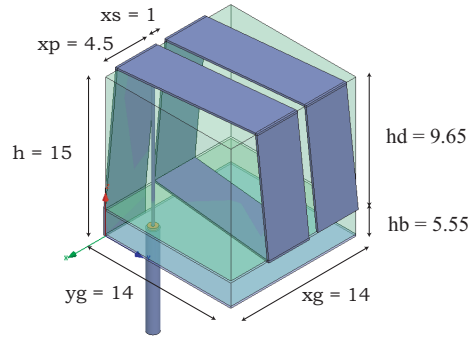
Figure B.10.: Geometry and main dimensions in [mm] of the FRH.
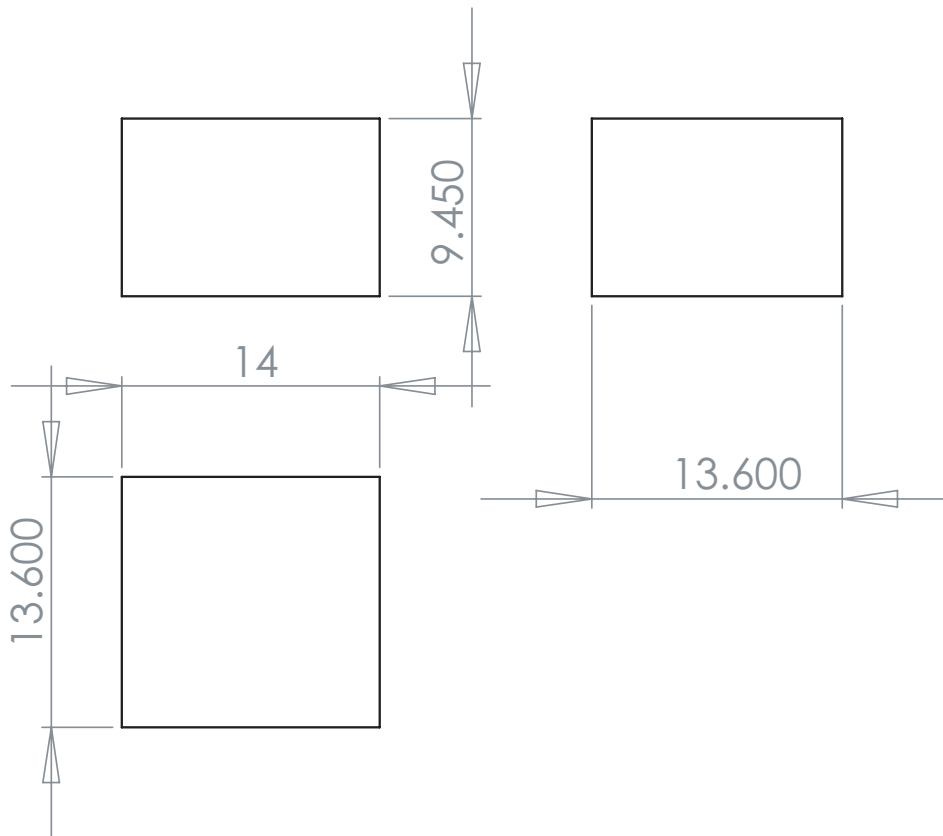
Figure B.11.: FRH dielectric piece (ECCOSTOCK HI-K500, $\varepsilon'_e = 11$), height: hd). Dimensions in [mm].
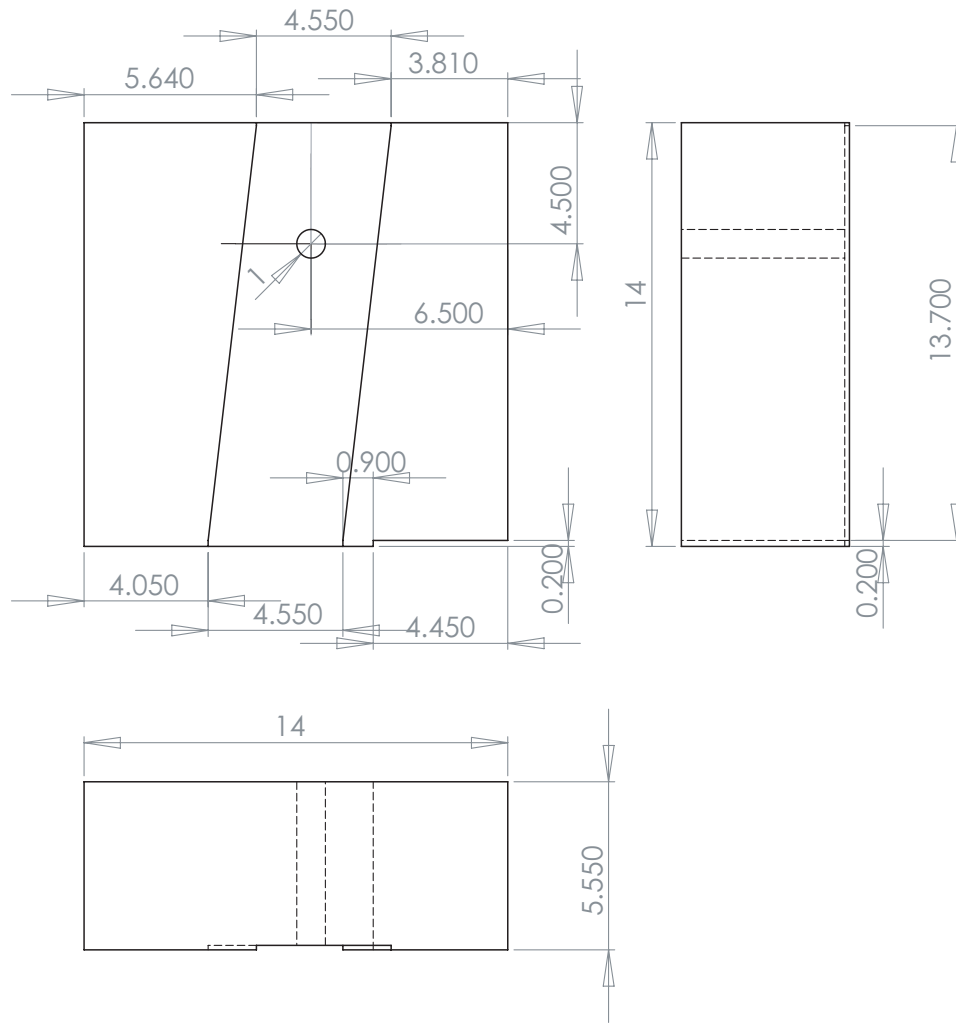
Figure B.12.: FRH dielectric piece (ECCOSTOCK HI-K500, $\varepsilon'_e = 11$), (height: hb). Dimensions in [mm].

C. Appendix: Comparison of SEMCAD X and HFSS

In order to evaluate the differences between SEMCAD X and HFSS, the proposed MSA radiator (characteristics described in Chapter 5, Section 5.4.2) was simulated in both software when inserted in the cylindrical body phantom. The conductivity of the metallic materials was found to be a very important parameter to properly realize the improved MSA, thus this aspect was also investigated with SEMCAD X. The MSA was simulated when made of Perfect Electric Conductor (PEC) and copper ($\sigma'_e = 58e^6$ and $29e^6$ S/m in the MedRadio and ISM bands, respectively) to check the feasibility of the least demanding choice. Figs. C.1 and C.2 illustrate the obtained reflection coefficients versus frequency, while the radiation performances are reported in Table C.1.
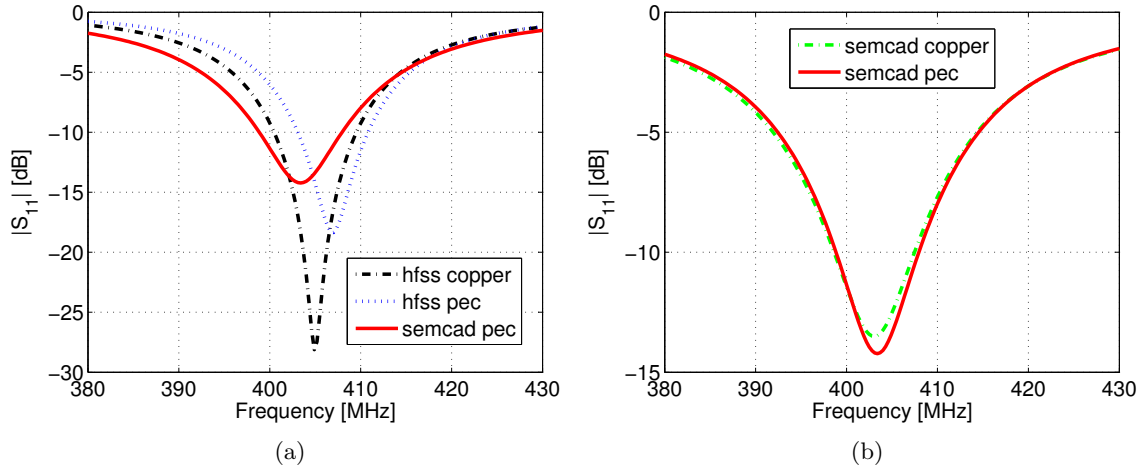
Figure C.1.: Simulated $|S_{11}(f)|$ in the MedRadio band of the proposed MSA inserted into the homogeneous cylindrical muscle phantom obtained with: (a) HFSS and SEMCAD X and (b) SEMCAD X with different conductivities.

A 1% difference is registered for the matching behaviors obtained by HFSS in the MedRadio band -Fig. C.1-(a)- while SEMCAD X results are almost superimposed[§] as illustrated in Fig. C.1-(b). A variation within 1% is also appreciated comparing the two software. As expected, the use of PEC improves the radiation performances. However, focusing on the radiation efficiency, one can notices that higher values are always obtained by SEMCAD X (1-1.5 dB).

The same behavior occurs in the higher frequency range. Indeed, the metallization choice does not modify the matching of the radiator in SEMCAD X as illustrated in Fig. C.2-(b), and

---

[§]SEMCAD X investigations are obtained considering metallic part with zero thickness to speed up the numerical analysis.
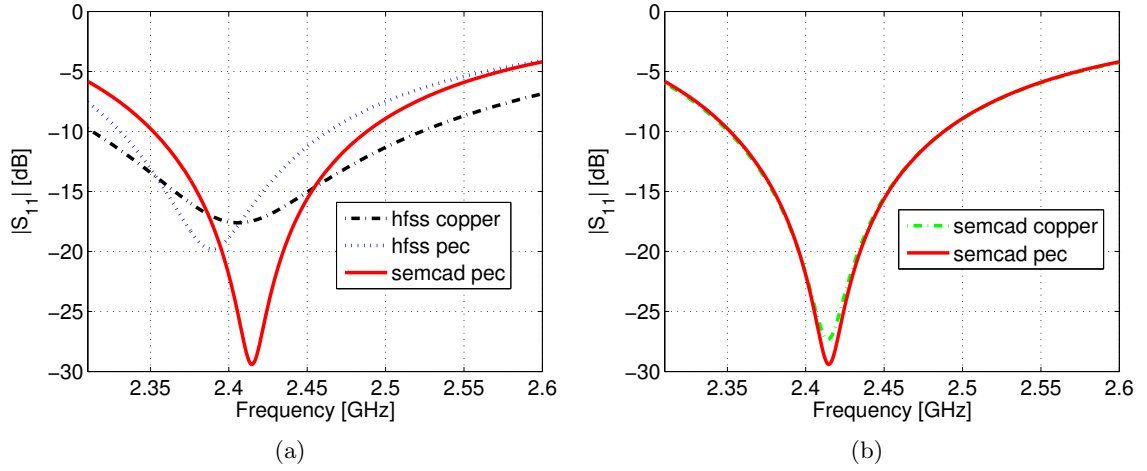
Figure C.2.: Simulated $|S_{11}(f)|$ in the 2.45 GHz frequency range of the proposed MSA inserted into the homogeneous cylindrical muscle phantom obtained with: (a) HFSS and SEMCAD X and (b) SEMCAD X with different conductivities.

**Table C.1.:** Simulated Radiation Results of the MSA inserted into the Homogeneous Cylindrical Muscle Phantom obtained with HFSS and SEMCAD X. Maximum Values are Reported for both Gain and Directivity.

Model	Frequency [MHz]	Gain [dBi]	Directivity [dBi]	e_{rad} [%]
HFSS copper	404.9	-29.4	3.5	0.051
HFSS pec	407.0	-27.9	3.6	0.070
SEMCAD X copper	403.4	-27.1	3.9	0.081
SEMCAD X pec	403.4	-26.9	3.9	0.085
HFSS copper	2406.5	-17.7	4.4	0.606
HFSS pec	2389.2	-17.5	4.5	0.636
SEMCAD X copper	2414.1	-16.2	4.4	0.912
SEMCAD X pec	2414.8	-15.9	4.4	0.928

the results are consistent with HFSS, Fig. C.2-(a). As for the Medradio case, the radiation efficiency is always higher in SEMCAD X regardless the selected conductivity.

The performed analysis led to some considerations on the computational requirement. First of all, the conductivity values of the metallic parts affects not only the EM performances but also the computational efforts: a four times longer simulation is performed by SEMCAD X in the MedRadio band when considering metals with finite conductivity instead of the ideal one. Second, the numerical analysis in SEMCAD X is more time consuming and requires extra computational resources than what is needed by HFSS. In fact, SEMCAD X analysis were running for several hours in a 2 x Six Core Intel Xeon X5670 at 2.93 GHz with 72 GByte of

RAM and graphic card acceleration (2 x nVidia TESLA M2050 GPU Computing Processor), while HFSS required less than an hour in an Intel(R) Core(TM)2 Quad CPU at 2.66 GHz with 8 GBytes of RAM.

Bibliography

[1] A. Rosen, M. A. Stuchly, and A. Vander Vorst, "Applications of RF/microwaves in medicine," *IEEE Trans. Microw. Theory Tech.*, vol. 50, no. 3, pp. 963–974, Mar. 2002.

[2] ——, "The role of engineering principles in the medical utilization of electromagnetic energies from kHz to visible light - examples," *International Journal of Infrared and Millimeter waves*, vol. 30, no. 12, pp. 1374–1386, Dec. 2009.

[3] D. Panescu, "Emerging technologies [wireless communication systems for implantable medical devices]," *IEEE Eng. Med. Biol. Mag.*, vol. 27, no. 2, pp. 96–101, Mar. 2008.

[4] R. Bashirullah, "Wireless implants," *IEEE Microw. Mag.*, vol. 11, no. 7, 2010.

[5] R. S. Mackay, "Radio telemetering from within the body: inside information is revealed by tiny transmitters that can be swallowed or implanted in man or animal," *Science*, vol. 134, no. 3486, pp. 1196–1202, Oct. 1961.

[6] W. H. Steinberg, F. A. Mina, P. G. Pick, and G. H. Frey, "Heidelberg capsule. in vitro evaluation of a new instrument for measuring intragastric pH," *J. Pharm. Sci.*, vol. 54, no. 5, pp. 772–776, May 1965.

[7] P. Valdastri, A. Menciassi, A. Arena, C. Caccamo, and P. Dario, "An implantable telemetry platform system for in vivo monitoring of physiological parameters," *IEEE Trans. Inf. Technol. Biomed.*, vol. 8, no. 3, pp. 271–278, Sept. 2004.

[8] K. Najafi, "Packaging of implantable microsystems," in *Proc. IEEE Sensors*, 2007, pp. 58–63.

[9] E. A. Johannessen, L. Wang, C. Wyse, D. R. S. Cumming, and J. M. Cooper, "Biocompatibility of a lab-on-a-pill sensor in artificial gastrointestinal environments," *IEEE Trans. Biomed. Eng.*, vol. 53, no. 11, pp. 2333–2340, Nov. 2006.

[10] D. Halperin, T. Kohno, T. S. Heydt-Benjamin, K. Fu, and W. H. Maisel, "Security and privacy for implantable medical devices," *IEEE Pervasive Comput.*, vol. 7, no. 1, pp. 30–39, Jan.–Mar. 2008.

[11] *Medical Device Radiocommunications Service (MedRadio)*, Federal Communication Commission (FCC) Std. CFR, Part 95.601-673 Subpart E, Part 95.1201-1221 Subpart I, 2009, formerly *Medical Implanted Communication System (MICS)*. [Online]. Available: http://wireless.fcc.gov/services/index.htm?job=service_home&id=medical_implant

[12] *Electromagnetic compatibility and Radio Spectrum Matters (ERM); Short Range Devices (SRD); Ultra Low Power Active Medical Implants (ULP-AMI) and Peripherals (ULP-AMI-P) operating in the frequency range 402 MHz to 405 MHz; Part 1 and Part 2*, European Telecommunications Standards Institute (ETSI) Std. EN 301 839-1/2 V1.3.1, 2007. [Online]. Available: www.etsi.org

[13] *Sharing between the Meteorological Aids Service and Medical Implant Communications Systems (MICS) operating in the Mobile Service in the Frequency Band 401-406 MHz.*, International Telecommunications Union Recommendation (ITU-R) Std. ITU-R Recommendation SA 1346, 2001, available (for registered users) at : www.itu.int.

[14] *Standard for Safety Levels with Respect to Human Exposure to Radio Frequency Electromagnetic Fields, 3 kHz to 300 GHz*, Institute of Electrical and Electronics Engineers (IEEE) Std. Std C95.^{TM}, 1999.

[15] *Standard for Safety Levels with Respect to Human Exposure to Radio Frequency Electromagnetic Fields, 3 kHz to 300 GHz*, Institute of Electrical and Electronics Engineers (IEEE) Std. C95.^{TM}, 2005.

[16] W. Xia, K. Saito, M. Takahashi, and K. Ito, "Performances of an implanted cavity slot antenna embedded in the human arm," *IEEE Trans. Antennas Propag.*, vol. 57, no. 4, pp. 894–899, Apr. 2009.

[17] L. Bolomey, "Generic DSP-based implantable body sensor node," Ph.D. dissertation, EPFL, Lausanne, June 2010.

[18] J. Kim and Y. Rahmat-Samii, "Implanted antennas inside a human body: simulations, designs, and characterizations," *IEEE Trans. Microw. Theory Tech.*, vol. 52, no. 8, pp. 1934–1943, Aug. 2004.

[19] R. W. P. King and G. S. Smith, *Antennas in Matter: Fundamentals, Theory, and Applications*, 1st ed. Cambridge, Massachusetts, and London, England: The MIT Press, 1981.

[20] C. Gabriel, "Compilation of the dielectric properties of body tissues at RF and microwave frequencies," Brooks Air Force Base, Texas (USA), Tech. Rep. Report N.AL/OE-TR-, June 1996. [Online]. Available: http://niremf.ifac.cnr.it/tissprop/htmlclie/htmlclie.htm

[21] R. E. Collin and F. J. Zucker, *Antenna Theory Part II*, ser. Inter-University Electronics Series. McGraw-Hill Book, 1969, vol. 7.

[22] P. S. Hall and Y. Hao, *Antennas and Propagation for Body-centric Wireless Communications*. Norwood, MA, USA: Artech House, 2006, ch. 9.

[23] R. Fenwick and W. Weeks, "Submerged antenna characteristics," *IEEE Trans. Antennas Propag.*, vol. 11, no. 3, pp. 296–305, 1963.

[24] R. Hansen, "Radiation and reception with buried and submerged antennas," *IEEE Trans. Antennas Propag.*, vol. 11, no. 3, pp. 207–216, 1963.

[25] R. Moore, "Effects of a surrounding conducting medium on antenna analysis," *IEEE Trans. Antennas Propag.*, vol. 11, no. 3, pp. 216–225, May 1963.

[26] A. Karlsson, "Physical limitations of antennas in a lossy medium," *IEEE Trans. Antennas Propag.*, vol. 52, no. 8, pp. 2027–2033, Aug. 2004.

[27] A. J. Johansson, "Wireless Communication with Medical Implants: Antennas and Propagation," Ph.D. dissertation, Lund University, Lund, June 2004.

[28] J. Lee and S. Nam, "Effective area of a receiving antenna in a lossy medium," *IEEE Trans. Antennas Propag.*, vol. 57, no. 6, pp. 1843–1845, 2009.

[29] A. Lea, P. Hui, J. Ollikainen, and R. G. Vaughan, "Propagation between on-body antennas," *IEEE Trans. Antennas Propag.*, vol. 57, no. 11, pp. 3619–3627, 2009.

[30] *IEEE Recommended Practice for Measurements and Computations of Radio Frequency Electromagnetic Fields With Respect to Human Exposure to Radio Frequency Electromagnetic Fields, 100 kHz-300 GHz*, Institute of Electrical and Electronics Engineers (IEEE) Std. C95.3^{TM}-(R2008), 2008.

[31] P. R. Wainwright, "Localized specific absorption rate calculations in a realistic phantom leg at 1-30 MHz using a finite element method," *Phys. Med. Biol.*, vol. 44, no. 4, pp. 1041–1052, Apr. 1999.

[32] ——, "The relationship of temperature rise to specific absorption rate and current in the human leg for exposure to electromagnetic radiation in the high frequency band," *Phys. Med. Biol.*, vol. 48, no. 19, pp. 3143–3155, Oct. 2003.

[33] P. Crespo-Valero, M. Christopoulou, M. Zefferer, A. Christ, P. Achermann, K. S. Nikita, and N. Kuster, "Novel methodology to characterize electromagnetic exposure of the brain," *Physics in Medicine and Biology*, vol. 56, no. 2, p. 383, 2011. [Online]. Available: http://stacks.iop.org/0031-9155/56/i=2/a=007

[34] A. K. Skrivervik, J. F. Zürcher, O. Staub, and J. R. Mosig, "PCS antenna design: the challenge of miniaturization," *IEEE Antennas Propag. Mag.*, vol. 43, no. 4, pp. 12–27, Aug. 2001.

[35] H. A. Wheeler, "Fundamental limitations of small antennas," *Proceedings of the IRE*, vol. 35, no. 12, pp. 1479–1484, 1947.

[36] L. J. Chu, "Physical limitations of omni-directional antennas," *Journal of Applied Physics*, vol. 19, no. 12, pp. 1163–1175, 1948.

[37] R. F. Harrington, "Effect of antenna size on gain, bandwidth and efficiency," *Journal of Research of the National Bureau of Standards-D Radio Propagation*, vol. 64-D, pp. 1–12, Jan.-Feb. 1960.

[38] J. S. McLean, "A re-examination of the fundamental limits on the radiation Q of electrically small antennas," *IEEE Trans. Antennas Propag.*, vol. 44, no. 5, 1996.

[39] M. Gustafsson, C. Sohl, and G. Kristensson, "Illustrations of new physical bounds on linearly polarized antennas," *IEEE Trans. Antennas Propag.*, vol. 57, no. 5, pp. 1319–1327, 2009.

[40] K. Jaber, "Analysis of body phantoms for implantable wireless system," Master's thesis, EPFL, Lausanne, Jan. 2010.

[41] *IEEE Trans. Antennas Propag., Special Issue on Electromagnetic Waves in the Earth*, vol. 11, May 1963.

[42] A. Baños, *Dipole Radiation in the Presence of a Conducting Medium.* Pergamon Press, 1966.

[43] H. Wheeler, "Fundamental limitations of a small VLF antenna for submarines," *IRE Transactions on Antennas and Propagation*, vol. 6, no. 1, pp. 123–125, Jan. 1958.

[44] ——, "Useful radiation from an underground antenna," *Journal of Research of the National Bureau of Standards-D Radio Propagation*, vol. 65-D, pp. 89–91, Jan.-Feb. 1961.

[45] H. P. Schwan, "Interaction of microwave and radio frequency radiation with biological systems," *IEEE Trans. Microw. Theory Tech.*, vol. 19, no. 2, pp. 146–152, 1971.

[46] A. W. Guy, "Analyses of electromagnetic fields induced in biological tissues by thermographic studies on equivalent phantom models," *IEEE Trans. Microw. Theory Tech.*, vol. 19, no. 2, pp. 205–214, 1971.

[47] J. C. Lin, A. W. Guy, and C. C. Johnson, "Power deposition in a spherical model of man exposed to 1-20 MHz electromagnetic fields," *IEEE Trans. Microw. Theory Tech.*, vol. 21, no. 12, pp. 791–797, 1973.

[48] K. Ito, "Human body phantoms for evaluation of wearable and implantable antennas," in *Proc. of the 2nd European Conference on Antennas and Propagation (EuCAP 2007)*, Edinburgh, Scotland, UK, Nov. 2007.

[49] A. Christ, W. Kainz, E. G. Hahn, K. Honegger, M. Zefferer, E. Neufeld, W. Rascher, R. Janka, W. Bautz, J. Chen, B. Kiefer, P. Schmitt, H.-P. Hollenbach, J. Shen, M. Oberle, D. Szczerba, A. Kam, J. W. Guag, and N. Kuster, "The virtual family–development of surface-based anatomical models of two adults and two children for dosimetric simulations," *Phys. Med. Biol.*, vol. 55, no. 2, pp. N23–N38, Jan. 2010.

[50] IT'IS Foundation: High-resolution whole-body human models of the virtual population. [Online]. Available: http://www.itis.ethz.ch/services/human-and-animal-models/human-models/

[51] P. S. Hall, Y. Hao, Y. I. Nechayev, A. Alomalny, C. C. Constantinou, C. Parini, M. R. Kamarudin, T. Z. Salim, D. T. M. Hee, R. Dubrovka, A. S. Owadally, W. Song, A. Serra, P. Nepa, M. Gallo, and M. Bozzetti, "Antennas and propagation for on-body communication systems," *IEEE Antennas Propag. Mag.*, vol. 49, no. 3, pp. 41–58, 2007.

[52] A. Alomainy, Y. Hao, A. Owadally, C. G. Parini, Y. Nechayev, C. C. Constantinou, and P. S. Hall, "Statistical analysis and performance evaluation for on-body radio propagation with microstrip patch antennas," *IEEE Trans. Antennas Propag.*, vol. 55, no. 1, pp. 245–248, 2007.

[53] Y. Koyanagi, H. Kawai, K. Ogawa, and K. Ito, "Consideration of the local SAR and radiation characteristics of a helical antenna using a cylindroid whole body phantom at 150 MHz," *Electronics and communications in Japan (Part I: Communications)*, vol. 87, no. 1, pp. 48–60, Jan. 2004.

[54] T. Dissanayake, K. P. Esselle, and M. R. Yuce, "Dielectric loaded impedance matching for wideband implanted antennas," *IEEE Trans. Microw. Theory Tech.*, vol. 57, no. 10, pp. 2480–2487, Oct. 2009.

[55] *Electromagnetic compatibility and Radio spectrum Matters (ERM); Ultra Low Power Active Medical Implants (ULP-AMI) operating in the 401 MHz to 402 MHz and 405 MHz to 406 MHz bands; System Reference Document*, European Telecommunications Standards Institute ETSI Std. TR 102 343 V1.1.1, 2004.

[56] W. Blair, "Experimental verification of dipole radiation in a conducting half-space," *IEEE Trans. Antennas Propag.*, vol. 11, no. 3, pp. 269–275, 1963.

[57] C. M. Rappaport and F. R. Morgenthaler, "Optimal source distribution for hyperthermia at the center of a sphere of muscle tissue," *IEEE Trans. Microw. Theory Tech.*, vol. 35, no. 12, pp. 1322–1327, Dec. 1987.

[58] K. S. Nikita, G. S. Stamatakos, N. K. Uzunoglu, and A. Karafotias, "Analysis of the interaction between a layered spherical human head model and a finite-length dipole," *IEEE Trans. Microw. Theory Tech.*, vol. 48, no. 11, pp. 2003–2013, Nov. 2000.

[59] C. Miry, R. Gillard, and R. Loison, "An application of the multi-level DG-FDTD to the analysis of the transmission between a dipole in free-space and an implanted antenna in a simplified body model with various positions," in *Proc. 3rd European Conference on Antennas and Propagation EuCAP 2009*, 23–27 Mar. 2009, pp. 67–70.

[60] ——, "Multi-level dual-grid finite-difference time-domain approach for the analysis of body implanted antennas," *IET Microwaves, Antennas and Propagation*, vol. 4, no. 6, pp. 659–666, 2010.

[61] C. Miry, T. Alves, R. Gillard, J. Laheurte, R. Loison, and B. Poussot, "Analysis of the transmission between on-body devices using the bilateral Dual-Grid FDTD technique," *Antennas and Wireless Propagation Letters, IEEE*, vol. 9, pp. 1073 –1075, 2010.

[62] E. Y. Chow, Y. Ouyang, B. Beier, W. J. Chappell, and P. P. Irazoqui, "Evaluation of cardiovascular stents as antennas for implantable wireless applications," *IEEE Trans. Microw. Theory Tech.*, vol. 57, no. 10, pp. 2523–2532, Oct. 2009.

[63] M. Gallo, P. S. Hall, Q. Bai, Y. I. Nechayev, C. C. Constantinou, and M. Bozzetti, "Simulation and measurement of dynamic on-body communication channels," *IEEE Trans. Antennas Propag.*, vol. 59, no. 2, pp. 623–630, 2011.

[64] The Visible Human project, U.S. National Library of Medicine. [Online]. Available: http://www.nlm.nih.gov/research/visible/visible_human.html

[65] W. G. Scanlon, B. Burns, and N. E. Evans, "Radiowave propagation from a tissue-implanted source at 418 MHz and 916.5 MHz," *IEEE Trans. Biomed. Eng.*, vol. 47, no. 4, pp. 527–534, Apr. 2000.

[66] L. C. Chirwa, P. A. Hammond, S. Roy, and D. R. S. Cumming, "Electromagnetic radiation from ingested sources in the human intestine between 150 MHz and 1.2 GHz," *IEEE Trans. Biomed. Eng.*, vol. 50, no. 4, pp. 484–492, Apr. 2003.

[67] A. Alomainy and Y. Hao, "Modeling and characterization of biotelemetric radio channel from ingested implants considering organ contents," *IEEE Trans. Antennas Propag.*, vol. 57, no. 4, pp. 999–1005, Apr. 2009.

[68] J.-H. Jung, S.-W. Kim, Y.-S. Kim, and S.-Y. Kim, "Electromagnetic propagation from the intestine-ingested source in the human body model," *IEEE Trans. Antennas Propag.*, vol. 58, no. 5, pp. 1683–1688, 2010.

[69] L. Xu, M. Q.-H. Meng, and Y. Chan, "Effects of dielectric parameters of human body on radiation characteristics of ingestible wireless device at operating frequency of 430 MHz," *IEEE Trans. Biomed. Eng.*, vol. 56, no. 8, pp. 2083–2094, 2009.

[70] P. J. Dimbylow, "Current densities in a 2 mm resolution anatomically realistic model of the body induced by low frequency electric fields," *Phys. Med. Biol.*, vol. 45, no. 4, pp. 1013–1022, Apr. 2000.

[71] I. G. Zubal, C. R. Harrell, E. O. Smith, Z. Rattner, G. Gindi, and P. B. Hoffer, "Computerized three-dimensional segmented human anatomy," *Med. Phys.*, vol. 21, no. 2, pp. 299–302, Feb. 1994.

[72] Center for NMR Research, Penn State College of Medicine, avaialbe in XFDTD software. [Online]. Available: http://www.pennstatehershey.org/web/nmrlab/home

[73] Z. N. Chen, G. C. Liu, and T. See, "Transmission of RF signals between MICS loop antennas in free space and implanted in the human head," *IEEE Trans. Antennas Propag.*, vol. 57, no. 6, pp. 1850–1854, 2009.

[74] M. Z. Azad and M. Ali, "A miniature implanted inverted-F antenna for GPS application," *IEEE Trans. Antennas Propag.*, vol. 57, no. 6, pp. 1854–1858, June 2009.

[75] T. Nagaoka, S. Watanabe, K. Sakurai, E. Kunieda, S. Watanabe, M. Taki, and Y. Yamanaka, "Development of realistic high-resolution whole-body voxel models of Japanese adult males and females of average height and weight, and application of models to radio-frequency electromagnetic-field dosimetry," *Phys. Med. Biol.*, vol. 49, no. 1, pp. 1–15, Jan. 2004.

[76] T. Nagaoka and S. Watanabe, "Postured voxel-based human models for electromagnetic dosimetry," *Phys. Med. Biol.*, vol. 53, no. 24, pp. 7047–7061, Dec. 2008.

[77] C. Miry, R. Loison, and R. Gillard, "An efficient bilateral Dual-Grid-FDTD approach applied to on-body transmission analysis and specific absorption rate computation," *Microwave Theory and Techniques, IEEE Transactions on*, vol. 58, no. 9, pp. 2375 – 2382, Sept. 2010.

[78] A. Sani, A. Alomainy, and Y. Hao, "Numerical characterization and link budget evaluation of wireless implants considering different digital human phantoms," *IEEE Trans. Microw. Theory Tech.*, vol. 57, no. 10, pp. 2605–2613, Oct. 2009.

[79] SEMCAD X, Schmid & Partner Engineering AG (SPEAG), version 14.4 Aletsch. [Online]. Available: http://www.speag.com/simulation/index.php

[80] T. Karacolak, A. Z. Hood, and E. Topsakal, "Design of a dual-band implantable antenna and development of skin mimicking gels for continuous glucose monitoring," *IEEE Trans. Microw. Theory Tech.*, vol. 56, no. 4, pp. 1001–1008, Apr. 2008.

[81] R. W. P. King, S. Prasad, and B. H. Sandler, "Transponder antennas in and near a three-layered body," *IEEE Trans. Microw. Theory Tech.*, vol. 28, no. 6, pp. 586–596, 1980.

[82] T. Houzen, M. Takahashi, K. Saito, and K. Ito, "Implanted planar inverted-F antenna for cardiac pacemaker system," in *Proc. International Workshop on Antenna Technology: Small Antennas and Novel Metamaterials iWAT 2008*, 4–6, 2008, pp. 346–349.

[83] *Evaluating Compliance with FCC Guidelines for Human Exposure to Radio Frequency Electromagnetic Fields*, Federal Communication Commission (FCC) Std. Supplement C, OET Bulletin 65, Edition 97-01, 2001.

[84] H. Usui, M. Takahashi, and K. Ito, "Radiation characteristics of an implanted cavity slot antenna into the human body," in *Proc. IEEE Antennas and Propagation Society International Symposium 2006*, 9–14 July 2006, pp. 1095–1098.

[85] H. Mizuno, K. Ito, M. Takahashi, and K. Saito, "A helical folded dipole antenna for implantable communication devices," in *Proc. IEEE Antennas and Propagation Society Int. Symp. (APSURSI)*, 2010, pp. 1–4.

[86] *IEEE Recommended Practice for Determining the Peak Spatial-Average Specific Absorption Rate (SAR) in the Human Head from Wireless Communications Devices: Measurement Techniques*, Institute of Electrical and Electronics Engineers (IEEE) Std. Std 1528^{TM}, 2003.

[87] M. Sun, "An efficient algorithm for computing multishell spherical volume conductor models in EEG dipole source localization," *IEEE Trans. Biomed. Eng.*, vol. 44, no. 12, pp. 1243–1252, Dec. 1997.

[88] X.-K. K. Le-Wei Li and M.-S. Leong, *Spheroidal Wave Functions in Electromagnetic Theory*, ser. Wiley Series in Microwave and Optical Engineering. USA: John Wiley & Sons., New York, 2002.

[89] S. M. S. Reyhani and S. A. Ludwig, "An implanted spherical head model exposed to electromagnetic fields at a mobile communication frequency," *IEEE Trans. Biomed. Eng.*, vol. 53, no. 10, pp. 2092–2101, Oct. 2006.

[90] G. Cerri, R. De Leo, and G. Rosellini, "Evaluation of electromagnetic power deposition in a spherical multilayer head in the near field of a linear antenna," *Wireless Networks*, vol. 3, pp. 499–510, 1997.

[91] P. B. Johnson, S. R. Whalen, M. Wayson, B. Juneja, C. Lee, and W. E. Bolch, "Hybrid patient-dependent phantoms covering statistical distributions of body morphometry in the U.S. adult and pediatric population," *Proc. IEEE*, vol. 97, no. 12, pp. 2060–2075, 2009.

[92] P. Soontornpipit, C. Furse, and Y. C. Chung, "Design of implantable microstrip antenna for communication with medical implants," *IEEE Trans. Microw. Theory Tech.*, vol. 52, no. 8, pp. 1944–1951, Aug. 2004.

[93] P. Soontornpipit, C. M. Furse, and Y. C. Chung, "Miniaturized biocompatible microstrip antenna using genetic algorithm," *IEEE Trans. Antennas Propag.*, vol. 53, no. 6, pp. 1939–1945, June 2005.

[94] J. Kim and Y. Rahmat-Samii, "Planar Inverted-F antennas on implantable medical devices: Meandered type versus spiral type," *Microwave and Optical Technology Letters*, vol. 48, no. 3, pp. 567–572, 2006.

[95] W.-C. Liu, S.-H. Chen, and C.-M. Wu, "Implantable broadband circular stacked PIfA antenna for biotelemetry communication," *Journal of Electromagnetic Waves and Applications*, vol. 22, no. 13, pp. 1791–1800, 2008.

[96] S. I. Kwak, K. Chang, and Y. J. Yoon, "The helical antenna for the capsule endoscope," in *Proc. IEEE Antennas and Propagation Society International Symposium*, Volume 2B,&–8 July 2005, pp. 804–807.

[97] A. J. Johansson, "Simulation and verification of pacemaker antennas," in *Proc. 25th Annual Int. Engineering in Medicine and Biology Society Conf. of the IEEE*, vol. 4, 2003, pp. 3279–3281.

[98] A. Sani, M. Rajab, R. Foster, and Y. Hao, "Antennas and propagation of implanted RFIDs for pervasive healthcare applications," *Proc. IEEE*, vol. 98, no. 9, pp. 1648–1655, 2010.

[99] P. M. Izdebski, H. Rajagopalan, and Y. Rahmat-Samii, "Conformal ingestible capsule antenna: a novel chandelier meandered design," *IEEE Trans. Antennas Propag.*, vol. 57, no. 4, pp. 900–909, Apr. 2009.

[100] R. Warty, M. R. Tofighi, U. Kawoos, and A. Rosen, "Characterization of implantable antennas for intracranial pressure monitoring: Reflection by and transmission through a scalp phantom," *IEEE Trans. Microw. Theory Tech.*, vol. 56, no. 10, pp. 2366–2376, Oct. 2008.

[101] G. Collin, A. Chami, C. Luxey, P. Le Thuc, and R. Staraj, "Small electrical antenna for saw sensor biotelemetry," *Microwave and Optical Technology Letters*, vol. 51, no. 10, pp. 2286–2293, 2009.

[102] J. Gemio, J. Parron, and J. Soler, "Human body effects on implantable antennas for ISM bands applications: Models comparison and propagation losses study," *Progress In Electromagnetics Research*, vol. 110, pp. 437–452, 2010.

[103] C. J. Sanchez-Fernandez, O. Quevedo-Teruel, J. Requena-Carrion, L. Inclan-Sanchez, and E. Rajo-Iglesias, "Dual-band microstrip patch antenna based on short-circuited ring and spiral resonators for implantable medical devices," *Microwaves, Antennas Propagation, IET*, vol. 4, no. 8, pp. 1048 –1055, Aug. 2010.

[104] J. W. Reeves, S. Meeson, and M. J. Birch, "Effect of insertion depth on helical antenna performance in a muscle-equivalent phantom," *Phys. Med. Biol.*, vol. 50, no. 12, pp. 2955–2965, June 2005.

[105] T. Takimoto, T. Onishi, K. Saito, S. Takahashi, M. Uebayashi, and K. Ito, "Characteristics of biological tissue equivalent phantoms applied to UWB communications," *Electronics and Communications in Japan*, vol. 90, no. 5, pp. 48 –55, 2007.

[106] Y. Okano, K. Ito, I. Ida, and M. Takahashi, "The SAR evaluation method by a combination of thermographic experiments and biological tissue-equivalent phantoms," *IEEE Trans. Microw. Theory Tech.*, vol. 48, no. 11, pp. 2094 – 2103, Nov. 2000.

[107] V. Vigneras, "Elaboration and characterization of biological tissues equivalent liquids in the frequency range 0.9-3 GHz," PIOM Lab., Bordeaux, France, Tech. Rep., Nov. 2011.

[108] M. Y. Kanda, M. Ballen, S. Salins, C.-K. Chou, and Q. Balzano, "Formulation and characterization of tissue equivalent liquids used for RF densitometry and dosimetry measurements," *IEEE Trans. Microw. Theory Tech.*, vol. 52, no. 8, pp. 2046–2056, 2004.

[109] A. Peyman and C. Gabriel, "Tissue equivalent liquids for SAR measurement at microwave frequencies," in *Proc. Bioelectromagnetics Society 24th Annual Meeting, Quebec, QC, Canada*, June 2002.

[110] K. Fukunaga, S. Watanabe, and Y. Yamanaka, "Dielectric properties of tissue-equivalent liquids and their effects on specific absorption rate," *IEEE Trans. Electromagn. Compat.*, vol. 46, no. 1, pp. 126–129, 2004.

[111] C. K. Chou, G. W. Chen, A. W. Guy, and K. H. Luk, "Formulas for preparing phantom muscle tissue at various radiofrequencies," *Bioelectromagnetics*, vol. 5, no. 4, pp. 435–441, 1984.

[112] G. Hartsgrove, A. Kraszewski, and A. Surowiec, "Simulated biological materials for electromagnetic radiation absorption studies," *Bioelectromagnetics*, vol. 8, no. 1, pp. 29–36, 1987.

[113] T. Yilmaz, T. Karacolak, and E. Topsakal, "Characterization and testing of a skin mimicking material for implantable antennas operating at ISM band (2.4 GHz-2.48 GHz)," *IEEE Antennas Wireless Propag. Lett.*, vol. 7, pp. 418–420, 2008.

[114] T. Karacolak, R. Cooper, and E. Topsakal, "Electrical properties of rat skin and design of implantable antennas for medical wireless telemetry," *IEEE Trans. Antennas Propag.*, vol. 57, no. 9, pp. 2806–2812, Sept. 2009.

[115] K. Fukunaga, S. Watanabe, H. Asou, and K. Sato, "Dielectric properties of non-toxic tissue-equivalent liquids for radiowave safety tests," in *Proc. IEEE Int. Conf. Dielectric Liquids ICDL 2005*, 2005, pp. 425–428.

[116] W. Wu and C. E. Smith, "Dielectric measurements using the HP 85070a probe," in *Proc. IEEE Southeastcon '92*, 1992.

[117] Federal Communication Commission (FCC) Std. Supplement C, OET Bulletin 65, Edition 97-01, June 2001.

[118] "Agilent 85070e Dielectric Probe Kit 200 MHz to 50 GHz Technical Overview," Agilent Technologies, Tech. Rep. [Online]. Available: http://cp.literature.agilent.com/litweb/pdf/5989-0222EN.pdf

[119] *Handbook of materials for medical device.* ASM international, 2003, ch. 1.

[120] N. Beshchasna, B. Adolphi, S. Granovsky, J. Uhlemann, and K. J. Wolter, "Biostability issues of flash gold surfaces," in *Proc. 59th Electronic Components and Technology Conference ECTC 2009*, 26–29 May 2009, pp. 1071–1079.

[121] A. R. Shapiro, R. F. Lutomirski, and H. T. Yura, "Induced fields and heating within a cranial structure irradiated by an electromagnetic plane wave," *IEEE Trans. Microw. Theory Tech.*, vol. 19, no. 2, pp. 187–196, 1968.

[122] C. Rappaport, "Determination of bolus dielectric constant for optimum coupling of microwaves through skin for breast cancer imaging," *International Journal of Antennas and Propagation*, vol. 2008, no. Article ID 359582.

[123] M. H. Seegenschmiedt, P. Fessenden, and C. Vernon, Eds., *Thermoradiotherapy and Thermochemotherapy: Biology, Physiology, and Physics.* Springer-Verlag, 1995, vol. 1, Section: Physical Principles and Engineering.

[124] J. W. Hand, J. E. Robinson, S. Szwarnowski, R. J. Sheppard, and E. H. Grant, "A physiologically compatible tissue-equivalent liquid bolus for microwave heating of tissues," *Phys. Med. Biol.*, vol. 24, no. 2, pp. 426–431, Mar. 1979.

[125] F. M. Waterman and R. E. Nerlinger, "The effect of coupling materials on specific absorption rate distributions at 915 MHz," *Med. Phys.*, vol. 13, no. 3, pp. 391–395, 1986.

[126] P. R. Stauffer, F. Rossetto, M. Leencini, and G. B. Gentilli, "Radiation patterns of dual concentric conductor microstrip antennas for superficial hyperthermia," *IEEE Trans. Biomed. Eng.*, vol. 45, no. 5, pp. 605–613, May 1998.

[127] T. Sunaga, H. Ikehira, S. Furukawa, M. Tamura, E. Yoshitome, T. Obata, H. Shinkai, S. Tanada, H. Murata, and Y. Sasaki, "Development of a dielectric equivalent gel for better impedance matching for human skin," *Bioelectromagnetics*, vol. 24, no. 3, pp. 214–217, Apr. 2003. [Online]. Available: http://dx.doi.org/10.1002/bem.10080

[128] R. C. Gupta and S. P. Singh, "Analysis of the SAR distributions in three-layered biomedia in direct contact with a water-loaded modified box-horn applicator," *IEEE Trans. Microw. Theory Tech.*, vol. 53, no. 9, pp. 2665–2671, Sept. 2005.

[129] M. de Bruijne, T. Samaras, J. F. Bakker, and G. C. van Rhoon, "Effects of waterbolus size, shape and configuration on the SAR distribution pattern of the lucite cone applicator." *Int. J. Hyperthermia*, vol. 22, no. 1, pp. 15–28, Feb. 2006. [Online]. Available: http://dx.doi.org/10.1080/02656730500384297

[130] H. Massoudi, C. H. Durney, P. W. Barber, and M. F. Iskander, "Electromagnetic absorption in multilayered cylindrical models of man," *IEEE Trans. Microw. Theory Tech.*, vol. 27, no. 10, pp. 825–830, Oct. 1979.

[131] O. P. Gandhi and A. Riazi, "Absorption of millimeter waves by human beings and its biological implications," *IEEE Trans. Microw. Theory Tech.*, vol. 34, no. 2, pp. 228–235, Feb. 1986.

[132] H.-Y. Chen and K.-Y. Shen, "Reduction of SAR in a human-head model wrapped in clothing materials," *Microwave and Optical Technology Letters*, vol. 37, no. 4, pp. 305–308, 2003.

[133] C. T. Tai and R. E. Collin, "Radiation of a hertzian dipole immersed in a dissipative medium," *IEEE Trans. Antennas Propag.*, vol. 48, no. 10, pp. 1501–1506, Oct. 2000.

[134] J. A. Stratton, *Electromagnetic theory.* USA: MGraw-Hill, Inc., 1941.

[135] S. Rondineau, "Modélisation de Lentilles Sphériques à Gradient d'Indice et Sources Conformes Associées," Ph.D. dissertation, Université de Rennes I, Rennes, Dec. 2002.

[136] B. Fuchs, "Lentilles Stratifiées et Sources Réelles Associées - Analyses Théoriques et Validations Expérimentales en Ondes Millimétriques," Ph.D. dissertation, Université de Rennes I, Rennes, Nov. 2007.

[137] B. Fuchs, S. Palud, L. Le Coq, O. Lafond, M. Himdi, and S. Rondineau, "Scattering of spherically and hemispherically stratified lenses fed by any real source," *IEEE Trans. Antennas Propag.*, vol. 56, no. 2, pp. 450–460, Feb. 2008.

[138] C. Tai, *Dyadic Green's Functions in Electromagnetics Theory.* Scranton, PA: Intext educational, 1971.

[139] C. Wilcox, "An expansion theorem for electromagnetic fields," *Comm. on Pure and Applied mathematics*, vol. 9, no. 22, pp. 115–134, May 1956.

[140] M. Abramowitz and I. A. Stegun, *Handbook of mathematical functions.* New York: Dover, 1965.

[141] H. Mieras, "Radiation pattern computation of a spherical lens using mie series," *IEEE Trans. Antennas Propag.*, vol. 30, no. 6, pp. 1221–1224, Nov. 1982.

[142] FEKO suite 5.3 (evaluation version, silver license). [Online]. Available: http://www.feko.info/

[143] R. F. Harrington, *Time-Harmonics Electromagnetic Fields.* New York, USA: McGraw-Hill, 1961.

[144] P. Wood, *Reflector antenna analysis and design*, ser. IEE Electromagnetic Waves. London, U.K: P. Peregrinus on behalf of the Institution of Electrical Engineers, 1980, vol. 7.

[145] J. E. Hansen, Ed., *Spherical Near-field Antenna Measurements*, ser. IEE Electromagnetic Waves. London, U.K: P. Peregrinus on behalf of the Institution of Electrical Engineers, 1988, vol. 26.

[146] F. Jensen and A. Frandsen, "On the number of modes in spherical wave expansion," in *Proc. AMTA-2004*, Oct. 2004, pp. 489–494.

[147] S. K. Khamas, "A generalized asymptotic extraction solution for antennas in multi-layered spherical media," *IEEE Trans. Antennas Propag.*, vol. 58, no. 11, pp. 3743–3747, 2010.

[148] J. C. de Munck and M. J. Peters, "A fast method to compute the potential in the multisphere model (EEG application)," *IEEE Trans. Biomed. Eng.*, vol. 40, no. 11, pp. 1166–1174, 1993.

[149] P. Berg and M. Scherg, "A fast method for forward computation of multiple-shell spherical head models," *Electroencephalogr. Clin. Neurophysiol.*, vol. 90, no. 1, pp. 58–64, Jan. 1994.

[150] F. Ting, "Fast solutions of electromagnetic fields in layered media," Ph.D. dissertation, National University of Singapore, Singapore, 2007.

[151] L.-W. Li, T. Fei, Q. Wu, and T.-S. Yeo, "Convergence acceleration for calculating radiated fields by a vertical electric dipole in the presence of a large sphere," in *Proc. IEEE Antennas and Propagation Society Int. Symp*, vol. 2, 2005, pp. 117–120.

[152] S. K. Khamas, "Asymptotic extraction approach for antennas in a multilayered spherical media," *IEEE Trans. Antennas Propag.*, vol. 58, no. 3, pp. 1003–1008, 2010.

[153] A. Fallahi and B. Oswald, "On the computation of electromagnetic dyadic green's function in spherically multilayered media," *IEEE Trans. Microw. Theory Tech.*, no. 99, 2011, early Access.

[154] Zeus. [Online]. Available: http://www.zeusinc.com/technicalservices /technicalbulletins/technicalinformation/biocompatibility.aspx

[155] PEEK^{TM} (polyetheretherketones) produced by VICTREX Polymers. [Online]. Available: http://www.victrex.com/en/products/victrex-peek-polymers/victrex-peek-polymers.php

[156] Material library, ansoft High Frequency Structure Simulator (HFSS) v. 11.1 (2009). [Online]. Available: http://www.ansoft.com/products/hf/hfss/

[157] T. Konaka, M. Sato, H. Asano, and S. Kubo, "Relative permittivity and dielectric loss tangent of substrate materials for high-Tc superconducting film," *Journal of Superconductivity*, vol. 4, no. 4, pp. 283–288, Aug. 1991.

[158] F. Merli, B. Fuchs, and A. K. Skrivervik, "Influence of insulation for implanted antennas," in *Proc. 3rd European Conference on Antennas and Propagation EuCAP 2009*, 23–27 Mar. 2009, pp. 196–199.

[159] Kaye&Laby, Tables of Physical and Chemical Constants, Section 2.6.5. [Online]. Available: http://www.kayelaby.npl.co.uk/toc/

[160] P. Atanasov, S. Yang, C. Salehi, A. L. Ghindilis, E. Wilkins, and D. Schade, "Implantation of a refillable glucose monitoring-telemetry device," *Biosens. Bioelectron.*, vol. 12, no. 7, pp. 669–680, 1997.

[161] Y. Rahmat-Samii and J. Kim, *Implanted Antennas in Medical Wireless Communications*, ser. Synthesis Lectures on Antennas. USA: Morgan & Claypool, 2006.

[162] C.-M. Lee, T.-C. Yo, F.-J. Huang, and C.-H. Luo, "Dual-resonant π-shape with double L-strips PIFA for implantable biotelemetry," *Electronics Letters*, vol. 44, no. 14, pp. 837–838, July 2008.

[163] T.-F. Chien, C.-M. Cheng, H.-C. Yang, J.-W. Jiang, and C.-H. Luo, "Development of nonsuperstrate implantable low-profile CPW-fed ceramic antennas," *IEEE Antennas Wireless Propag. Lett.*, vol. 9, pp. 599–602, 2010.

[164] C. M. Lee, T. C. Yo, C. H. Luo, C. H. Tu, and Y. Z. Juang, "Compact broadband stacked implantable antenna for biotelemetry with medical devices," *Electronics Letters*, vol. 43, no. 12, pp. 660–662, June 7 2007.

[165] W.-C. Liu, F.-M. Yeh, and M. Ghavami, "Miniaturized implantable broadband antenna for biotelemetry communication," *Microwave and Optical Technology Letters*, vol. 50, no. 9, pp. 2407–2409, 2008.

[166] W.-C. Liu, S.-H. Chen, and C.-M. Wu, "Bandwidth enhancement and size reduction of an implantable PIFA antenna for biotelemetry devices," *Microwave and Optical Technology Letters*, vol. 51, no. 3, pp. 755–757, 2008.

[167] A. Kiourti, M. Christopoulou, S. Koulouridis, and K. Nikita, "Design of a novel miniaturized implantable PIFA for biomedical telemetry," in *Proc. International ICST Conference on Wireless Mobile Communication and Healthcare (MobiHealth 2010)*, 18-20 Oct. 2010.

[168] K. Gosalia, G. Lazzi, and M. Humayun, "Investigation of a microwave data telemetry link for a retinal prosthesis," *IEEE Trans. Microw. Theory Tech.*, vol. 52, no. 8, pp. 1925–1933, Aug. 2004.

[169] K. Gosalia, M. S. Humayun, and G. Lazzi, "Impedance matching and implementation of planar space-filling dipoles as intraocular implanted antennas in a retinal prosthesis," *IEEE Trans. Antennas Propag.*, vol. 53, no. 8, pp. 2365–2373, Aug. 2005.

[170] S. Soora, K. Gosalia, M. S. Humayun, and G. Lazzi, "A comparison of two and three dimensional dipole antennas for an implantable retinal prosthesis," *IEEE Trans. Antennas Propag.*, vol. 56, no. 3, pp. 622–629, Mar. 2008.

[171] K. Ito, W. Xia, M. Takahashi, and K. Saito, "An implanted cavity slot antenna for medical communication systems," in *Proc. 3rd European Conference on Antennas and Propagation EuCAP 2009*, 23–27, 2009, pp. 718–721.

[172] E. Y. Chow, A. Kahn, and P. P. Irazoqui, "High data-rate 6.7 GHz wireless asic transmitter for neural prostheses," in *Proc. 29th Annual International Conference of the IEEE Engineering in Medicine and Biology Society EMBS 2007*, 22–26, 2007, pp. 6580–6583.

[173] Y. Yasir Ahmed, Y. Hao, and C. Parini, "A 31.5 GHz patch antenna design for medical implants," *International Journal of Antennas and Propagation*, no. doi:10.1155/2008/167980, p. 6, Article ID 167980 2008.

[174] T. Karacolak, R. Cooper, J. Butler, S. Fisher, and E. Topsakal, "In vivo verification of implantable antennas using rats as model animals," *IEEE Antennas Wireless Propag. Lett.*, vol. 9, pp. 334–337, 2010.

[175] M. Norris, J.-D. Richerd, and D. Raynes, "Sub minature antenna design for wireless implants," in *Proc. IET Seminar Antennas and Propagation for Body-Centric Wireless Communications*, 2007, pp. 57–62.

[176] C. A. Roopnariane, M.-R. Tofighi, and C. M. Collins, "Radiation performance of small implanted antennas in head at MICS, ISM, and GPS bands," in *Proc. IEEE 36th Annual Northeast Bioengineering Conf*, 2010, pp. 1–2.

[177] K. Y. Yazdandoost and R. Kohno, "An antenna for medical implant communications system," in *Proc. European Microwave Conference*, 9–12, 2007, pp. 968–971.

[178] V. Shirvante, F. Todeschini, X. Cheng, and Y.-K. Yoon, "Compact spiral antennas for MICS band wireless endoscope toward pediatric applications," in *Proc. IEEE Antennas and Propagation Society Int. Symp. (APSURSI)*, 2010, pp. 1–4.

[179] D. Valderas, C. Schmidt, and X. Chen, "Broadband implanted UHF RFID antenna," in *Proc. IEEE Antennas and Propagation Society Int. Symp. (APSURSI)*, 2010, pp. 1–4.

[180] U. Kawoos, G. K. Mugalodi, M. R. Tofighi, S. Neff, and A. Rosen, "A permanently implantable intracranial pressure monitor," in *Proc. IEEE 31st Annual Northeast Bioengineering Conference*, 2–3, 2005, pp. 17–19.

[181] U. Kawoos, M.-R. Tofighi, R. Warty, F. A. Kralick, and A. Rosen, "In-vitro and in-vivo trans-scalp evaluation of an intracranial pressure implant at 2.4 GHz," *IEEE Trans. Microw. Theory Tech.*, vol. 56, no. 10, pp. 2356–2365, Oct. 2008.

[182] S. il Kwak, K. Chang, and Y. J. Yoon, "Ultra-wide band spiral shaped small antenna for the biomedical telemetry," in *Proc. Asia-Pacific Microwave Proceedings APMC 2005*, vol. 1, 4–7 Dec. 2005, p. 4pp.

[183] S. H. Lee and Y. J. Yoon, "Fat arm spiral antenna for wideband capsule endoscope systems," in *Proc. IEEE Radio and Wireless Symp. (RWS)*, 2010, pp. 579–582.

[184] K. Fujimoto, A. Henderson, K. Hirasawa, and J. James, *Small Antennas*, 1st ed., ser. Antenna Series.   Letchworth, England: Electronic & Electrical Research Studies Press, Ltd., 1987.

[185] O. Staub, "Electrically Small Antennas," Ph.D. dissertation, EPFL, Lausanne, 2001.

[186] E. Y. Chow, C.-L. Yang, A. Chlebowski, W. J. Chappell, and P. P. Irazoqui, "Miniature antenna for RF telemetry through ocular tissue," in *Proc. IEEE MTT-S International Microwave Symposium Digest*, 15–20, 2008, pp. 1309–1312.

[187] E. Y. Chow, C.-L. Yang, A. Chlebowski, S. Moon, W. J. Chappell, and P. P. Irazoqui, "Implantable wireless telemetry boards for in vivo transocular transmission," *IEEE Trans. Microw. Theory Tech.*, vol. 56, no. 12, pp. 3200–3208, Dec. 2008.

[188] E. A. Johannessen, L. Wang, L. Cui, T. B. Tang, M. Ahmadian, A. Astaras, S. W. J. Reid, P. S. Yam, A. F. Murray, B. W. Flynn, S. P. Beaumont, D. R. S. Cumming, and J. M. Cooper, "Implementation of multichannel sensors for remote biomedical measurements in a microsystems format," *IEEE Trans. Biomed. Eng.*, vol. 51, no. 3, pp. 525–535, Mar. 2004.

[189] E. A. Johannessen, L. Wang, S. W. J. Reid, D. R. S. Cumming, and J. M. Cooper, "Implementation of radiotelemetry in a lab-in-a-pill format," *Lab Chip*, vol. 6, no. 1, pp. 39–45, Jan. 2006.

[190] P. Mohseni and K. Najafi, "Wireless multichannel biopotential recording using an integrated FM telemetry circuit," in *Proc. 26th Annual Int. Conf. of the IEEE Engineering in Medicine and Biology Society IEMBS '04*, vol. 2, 2004, pp. 4083–4086.

[191] Y. Kim, G. Lee, S. Park, B. Kim, J.-O. Park, and J. ho Cho, "Pressure monitoring system in gastro-intestinal tract," Apr. 2005, pp. 1321 – 1326.

[192] P. Valdastri, A. Menciassi, and P. Dario, "Transmission power requirements for novel zigbee implants in the gastrointestinal tract," *IEEE Trans. Biomed. Eng.*, vol. 55, no. 6, pp. 1705–1710, 2008.

[193] M. R. Yuce, T. Dissanayake, and C. Ho, "Wireless telemetry for electronic pill technology," in *Proc. IEEE Conference SENSORS*, Oct. 2009.

[194] T. Dissanayake, M. R. Yuce, and C. Ho, "Design and evaluation of a compact antenna for implant-to-air UWB communication," *IEEE Antennas Wireless Propag. Lett.*, vol. 8, pp. 153–156, 2009.

[195] H. Yu, G. Irby, D. Peterson, M.-T. Nguyen, G. Flores, N. Euliano, and R. Bashirullah, "Printed capsule antenna for medication compliance monitoring," *Electronics Letters*, vol. 43, no. 22, 25 2007.

[196] H. Yu, G. Flores, S. Reza, G. Irby, C. Batich, R. Bashirullah, V. Meka, D. Peterson, and N. Euliano, "Feasibility study of printed capsule antennas for medication compliance monitoring," in *Biomedical Circuits and Systems Conference, 2007. BIOCAS 2007. IEEE*, Nov. 2007, pp. 41 –44.

[197] R. Bashirullah and N. Euliano, "Capsule antennas for medication compliance monitoring," in *Radio and Wireless Symposium, 2009. RWS '09. IEEE*, Jan. 2009, pp. 123 –126.

[198] H. Yu, C.-M. Tang, and R. Bashirullah, "An asymmetric RF tagging IC for ingestible medication compliance capsules," in *Radio Frequency Integrated Circuits Symposium, 2009, RFIC 2009 IEEE*, June 2009, pp. 101 –104.

[199] Ansoft High Frequency Structure Simulator (HFSS) v. 13.0 (2010). [Online]. Available: http://www.ansoft.com/products/hf/hfss/

[200] P. D. Bradley, "An ultra low power, high performance medical implant communication system (MICS) transceiver for implantable devices," in *Proc. IEEE Biomedical Circuits and Systems Conference BioCAS 2006*, Nov. 2006, pp. 158–161.

[201] ——, "Implantable ultralow-power radio chip facilitates in-body communications," in *RF Design (online magazine)*, 2007. [Online]. Available: http://rfdesign.com/next_generation_wireless/short_range_wireless/706RFDF1.pdf

[202] Zarlink Semiconductors, Integrated Circuit ZL70101. [Online]. Available: http://www.zarlink.com

[203] S. M. Kurtz and J. N. Devine, "PEEK biomaterials in trauma, orthopedic, and spinal implants," *Biomaterials*, vol. 28, no. 32, pp. 4845–4869, Nov. 2007.

[204] ECCOSTOCK HIK 500F produced by Emerson & Cuming. [Online]. Available: http://www.eccosorb.com/products/104/ECCOSTOCK%20HIK%20500

[205] S. Best and J. Morrow, "The effectiveness of space-filling fractal geometry in lowering resonant frequency," *Antennas and Wireless Propagation Letters, IEEE*, vol. 1, pp. 112 – 115, 2002.

[206] ——, "On the significance of current vector alignment in establishing the resonant frequency of small space-filling wire antennas," *Antennas and Wireless Propagation Letters, IEEE*, vol. 2, pp. 201 – 204, 2003.

[207] A. Barraud, "Molecular selective interface for an implantable glucose sensor based on the viscosity variation of a sensitive fluid containing Dextran and Concanavalin A," Ph.D. dissertation, EPFL, Lausanne, Dec. 2008.

[208] L. Bolomey, E. Meurville, and P. Ryser, "Implantable ultra-low power DSP-based system for a miniature chemico-rheological biosensor," in *Proceedings of the Eurosensors XXIII conference*, no. 1, 2009, pp. 1235 – 1238.

[209] W. A. Qureshi, "Current and future applications of the capsule camera." *Nat Rev Drug Discov*, vol. 3, no. 5, pp. 447–450, May 2004.

[210] J. Abadia, F. Merli, J.-F. Zürcher, J. R. Mosig, and A. K. Skrivervik, "3D-spiral small antenna for biomedical transmission operating within the MICS band," *Radioengineering*, vol. 18, no. 4, pp. 359–367, Dec. 2009.

[211] A. D. Yaghjian and S. R. Best, "Impedance, bandwidth, and Q of antennas," *IEEE Trans. Antennas Propag.*, vol. 53, no. 4, pp. 1298–1324, 2005.

[212] U.-M. Jow and M. Ghovanloo, "Design and optimization of printed spiral coils for efficient transcutaneous inductive power transmission," *IEEE Trans. Biomed. Circuits Syst.*, vol. 1, no. 3, pp. 193–202, 2007.

[213] K. M. Silay, C. Dehollain, and M. Declercq, "Improvement of power efficiency of inductive links for implantable devices," in *Proc. Ph.D. Research in Microelectronics and Electronics PRIME 2008*, 2008, pp. 229–232.

[214] U.-M. Jow and M. Ghovanloo, "Modeling and optimization of printed spiral coils in air, saline, and muscle tissue environments," *IEEE Trans. Biomed. Circuits Syst.*, vol. 3, no. 5, pp. 339–347, 2009.

[215] S. Kuenzi, "Implantable glucose sensor: An approach based on a rotating microviscometer combined with a sensitive liquid containing Dextran and Concanavalin A," Ph.D. dissertation, EPFL, Lausanne, Sept. 2007.

[216] S. Kuenzi, E. Meurville, and P. Ryser, "Automated characterization of dextran/concanavalin a mixtures–a study of sensitivity and temperature dependence at low viscosity as basis for an implantable glucose sensor," *Sensors and Actuators B: Chemical*, vol. 146, no. 1, pp. 1 – 7, 2010.

[217] Brouard and Barrandon, *Private Communication*.

[218] S. Lopez-Peña, J.-F. Zürcher, R. Torres, A. G. Polimeridis, and J. R. Mosig, "Modeling and manufacturing of a series of identical antennas for a P-band ice sounder," in *Proc. Fourth European Conf. Antennas and Propagation (EuCAP)*, 2010, pp. 1–5.

[219] J.-F. Zürcher, O. Staub, A. K. Skrivervik, and M. Hermanjat, "Accurate measurement of the maximum gain of electrically small antennas," *Microwave and Optical Technology Letters*, vol. 23, no. 6, pp. 328–331, Nov. 1999.

[220] W. Hurter, F. Reinbold, and W. J. Lorenz, "A dipole antenna for interstitial microwave hyperthermia," *IEEE Trans. Microw. Theory Tech.*, vol. 39, no. 6, pp. 1048–1054, June 1991.

[221] J. C. Lin and Y.-J. Wang, "The cap-choke catheter antenna for microwave ablation treatment," *IEEE Trans. Biomed. Eng.*, vol. 43, no. 6, pp. 657–660, June 1996.

[222] M. E. Ladd and H. H. Quick, "Reduction of resonant RF heating in intravascular catheters using coaxial chokes," *Magn. Reson. Med.*, vol. 43, no. 4, pp. 615–619, Apr. 2000.

[223] I. Longo, G. B. Gentili, M. Cerretelli, and N. Tosoratti, "A coaxial antenna with miniaturized choke for minimally invasive interstitial heating," *IEEE Trans. Biomed. Eng.*, vol. 50, no. 1, pp. 82–88, Jan. 2003.

[224] D. Yang, J. M. Bertram, M. C. Converse, A. P. O'Rourke, J. G. Webster, S. C. Hagness, J. A. Will, and D. M. Mahvi, "A floating sleeve antenna yields localized hepatic microwave ablation," *IEEE Trans. Biomed. Eng.*, vol. 53, no. 3, pp. 533–537, Mar. 2006.

[225] J. M. Bertram, D. Yang, M. C. Converse, J. G. Webster, and D. M. Mahvi, "Antenna design for microwave hepatic ablation using an axisymmetric electromagnetic model," *Biomed. Eng. Online.*, vol. 5, p. 15, 2006.

[226] J. Wu, S. K. Khamas, and G. G. Cook, "An efficient asymptotic extraction approach for the green's functions of conformal antennas in multilayered cylindrical media," *IEEE Trans. Antennas Propag.*, vol. 58, no. 11, pp. 3737–3742, 2010.

List of Acronyms

1D	One Dimensional
3D	Three Dimensional
3G	Third Generation
AEM	Atelier d'électromécanique (Electro-mechanical Workshop)
BS	Base Station
BSN	Body Sensor Node
CHUV	Centre Hospitalier Universitaire Vaudois (University Hospital of Canton Vaud)
DGBE	Diethylene Glycol monoButyl Ether
DSP	Digital signal Processor
EIRP	Equivalent Isotropic Radiated Power
EM	Electromagnetic
ESA	Electrically Small Antenna
ETSI	European Telecommunications Standards Institute
FCC	Federal Communication Commission
FF	Far Field
FIFA	Folded Inverted-F Antenna
FRH	Folded Rectangular Helix
GPS	Global Positioning System
HEC	HydroxylEthylCelulose
HFSS	High Frequency Structure Simulator
HP	Hewlett-Packard
IC	Integrated Circuit
IEEE	Institute of Electrical and Electronics Engineers
IF	Intermediate Filter
ISM	Industrial, Scientific and Medical (at 2.45 GHz otherwise stated)

LDCS	Laboratoire de Dynamique des Cellules Souches (Laboratory of Stem Cell Dynamics)
LPM	Laboratoire de Production Microtechnique 2 (Laboratory of Microengineering for Manufacturing 2)
LSI	Laboratoire des Systèmes Intégrés (Integrated System Laboratory)
MAS	Method of Auxiliary Sources
MedRadio	Medical Device Radiocommunications Service (formerly MICS)
MICS	Medical Implanted Communication System
MMT	Mode Matching Technique
MoM	Method of Moments
MSA	Multilayered Spiral Antenna
NF	Near Field
NMHA	Normal Mode Helical Antenna
PCB	Printed Circuit Board
PEC	Perfect Electric Conductor
PEEK	Polyetheretherketones
PIFA	Planar Inverted-F Antenna
PMMA	Poly(methyl methacrylate)
Q	Quality Factor
RF	Radio Frequency
SAR	Specific Absorption Rate
SEP	Surface Equivalence Principle
STI	School of Engineering (at EPFL)
SWE	Spherical Wave Expansion
UNIL	Université de Lausanne (University of Lausanne)
USB	Universal Serial Bus
UWB	Ultra-WideBand
VLF	Very Low Frequency
WBAN	Wireless Body Area Network

CV

Francesco Merli was born on February 24, 1981 in Faenza, Italy. He received the Diploma degree in Telecommunication Engineering (laurea) from the University of Florence, in December 2006 with a final mark of 110/110 cum laude and honors (top 2%).

In April 2007 he enrolled the PhD studies at the Laboratoire d'Electromagnétisme et d'Acoustique (LEMA) of the Ecole Polytechique Fédérale de Lausanne (EPFL) where he is currently a Research and Teaching Assistant. As a Research Assistant in LEMA, he has been responsible for several projects:

- NANO-TERA Swiss federal program funding for engineering complex systems for health, security and the environment: "BioAnt (Bio Implantable Antennas)", Theoretical study, design and characterization of implantable antennas dedicated to in-body telemetry `http://www.nano-tera.ch/projects/32`.php (2010-present)

- Swiss National Science Foundation (SNSF) Sinergia: "Miniature Atomic Clocks and Quantum Sensors", Analysis, design and realization of small microwave cavities for RB atomic watch applications `http://www.snf.ch/E/funding/projects/sinergia/Pages/default.aspx` (2009-present)

- EPFL Commission for Technology and Innovation (CTI): "ROSE (ROund SEnsor)", Design of a new generation of wireless sensor network nodes and production tests and calibration environment for US and EU markets (2007-2010) `http://esplab.epfl.ch/page-9450-en.html`

- EPFL School of Engineering (STI): "Implantable antennas for biomedical applications", Analysis, design, realization and measurements of implantable antennas and field propagation for medical telemetry applications (2007-2009)

As a Teaching Assistant he has been involved in the exercises and teaching of classes on Electromagnetics I, II and Microwave courses, respectively. He supervised several semester and master projects.

He was a Research visitor at the at the Institut d'Electronique et de Télécommunications de Rennes (IETR), University of Rennes 1, Rennes, France in September 2009 in the frame of a COST 1603 Short Term Scientific Mission working on spherical wave expansion and implantable applications.

In Summer 1999 he was a visiting student at Cabra Dominican College, Adelaide, Australia.

Francesco Merli is a student member of the IEEE.

List of Publications

REFEREED JOURNAL PAPERS

1. M. Tanevski, F. Merli, A. Boegli, A.K. Skrivervik, J.-F. Zürcher and P.-A. Farine, "Sub-GHz wireless sensor platform with housing integrated overmolded antenna," submitted for publication in *IEEE Transactions on Instrumentation and Measurement.*

2. F. Merli, L. Bolomey, J.-F. Zürcher, G. Corradini, E. Meurville and A.K. Skrivervik, "Design, realization and measurements of a miniature antenna for implantable wireless communication systems," *IEEE Transactions on Antennas and Propagation*, accepted for publication.

3. F. Merli, B. Fuchs, J.R. Mosig and A.K. Skrivervik, "The effect of insulating layers on the performance of implanted antennas," *IEEE Transactions on Antennas and Propagation*, vol. 59, no. 1, pp. 21–31, Jan. 2011.

4. I. Stevanović, F. Merli, P. Crespo-Valero, W. Simon, S. Holzwarth, M. Mattes and J.R. Mosig, "Integral equation modeling of waveguide-fed planar antennas," *IEEE Antennas and Propagation Magazine*, vol. 51, no. 6, pp. 82–92, Dec. 2009.

5. J. Abadia, F. Merli, J.-F. Zürcher, J.R. Mosig and A.K. Skrivervik, "3D-spiral small antenna design and realization for biomedical telemetry in the MICS band," *Radioengineering*, vol. 18, num. 4, pp. 359–367, Dec. 2009.

6. F. Merli, J.-F. Zürcher, A. Freni and A.K. Skrivervik, "Analysis, design and realization of a novel directive ultra-wideband antenna," *IEEE Transactions on Antennas and Propagation*, vol. 57, no. 11, pp. 3458–3466, Nov. 2009.

PATENTS

1. L. Bolomey, F. Merli, E. Meurville, J.-F. Zürcher, and A.K. Skrivervik, "Telemetry system for sensing applications in lossy media," International Request PCT/IB2011/050991 for the Swiss Patent Application: 00335/10, 11$^{\text{th}}$ Mar. 2010.

REFEREED CONFERENCE PAPERS

1. A.K. Skrivervik and F. Merli, "Design strategies for implantable antennas (Invited)," submitted to the 7$^{\text{th}}$ *Loughborough Antennas & Propagation Conference 2011 (LAPC 2011)*, Loughborough, United Kingdom, Nov. 14–15, 2011.

2. F. Merli, L. Bolomey, F. Gorostidi, Y. Barrandon E. Meurville, and A.K. Skrivervik, "In vitro and in vivo operation of a wireless body sensor node," submitted to the 2$^{\text{nd}}$ *Interna-*

213

tional ICST Conference on Wireless Mobile Communication and Healthcare (MobiHealth 2011), Kos Island, Greece, Oct. 5–7, 2011.

3. F. Merli, L. Bolomey, J.-F. Zürcher, E. Meurville, and A.K. Skrivervik, "Versatility and tunability of an implantable antenna for telemedicine," in *Proc. 5ᵗʰ European Conference on Antennas and Propagation (EuCAP 2011)*, Rome, Italy, Apr. 11–15, 2011.

4. M. Tanevski, A. Boegli, P.-A. Farine, F. Merli, J.-F. Zürcher and A.K. Skrivervik, "Robust ultra low power wireless sensor platform with embedded over-molded antenna," in *Proc. IEEE Sensors Applications Symposium*, San Antonio, TX, USA, Feb. 22–24, 2011.

5. A.K. Skrivervik and F. Merli, "On the design and characterization of bio-implantable antennas," in *Proc. 20ᵗʰ International Conference of Applied Electromagnetics and Communications, ICECom 2010*, Dubrovnik, Croatia, Sept. 20–23, 2010.

6. A.K. Skrivervik and F. Merli, "On the efficient design, analysis and measurement of bio-implantable electrically small antennas (Invited)," *20ᵗʰ International Symposium on Electromagnetic Theory and USNC/URSI National Radio Science Meeting*, Berlin, Germany, Aug. 16–19, 2010.

7. F. Merli, L. Bolomey, E. Meurville, and A.K. Skrivervik, "Dual band antenna for subcutaneous telemetry applications," in *Proc. IEEE Antennas and Propagation Society Symposium (AP-S)*, Toronto, Ontario, Canada, July 11–17, 2010.

8. F. Merli and A.K. Skrivervik, "Design and measurement considerations for implantable antennas for telemetry applications," in *Proc. 4ᵗʰ European Conference on Antennas and Propagation (EuCAP 2010)*, Barcelona, Spain, Apr. 12–16, 2010.

9. F. Merli, B. Fuchs, and A.K. Skrivervik, "Influence of insulation for implanted antennas," in *Proc. 3ʳᵈ European Conference on Antennas and Propagation (EuCAP 2009)*, Berlin, Germany, Mar. 23–27, 2009.

10. J. Abadia, F. Merli, J.-F. Zürcher, J.R. Mosig and A.K. Skrivervik, "3D-spiral small antenna for biomedical transmission operating within the MICS band," in *Proc. 3ʳᵈ European Conference on Antennas and Propagation (EuCAP 2009)*, Berlin, Germany, Mar. 23–27, 2009.

11. F. Merli, L. Bolomey, E. Meurville, and A.K. Skrivervik, "Implanted antenna for biomedical sensors," in *Proc. European Electromagnetics (EUROEM 08)*, Lausanne, Switzerland, Jul. 21–25, 2008.

12. F. Merli, L. Bolomey, E. Meurville, and A.K. Skrivervik, "Implanted antenna for biomedical applications," in *Proc. IEEE Antennas and Propagation Society Symposium (AP-S)*, San Diego, CA, USA, Jul. 4–12, 2008.

13. F. Merli, J.-F. Zürcher, A. Freni and A.K. Skrivervik, "Design of a directive ultra-wideband antenna," in *Proc. 2ⁿᵈ European Conference on Antennas and Propagation (EuCAP 2007)*, Edinburgh, UK, Nov. 11–16, 2007.

WORKSHOP PRESENTATIONS

1. F. Merli and A.K. Skrivervik, "Recent advancements in implanted devices for data telemetry," *NANO-TERA Plenary Meeting*, Bern, Switzerland, May 12–13, 2011.

2. F. Merli, K. Jaber and A.K. Skrivervik, "Implantable antennas & body phantoms," *SEMCAD Worshop* at 5th *European Conference on Antennas and Propagation (EuCAP 2011)*, Rome, Italy, Apr. 11–15, 2011.

3. F. Merli, B. Fuchs, J.R. Mosig and A.K. Skrivervik, "Effectiveness of biocompatible insulations on the radiation of implanted antennas," *COST IC0603 "ASSIST"*, Les Diablerets , Mar. 16-18, 2011.

4. F. Merli, L. Bolomey, B. Fuchs, J.-F. Zürcher, E. Meurville, and A.K. Skrivervik, "Design and realization of an implantable system for biomedical applications," *IET Body centric wireless communications workshop*, London, Apr. 20, 2009.

5. J. Abadia, F. Merli, J.-F. Zürcher, J.R. Mosig and A.K. Skrivervik, "Design of a small antenna operating within the MICS band," *Journeés des ondes (GDR ONDES) - CNRS Champ proche optique, THz et microonde - CEM*, Lausanne, Feb. 5–6, 2009.

6. F. Merli and A.K. Skrivervik, "Design and realization of an implantable system for biomedical applications," *EPFL STI Oktoberfest*, Lausanne, Oct. 28, 2008.

7. F. Merli and A.K. Skrivervik, "Implantable antenna for biomedical purpose," *EPFL Research Day*, Lausanne, Apr. 15, 2008.